Development of Creep-Resistant Al-Si Cast Alloys Strengthened with Nanoscale Dispersoids

Amir Rezaei Farkoosh

Mining and Materials Engineering

McGill University
Montreal
September 2014

A thesis submitted to McGill University in partial fulfillment of the requirements of the degree of Doctor of Philosophy

ABSTRACT

This doctoral thesis aimed at creating thermally stable precipitates (dispersoids) via the use of slow-diffusing elements, Ni, Mo and Mn to develop creep resistant Al-Si cast alloys to be used for Diesel engine applications above 250°C and in the 20-30MPa stress range. CALPHAD-based thermodynamic calculations (FactSage, ThermoCalc) were carried out to determine the phase selections and solidification paths in the alloy systems. The precipitates and their influence on creep deformation were studied via conventional and high-resolution transmission electron microscopy.

Ni up to 0.6wt.% increased the strength of the base alloy, Al-7Si-0.5Cu-0.3Mg at 300°C, but lowered the creep resistance because of the severe cracking of the brittle *T*-Al_9FeNi intermetallics. Mn addition imparted ductility to *T*-Al_9FeNi, preventing cracking during creep and led to improved creep resistance. No dispersoid phase was observed in this alloy system.

The second stage of the study investigated the effect of Mo addition on dispersoid formation. Mo formed nanoscale coherent dispersoids through a high temperature solution-treatment. The Mo-containing alloy exhibited significant improvement in mechanical properties at 300°C compared to the base alloy. A 90-95% decrease in the minimum creep rate was observed at 300°C and 30MPa, and the creep time-to-fracture increased by two orders of magnitude. The tensile yield strength and elongation at 300°C increased by 25% and 34%, respectively. These effects were attributed to the formation of the dispersoids with approximate stoichiometric formula of $Al_{22}(Fe_{6-8}Mo)Si_4$ as determined by quantitative EDS. Their crystal structure was BCC with lattice parameter, a_o =12.54±0.03 A° and space group Im3. The orientation relationship most commonly observed between the Al matrix and dispersoids was ⟨001⟩d//⟨001⟩m and {350}d//{002}m. The precipitation of the dispersoids in large amounts and their coherency was accounted for by the structural correlation that was found between the BCC dispersoid phase and the FCC Al matrix. The creep behaviour of the Mo-containing alloy was studied in details. On the basis of the TEM studies and steep changes in the stress exponent, three distinct creep deformation regions were identified as: I- diffusion creep (n_a ~1.5), II- dislocation creep (n_a ~20) and III- Orowan bowing (n_a >> 20).

In the third phase of the study, Mn was added to the Mo-containing alloy to enhance the precipitation of the dispersoids. The combined additions of Mo and Mn increased the volume fraction of the dispersoids and lead to a more uniform distribution of the dispersoids. The beneficial effect of Mn was attributed to its solute characteristics in Al: Mn is a slow-diffuser, with relatively high solid solubility, and its solute partitioning behavior during solidification is opposite to Mo ($k_{Mn}<1$ vs. $k_{Mo}>1$). The minimum creep rate decreased with Mn content at 300°C, 30MPa. The creep time-to-fracture also increased from ~25 to ~180 hours as Mn increased from 0.0 to 0.5%. In this study, this alloy was determined to be the best candidate for use in elevated temperature engine applications.

The final part of the thesis determined the effect of Mg level (0.3-0.7wt.%) on the strength and creep resistance of the base alloy at 300°C. Increasing the Mg to the solubility limit of 0.47wt.% increased the amount of *Q* and improved the strength and creep resistance at 300°C. The improvement was not as high as the combined addition of Mo and Mn to the base alloy.

In conclusion, this thesis project was successful in developing a new alloy exhibiting significant improvements over existing alloys used in Diesel applications. The Al-Si-Mo-Mn system was introduced, which offers significant potential for development of elevated temperature cast alloys. This alloy system can be used for lightweighting in automotive industry and promote the wide use of Al-Si alloys in more severe operating conditions such as Diesel engine applications.

RÉSUMÉ

Cette thèse de doctorat avait pour objectif principal la formation de fins précipités thermiquement stables (dispersoïdes) par l'addition d'éléments de diffusion lent, tels que: Ni, Mo et Mn, pour développer d'alliages Al-Si résistant au fluage pour l'utilisation dans de moteur Diésel à des températures au-dessus de 250ºC et de 20-30MPa. Des calculs thermodynamiques (FactSage et ThermoCalc) ont été réalisés afin d'effectuer la sélection de phases ainsi que les modes de solidification. Les précipités ainsi que leur influence sur la déformation par le fluage ont alors été étudiés par la méthode d'examen par la microscopie électronique conventionnelle et à haute résolution.

Ni jusqu'à 0.6 % poids augmente la résistance des alliages à 300ºC, mais réduit la résistance au fluage à cause de la fissuration de la phase fragile du compose intermétallique T-Al_9FeNi au début de la déformation lors des essais de fluage. Le Mn a permis d'améliorer la ductilité du T-Al_9FeNi, éliminer sa fissuration lors du fluage et conduit à une résistance améliorée au fluage. Aucun dispersoïdes n'a été observé dans les alliages.

L'étape 2 de cette étude a été orientée vèrs l'addition de Mo à cause de son potentiel pour la formation de dispersoïdes dans les alliages Al-Si. Le Mo a formé de dispersoïdes cohérents à l'échelle nanométrique au cours de traitements-thermiques effectués à haute température. L'alliage contenant du Mo a montré une amélioration significative des propriétés mécaniques à 300ºC. Une diminution de 90 à 95% du taux minimal de fluage a été observée à la température de 300ºC et à une contrainte de 30MPa et de plus, le temps de rupture au fluage a alors augmenté selon un ordre de magnitude de deux fois. La force de cédage en tension et l'allongement à 300ºC ont respectivement augmentés de 25% et 34%. Ces effets ont été attribués à la formation de dispersoïdes, $Al_{22}(Fe_{6-8}Mo)Si_4$ avec structure cristalline CVC (a_o =12.54±0.03 A°; groupe spatial Im3). La relation d'orientation observé le plus entre la matrice Al et le dispersoïdes était ⟨001⟩d//⟨001⟩m et {350}d//{002}m. La précipitation des dispersoïdes en grande quantité et leur cohérence a été expliqué par la corrélation structurale entre les dispersoïdes et la matrice Al. Trois différentes zones de fluage ont alors été identifiées pour l'alliage contenant du Mo telles que: I- fluage par diffusion (n_a ~1.5), II- fluage par le mouvement des dislocations (n_a ~20) and III- le mécanisme Orowan (n_a >> 20).

Dans Phase 3, les additions combinées du Mo et du Mn ont augmenté la proportion en volume des dispersoïdes et ont conduit à une dispersion plus uniforme. Le taux minium de fluage a diminué avec la teneur en Mn à 300ºC, 30MPa. Le temps menant à la rupture lors du fluage a augmenté d'environ 25 à 180h en fonction de l'augmentation de la teneur en Mn de 0.0 à 0.5%. Ainsi, dans cette étude, cet alliage est le meilleur candidat pour ce qui a trait aux applications pour les moteurs à température élevée.

La dernière partie de cette thèse est sur l'effet de la teneur en Mg (0.3-0.7% poids) sur la force et la résistance au fluage des alliages de base à 300 ºC. En augmentant la teneur en Mg jusqu'à sa limite de solubilité de 0.47% poids, celui-ci a augmenté la teneur du précipités *Q*, et a amélioré la résistance au fluage à 300ºC. L'amélioration n'a pas été aussi élevée que la combinaison des additions de Mo et de Mn dans l'alliage de base.

Ce projet de thèse a été un succès pour ce qui a trait au développement d'un nouvel alliage qui procure des améliorations significatives relativement aux alliages conventionnels utilisé pour la fabrication des moteurs au Diésel. Le système Al-Si-Mo-Mn qui a été élaboré lequel offre un potentiel prometteur pour le développement des alliages pour l'application à température élevée. Ce système d'alliage peut ainsi faire la promotion d'un plus large éventail pour l'utilisation des alliages Al-Si dans des conditions exigeantes.

ACKNOWLEDGEMENTS

There are many individuals that I wish to thank for making my experience at McGill productive and pleasant. First and foremost, I would like to thank Prof. Mihriban Pekguleryuz for her guidance, support and encouragement throughout the course of my doctoral studies. I learned a great deal from her about alloy development and physical metallurgy. It is a great honour to work with her. I am also grateful to Pierre Vermette for his invaluable technical support and assistance in experimental work.

I would like to thank all my fellow graduate students and postdocs on the second floor of the Wong building for contributing to a cheerful and friendly environment. Sincere thanks to Mohsen Masoumi, Alireza Sadeghi, Deniz Sultan Temur, Mert Celikin, Hemant Borkar, Mandana Bornapour, Majid Hoseini, Naser Muja, Huseyin Aydin, Mehdi Sanjari, Amir Farzadfar, Jinke Xu, Hesam Mahjoubi, Nima Parsi, Maziar Shah Mohammadi, Amir K. Miri, Abu Syed Kabir, Sazol Das and others whose names may have escaped.

I am indebted to Prof. Daniel Larouche and Mousa Javidani (Laval University) for helping me perform thermodynamic calculations required for my research. I wish to thank Dr. Fred Major of Rio Tinto Alcan for valuable discussions and his intellectual contribution and support. My special gratitude goes to Prof. Hojatollah Vali (McGill University) for his kind help and support. Likewise, I wish to thank Dr. Xue-Dong Liu of McGill FEMR (Facility for Electron Microscopy Research) and Lang Shi of the department of earth and planetary sciences for fruitful discussions. I am grateful to Prof. Philippe Bocher of École de technologie supérieurefor allowing me to conduct hot tensile tests in his laboratory. I would also like to thank Prof. X.Grant Chen of the University of Québec at Chicoutimi for his research support provided during the two years of the light metals laboratory closure. I wish to express my gratitude to Dr. Celil Aliravci for his additional motivation and support during the preparation of this dissertation. Many thanks also to Barbara Hanley, Courtney Jelaco and Terry Zatylny for their kindness and assistance with departmental matters.

I deeply appreciate the neverending encouragement, support and love that I received from my wife and best friend, Tabassom throughout the course of my doctoral studies. Thank you for being so understanding, patient and caring. I am indebted to my mom and dad and all my dear friends for their heartfelt love and encouragement.

I would like to gratefully acknowledge the financial support of McGill University through the Lorne Trottier engineering graduate fellowship-MEDA (McGill Engineering Doctoral Award) and MIDA (McGill International Doctoral Award). Department of Mining and Materials Engineering at McGill University is acknowledged for the Research Excellence Recognition Award, and GREAT Award. Likewise I wish to acknowledge Aluminium Research Centre – REGAL for travel awards. Financial support during my PhD was provided in part by the NSERC (Natural Sciences and Engineering Research Council) of Canada and Rio Tinto Alcan. A part of the research presented in this work was financed by the Fonds de recherche du Québec - Nature et technologies by the intermediary of the Aluminium Research Centre – REGAL.

CONTRIBUTION OF AUTHORS

This dissertation presents seven manuscripts written by the candidate according to the guidelines for a manuscript-based dissertation. These guidelines are published by the Graduate and Postdoctoral Studies office of McGill University. All the manuscripts have been published, accepted or submitted for publication as indicated:

1. **A.R. Farkoosh**, M. Javidani, M. Hoseini, D. Larouche, M. Pekguleryuz, "*Phase formation in as-solidified and heat-treated Al–Si–Cu–Mg–Ni alloys: Thermodynamic assessment and experimental investigation for alloy design*", ***J. Alloys Compd.***, 551 (2013) 596-606.
2. **A.R. Farkoosh**, M. Pekguleryuz, "*The effects of manganese on the T-phase and creep resistance in Al–Si–Cu–Mg–Ni alloys*", ***Mater. Sci. Eng., A***, 582 (2013) 248-256.
3. **A.R. Farkoosh**, X-G. Chen, M. Pekguleryuz, "*Dispersoid strengthening of a high temperature Al-Si-Cu-Mg alloy via Mo addition*", ***Mater. Sci. Eng., A***, 620 (2014) 181-189.
4. **A.R. Farkoosh**, X-G. Chen, M. Pekguleryuz, "*Precipitation of coherent α-Al(Fe,Mo)Si dispersoids in an Al-Si-Cu-Mg cast alloy via Mo addition*", submitted to ***J. Alloys. Comp.*** 2014.
5. **A.R. Farkoosh**, X-G. Chen, M. Pekguleryuz, "*Al-Si-Cu-Mg-Mo alloy strengthened by thermally stable coherent dispersoids: creep resistance and mechanisms at 300-350 ^oC*", submitted to ***Mater. Sci. Eng., A*** 2014.
6. **A.R. Farkoosh**, X-G. Chen, M. Pekguleryuz, "*Interaction between molybdenum and manganese to form effective dispersoids in an Al-Si-Cu-Mg alloy and its influence on creep resistance*", accepted by ***Mater. Sci. Eng., A*** 2014.
7. **A.R. Farkoosh**, M. Pekguleryuz, "*Enhanced mechanical properties of an Al-Si-Cu-Mg alloy at 300 ^oC: effects of Mg and the Q-Precipitate phase*", ***Mater. Sci. Eng., A***, 621 (2015) 277-286.

All the experiments and simulations are designed, planned and conducted by the candidate as well as material preparation, data collection and analyses. All the manuscripts are co-authored by Prof. Mihriban Pekguleryuz as the candidate's supervisor. She provided guidance throughout the whole research project, reviewed the manuscripts and contributed to the general layout and discussions. The role of the other co-authors are explained below:

Mousa Javidani (PhD candidate, Department of Mining, Metallurgy and Materials Engineering, Laval University) and **Dr. Majid Hoseini** (previous postdoctoral researcher, Department of Mining and Materials Engineering, McGill University) reviewed the manuscript 1 and provided helpful discussions on thermodynamic calculations.

Prof. Daniel Larouche (Department of Mining, Metallurgy and Materials Engineering, Laval University) provided us with ThermoCalc software and reviewed the manuscript 1.

Prof. X-G. Chen (Department of Applied Science, University of Québec at Chicoutimi) provided us with casting facilities, reviewed the manuscripts 3-6 and provided insightful comments.

TABLE OF CONTENTS

CHAPTER 10: CONCLUSIONS AND SUGGESTIONS FOR FUTURE RESEARCH 210

CHAPTER 11: CONTRIBUTIONS TO ORIGINAL KNOWLEDGE 217

LIST OF FIGURES

CHAPTER 1

CHAPTER 2

CHAPTER 3

CHAPTER 4

CHAPTER 5

CHAPTER 6

CHAPTER 7

CHAPTER 8

CHAPTER 9

LIST OF TABLES

CHAPTER 2

CHAPTER 3

CHAPTER 4

CHAPTER 5

CHAPTER 6

CHAPTER 7

CHAPTER 8

CHAPTER 9

CHAPTER 1

INTRODUCTION

1.1 Introduction

TDI clean Diesel offers compelling advantages over common gasoline engines, which make it a sustainable environmentally friendly technology for vehicles. Diesel engines use the heat of compression to ignite the fuel injected into the combustion chamber. Because of their very high compression ratio (20 : 1 vs. 8 : 1 for gasoline engine), Diesel engines generate significantly higher torque output, with higher fuel efficiency and lower CO_2 emissions per mile (13.4 lbs vs. 19.4 lbs for gasoline engine) [1]. Currently, Diesel engine components such as the engine block and cylinder head are mostly made of cast iron in order to withstand the severe operating conditions. These components (Fig. 1.1) are complex cast structures as they house the cylinders and surrounding structures such as coolant passages. *Thermal fatigue* in the inter-valve regions is one of the most challenging design problems, which often causes cracking in these regions [2].

Lightweighting through Al substitution would result in greater fuel economy and increased environmental benefits. However, commercial aluminum engine alloys, the A356 (Al-7Si-0.3Mg) and A319 (Al-6Si-4Cu), do not perform adequately under Diesel engine operating conditions. Aluminum alloy development activities for Diesel engines began in 1998 by VAW [3, 4] with early alloy development efforts mostly based on the modification of the existing commercial alloys (based on the Al-7Si system). As a result, one alloy, the A356 with low level addition of Cu, attained small market share in the Diesel application [2]. Cu was added to enhance the age-hardening response [3, 4]. However, strength drops dramatically with increasing temperature, because of the metallurgical instabilities at elevated temperatures, which results in poor thermal fatigue resistance of these alloys [1, 5].

Currently, the peak firing pressure is limited to low pressures of ~ 150 bar (temperature below 250 °C) for aluminum engines [2, 6, 7], since the existing alloys cannot endure the severe thermal fatigue conditions [2]. Increasing torque requirements in newer common rail TDI Diesel engines necessitate new alloys with improved performance under thermal fatigue conditions [2, 8].

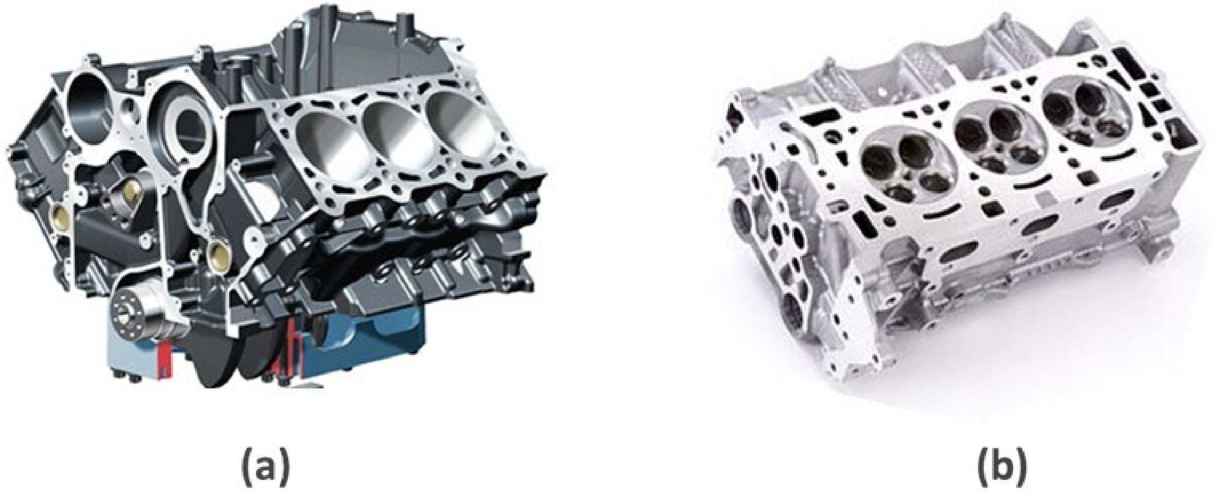

Fig. 1.1 (a) An Audi 3L V6 cast iron Diesel engine block and (b) cylinder head [9].

In 2008, Prof. Pekguleryuz's team at McGill embarked on adding dispersoid formers such as Cr, Ti and Mn to the Al-Si-Cu-Mg alloys in collaboration with Rio Tinto Alcan [1, 2, 10-12]. During the same time, groups in Europe concentrated on V additions to the Al-Si-Cu alloys as dispersoid formers. Here, developing high temperature aluminum alloys faces several challenges in producing effective dispersoids and intermetallics. In particular, because of the low solid solubility of the dispersoid-forming solute atoms in the Al matrix [13, 14], especially in the case of the Al-Si cast alloys, the volume fraction of the dispersoids formed is not sufficiently high to impart significant strength [15, 16]. Because of the aforementioned problem associated with dispersoid formation in Al-Si alloys, all the efforts in developing elevated temperature cast alloys for Diesel engine applications were partially successful [2]. In this doctoral work, a step-by-step approach is used to form new effective dispersoids in large volume fractions. Combined addition of alloying elements is targeted to produce high volume fractions of thermally stable and coherent dispersoids.

1.2 Research hypothesis, aims and objectives

The long-term aim of this research is to develop creep resistant Al-7Si cast alloys that can be used for Diesel engine applications at temperatures above 250 °C and stress levels in the range of 20-30 MPa. It is hypothesized that the combined addition of strategically selected slow-diffusing solute atoms at low levels in Al-Si cast alloys may give rise to a large volume fraction of dispersoids. This doctoral thesis aims to study the behavior of slow-diffusing alloying elements in Al-7Si cast alloys with the purpose of creating thermally stable dispersoids. Three transition metals, Ni, Mn and Mo were selected on the basis of their low diffusivity in the Al matrix and potential for dispersoid formation. An effective dispersoid phase should be coherent with the matrix, have large coherency strain and form in a large amount [13, 17]. The ultimate selection of alloying elements was to be made on the basis of the type of dispersoids that they form. One of the evaluation criteria was creep resistance at the Diesel operating temperatures. The specific objectives were to:

I. Study the behavior of Ni in the Al-7Si cast alloys, determine the phase selection and investigate the influence of microstructural factors on the creep deformation and strengthening mechanisms. Determine their effectiveness on creep resistance and determine the underlying mechanism.

II. Investigate the Mo alloying of Al-7Si alloys via thermodynamic calculations and experimental investigation to acquire fundamental knowledge on the solidification, phase selection and dispersoid formation. Evaluate the influence of dispersoids on mechanical properties at elevated temperatures. Study the crystallography of the dispersoids embedded in the Al matrix to understand the nature of the dispersoids and their strengthening potency. Investigate the creep deformation mechanisms of the Mo-containing alloys via calculation of activation energies for creep, determination of stress exponents and TEM analysis.

Investigate the role of the Mo-containing dispersoids and their particle size distribution in creep deformation processes.

III. Investigate further alloying with solutes to either (i) enhance dispersoid formation (e.g. Mn) or (ii) improve the creep resistance in the base alloy (e.g Mg)

1.3 Thesis outline

The present research work is directed towards the development of creep resistant Al-Si cast alloys as materials for Diesel engine applications. *This is a manuscript based thesis*. The thesis comprises 11 chapters. Chapter 1 (the present chapter) provides a general introduction, research hypotheses, objectives and the thesis outline. Chapter 2 states the research question, and provides a literature review and background on the Al-Si engine alloys.

Chapters 3 and 4 present the results on Ni alloying of the Al-7Si-0.5Cu-0.3Mg base alloy. Chapter 3 contains the manuscript "A.R. Farkoosh, M. Javidani, M. Hoseini, D. Larouche, M. Pekguleryuz, "*Phase formation in as-solidified and heat-treated Al–Si–Cu–Mg–Ni alloys: Thermodynamic assessment and experimental investigation for alloy design*", J. Alloys Compd., 551 (2013) 596-606". Chapter 4 is on the elevated temperature mechanical properties (strength, creep resistance) of the Al-7Si-0.5Cu-0.3Mg-(0.3-1)Ni-(0.0-1.0Mn) alloys, the role of the microstructure and further alloying with Mn. The results have been published as "A.R. Farkoosh, M. Pekguleryuz, "*The effects of manganese on the T-phase and creep resistance in Al–Si–Cu–Mg–Ni alloys*", Mater. Sci. Eng., A, 582 (2013) 248-256".

Chapters 5, 6 and 7 are on Mo additions to the Al-7Si-0.5Cu-0.3Mg alloy. Chapter 5, contains the manuscript "A.R. Farkoosh, X-G. Chen, M. Pekguleryuz, "*Dispersoid strengthening of a high temperature Al-Si-Cu-Mg alloy via Mo addition*", Mater. Sci. Eng., A 620 (2014) 181-189" Chapter 6 presents the TEM and HRTEM investigation of the formation and evolution of nanoscale dispersoid phase during the solution treatment of the Al-7Si-0.5Cu-0.3Mg-0.3Mo alloy. The results are reported in the manuscript "A.R. Farkoosh, X-G. Chen, M. Pekguleryuz, "*Precipitation of coherent α-Al(Fe,Mo)Si dispersoids in an Al-Si-Cu-Mg cast alloy via Mo addition*", submitted to J. Alloys. Comp. 2014". A detailed creep investigation of the Mo-containing alloy is presented in this Chapter 7, which contains "A.R. Farkoosh, X-G. Chen, M.

Pekguleryuz, "*Al-Si-Cu-Mg-Mo alloy strengthened by thermally stable coherent dispersoids: creep resistance and mechanisms at 300-350 °C*", submitted to Mater. Sci. Eng., A 2014".

Chapter 8 presents the key results of this thesis work, namely the combined addition of Mo and Mn to the base alloy. Al-Si-Cu-Mg-Mo-Mn alloy developed in the course of this study is the most performant of the alloys investigated and it shows good promise for use in the Diesel application. The findings are reported in the manuscript "A.R. Farkoosh, X-G. Chen, M. Pekguleryuz, "*Interaction between molybdenum and manganese to form effective dispersoids in an Al-Si-Cu-Mg alloy and its influence on creep resistance*", accepted by Mater. Sci. Eng., A 2014".

Chapter 9 presents a study on Mg addition in the range of 0.3 - 0.7 wt.% to the Al-7Si-0.5Cu base alloy and the effect of the Mg level on its strength and creep resistance at 300 °C. The findings are reported in the manuscript" A.R. Farkoosh, M. Pekguleryuz, "*Enhanced mechanical properties of an Al-Si-Cu-Mg alloy at 300 °C: effects of Mg and the Q-Precipitate phase*", Mater. Sci. Eng., A 621 (2015) 277-286".

Chapter 10 presents the main conclusions and suggestions for future research. Contributions to original knowledge are stated in Chapter 11. A description of the contributions of the co-authors of the manuscripts is provided at the beginning of the thesis.

1.4 References

[1] E. Ozbakir, Development of aluminum alloys for diesel-engine applications, in, McGill University, 2008.
[2] M. Garat, G. Laslaz, Improved Aluminum Alloys for Common Rail Diesel Cylinder Heads, in: AFS, IL, USA, 2007, pp. 1-8.
[3] F.J. Feikus, Optimisation of AlSi Cast-Alloys for Cylinder Head Applications, in: AFS, Georgia, USA, 1998, pp. 1-21.
[4] L. Heusler, F.J. Feikus, M.O. Otte, Alloy and Casting Process Optimization for Engine Block Application, in: AFS Trans, 2001, pp. 215-223.
[5] F. Stadler, H. Antrekowitsch, W. Fragner, H. Kaufmann, P.J. Uggowitzer, Effect of main alloying elements on strength of Al-Si foundry alloys at elevated temperatures, Int. J. Cast Met. Res., 25 (2012) 215-224.

[6] W.L. Guesser, P. Duran, W. Krause, Compacted graphite iron for diesel engine cylinder blocks, Congrès Le diesel: aujourd'hui et demain Ecole centrale, (2004) 12-13.

[7] W.L. Guesser, Compacted Graphite Iron–a New Material for Diesel Engine Cylinder Blocks, in: II Encontro da SBPMat Brazilian MRS Meeting, 2003.

[8] G. Laslaz, M. Garat, Part cast made from aluminum alloy with high hot strength, in, Google Patents, 2003.

[9] http://www.audiworld.com/ access: September 2014.

[10] S.K. Shaha, F. Czerwinski, W. Kasprzak, J. Friedman, D.L. Chen, Monotonic and cyclic deformation behavior of the Al-Si-Cu-Mg cast alloy with micro-additions of Ti, V and Zr, Int. J. Fatigue.

[11] S.K. Shaha, F. Czerwinski, W. Kasprzak, J. Friedman, D.L. Chen, Effect of Zr, V and Ti on hot compression behavior of the Al–Si cast alloy for powertrain applications, J. Alloys Compd., 615 (2014) 1019-1031.

[12] D. Casari, T.H. Ludwig, M. Merlin, L. Arnberg, G.L. Garagnani, The effect of Ni and V trace elements on the mechanical properties of A356 aluminium foundry alloy in as-cast and T6 heat treated conditions, Mater. Sci. Eng., A, 610 (2014) 414-426.

[13] K.E. Knipling, D.C. Dunand, D.N. Seidman, Criteria for developing castable, creep-resistant aluminum-based alloys-A review, Zeitschrift fur Metallkunde, 97 (2006) 246.

[14] K.E. Knipling, Development of a nanoscale precipitation-strengthened creep-resistant aluminum alloy containing trialuminide precipitates, in, Northwestern University, Ann Arbor, 2006.

[15] L. Lodgaard, N. Ryum, Precipitation of dispersoids containing Mn and/or Cr in Al–Mg–Si alloys, Mater. Sci. Eng., A, 283 (2000) 144-152.

[16] Y.J. Li, A.M.F. Muggerud, A. Olsen, T. Furu, Precipitation of partially coherent α-Al(Mn,Fe)Si dispersoids and their strengthening effect in AA 3003 alloy, Acta Mater., 60 (2012) 1004-1014.

[17] M.E. Krug, Microstructural Evolution and Mechanical Properties in Aluninum-Scandium Alloys With Lithium and Rare Earth Additions, in, Northwestern University, Ann Arbor, 2011.

CHAPTER 2

LITERATURE REVIEW

2.1 Introduction

Currently cast iron is commonly used for Diesel engine applications [1]. As the automotive industry addresses the environmental concerns, weight reduction becomes more critical and the use of lightweight materials such as aluminum and magnesium alloys becomes strategically important. Recently developed Mg alloys offer extensive weight reduction, but, their mechanical performance is well below what is required for Diesel engine applications [2-5]. Substituting cast iron with aluminum would result in ~ 25% weight reduction of the engine blocks and increased environmental benefits. In Fig. 2.1, the material properties of compact graphite iron (CGI), cast iron and an aluminum alloy are compared. The low density and the modulus of elasticity, high thermal conductivity, as well as good castability, machinability and relatively low cost make Al an attractive candidate. The main shortcomings of the commercial aluminum alloys are the loss of strength and creep resistance with temperature, which have limited their use in Diesel engine components. The peak firing pressure for aluminum Diesel engines is set to below 170 bar for inline and 150 bar for V engines [1]. Presently. only a small portion of the Diesel engines, mainly the cylinder head, is cast in aluminum [2, 6]. With the continued developments in Diesel engines, which produce increasingly more severe temperatures and stresses, the Al alloys have reached their limits.

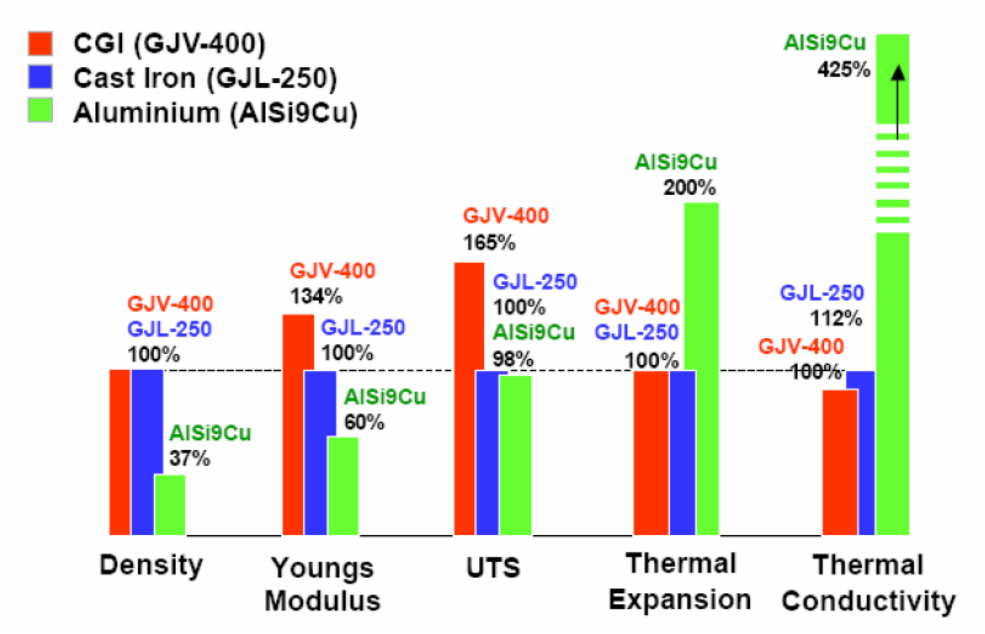

Fig. 2.1 Comparative properties of CGI, Gray Iron and AlSi9Cu [7].

This chapter explains the mechanical property requirements for Diesel engine materials and the challenges for aluminum alloys. Current research in the physical materials science principles for developing performant aluminum alloys for use in the Diesel applications are also reviewed.

2.2 Diesel engine operation and thermal fatigue

Diesel engine components such as engine blocks and cylinder heads experience severe thermal and mechanical loadings, under both steady-state and transient conditions [6, 8-10]. These components often fail during service because of fatigue cracking in certain critical regions (Fig. 2.2) where cooling is limited such as the narrow bridges between valves [11-13]. Generally engine materials are subjected to two modes of fatigue [14]: (i) *mechanical fatigue* or high cycle fatigue (HCF) and (ii) thermal fatigue.

2.2.1 Mechanical fatigue

Mechanical fatigue is driven by the pressure variations in the combustion chamber during each Diesel cycle, or by speed or load changes. The thin walls (~ 10 mm) in proximity to the water ducts are critical locations for the mechanical fatigue crack initiation. Temperature in these regions can be in the range of 120-170 ºC [6]. The engine geometry, residual stresses, cast structure (porosity, secondary dendrite arm spacing and intermetallic phase morphology) and the intrinsic fatigue strength of the alloy are the major factors that determine the mechanical fatigue performance [15].

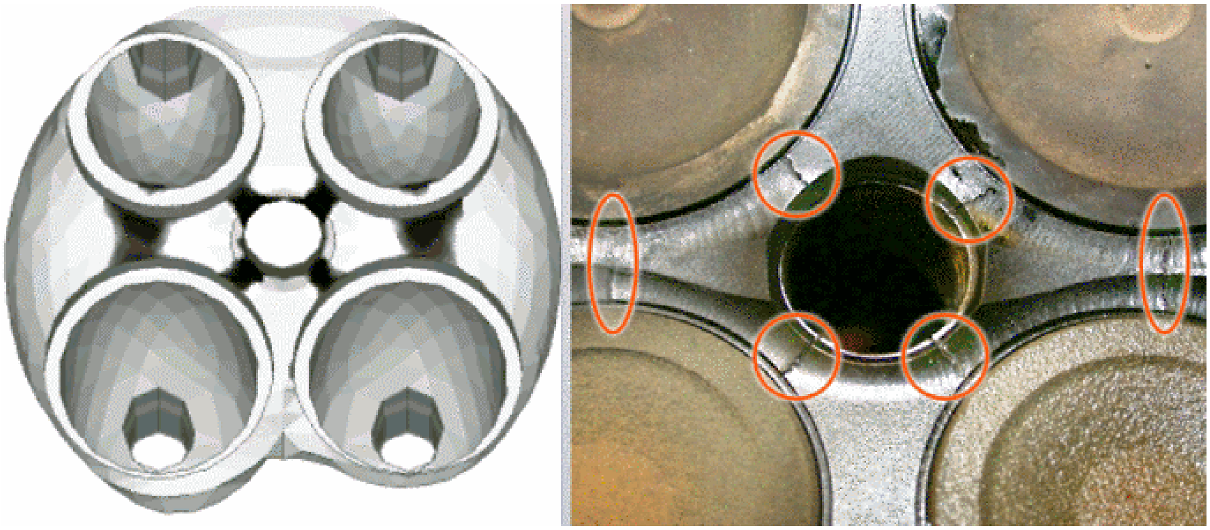

Fig. 2.2 Thermal fatigue cracks in an A319 cylinder head [16], the circles indicate the inter-valve regions between where cracks occur.

2.2.2 Thermal (thermo-mechanical) fatigue

Thermal fatigue is a complex phenomenon which is related to the steep temperature gradients that occur during the start-stop cycle of the engines. It is been reported that the damage caused by this mode of fatigue is more severe and determines the lifetime of the engine components [6]. It occurs in the inter-valve regions and is considered as low cycle fatigue. Thermal fatigue is not a direct material property but is related to a combination of material responses to loading conditions that occur during Diesel engine operation; these material responses ultimately lead to crack initiation and failure. The loading conditions and material responses are explained below.

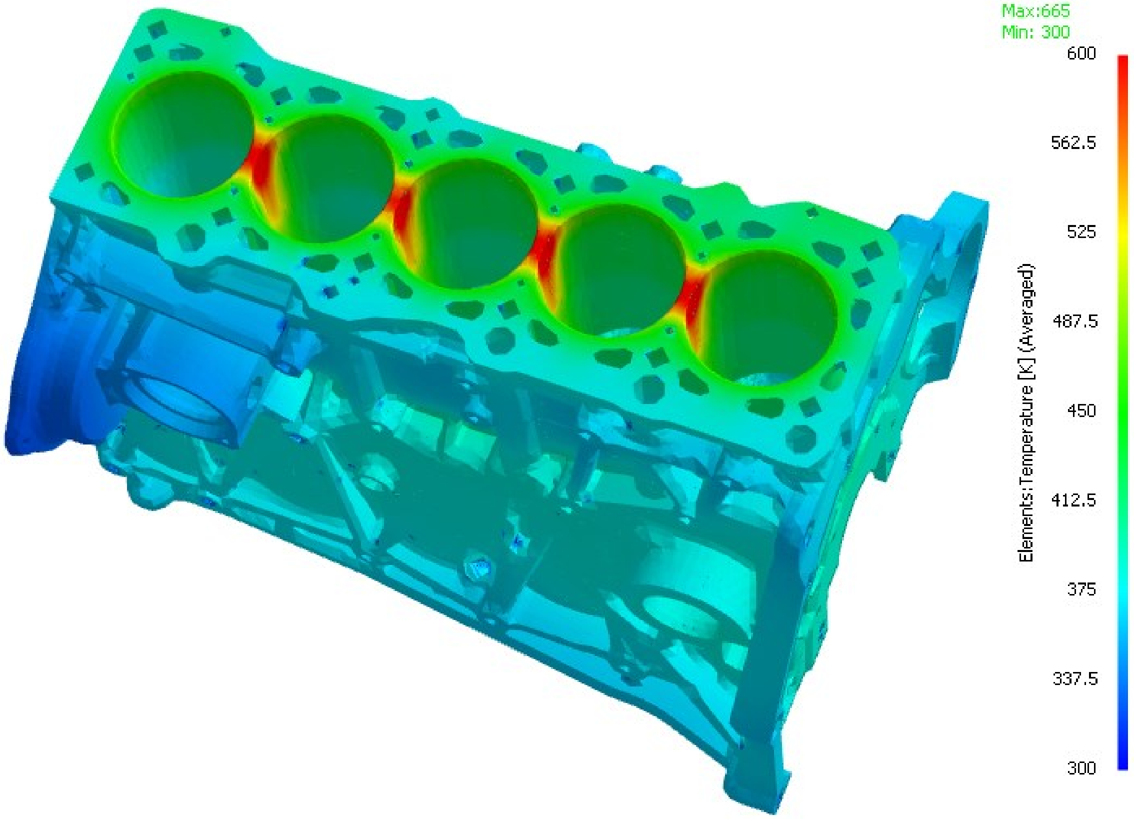

Fig. 2.3 Temperature distribution in an in-line Diesel engine, hot spots can be seen between the combustion chambers [17].

During engine heat-up, the cylinder surface temperature (Fig. 2.3) reaches near 300 ^{o}C instantly, while the interior remains at the ambient temperature (sometimes as low as -30 ^{o}C). The natural expansion of the surface material (the amount of which depends on the coefficient of thermal expansion, α) is restricted by the rigidity of the water-cooled bulk which remains at relatively lower temperatures. This induces local compressive stresses causing creep deformation in the material (Fig. 2.4). An important property requirement of the material is therefore *creep resistance* during engine heat-up (up to a maximum temperature of 300 ^{o}C). It is noteworthy that the stresses generated are more severe immediately after engine start-up and becomes less significant as the steady-state condition stablishes. Because of the compressive nature of the stress field, the creep deformation does not cause crack generation during engine operation [18, 19].

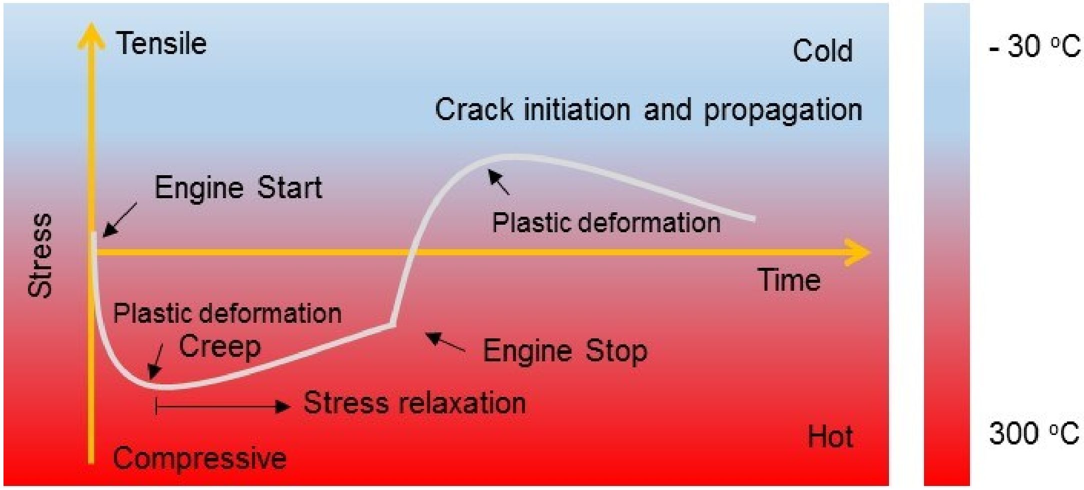

Fig. 2.4 Thermo-mechanical stresses and damage mechanisms during engine start-stop cycle.

During engine cool-down, when the engine stops running, the regions that are in contact with the coolant, contract to return to the initial conditions. This creates local tensile stresses. Thermal fatigue cracks can be nucleated during the engine cool-down period if the initial creep deformation is high and the material does not have sufficient ductility to accommodate these stresses by local plastic deformations. Even when the material is ductile, the repetition of these alternating compressive and tensile stresses (also called thermal fatigue) can cause crack initiation due to plastic damage accumulation and eventually lead to failure in Diesel engines. The thermal stresses developed during engine operation and related damage mechanisms are shown in Fig. 2.4. Limited information exists on actual stress measurements during Diesel operation because of the inherent difficulties in measuring stress fields near critical regions. However, a number of studies on modeling and predicting thermo-mechanical fatigue (via finite element method) in engine components have been conducted [20-23].

2.2.3 Materials performance requirements

Thermal fatigue resistance is not an intrinsic material property and the mechanical fatigue-strength has little correlation with the thermal fatigue resistance [6, 24]. Therefore, alloy design for Diesel engine applications is a challenging task as it requires consideration of all the relevant properties that have impact on the thermal fatigue resistance. As understood, for an enhanced thermal fatigue performance, a combination of three properties is required:

- *Compressive creep resistance* at 300 ºC to resist creep deformation in the inter-valve regions during engine heat-up.
- *Ductility* to accommodate the tensile stresses either elastically or plastically during engine cool-down and avoid catastrophic failure.
- *Strength* to accommodate the tensile stresses elastically when ductility is low.

It is usually difficult to attain all three requirements when developing an alloy. While there is not real discussion on the relative importance of these properties, it seems that certain researchers have considered tensile strength to be a key property and have therefore based their alloy development efforts on Al-Si-Cu alloys that are known to have higher strength than the Al-Si-Mg alloys. However, there have also been attempts to optimize alloys based on the Al-Si-Mg system which is known for lower strength but higher ductility than the Al-Si-Cu alloy. In view of the mechanisms of crack formation, it can be considered that tensile ductility is more important than the tensile yield strength, because plastic deformation would delay crack nucleation and propagation. Sometimes the thermal shock resistance parameter is used for material selection purposes to compare the tendency of different base materials to thermal fatigue [24]:

$$R_{TS} = \sigma_f k/E\alpha \tag{1}$$

Here σ_f is the mechanical fatigue strength at mean temperature, k is thermal conductivity, E is the modulus of elasticity and α is the coefficient of thermal expansion. Generally alloys with high thermal conductivity, low modulus of elasticity and low coefficient of thermal expansion are favorable for thermal shock resistance.

Recently Wong et al. [25] by including the creep damage in the Coffin–Manson fatigue equation have shown that in creep-fatigue situation (i.e. thermal fatigue), at low cycle times or temperatures, pure fatigue is the dominant damage mechanism and as the cycle time or temperature increases, creep becomes significant (Fig. 2.5). Ultimately, at high temperatures or long cycle times, pure creep is the dominant damage mechanism. On the basis of these analyses, because of the relatively long start-stop cycle time and high temperature of Diesel engines, creep can be considered to be more critical than fatigue in the inter-valve regions.

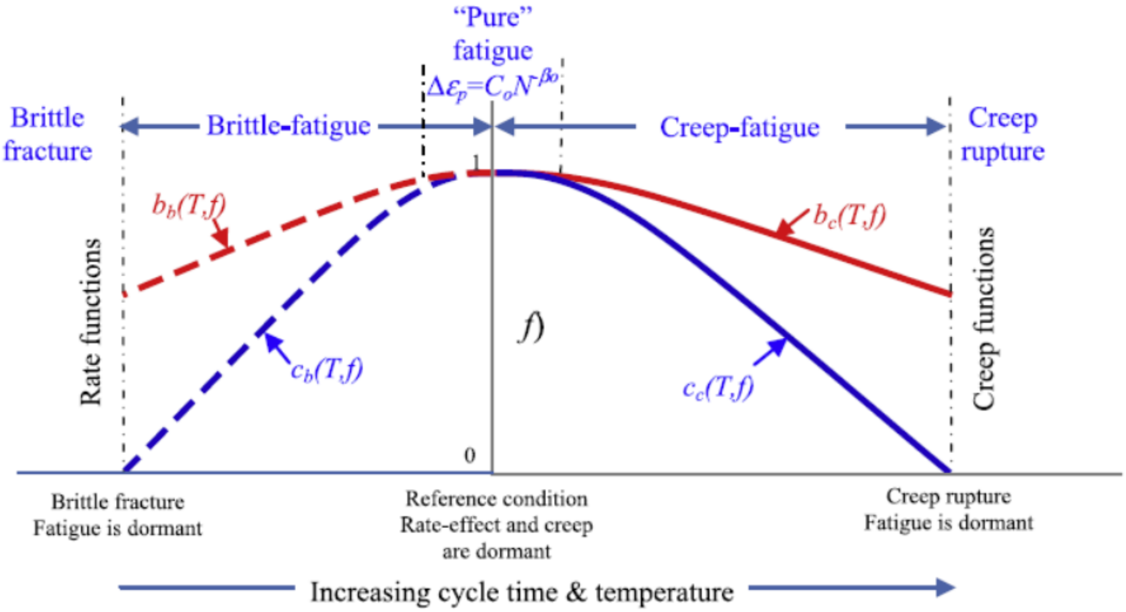

Fig. 2.5 Mechanism change with cycle time and temperature [25].

2.3 Aluminum alloys for engine applications and recent developments for Diesel engine use

Aluminum alloys are extensively used in combustion engine applications; these are based on Al-7wt%Si with Mg or Cu additions, namely A356 (Al-7Si-0.3Mg) and A319 (Al-7Si-4Cu) [6]. The Si provides fluidity, which makes them suitable for large and complex casting such as engine blocks or cylinder heads. The alloys can be cast by a variety of techniques ranging from relatively simple sand casting to very intricate permanent mold casting, investment casting, high pressure die casting, thixocasting, and squeeze casting [26-28]. Mg and Cu are generally added to improve strength and creep resistance at elevated temperatures through the precipitation of the θ-Al_2Cu, M-Mg_2Si and Q-$Al_5Mg_8Cu_2Si_6$ precipitates after heat treatment (T6 or T7). Fe level is usually kept as low as possible (0.1wt.%), especially in the case of the A356 alloys to minimize the formation of the brittle Fe-containing intermetallics. A319 alloys (sometimes with Mg additions) contain Cu (3-4 wt.%) and exhibit high strength and moderate creep resistance at elevated temperatures (150-250 ^{o}C). However, their ductility and fracture toughness are often low at elevated and ambient temperatures. The A356 alloy family has found greater acceptance in engine production owing to their high ductility [6, 9, 10] despite their the poor creep resistance and lower strength compared to the A319 family. Development activities to convert cast iron Diesel engines to aluminum engines initially began in 1998 [10]. Historically, Diesel engine alloy development has followed two different routes: (1) improving the strength and creep resistance of the A356 alloys without impairing the ductility or (2) improving the ductility and creep resistance of the A319 alloys while maintaining the strength.

2.3.1 Cu addition to Al-7Si-0.3Mg

One of the first advancements in improving the high temperature performance of Diesel engine alloys involved the addition of low levels of copper to the A356 alloy. The addition of Cu leads to the formation of two Cu-rich second phases, θ-Al_2Cu and Q-$Al_5Mg_8Cu_2Si_6$, which seem to coexist in the Al-Si-Cu-Mg alloy systems [2, 29, 30]. Li et al. [31] observed that the peak aged hardness and the tensile strength of an A356 alloy increases with increasing the Cu content of the alloys. They attributed this outcome to the increased density of the β″-Mg_2Si and the precipitation of the precursors of the Q-$Al_5Mg_8Cu_2Si_6$ in the peak-aged condition (Fig. 2.6). In the alloy with 1% Cu (Fig. 2.6b) only the Q′-$Al_5Mg_8Cu_2Si_6$ and β″-Mg_2Si precipitates coexist. At higher Cu content (Fig. 2.6c), the θ′-Al_2Cu precipitates were also observed. Cáceres et al. [32] have studied the effect of Cu addition on the porosity level in the A356 alloys. It has been shown that Cu in excess of 0.2% increases the amount of microporosity significantly (Fig. 2.7). This is related to the significant reduction of the eutectic temperature and an increase in the solidification range.

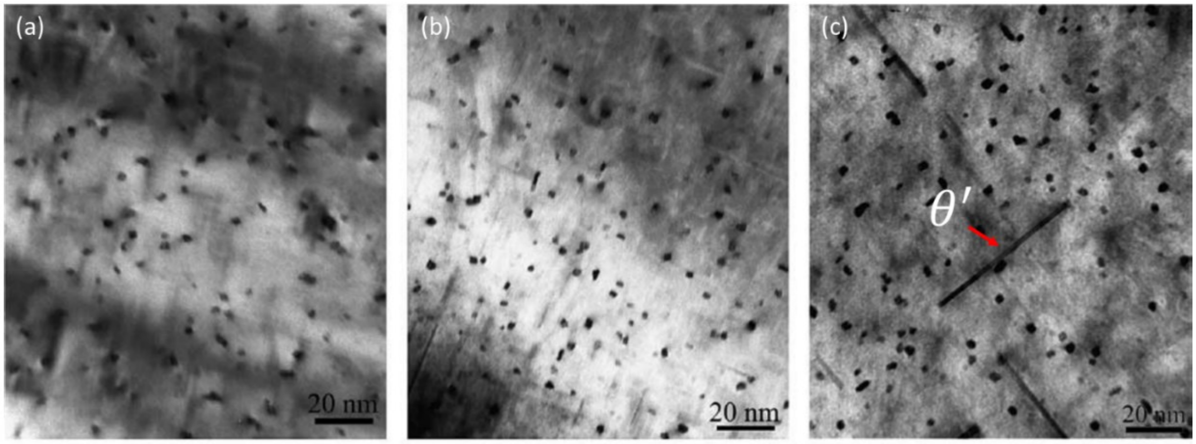

Fig. 2.6 The influence of Cu on the microstructure of the A356 alloy after T6 heat treatment, (a) A356, (b) A356 + 1%Cu and (c) A356 + 3%Cu [31].

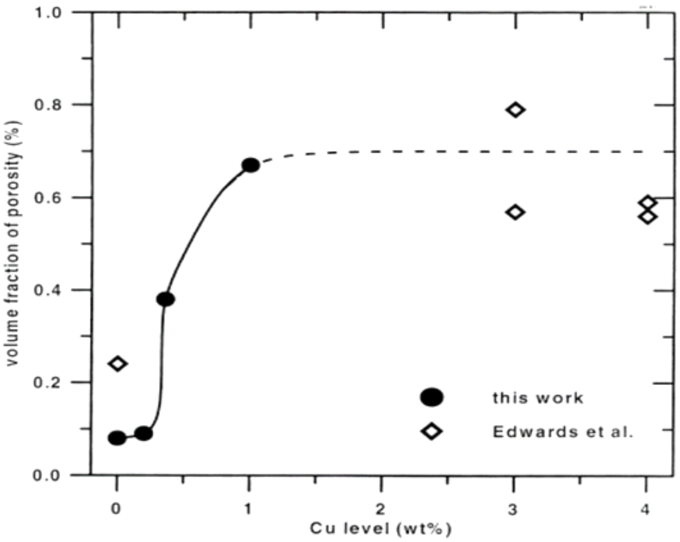

Fig. 2.7 The effect of Cu addition on the porosity level of an A356 alloy [32].

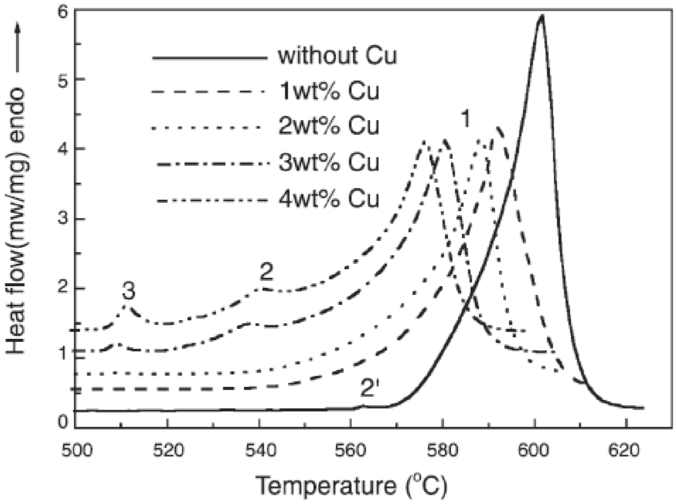

Fig. 2.8 The effect of Cu level on the DSC curves of the as-cast Al11Si0.3Mg alloys [33]. Peak 1: α-Al + Si + β-Al_5SiFe → Liq., peak 2: α-Al + θ-Al_2Cu+Si → Liq., peak 2´: α-Al + Si +β-Mg_2Si → Liq. and peak 3: α-Al + θ-Al_2Cu + Si + Q-$Al_5Cu_2Mg_8Si_6$ → Liq.

Usually, a two-step solution treatment (solution treatment at ~ 500 °C followed by a high temperature solution treatment) is suggested for Cu-containing A356 alloys to avoid incipient melting [6, 33]. Using DSC analysis (Fig. 2.8) Wang et al. [33] have shown that when a conventional, one-step solution treatment is used, the solution temperature should be restricted to below 555, 535 and 500 °C, for the Al-11Si-0.3Mg alloys with 0.0, 1.0 and 2.0% Cu respectively.

Feikus [10] has shown that Cu up to 0.5 wt.% improves strength at 150-250 °C without impairing the ambient temperature ductility, while increasing the creep time-to-fracture at 200 °C, 120 MPa from 22 to 214 h. Further Cu addition has no significant influence on strength or creep resistance but adversely affects ductility. In 1998, VAW developed the A356 + 0.5Cu alloy for Diesel cylinder heads. This first generation of aluminum Diesel alloy obtained limited market share in Europe. However, the alloy is no longer used in today's Diesel engines because the strengthening effect of Cu is lost at 300 °C due to precipitate coarsening. This alloy later was modified by Ni, Zr, V and Mn additions [6, 9].

2.3.2 Zr, Mn, Cr and V modification of Al-7Si-0.5Cu-0.3Mg

Recently a cylinder head alloy was developed by Rio Tinto Alcan (France) [6] via Zr and Mn modification of the A356 + 0.5Cu alloy. These elements, at a low amount of (~ 0.15%), have been added to increase dispersion strengthening. Although no significant increase in tensile strength at elevated temperatures was observed, the creep resistance increased due to the precipitation of fine, thermally stable ε-AlSiZr dispersoids (Fig. 2.9) within the intradendritic regions. Because of Mn addition and modification of iron-rich intermetallics, this alloy has better ductility over a broad temperature range.

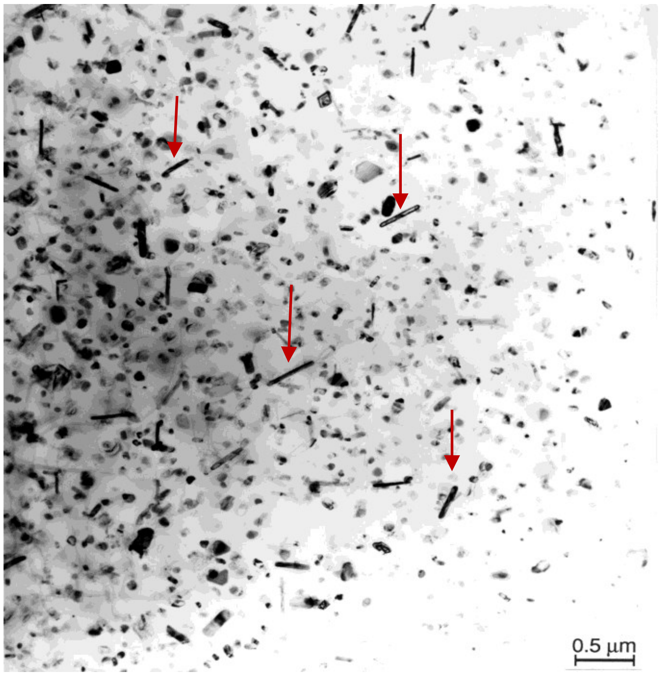

Fig. 2.9 Al-Si-Zr-Ti precipitation (indicated by arrows) inside the dendrites [6].

Two similar alloys, MG1 (*Al-7Si-0.3Mg-0.15Cr-0.15Zr-0.15Mn-0.1Ti-0.1Fe*) and MG2 (*Al-7Si-0.5Cu-0.3Mg-0.15Cr-0.15Zr-0.15Mn-0.1Ti-0.1Fe*) for Diesel engine applications were developed at McGill by our research team [2]. Cr in combination with Mn and Zr was added to produce submicron dispersoids to enhance creep resistance. The MG2 alloy showed higher peak strength (T6) and higher overaged strength (T7) compared to the MG1 alloy (Fig. 2.10). The mechanical properties of the MG1 and MG2 alloys along with the reference alloys, R1 (A356) and R2 (A356 + 0.5Cu) are in Table 2.1. The Cr, Zr and Mn additions into the A356 alloy lead to an 8% improvement in creep resistance but strength remained unchanged. Combined addition of Cu with Cr, Zr and Mn in the MG2 alloy significantly improved the mechanical properties; the MG2 alloy showed 3 times higher creep resistance. Microstructural studies in this work revealed the presence of the AlSiZr ternary phase, a complex Cr phase (Al-Cr-Mn-Fe-Si) and submicron phases in the grain interiors (Fig. 2.11). The brittle (β-Al_5SiFe) phase was not observed within the microstructure. It is known that Mn addition modifies acicular β-Al_5SiFe phase into the less harmful α-Al(Mn,Fe)Si phase [34].

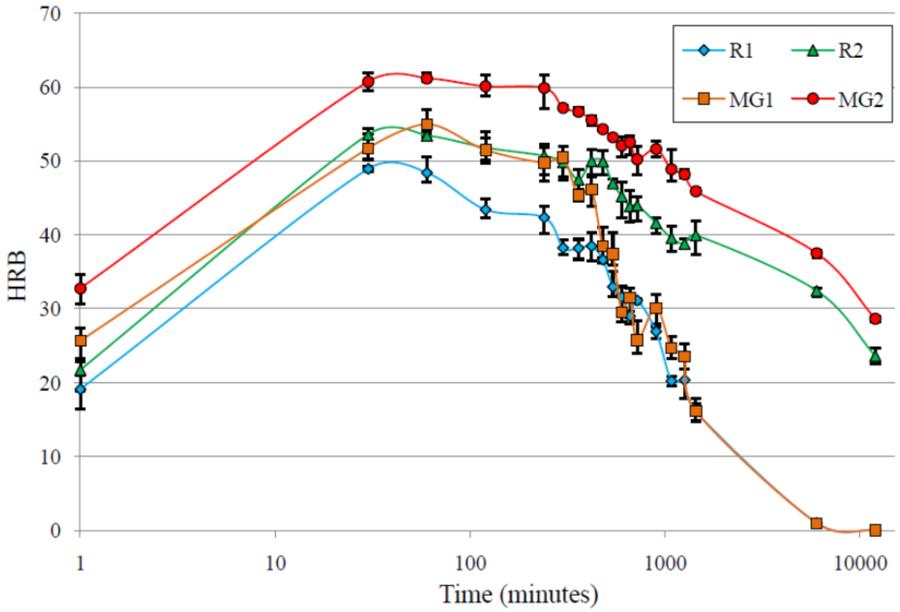

Fig. 2.10 Comparison of the aging curves for the alloys developed at McGill for Diesel engine applications, MG1: Al-7Si-0.3Mg-0.15Cr-0.15Zr-0.15Mn-0.1Ti-0.1Fe, MG2: Al-7Si-0.5Cu-0.3Mg-0.15Cr-0.15Zr-0.15Mn-0.1Ti-0.1Fe, R1: A356 and R2: A356 + 0.5Cu [2].

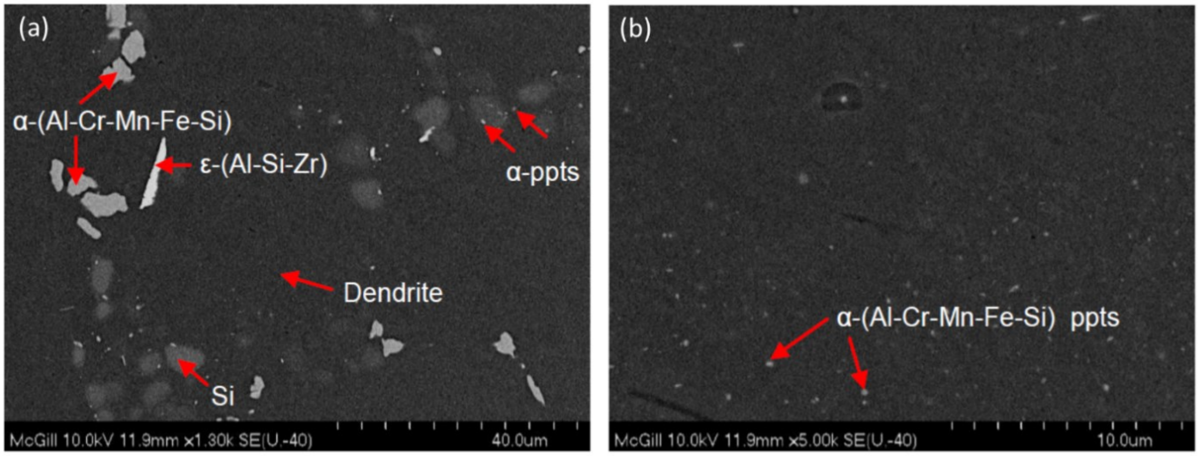

Fig. 2.11 (a) Microstructure of the *Al7Si0.3Mg0.15Mn0.15Cr0.15Zr0.5Cu* alloy developed at McGill, (b) intradendritic regions of the same alloy at a higher magnification [2].

Table 2.1 Mechanical properties of the MG1, MG2, R1 and R2 alloys [2]

Alloy Code	At 250°C		At 200°C, 200 hours	At 300°C, 300hours, 30 MPa
	UTS [MPa]	% E	Hardness (HRB)	% Creep
R1	126	5.06	-	15.52
R2	152	3.17	23.6	16.82
MG1	128	4.86	-	14.27
MG2	161	4.07	28.7	4.95

2.3.3 Modification of A319 (Al-7Si-4Cu)

Low ductility of the A319 alloys has limited their use for Diesel engine applications, despite the higher strength and creep resistance of these alloys compared to the A356 alloy family (Table 2.2). Therefore, improving the ductility of these alloys was one of the primary alloy development routes for Diesel engine applications. Garat et al. [6] formulated a new Al-7Si-(3-4)Cu alloy with lower amounts of Fe content (~ 0.1%) and low additions of Zr (0.15%), V (0.25%) and Mn (0.15%). This alloy showed remarkably high strength and creep resistance at 300 °C (Table 2.2). The high creep resistance is attributed to the formation of the thermally stable precipitates inside the dendrites. However, its ductility was ~ 40% lower than that of the modified A356 + 0.5Cu alloy.

Table 2.2 Mechanical properties of the A356- and A319-based Diesel engine alloys [6]

Alloy	Room temperature			300 ºC			
	YS (MPa)	UTS (MPa)	E (%)	YS (MPa)	UTS (MPa)	E (%)	Creep $\sigma_{0.1\%}$ (MPa)
A356	257	299	9.9	40	43	34.5	21.7
A356+0.5Cu	275	327	9.8	40	44	34.6	21.8
A356+0.5Cu0.14Zr0.15Mn	264	319	11.3	44	51	46	22.5
Al7Si3.8CuMnVZrTi	234	368	6	63	77	26	31.8

2.3.4 Ni modification of Al-7Si-0.5Cu-0.3Mg

Ni is known to enhance the strength and hardness of Al-Si alloys at elevated temperature by forming thermally stable nickel aluminides [35-37]. Ni-containing Al-Si alloys are used extensively as engine piston alloys that require high strength at elevated temperatures [36]. Heusler et al. [9], developed a new Diesel engine alloy by adding Ni at low levels to the A356 + 0.5Cu alloy. The chemical composition was adjusted to give the Al–7Si–0.4Mg–0.4Cu–0.5Ni–0.4Fe alloy. This alloy showed a 20% increase in fatigue strength and improvements in tensile strength over the A356 + 0.5Cu alloy, however, ductility decreased because of the large amount of brittle intermetallics that formed as a result of Ni addition.

2.4 Ductility improvement in Al-Si hypoeutectic alloys

The binary Al–Si system (Fig. 2.12) is a simple eutectic system with about 12% Si being the eutectic composition at 577 ºC [38]. Al–Si eutectic is an irregular coupled eutectic with a flake-like Si morphology. These brittle flake-like Si particles act as stress risers and an easy crack propagation path, which lead to low ductility and fracture toughness of Al-Si alloys [39]. To increase the ductility, the flake-like Si is usually changed into a fibrous structure through modification treatments. This can be achieved in two different ways: (1) chemical modification, by adding certain elements at trace levels (2) quench modification, by a rapid cooling rate [40]. Among several elements that are known to cause modifications [40-50], Na and Sr are considered to be the most effective.

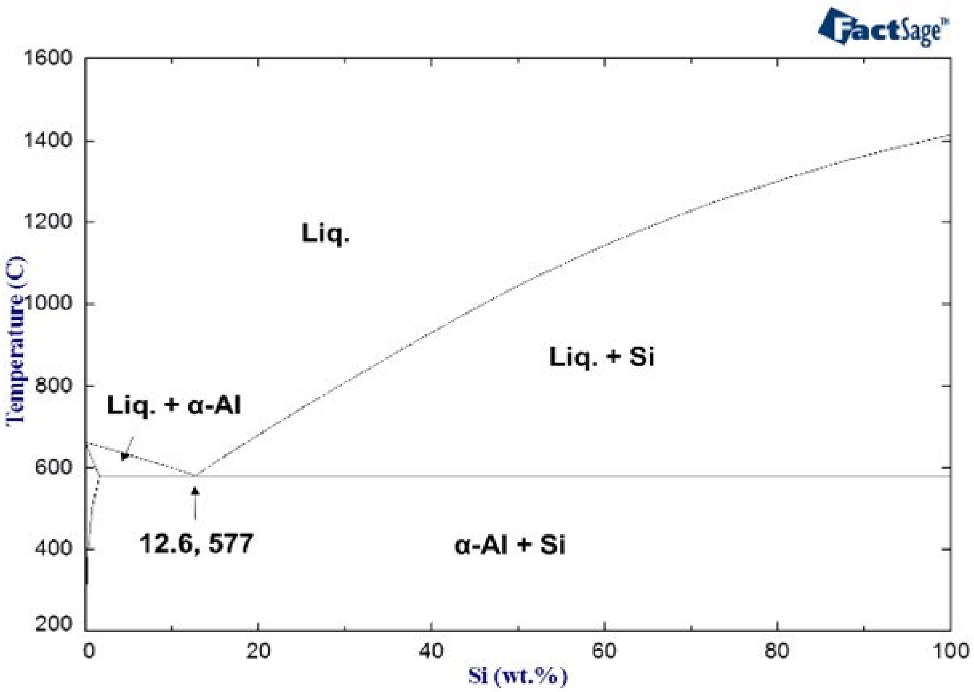

Fig. 2.12 Al-Si binary phase diagram, calculated using FactSage.

2.4.1 Iron rich intermetallics in aluminum alloys and their effects on ductility

Commercial aluminum alloys contain a considerable amount of Fe as impurities and occasionally as alloying additions. Fe levels are usually maintained as low as possible (0.1%) to moderate any adverse effects on fluidity and mechanical properties [51]. However, because of the high solubility of Fe in liquid Al (~ 1.8% at eutectic temperature, 655 ºC), melt contamination with Fe during the melting and casting processes (through the use of steel tools) is inevitable. Upon solidification, Fe appears as different stable and metastable Fe-rich intermetallics because of its negligible solid solubility in Al (~ 0.04% at 655 ºC) [51]. The composition, stability, size and morphology of these Fe-rich intermetallics are determined by both the solidification rate and chemical composition of the alloy [52, 53]. Different Fe-rich intermetallics in Al alloys, their crystal structure and properties are reviewed in [53-56]. Depending on their size and morphology, they may have varying adverse effects on mechanical properties.

The β-Al_5FeSi and π-$Al_8Mg_3FeSi_6$ intermetallics are the main Fe-containing constituents that are frequently observed in alloys of the Al-Si-Cu-Mg-Fe system with high Si contents (engine cast alloys, Fig. 2.13). The β-Al_5FeSi phase has a plate-like morphology, and low interfacial bond strength with the Al matrix. This phase is known to be the most detrimental Fe-containing intermetallic in Al alloys (Fig. 2.14a) [51, 57-59]. These platelets are known to form at the end of solidification, impeding interdendritic feeding, and giving rise to shrinkage pores [60, 61]. Compared to the β-Al_5FeSi platelets, the π-$Al_8Mg_3FeSi_6$ phase is less detrimental to mechanical properties and has a Chinese script morphology. At low Mg contents, this phase usually decomposes at high solutionizing temperatures [62].

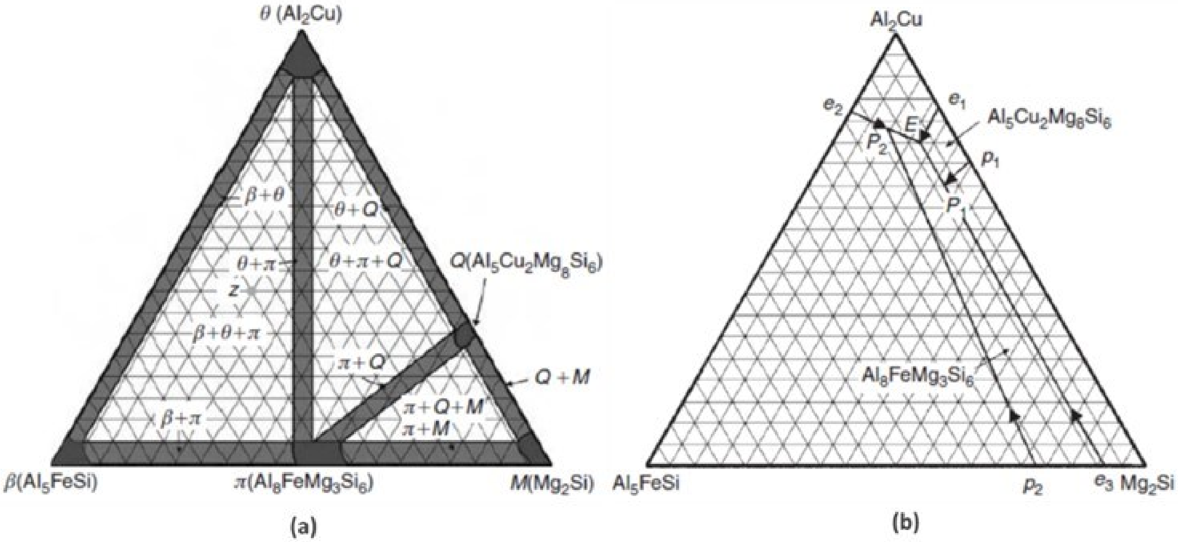

Fig. 2.13 Al-Si-Cu-Mg-Fe system (a) phase distribution in solid state and (b) polythermal diagram [56].

It is important to modify β-Al_5FeSi platelets into a less harmful phase such as α-AlFeSi with script or skeleton type of morphologies (see Fig. 2.14b) or its isomorphs [57, 58]. The modification sometimes leads to an increase of ~ 200% in elongation [63]. The formation of the β-Al_5FeSi platelets has been shown to be suppressed by (i) rapid cooling (allowing less time for growth), (ii) melt superheating (dissolution of the primary phase) or (iii) chemical modifications by single or combined addition of alloying element such as Mn (Mn:Fe ~ 1:2), Cr, Mo, V, Co, Be and B [57-59, 64]. Modifications with each element have different effects on mechanical properties, depending on the type of the substitute intermetallic. The highly desirable substitute intermetallic should have higher density, with Fe being the main constituent element (high Fe concentration). These properties help bind the Fe content of the alloy in a compact intermetallic phase that forms in a low volume fraction. The ductility of the substitute intermetallic is another factor that must be taken into account.

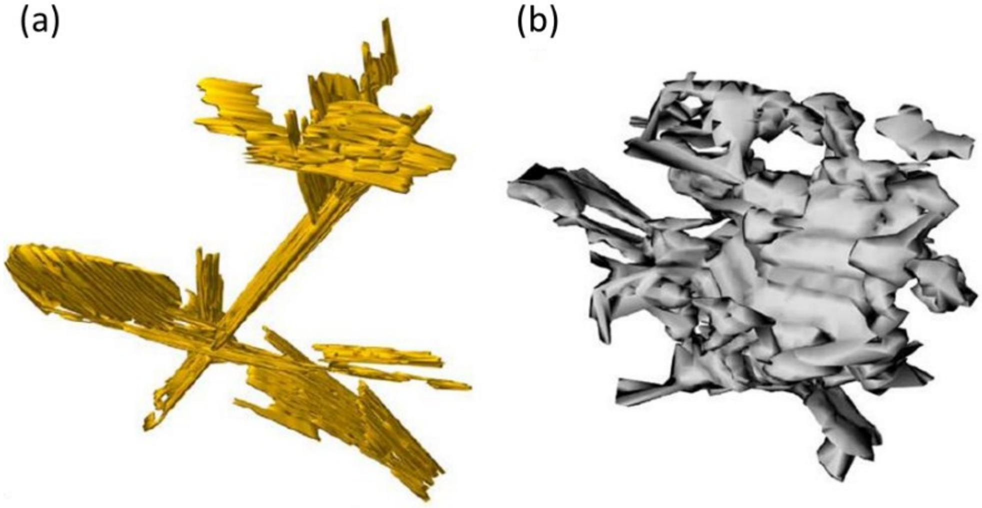

Fig. 2.14 Three-dimensional reconstruction of a group of a) β-Al5FeSi platelets, b) α-$Al_{15}(Mn,Fe)_3Si_2$ particle [65].

2.5 Creep resistance in aluminum

2.5.1 Creep deformation

Creep is usually defined as the progressive deformation of materials under constant stresses (or load) that are below the macroscopic yield stress of the material [24]. Although creep occurs at any temperature, it becomes more pronounced at elevated temperatures (upon reaching 0.4 T_m, where T_m is the absolute melting point of the material), where rapid diffusional processes take place [66]. The deformation rate depends on the temperature, applied stress, material properties and exposure time [67]. Fig. 2.15 shows a typical creep curve (strain vs. time) for a metal where three distinct regions can usually be observed. In the initial stage, or primary creep region, the strain rate, $\dot{\varepsilon}$ $(= d\varepsilon/dt)$ is relatively high, but decreases with time or strain $(d^2\varepsilon/dt^2 < 0)$ because of work hardening processes [68]. The strain rate then reaches a minimum $(\dot{\varepsilon_m})$ and becomes almost constant $(d^2\varepsilon/dt^2 = 0)$ because of the balance between work hardening and annealing (thermal softening). The stress and temperature dependence of $\dot{\varepsilon_m}$ depends on the creep mechanism. This stage is known as secondary or steady-state creep. Sometimes the secondary creep is differentiated from steady-state creep and referred to a transition stage from primary to tertiary creep, where true steady state is not established (only a minimum in creep deformation rate is observed) [69]. In tertiary creep, the strain rate exponentially increases with strain because of cavitation and/or cracking phenomena and eventually leads to fracture. Failure occurs by either transgranular (intradendritic) or intergranular (interdendritic) modes of creep fracture [70]. Fig. 2.16 shows a fracture-mechanism map for a commercial purity (99.3%) aluminum. Both intergranular and transgranular fracture modes can occur in different stress and temperature ranges.

The steady state creep strain rate ($\dot{\varepsilon_m}$) is often used as an important design parameter [24, 71-76], as it determines the lifetime of the components under creep conditions. The stress and temperature dependence is phenomenologically described as a power-law relationship of the form [77]:

$$\dot{\varepsilon}_m = A\sigma^{n_a}\exp\left(-\frac{Q_a}{RT}\right) \tag{2}$$

where, A is a constant, σ is the applied stress, n_a is the apparent stress exponent, Q_a is the apparent activation energy and RT has its usual meaning. The stress exponent $n_a\left(=\frac{\partial \ln \dot{\varepsilon}_m}{\partial \ln \sigma}|_T\right)$, and activation energy $Q_a(= -R\frac{\partial \ln \dot{\varepsilon}_m}{\partial\left(\frac{1}{T}\right)}|_\sigma)$ are experimentally related to the predominant creep mechanism.

2.5.2 Creep deformation mechanisms

It is known that different creep mechanisms are operative at elevated temperatures. Creep deformation-mechanism map (Ashby map) is a useful means of summarizing the dominance range for each mechanism (Fig. 2.17). Ashby maps are usually constructed for a constant grain size by plotting the normalised stress, σ/G vs. the homologous temperature, T/T_m where G is the shear modulus and T_m is the melting temperature [72, 78]. Fig. 2.17 shows a typical deformation-mechanism map for a pure Al with grain size 10 µm. The main creep deformation mechanisms can be categorized into 4 groups [24, 66-68, 79-83]:

1- Diffusion creep: when creep occurs only as a result of atom diffusion without the major role of dislocations. Diffusion creep includes two phenomena: *Grain boundary diffusion* known as Coble creep where atoms diffuse along the grain boundaries to elongate the grains along the stress axis ($n \approx 1$, and Q = activation energy for self-diffusion along grain boundaries), and *volume lattice diffusion* through the grain interior or Nabarro-Herring creep ($n \approx 1$, and Q = activation energy for self-diffusion).

2- Harper-Dorn creep: often occurs at low stresses and high temperatures. The steady-state creep rate shows a Newtonian behaviour ($n \approx 1$) and the activation energy is close to that of self-diffusion. The Harper-Dorn creep rate is orders of magnitude higher than the Nabarro–Herring or Coble creep rates.

3- Grain boundary sliding: it occurs during diffusion creep to maintain the integrity of the grains; it is seen mostly at high stresses but lower temperatures. Deformation of grain interiors is essential for this creep mechanism ($n \approx$1-3).

4- Dislocation creep: dislocations overcome barriers by thermally assisted mechanisms involving self-diffusion (diffusion of vacancies) or diffusion of solute atoms ($n \approx$3-7, and Q = activation energy for self-diffusion or solute diffusion).

2.5.3 Creep of dispersion-strengthened alloys

The creep behaviour of the dispersion-strengthened alloys is characterized by high and variable n_a and Q values which seems to be inexplicable in terms of the thermally-activated dislocation processes. For such alloys, the threshold stress approach is often applied to account for the anomalously high and variable n_a and Q values. Introduction of the threshold stress, σ_{th}, below which dislocation creep is not significant and modulus corrections gives a modified constitutive equation of the form [84, 85]:

$$\dot{\varepsilon}_m = A' \left(\frac{\sigma - \sigma_{th}}{G}\right)^n \exp\left(-\frac{Q}{RT}\right) \tag{3}$$

here, n is stress exponent of the matrix and A' is a constant. Although the existence of creep threshold stress is explained by mechanisms such as bypass by climb or dislocation detachment, the exact nature of the threshold stress is unknown and requires further investigations [86-90]. Recently Krug and Dunand [91] proposed a model for estimation of the threshold stress in the alloys strengthened by coherent dispersoids. They have shown that the dislocation trap after climb process may account for the presence of threshold stress in alloys strengthened via coherent dispersoids.

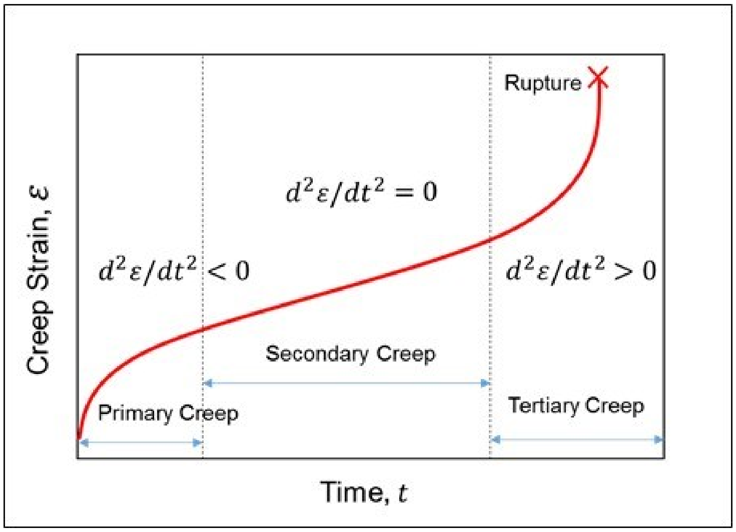

Fig. 2.15 Typical creep curve showing the three stages of creep deformation.

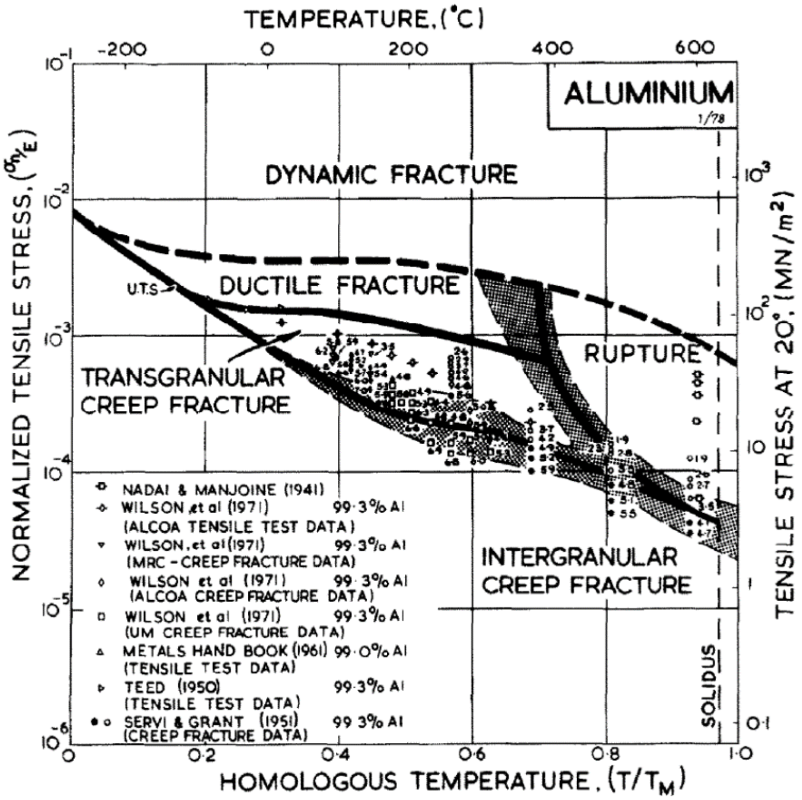

Fig. 2.16 Fracture-mechanism map for a commercial purity (99.3%) aluminum, at creep temperatures both intergranular and transgranular fracture modes occurs [70].

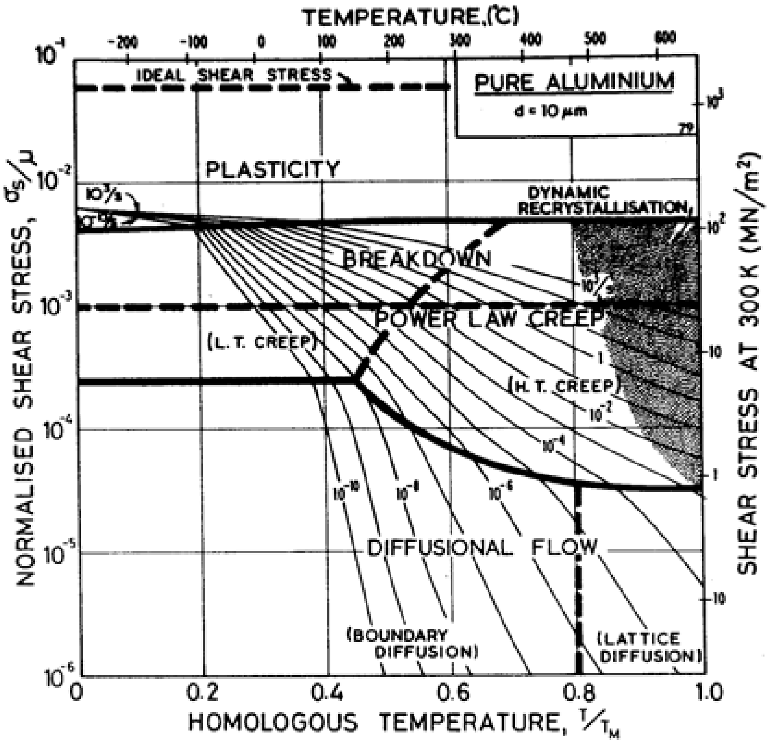

Fig. 2.17 Various regions of creep deformation in pure Al (grain size 10 μm) [72].

2.5.4 Alloy design for creep resistance

For aluminum alloys, dislocation creep processes are known to be the rate-controlling creep mechanism in the temperature-stress ranges of Diesel engines [87]. Fine particles or precipitates can hinder dislocation motion and improve strength and creep resistance of metallic alloys when dislocation activities are the rate controlling processes [92].

Dispersion strengthening of aluminum cast alloys

The microstructures of aluminum cast alloys consist of α-Al dendrites (solid solution) usually strengthened by intradendritic dispersoids and/or precipitates and interdendritic intermetallics. The yield strength of such alloys in over aged conditions can be expressed by the classical law of mixtures as [93]:

$$YS = \sigma_i + \sigma_{SS} + \sigma_{GB} + \sigma_{DIS} \tag{4}$$

where σ_i is the friction stress, σ_{SS} is the solid solution strengthening, σ_{GB} is related to the Hall-Petch relationship, and σ_{DIS} represents dispersion strengthening which is related to the interaction of the dislocations with precipitates. At elevated temperatures, the intradendritic age-hardening precipitates are coarse and non-coherent (non-shearable). Consequently, precipitate bypass by dislocation bowing mechanism (Orowan mechanism) can be dominant. The increase in yield strength due to Orowan mechanism is [94]:

$$\sigma_{or} = \sigma_{DIS} = M\,\frac{0.4G_{Al}b\ln\left(\frac{\pi R}{2b}\right)}{\pi\lambda\sqrt{1-\upsilon}} \tag{5}$$

Here, M is Taylor factor, b is the magnitude of Burgers vector, v and G are Poisson's ratio and shear modulus for Al, R is the mean precipitate radius and λ is interparticle spacing. It can be seen from equation (5) that the increase in the yield strength by dispersion hardening depends on the precipitate size, distribution and interparticle spacing (which depends on volume fraction of the precipitates). Therefore, for an effective dispersion hardening, fine closely-spaced precipitates are required. These precipitates should remain stable at elevated temperatures and resist Ostwald ripening.

Precipitates stability during creep deformation

The rate constant of Oswald ripening is given by [95]:

$$K \approx \frac{D\gamma}{(C_e^{\beta} - C_e^{\alpha})^2} \tag{6}$$

where D is diffusivity of the rate-controlling solutes, γ is interfacial energy, C_e^{α} is the solute solubility in the Al matrix and C_e^{β} is the solute concentration of the precipitate. To have a thermally stable precipitate, the constituent solute atoms should have low solid solubility and low diffusivity in the Al matrix.

Alloying with slow-diffusing solute atoms that have solid solubility in the precipitates is also known to increase the resistance to Oswald ripening. Kuehmann and Voorhees [96] have shown that addition of a third alloying element with low diffusivity to a binary system can decrease the rate constant of Oswald ripening. When the diffusivities of the third component (D_3) and the second component (D_2) are identical (Fig. 2.18, $D_3 = D_2$), the rate constant deceases equally via addition of the either of the components. However, in the case where the third component has a higher diffusivity (Fig. 2.18, $D_3 = 10D_2$), the addition of the second component leads to a rapid decrease in the rate constant.

Coherency strengthening

Coherency of the precipitates can lead to an increase in the yield strength of the alloys via interaction between the strain field of the precipitates and dislocations. The coherency strengthening, σ_c, is given by [97, 98]:

$$\sigma_c = 2.6M(\varepsilon G)^{3/2}\left(\frac{RV_f}{0.18Gb}\right) \tag{7}$$

where, $\varepsilon(= 2\Delta a/3a)$ is the lattice parameter (a) misfit. It is highly desirable that the dispersoid phase have a crystal structure similar to that of the Al matrix (FCC). This similarity can potentially lead to a coherent (low energy) dispersoid/matrix interface, which can increase the strengthening effect of the dispersoids.

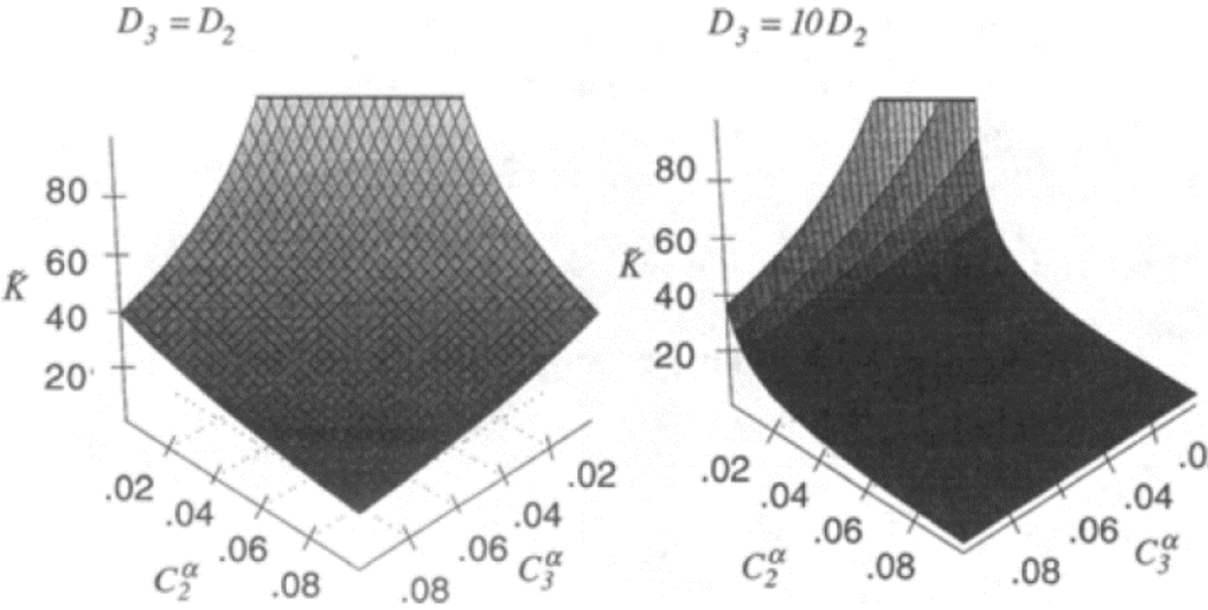

Fig. 2.18 The normalized coarsening coefficient of precipitates for a dilute ideal ternary alloy, showing the effect of ternary addition. Indices 2 and 3 represent the second and the third components in the alloy system, respectively [96].

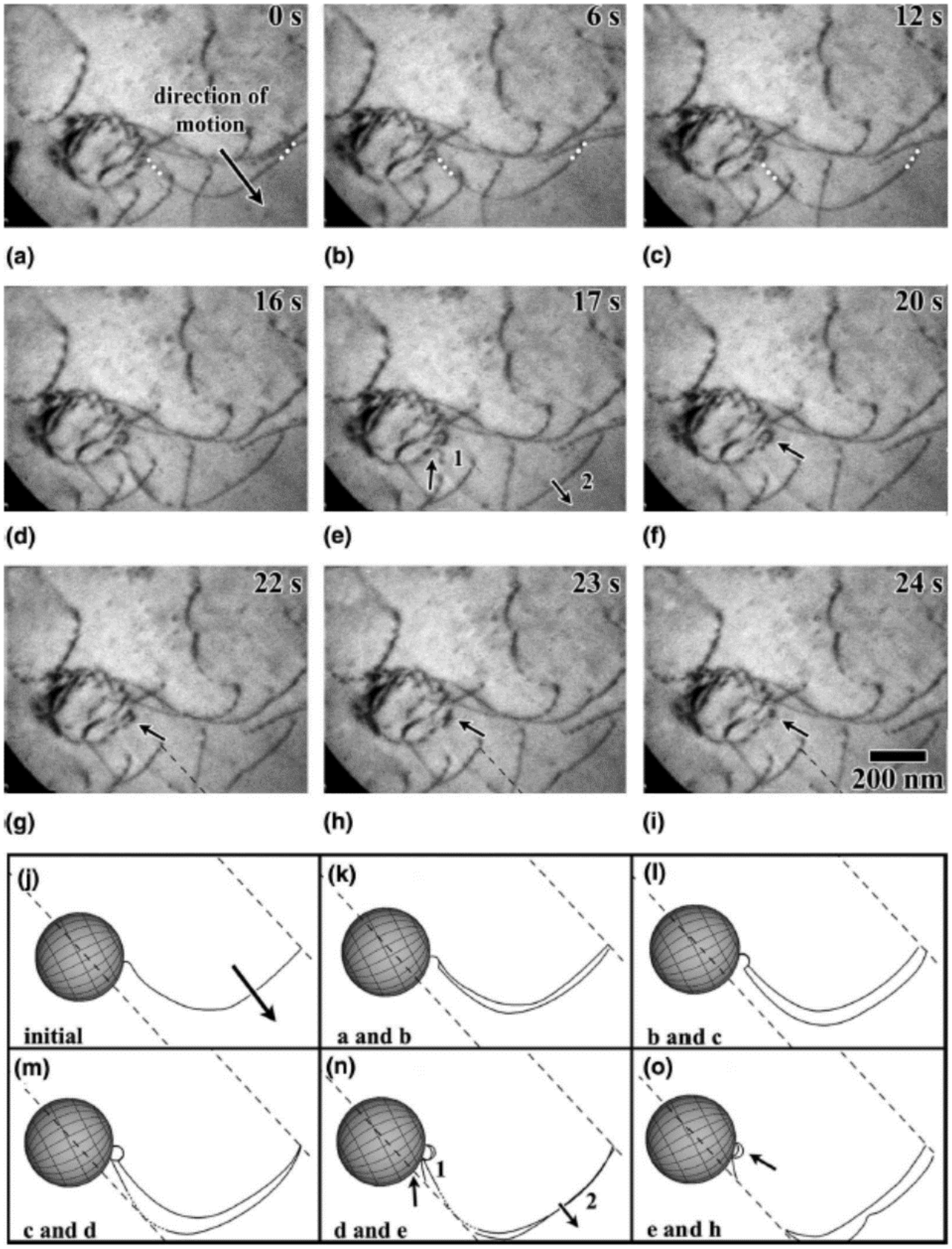

Fig. 2.19 (a–i) In-situ TEM study of the elastic interaction of dislocations with an Al_3Sc semicoherent dispersoid during slow deformation ($\dot{\varepsilon} = 10^{-3} s^{-1}$) at ~ 400 ºC. (j–o) Schematic illustrations showing the dislocation/dispersoid interaction [99].

Fig. 2.19 shows a series of TEM micrographs taken by Clark et al. [99] demonstrating a strong elastic interaction between a large semicoherent Al_3Sc dispersoid and dislocations during deformation at ~ 400 ºC. This strong elastic interaction hinders the movement of the dislocations. As shown in the schematic illustrations in Figs. 2.19j-o, a matrix dislocation is attached to the dispersoid. As it moves in the matrix it drags the segment that is attached to the dispersoid.

Eventually dislocation is freed by breaking into two segments and making a dislocation loop attached to the dispersoid.

Influence of dispersoids on ductility

The behaviour of hard dispersoids/particles in a ductile matrix during plastic deformation has been extensively studied by Eshelby [100, 101], Ashby [102, 103] and Argon et al. [104] in the past. Models based on plastic accommodation of displacement incompatibilities, suggest that during plastic deformation, elastic energy stored around fine dispersoids is insufficient for cavity nucleation. It was shown that stable cavities can form only when the particles or inclusions are large.

In Al-Si cast alloys, damage mechanisms are generally associated with large eutectic Si particles or intermetallics as well as structural defects (porosity) rather than fine particles or precipitates in the intradendritic regions [62, 105-110]. Cracking of the large eutectic particles usually accounted for most of the damage occurring during deformation [111, 112]. The size and aspect ratio of these particles have significant influence on the strength and ductility of the alloys [110].

2.6 Supersaturation of solid solution during non-equilibrium solidification and dispersoid formation

In conventional age-hardening process (solution treatment and subsequent ageing), solid solubility at the solution treatment temperature determines the amount of the age-hardening precipitates. However, in dispersoid forming process, the amount of the dispersoids is determined by the amount of the solute atoms trapped within the matrix during non-equilibrium solidification. Slow-diffusing solute atoms form the dispersoid phase during high-temperature solution treatment. The degree of supersaturation at a constant solidification rate mostly depends on two factors:

1. Solid solubility of solute atoms at the invariant reaction temperature (C_S)

2. Liquid solubility of solute atoms at the invariant reaction temperature (C_L)

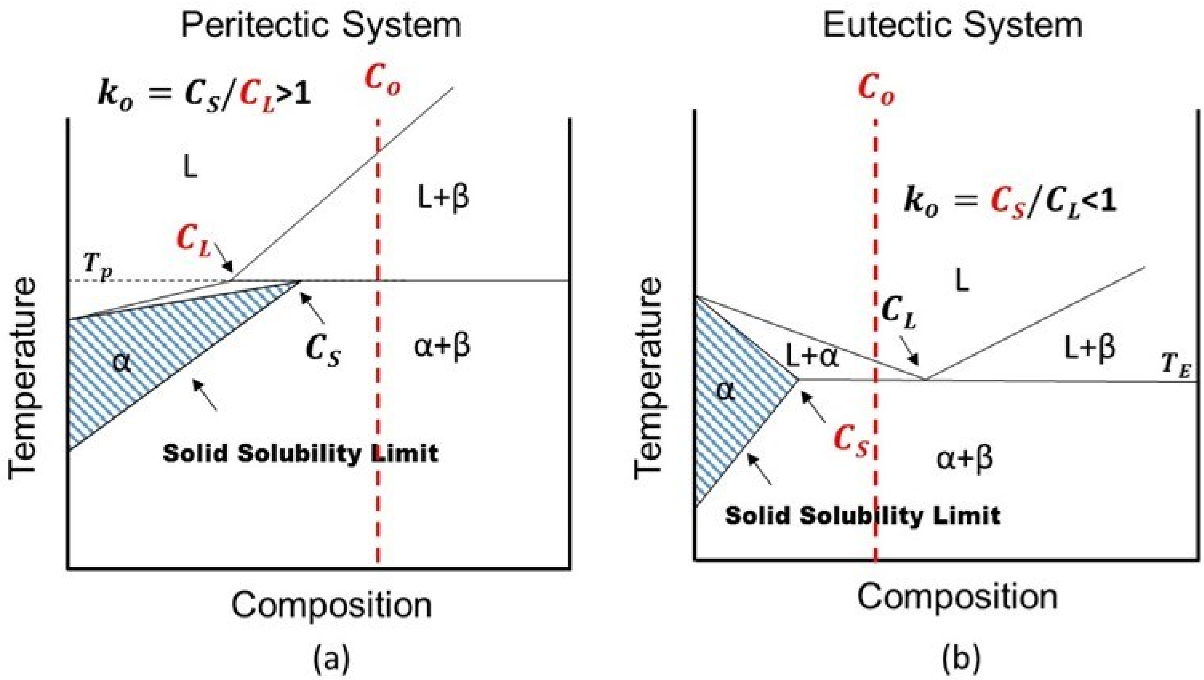

Fig. 2.20 A (a) peritectic and (b) eutectic system.

2.6.1 Peritectic systems

For peritectic systems (Fig. 2.20a), liquid solubility is the most important parameter that determines the amount of the solute atoms trapped during solidification. During non-equilibrium solidification (conventional casting), most of the peritectic reactions are incomplete. Alloys with compositions (C_o) above liquid solubility (C_L) form a pro-peritectic phase that does not undergo peritectic reaction ($L + \alpha \rightarrow \beta$) and remains within the microstructure till the end of solidification. Therefore, in such alloys, α-Al dendrites form from a liquid with composition equal to C_L, independent of the alloy composition (C_o). Solute atoms partition mostly to the dendrite cores (Fig. 2.21). A concentration profile of the solid Al (dendrite arms) can be estimated at any step during solidification by Scheil equation:

$$\mathrm{C} = k_o C_L (1 - f_s)^{k_o - 1} \tag{8}$$

where $k_o = C_S/C_L$ is the partition coefficient and f_s is the fraction solidified. Fig. 2.21 shows solute distribution during solidification of a peritectic system.

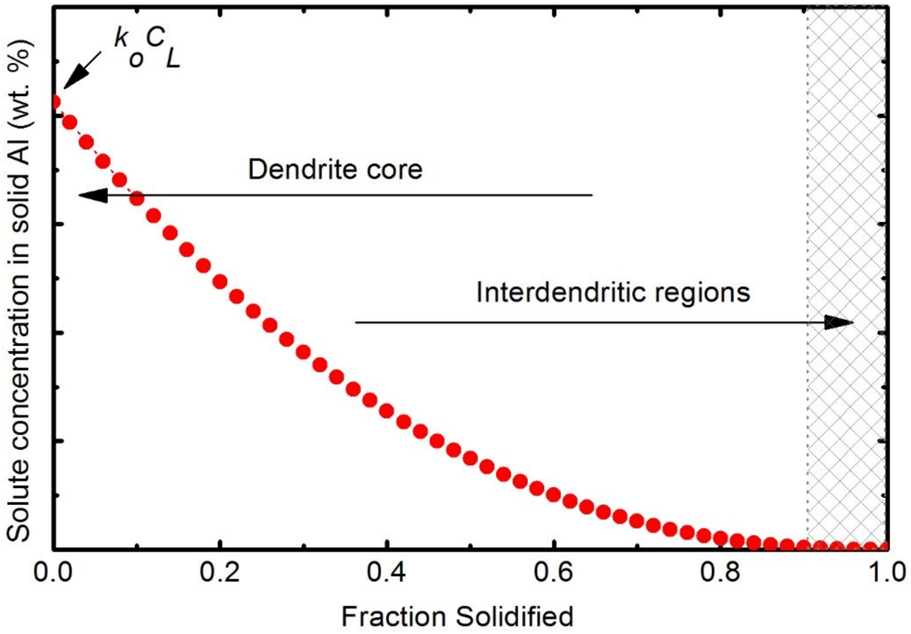

Fig. 2.21 Schematic concentration profile on the scale of the dendrite arm spacing in a peritectic system.

On the basis of the foregoing, alloying additions that form a peritectic system with Al must have high liquid solubility (C_L) at the peritectic temperature to be able to produce large amounts of dispersoids. Fig. 2.22 compares two peritectic systems, Al-Nb and Al-Mo. It can be seen that C_L ~ 0% for the Al-Nb system. Therefore, no supersaturation in this system is expected. For the Al-Mo system some degree of supersaturation is expected as C_L ~ 0.1%. It is worth mentioning that C_L strongly depends on the type of the pro-peritectic intermetallic, which might change in multicomponent alloy systems. However, C_L of binary systems can be a good primary tool for the selection of the potential dispersoid-formers in peritectic systems.

2.6.2 Eutectic systems

For eutectic systems (Fig. 2.20b), contrary to peritectic systems, solid solubility of the solute atoms at the eutectic temperature (C_S) dictates the degree of supersaturation. Solidification in these alloys starts with the formation of Al dendrites and solute atoms distribute according to:

$$\mathrm{C} = k_o C_o (1 - f_s)^{k_o - 1} \tag{9}$$

For the alloys with compositions (C_o) above C_S, solidification terminates by the eutectic reaction ($L \rightarrow \alpha + \beta$). Fig. 2.23 compares two eutectic systems, Al-Mn and Al-Fe. Because of negligible solid solubility of Fe in Al, no supersaturation in the Al-Fe system is expected, while Al-Mn system can form a supersaturated solid solution with ~ 1.25% Mn.

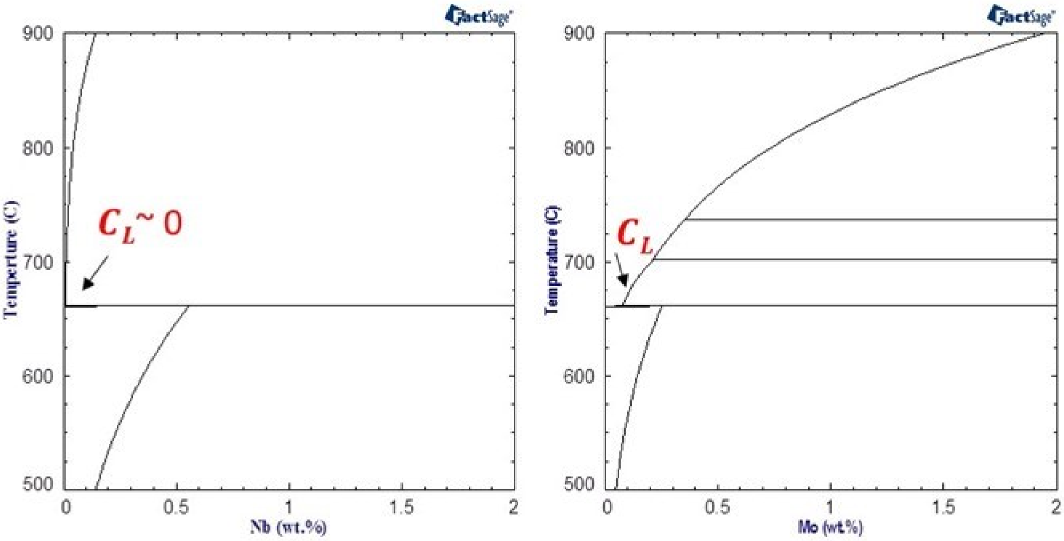

Fig. 2.22 Al-Nb (left) and Al-Mo (right) binary phase diagram.

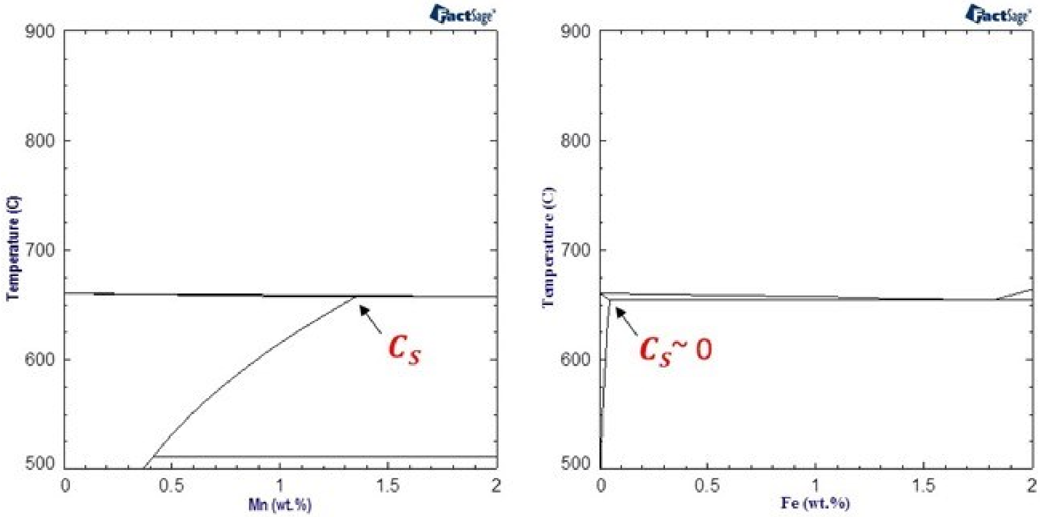

Fig. 2.23 Al-Mn (left) and Al-Fe (right) binary phase diagram.

2.7 References

[1] W.L. Guesser, P. Duran, W. Krause, Compacted graphite iron for diesel engine cylinder blocks, Congrès Le diesel: aujourd'hui et demain Ecole centrale, (2004) 12-13.

[2] E. Ozbakir, Development of aluminum alloys for diesel-engine applications, MS thesis, McGill University, 2008.

[3] M.O. Pekguleryuz, A.A. Kaya, Creep resistant magnesium alloys for powertrain applications, Adv. Eng. Mater., 5 (2003) 866-878.

[4] I.J. Polmear, Light alloys from traditional alloys to nanocrystals, in, Elsevier/Butterworth-Heinemann, Oxford; Burlington, MA, 2006.

[5] G.S. Cole, A.M. Sherman, Light weight materials for automotive applications, Mater. Charact., 35 (1995) 3-9.

[6] M. Garat, G. Laslaz, Improved Aluminum Alloys for Common Rail Diesel Cylinder Heads, in: AFS, IL, USA, 2007, pp. 1-8.

[7] W.L. Guesser, Compacted Graphite Iron–a New Material for Diesel Engine Cylinder Blocks, in: II Encontro da SBPMat Brazilian MRS Meeting, 2003.

[8] M. Diviš, R. Tichánek, M. Španiel, Heat transfer analysis of a diesel engine head, Acta Polytechnica, 43 (2003).

[9] L. Heusler, F.J. Feikus, M.O. Otte, Alloy and Casting Process Optimization for Engine Block Application, in: AFS Trans, 2001, pp. 215-223.

[10] F.J. Feikus, Optimisation of AlSi Cast-Alloys for Cylinder Head Applications, in: AFS, Georgia, USA, 1998, pp. 1-21.

[11] R. Fuoco, M. Moreira, 09-117 Fatigue Cracks in Aluminum Cylinder Heads for Diesel Engines, Transactions of the American Foundrymen's Society, 117 (2009) 225.

[12] S. Thalmair, A. Fischersworring-Bunk, F. Klinkenberg, K. Lang, M. Frikha, Microstructural damage evolution in Aluminium-Silicon cylinder head alloys under thermomechanical loading, BULLETIN-CERCLE D ETUDES DES METAUX SAINT ETIENNE, 17 (2007) 83.

[13] R. Minichmayr, M. Riedler, G. Winter, H. Leitner, W. Eichlseder, Thermo-mechanical fatigue life assessment of aluminium components using the damage rate model of Sehitoglu, Int. J. Fatigue, 30 (2008) 298-304.

[14] M. Riedler, H. Leitner, B. Prillhofer, G. Winter, W. Eichlseder, Lifetime simulation of thermo-mechanically loaded components, Meccanica, 42 (2007) 47-59.

[15] H. Ye, An overview of the development of Al-Si-Alloy based material for engine applications, J. Mater. Eng. Perform., 12 (2003) 288-297.

[16] S. Thalmair, J. Thiele, A. Fischersworring-Bunk, R. Ehart, M. Guillou, Cylinder Heads for High Power Gasoline Engines-Thermomechanical Fatigue Life Prediction, in, SAE Technical Paper, 2006.

[17] http://www.software.ricardo.com/support/manuals, access: September 2014.

[18] K.S. Lee, D.N. Assanis, J. Lee, K.M. Chun, Measurements and predictions of steady-state and transient stress distributions in a diesel engine cylinder head, in, SAE Technical Paper, 1999.

[19] M. Shalev, Y. Zvirin, A. Stotter, Experimental and analytical investigation of the heat transfer and thermal stresses in a cylinder head of a diesel engine, International Journal of Mechanical Sciences, 25 (1983) 471-483.

[20] T. Smith, H. Sehitoglu, E. Fleury, H. Maier, J. Allison, Modeling high-temperature stress-strain behavior of cast aluminum alloys, Metallurgical and Materials Transactions A, 30 (1999) 133-146.

[21] S. Trampert, T. Gocmez, S. Pischinger, Thermomechanical Fatigue Life Prediction of Cylinder Heads in Combustion Engines, Journal of Engineering for Gas Turbines and Power, 130 (2008) 012806-012806.

[22] S. Fontanesi, D. Carpentiero, S. Malaguti, M. Giacopini, S. Margini, L. Arnone, A New Decoupled CFD and FEM Methodology for the Fatigue Strength Assessment of an Engine Head, in, SAE Technical Paper, 2008.

[23] C.D. Rakopoulos, G.C. Mavropoulos, D.T. Hountalas, Measurements and analysis of load and speed effects on the instantaneous wall heat fluxes in a direct injection air-cooled diesel engine, International Journal of Energy Research, 24 (2000) 587-604.

[24] G.E. Dieter, Mechanical metallurgy, McGraw-Hill, New York, 1986.

[25] E.H. Wong, Y.W. Mai, A unified equation for creep-fatigue, Int. J. Fatigue, 68 (2014) 186-194.

[26] J.G. Kaufman, Introduction to aluminum alloys and tempers, in, ASM International, Materials Park, OH, 2000.

[27] G.E.M.D.S. Totten, Handbook of aluminum, M. Dekker, New York; Basel, 2003.

[28] J.R. Davis, A.S.M.I.H.C. Associates, Aluminum and aluminum alloys, ASM International, Materials Park, OH, 1993.

[29] D.J. Chakrabarti, D.E. Laughlin, Phase relations and precipitation in Al–Mg–Si alloys with Cu additions, Prog. Mater Sci., 49 (2004) 389-410.

[30] A. Biswas, D.J. Siegel, D.N. Seidman, Compositional evolution of Q-phase precipitates in an aluminum alloy, Acta Mater., 75 (2014) 322-336.

[31] Y. Li, S. Brusethaug, A. Olsen, Influence of Cu on the mechanical properties and precipitation behavior of AlSi7Mg0. 5 alloy during aging treatment, Scripta Mater., 54 (2006) 99-103.

[32] C.H. Cáceres, M.B. Djurdjevic, T.J. Stockwell, J.H. Sokolowski, The effect of Cu content on the level of microporosity in Al-Si-Cu-Mg casting alloys, Scripta Mater., 40 (1999) 631-637.

[33] G. Wang, X. Bian, W. Wang, J. Zhang, Influence of Cu and minor elements on solution treatment of Al–Si–Cu–Mg cast alloys, Mater. Lett., 57 (2003) 4083-4087.

[34] J.Y. Hwang, H.W. Doty, M.J. Kaufman, The effects of Mn additions on the microstructure and mechanical properties of Al–Si–Cu casting alloys, Mater. Sci. Eng., A, 488 (2008) 496-504.

[35] V.S. Zolotorevskiĭ, N.A. Belov, M.V. Glazoff, Casting aluminum alloys, Elsevier Science Ltd, 2007.

[36] N.A. Belov, D.G. Eskin, N.N. Avxentieva, Constituent phase diagrams of the Al–Cu–Fe–Mg–Ni–Si system and their application to the analysis of aluminium piston alloys, Acta Mater., 53 (2005) 4709-4722.

[37] N.A. Belov, D.G. Eskin, A.A. Aksenov, Multicomponent phase diagrams: applications for commercial aluminum alloys, Elsevier Science, 2005.

[38] L.F. Mondolfo, Aluminum alloys: structure and properties, Butterworths London, 1976.

[39] I. olmear, Light alloys: from traditional alloys to nanocrystals, Butterworth-Heinemann, 2006.

[40] A. Knuutinen, K. Nogita, S.D. McDonald, A.K. Dahle, Modification of Al–Si alloys with Ba, Ca, Y and Yb, Journal of Light Metals, 1 (2001) 229-240.

[41] K. Nogita, A.K. Dahle, Effects of boron on eutectic modification of hypoeutectic Al–Si alloys, Scripta Mater., 48 (2003) 307-313.

[42] A.K. Dahle, K. Nogita, S.D. McDonald, C. Dinnis, L. Lu, Eutectic modification and microstructure development in Al–Si Alloys, Mater. Sci. Eng., A, 413–414 (2005) 243-248.

[43] W.R. Osório, L.R. Garcia, P.R. Goulart, A. Garcia, Effects of eutectic modification and T4 heat treatment on mechanical properties and corrosion resistance of an Al–9wt% Si casting alloy, Mater. Chem. Phys., 106 (2007) 343-349.

[44] J. Chang, I. Moon, C. Choi, Refinement of cast microstructure of hypereutectic Al-Si alloys through the addition of rare earth metals, J Mater. Sci, 33 (1998) 5015-5023.

[45] L. Lu, K. Nogita, A. Dahle, Combining Sr and Na additions in hypoeutectic Al–Si foundry alloys, Mater. Sci. Eng., A, 399 (2005) 244-253.

[46] B. Suárez-Peña, J. Asensio-Lozano, Influence of Sr modification and Ti grain refinement on the morphology of Fe-rich precipitates in eutectic Al–Si die cast alloys, Scripta Mater., 54 (2006) 1543-1548.

[47] M. Kim, Y. Hong, H. Cho, The effects of Sc on the microstructure and mechanical properties of hypo-eutectic Al−Si alloys, Metals and Materials International, 10 (2004) 513-520.

[48] W. Prukkanon, N. Srisukhumbowornchai, C. Limmaneevichitr, Influence of Sc modification on the fluidity of an A356 aluminum alloy, J. Alloys Compd., 487 (2009) 453-457.

[49] W. Prukkanon, N. Srisukhumbowornchai, C. Limmaneevichitr, Modification of hypoeutectic Al–Si alloys with scandium, J. Alloys Compd., 477 (2009) 454-460.

[50] S.D. McDonald, K. Nogita, A.K. Dahle, Eutectic nucleation in Al–Si alloys, Acta Mater., 52 (2004) 4273-4280.

[51] L.F. Mondolfo, Aluminum alloys : structure and properties, Butterworths, London; Boston, 1976.

[52] S.G. Shabestari, The effect of iron and manganese on the formation of intermetallic compounds in aluminum–silicon alloys, Mater. Sci. Eng., A, 383 (2004) 289-298.

[53] N.A.A.A.A.E.D.G. Belov, Iron in aluminum alloys : impurity and alloying element, Taylor & Francis, London, 2002.

[54] A. Aliravci, Kinetics, thermodynamics and mechanism of metastable Al-AlmFe phase and fir-tree zone formation in DC-cast Al-Fe-Si alloy ingots, PhD thesis, 2006.

[55] W. Khalifa, F.H. Samuel, J.E. Gruzleski, Iron intermetallic phases in the Al corner of the Al-Si-Fe system, Metallurgical and Materials Transactions A, 34 (2003) 807-825.

[56] V.S. Zolotorevskii, N.A. Belov, M. Glazoff, Casting aluminum alloys, in, Elsevier, Amsterdam; Boston; London, 2007.

[57] L.A. Narayanan, F.H. Samuel, J.E. Gruzleski, Crystallization behavior of iron-containing intermetallic compounds in 319 aluminum alloy, Metallurgical and Materials Transactions A, 25 (1994) 1761-1773.

[58] L. Narayanan, F. Samuel, J. Gruzleski, Dissolution of iron intermetallics in Al-Si Alloys through nonequilibrium heat treatment, Metallurgical and Materials Transactions A, 26 (1995) 2161-2174.

[59] M.H. Mulazimoglu, A. Zaluska, J.E. Gruzleski, F. Paray, Electron microscope study of Al-Fe-Si intermetallics in 6201 aluminum alloy, Metallurgical and Materials Transactions A, 27 (1996) 929-936.

[60] J.Y. Hwang, H.W. Doty, M.J. Kaufman, Crystallographic studies on the iron-containing intermetallic phases in the 319-type aluminium casting alloys, Philosophical Magazine, 88 (2008) 607-619.

[61] Q. Wang, P. Jones, M. Osborne, Effect of Iron on the Microstructure and Mechanical Properties of an Al-7% Si-0.4% Mg Casting Alloy, in, SAE Technical Paper, 2003.

[62] Q. Wang, C. Caceres, J. Griffiths, Damage by eutectic particle cracking in aluminum casting alloys A356/357, Metallurgical and Materials Transactions A, 34 (2003) 2901-2912.

[63] H.Y. Kim, S.W. Han, H.M. Lee, The influence of Mn and Cr on the tensile properties of A356–0.20Fe alloy, Mater. Lett., 60 (2006) 1880-1883.

[64] G. Gustafsson, T. Thorvaldsson, G.L. Dunlop, The influence of Fe and Cr on the microstructure of cast Al-Si-Mg alloys, Metall. Trans. A, 17 (1986) 45-52.

[65] C.M. Dinnis, J.A. Taylor, A.K. Dahle, As-cast morphology of iron-intermetallics in Al–Si foundry alloys, Scripta Mater., 53 (2005) 955-958.

[66] M.E. Kassner, Fundamentals of creep in metals and alloys, in, Elsevier, Amsterdam; London, 2009.

[67] R.E. Reed-Hill, R. Abbaschian, Physical metallurgy principles, (1973).

[68] F.R.N. Nabarro, F. De Villiers, Physics of creep and creep-resistant alloys, CRC press, 1995.

[69] P. Kumar, Creep in pure single and polycrystalline aluminum at very low stresses and high temperatures: An evaluation of Harper-Dorn creep, in, University of Southern California, United States -- California, 2007.

[70] M. Ashby, C. Gandhi, D. Taplin, Overview No. 3 Fracture-mechanism maps and their construction for fcc metals and alloys, Acta Metall., 27 (1979) 699-729.

[71] R.W. Hertzberg, Deformation and fracture mechanics of engineering materials, Wiley, New York, 1989.

[72] H.J.A.M.F. Frost, Deformation-mechanism maps : the plasticity and creep of metals and ceramics, Pergamon Press, Oxford [Oxfordshire]; New York, 1982.

[73] J.D. Lubahn, R.P. Felgar, Plasticity and creep of metals, Wiley, New York, 1961.

[74] A.R.K. Rusinko, Plasticity and creep of metals, in, Springer, New York, 2011.

[75] J. Jelwan, M. Chowdhury, G. Pearce, Design for creep: A critical examination of some methods, Engineering Failure Analysis, 27 (2013) 350-372.

[76] R.K. Penny, D.L. Marriott, Design for Creep, Springer Netherlands, 2012.

[77] K.E. Knipling, D.C. Dunand, Creep resistance of cast and aged Al–0.1Zr and Al–0.1Zr–0.1Ti (at.%) alloys at 300–400 °C, Scripta Mater., 59 (2008) 387-390.

[78] M.F. Ashby, A first report on deformation-mechanism maps, Acta Metall., 20 (1972) 887-897.

[79] F.R.N. Nabarro, Creep in commercially pure metals, Acta Mater., 54 (2006) 263-295.

[80] A.J. Ardell, Harper–Dorn creep – The dislocation network theory revisited, Scripta Mater., 69 (2013) 541-544.

[81] T.G. Langdon, P. Yavari, An investigation of Harper-Dorn creep—II. The flow process, Acta Metall., 30 (1982) 881-887.

[82] F.R.N. Nabarro, The mechanism of Harper-Dorn creep, Acta Metall., 37 (1989) 2217-2222.

[83] P. Yavari, D.A. Miller, T.G. Langdon, An investigation of harper-dorn creep—I. Mechanical and microstructural characteristics, Acta Metall., 30 (1982) 871-879.

[84] H. Watanabe, H. Tsutsui, T. Mukai, M. Kohzu, S. Tanabe, K. Higashi, Deformation mechanism in a coarse-grained Mg–Al–Zn alloy at elevated temperatures, Int. J. Plast., 17 (2001) 387-397.

[85] S. Spigarelli, Interpretation of creep behaviour of dispersion-strengthened Al–Fe–V–Si alloys in terms of detachment mechanisms: an overview, Mater. Sci. Eng., A, 337 (2002) 306-314.

[86] Y. Li, T. Langdon, Fundamental aspects of creep in metal matrix composites, Metallurgical and Materials Transactions A, 30 (1999) 315-324.

[87] E. Arzt, Creep of dispersion strengthened materials: a critical assessment, Res. Mechanica, 31 (1991) 399.

[88] J. Rösler, E. Arzt, The kinetics of dislocation climb over hard particles—I. Climb without attractive particle-dislocation interaction, Acta Metall., 36 (1988) 1043-1051.

[89] J. Rösler, R. Joos, E. Arzt, Microstructure and creep properties of dispersion-strengthened aluminum alloys, Metall. Mater. Trans. A, 23 (1992).

[90] E.A. Marquis, D.C. Dunand, Model for creep threshold stress in precipitation-strengthened alloys with coherent particles, Scripta Mater., 47 (2002) 503-508.

[91] M.E. Krug, D.C. Dunand, Modeling the creep threshold stress due to climb of a dislocation in the stress field of a misfitting precipitate, Acta Mater., 59 (2011) 5125-5134.

[92] D.C. Dunand, A.M. Jansen, Creep of metals containing high volume fractions of unshearable dispersoids—Part I. Modeling the effect of, Acta Mater., 45 (1997) 4569-4581.

[93] J. Kim, M.-G. Lee, D. Kim, R.H. Wagoner, Micromechanics-based strain hardening model in consideration of dislocation-precipitate interactions, Metals and Materials International, 17 (2011) 291-300.

[94] K.E. Knipling, D.N. Seidman, D.C. Dunand, Ambient- and high-temperature mechanical properties of isochronally aged Al–0.06Sc, Al–0.06Zr and Al–0.06Sc–0.06Zr (at.%) alloys, Acta Mater., 59 (2011) 943-954.

[95] K.E. Knipling, D.C. Dunand, D.N. Seidman, Criteria for developing castable, creep-resistant aluminum-based alloys-A review, Zeitschrift fur Metallkunde, 97 (2006) 246.

[96] C.J. Kuehmann, P.W. Voorhees, Ostwald ripening in ternary alloys, Metallurgical and Materials Transactions A, 27 (1996) 937-943.

[97] C.B. Fuller, D.N. Seidman, D.C. Dunand, Mechanical properties of Al(Sc,Zr) alloys at ambient and elevated temperatures, Acta Mater., 51 (2003) 4803-4814.

[98] A.S. Argon, Strengthening mechanisms in crystal plasticity, Oxford University Press, Oxford; New York, 2008.

[99] B.G. Clark, I.M. Robertson, L.M. Dougherty, D.C. Ahn, P. Sofronis, High-temperature Dislocation-precipitate Interactions in Al Alloys: An in situ Transmission Electron Microscopy Deformation Study, J. Mater. Res., 20 (2005) 1792-1801.

[100] J. Eshelby, The elastic field outside an ellipsoidal inclusion, Proceedings of the Royal Society of London. Series A. Mathematical and Physical Sciences, 252 (1959) 561-569.

[101] J.D. Eshelby, The determination of the elastic field of an ellipsoidal inclusion, and related problems, Proceedings of the Royal Society of London. Series A. Mathematical and Physical Sciences, 241 (1957) 376-396.
[102] M.F. Ashby, The deformation of plastically non-homogeneous materials, Philosophical Magazine, 21 (1970) 399-424.
[103] M.F. Ashby, Work hardening of dispersion-hardened crystals, Philosophical Magazine, 14 (1966) 1157-1178.
[104] A.S. Argon, J. Im, R. Safoglu, Cavity formation from inclusions in ductile fracture, Metall. Trans. A, 6 (1975) 825-837.
[105] A. Saigal, E.R. Fuller Jr, Analysis of stresses in aluminum–silicon alloys, Computational Materials Science, 21 (2001) 149-158.
[106] G. Guiglionda, W.J. Poole, The role of damage on the deformation and fracture of Al–Si eutectic alloys, Mater. Sci. Eng., A, 336 (2002) 159-169.
[107] Q. Wang, C. Caceres, On the strain hardening behaviour of Al-Si-Mg casting alloys, Mater. Sci. Eng., A, 234 (1997) 106-109.
[108] Q. Wang, Microstructural effects on the tensile and fracture behavior of aluminum casting alloys A356/357, Metallurgical and Materials Transactions A, 34 (2003) 2887-2899.
[109] C.H. Caceres, J.R. Griffiths, Damage by the cracking of silicon particles in an Al-7Si-0.4Mg casting alloy, Acta Mater., 44 (1996) 25-33.
[110] K. Gall, M. Horstemeyer, D.L. McDowell, J. Fan, Finite element analysis of the stress distributions near damaged Si particle clusters in cast Al–Si alloys, Mech. Mater., 32 (2000) 277-301.
[111] M. Tiryakioğlu, J. Campbell, J.T. Staley, The influence of structural integrity on the tensile deformation of cast Al–7wt.%Si–0.6wt.%Mg alloys, Scripta Mater., 49 (2003) 873-878.
[112] D.L. McDowell, K. Gall, M.F. Horstemeyer, J. Fan, Microstructure-based fatigue modeling of cast A356-T6 alloy, Engineering Fracture Mechanics, 70 (2003) 49-80.

CHAPTER 3

PHASE FORMATION IN AS-SOLIDIFIED AND HEAT TREATED AL-SI-CU-MG-NI ALLOYS: THERMODYNAMIC ASSESSMENT AND EXPERIMENTAL INVESTIGATION FOR ALLOY DESIGN

Owing to its low solid solubility and low diffusivity in Al, Ni is known to impart elevated temperature strength to aluminum alloys by forming thermally-stable aluminides within the microstructure. This doctoral study, therefore, focused initially on the effects of Ni on an Al-Si base alloy selected for the investigation. In this chapter, the results of the study of low level ($\leq 1\, wt.\%$) Ni additions to an Al-7Si-0.5Cu-0.3Mg alloy (MG3R, base alloy) are presented. Thermodynamic calculations and the microstructural investigations are conducted to understand the solidification and phase selection in the compositional ranges used for engine applications. This chapter has been published as a journal article: *A.R. Farkoosh, M. Javidani, M. Hoseini, D. Larouche, M. Pekguleryuz, Phase formation in as-solidified and heat-treated Al–Si–Cu–Mg–Ni alloys: Thermodynamic assessment and experimental investigation for alloy design, J. Alloys Compd., 551 (2013) 596-606.*

ABSTRACT

Thermodynamic simulations based on the CALPHAD method have been carried out to assess the phase formation in Al-7Si-(0-1)Ni-0.5Cu-0.35Mg alloys (in wt.%) under equilibrium and non-equilibrium (Scheil cooling) conditions. Calculations showed that the T-Al_9FeNi, γ-Al_7Cu_4Ni, δ-Al_3CuNi and ε-Al_3Ni phases are formed at different Ni levels. By analyzing the calculated isothermal sections of the phase diagrams it was revealed that the Ni:Cu and Ni:Fe ratios control precipitation in this alloy system. In order to verify the simulation results, microstructural investigations in as-cast, solution treated and aged conditions were carried out using electron probe microanalysis (EPMA), scanning electron microscopy (SEM), X-ray diffraction (XRD) and transmission electron microscopy (TEM). Furthermore, cooling curve analysis (CCA) was also performed to determine the freezing range of the new alloys and porosity formation during solidification. Hardness measurements of the overaged samples showed that in this alloy system the δ-Al_3CuNi phase has a greater influence on the overall strength of the alloys compared to the other Ni-bearing precipitates.

Keywords: Al-Si Casting alloys; Thermodynamic calculations; Nickel intermetallic precipitates; Aluminum engine alloys

3.1 Introduction

Al-Si casting alloys with Cu and Mg additions, such as A356 (Al7Si0.3Mg) and A319 (Al7Si4Cu), are widely used in automotive engine applications [1-5]. The silicon provides good fluidity and a broad range of high strengths at room temperature can be obtained by age hardening [6, 7]. However, the major disadvantages of these age-hardened alloys are poor thermal and metallurgical stability. These alloys lose their strength at high temperatures due to Ostwald ripening [5, 8, 9]. Over the last fifteen years, research has been carried out to develop new aluminum alloys with improved high temperature performance. This new generation of alloys rely on the presence of thermally stable intermetallic precipitates which retain their strength when the age-hardening precipitates have lost their strengthening effect [5, 10]. Different alloying elements such as Cu, Ni, Mn, Cr, Zr and most recently Sc and Er have been added to Al alloys [5, 11, 12]. Such alloying additions form thermally stable dispersoids within the microstructure that reinforce the Al matrix and grain boundaries at high temperatures.

By adding Cu to the A356 alloy, Feikus [13] developed an Al-7Si-0.3Mg-0.5Cu alloy which showed substantial improvement in mechanical properties at 250 ^{o}C. Copper additions enhanced the age-hardening response via the introduction of two new age-hardening precipitates, Q-$Al_5Mg_8Cu_2Si_6$ and θ-Al_2Cu into the microstructure [14]. Based on the improvement of the Al-7Si-0.3Mg-0.5Cu alloy with Ni additions, Heusler et al. [15] presented a new alloy for Diesel engine applications in which the Cu, Mg and Fe levels were adjusted to give an Al-7Si-0.4Mg-0.4Cu-0.5Ni-0.4Fe alloy. This alloy exhibited a 20% increase in fatigue strength and positive effects on tensile strength. This improvement was attributed to the presence of Ni-bearing intermetallics which formed due to the large driving force for compound formation between Al and Ni (size factor, electronegativity) and low solubility of Ni in aluminum (max~ 0.05% at the eutectic temperature) [16]. According to the phase diagrams, Ni can combine with Al, Cu and Fe forming the following intermetallics which could be in equilibrium with other phases in this alloy system [17]: ε-Al_3Ni, δ-Al_3CuNi, γ-Al_7Cu_4Ni, T-Al_9FeNi. These intermetallics are thermally stable and impart high strength at elevated temperatures [18]. However, the brittleness of Ni-bearing intermetallics lowers the ductility, hence high temperature heat-treatment is usually conducted to increase ductility. Ni is also known as a Fe corrector. Through a peritectic reaction the brittle plate-like β-Al_5FeSi intermetallics transform into T-Al_9FeNi phase [19, 20].

Al-Si alloys with a substantial amount of Ni are used extensively for engine pistons in which high strength at elevated temperatures is required [21-24]. The Si, Fe, Cu and Ni contents of these alloys are relatively high, ranging from 10 to 25 wt.%, 0.4 to 1.5 wt.%, 0.5 to 6 wt.% and 0.5 to 4 wt.% respectively [17, 18, 21, 22, 24]. The phase equilibria of the Al-Si-Mg-Cu-Fe-Ni system in the range of piston alloys have recently been studied by different investigators [17, 18]. Nevertheless, the compositional range of the new engine alloys is outside those of the piston alloys. Thus, the development and optimization of these alloys require the reassessment of the alloy system with much lower amounts of Si, Cu, Mg, Ni and Fe, wherein, thermodynamic calculations can be a powerful tool. Rigorous thermodynamic analysis of this alloy system requires the calculation of the multicomponent Al-Si-Cu-Mg-Ni-Fe phase diagram; this is a complicated task but has great practical significance. In the present work, the influence of Ni on the microstructure and precipitation of Al-7Si-0.3Mg-0.5Cu alloys with 0.1-1.0% Ni was investigated. Thermodynamic calculations were carried out via ThermoCalc software using the TTAL7 database [25] and combined with experimental data to generate information for alloy design.

3. 2 Experimental procedures

Commercial grade A356 alloy supplied by Rio Tinto Alcan Inc. was melted in a silicon carbide crucible using a high frequency NORAX (Canada) induction furnace. Ni and Cu were added to the melt from a set of master alloys (Al-20wt.% Ni and Al-33wt.% Cu) at 760 and 730 ^{o}C, respectively, holding for 15 min to dissolve at the specified temperatures. After 3 minutes of degassing with high purity argon gas, the alloys were cast into a pre-heated (400 ^{o}C) permanent mold at 730 ^{o}C to obtain thin-plate castings with thickness of 6mm. Alloys were modified by the addition of 150 ppm Sr, using Al-10wt.% Sr master alloy just prior to degassing. Inductively coupled plasma (ICP) technique was used to determine the chemical compositions of the alloys, which are presented in Table 3.1. All compositions are given in wt.% hereafter, unless otherwise specified.

Table 3.1 Chemical compositions of the alloys

Alloy	**Chemical Composition (wt.%)**								
	Si	Mg	Cu	Ni	Fe	Ti	Mn	Sr	Al
R (A356 + 0.5Cu)	6.88	0.33	0.55	<0.01	0.10	0.10	<0.01	0.015	Bal.
R+0.1Ni	6.49	0.33	0.55	0.10	0.13	0.11	<0.01	0.014	Bal.
R+0.3Ni	6.64	0.36	0.58	0.31	0.13	0.11	<0.01	0.013	Bal.
R+0.6Ni	6.50	0.31	0.53	0.62	0.10	0.10	<0.01	0.015	Bal.
R+1.0Ni	6.94	0.32	0.57	1.02	0.13	0.10	<0.01	0.017	Bal.

An electrically heated, air-circulating chamber furnace was used for heat treatments. To avoid probable incipient melting, solution annealing was carried out in two stages: 4 hours at 500 ^{o}C followed by 10 hours at 545 ^{o}C. The samples were then quenched in water at room temperature and aged at 200 ^{o}C for up to 600 hours. HRF hardness measurements were carried out using a Mitutoyo HR-500 hardness testing machine.

Cooling curve analysis (CCA) was conducted in order to determine the liquidus and the freezing range of the alloys by recording the temperature of the melt (~ 200 g) during solidification.

K-Type (Chromel-alumel) thermocouples were positioned at the bottom of the sand molds and a data acquisition system (Squirrel Data Logger Grant2020) was used to log the temperature variations. All efforts were made to keep the experimental conditions constant. Thermal arrests were obtained from the first derivative of the cooling curves. Data acquisition rate was 10 Hz and a cooling rate of 9 ^{o}C/s was observed.

XRD phase analysis was carried out using a Bruker D8 diffractometer equipped with a GADDS 2D detector and Cu Kα radiation (λ = 0.15406 nm). Samples for microstructural investigation were taken from thin plate castings and ground with a series of SiC paper and polished on porous neoprene polishing cloth with Al_2O_3 solution. A Buehler vibratory polisher was used for final polishing using colloidal silica solution. Samples were inspected using a Hitachi S-4700 field emission gun scanning electron microscope (FEG-SEM) equipped with an Oxford INCA energy dispersive spectroscopy (EDS) detector. Accelerating voltage was 15 kV at a beam current of 10 μA to minimize the penetration volume. Quantitative analysis was performed using a JEOL-8900 electron probe microanalyzer (EPMA) coupled with wavelength dispersive spectroscopy (WDS) detectors, operating at 15 kV. Detailed microstructural and phase analysis of the aged samples were performed by transmission electron microscopy (TEM). The TEM samples were prepared by mechanical grinding and electropolished to electron transparency using a Struers Tenupol 3 jet polisher. The etchant used was a solution of 10% nitric acid and 90% methanol. TEM images were acquired using a Philips CM200 microscope with a beam energy of 200 kV. The EDS spectra were obtained by EDAX detector connected to the column.

3.3 Results and discussion

3.3.1 Thermodynamic calculations

Fig. 3.1a shows a calculated isopleth of the Al-Si-Cu-Mg-Fe-Ni system (Al-Si with fixed values of 1% Ni, 0.5% Cu, 0.35% Mg, and 0.1% Fe). The broken line represents the Al-7Si-0.5Cu-0.35Mg-0.1Fe alloy with 1%Ni. Since the Fe level is important in these alloys, Fe was included in all calculations. Fe in Al alloys is generally considered to be an impurity which may form brittle phases and, consequently, the Fe level is kept as low as possible to minimize any adverse effects on mechanical properties. However, Fe combined with elements such as Ni, Mo, Cr, Mn or Ce can form thermally stable dispersoids which may be beneficial for the high temperature stability of these alloys. The polythermal section in Fig. 3.1a illustrates the different reactions (Table 3.2) occurring during equilibrium solidification.

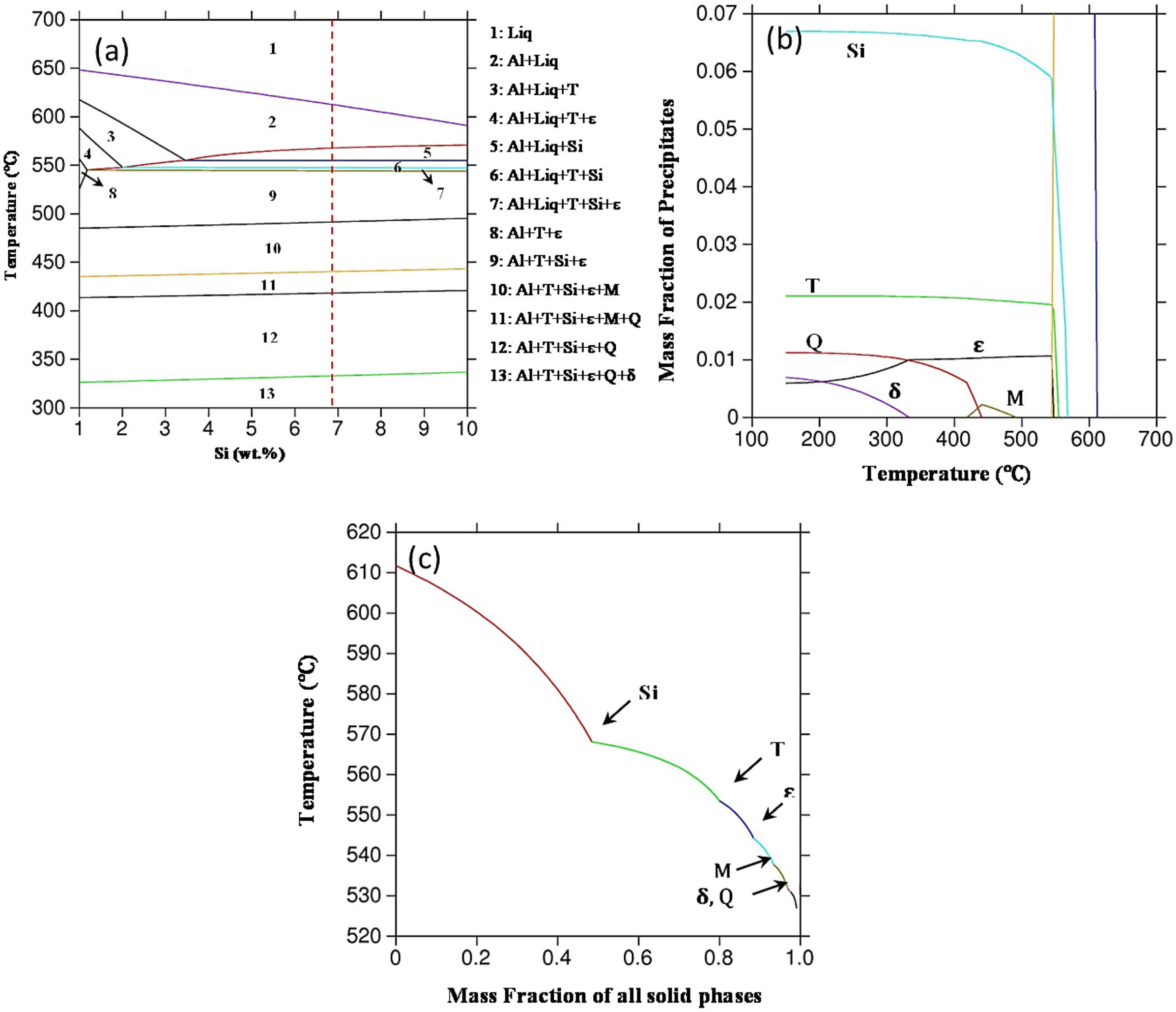

Fig. 3.1 Al-Si-Cu-Mg-Fe-Ni (a) calculated isopleth at 0.35Mg, 0.5Cu, 0.1Fe, 1.0Ni, (b) amount of different phases as a function of temperature in equilibrium conditions and (c) weight fraction of solids as a function of temperature in Scheil cooling conditions; ε-Al_3Ni, δ-Al_3CuNi, T-Al_9FeNi, M-Mg_2Si, Q-$Al_5Cu_2Mg_8Si_6$.

Calculations show that solidification starts with the precipitation of the primary Al phase at 615 °C followed by a eutectic reaction at 570 °C. The eutectic α(Al)-Si mixture continues to form as the temperature decreases to 554 °C. At this point, the T-Al_9FeNi phase forms according to the following ternary reaction:

$$L \rightarrow \alpha\text{-Al} + Si + T. \quad (1)$$

Solidification continues according to this reaction as the temperature decreases to 548 °C, below which the ternary reaction turns into a quaternary reaction forming the ε-Al_3Ni phase:

$$L \rightarrow \alpha\text{-Al} + Si + T + \varepsilon. \tag{2}$$

Solidification terminates at 546 °C with this quaternary reaction. It is worth mentioning that the T-Al_9FeNi and ε-Al_3Ni phases form over a relatively narrow range of temperatures.

Table 3.2 Reactions in the Al-7Si-0.5Cu-0.35Mg-0.1Fe-1.0Ni alloy

Reaction	**Temperature (°C)**	
	Equilibrium	Scheil /CCA*
L→α-Al	615	612/612
L→ α-Al+Si	570	568/551
L→ α-Al+Si+T	554	553
L→ α-Al+Si+T+ε	548	544
L→Al+Si+M	-	538
L+M→Al+Si+Q	-	532
L+ε→Al+Si+δ	-	531
α-Al→M	492	-
α-Al+M→Q	441	-
α-Al+ϵ→δ	333	-

* CCA: cooling curve analysis

As the temperature continues to decrease, Si particles precipitate from the α-Al matrix. A negligible amount (max 0.2%) of the M-Mg_2Si phase forms at 492 °C. However, this phase transforms into the Q-$Al_5Cu_2Mg_8Si_6$ phase at 441 °C through a peritectoid reaction:

$$\alpha\text{-Al} + M \rightarrow Q. \tag{3}$$

It was noted that the amount of the Q-$Al_5Cu_2Mg_8Si_6$ phase increased with decreasing temperature to a maximum of 1% at room temperature. Another ternary phase forms as a result of a peritectoid reaction at 333 °C. At this point the α-Al reacts with the ε-Al_3Ni phase forming the δ-$Al_3(CuNi)_2$ phase:

$$\alpha\text{-Al} + \varepsilon \rightarrow \delta. \tag{4}$$

Consequently, the amount of ε-Al_3Ni phase decreases from 1% at 333 °C to 0.7% at room temperature. Fig. 3.1b shows the calculated amount of the phases at different temperatures for the Al-7Si-0.5Cu-0.35Mg-0.1Fe-1.0Ni alloy. According to these calculations, the equilibrium microstructure of this alloy consists of 6.7% Si, 2.1% T, 1% Q, 0.85% ε and 0.3% δ phases at 300 °C which is the working temperature of Diesel engines.

In order to simulate the as-cast microstructure, thermodynamic calculations were repeated for the same alloy using the Scheil (non-equilibrium cooling) approach (Table 3.2). Scheil assumes that no solute back diffusion occurs in the solid phase and that the local concentration of the solid remains constant during solidification. Also, the liquid phase is assumed to have a uniform concentration during solidification due to mixing. Results are presented in Fig. 3.1c; as expected, the temperatures at which the phases are formed differ from equilibrium calculations. The phases present at room temperature are Si, T, Q, ε and δ according to Scheil cooling calculation, showing no large departure from the equilibrium calculations. This similarity could be explained in terms of the Scheil equation as follows: At any step during solidification, the differential form of Scheil equation can be expressed as:

$$\left(C_{Ni}^{L} - C_{Ni}^{S}\right) df^{S} = (1 - f^{S}) dC_{Ni}^{L} , \tag{5}$$

where C_{Ni}^{L} and C_{Ni}^{S} are the Ni concentration in liquid and solid phases at the solidification front respectively, and f^{S} is the mass fraction of the solid phase. Since Ni has a very low solid solubility in Al even at high temperatures (~ 0.05%), which becomes negligible with the presence of 7% Si, practically no Ni dissolves in the Al matrix during solidification. Therefore, C_{Ni}^{S}could be considered:

$$C_{Ni}^{S} \approx 0 . \tag{6}$$

With this assumption and applying the boundary conditions of $C_{Ni}^{L} = C_0$ at $f^{S} = 0$, equation (5) has an analytical solution as:

$$C_{Ni}^{L} = \frac{C_0}{1-f^{S}} . \tag{7}$$

In the case of equilibrium solidification, infinite diffusion is assumed in both solid and liquid phases. Based on mass conservation,

$$C_{Ni}^{S} f^{S} + C_{Ni}^{L} f^{L} = C_0 . \tag{8}$$

Here, $f^{L}$is the mass fraction of liquid phase. Setting $C_{Ni}^{S} \approx 0$ and $f^{L} = 1 - f^{S}$in this equation, gives the same solution as equation (7). With this assumption, both approaches (equilibrium and Scheil cooling) give the same concentration of Ni in the liquid at any step during solidification.

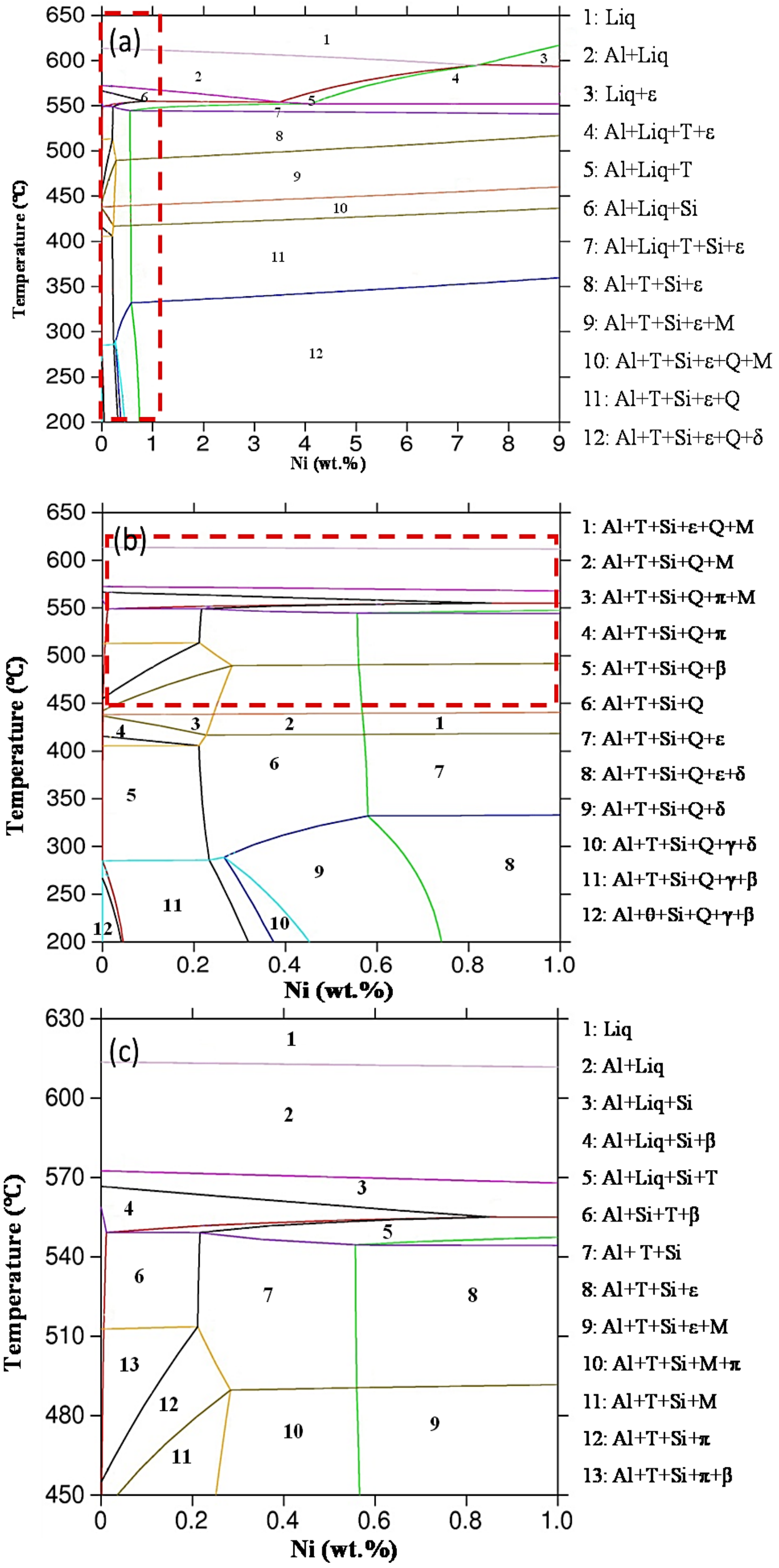

Fig. 3.2 (a), (b), (c) Calculated Al-Ni phase diagrams at 7Si, 0.5Cu, 0.35Mg and 0.1Fe for different temperature and Ni ranges.

It therefore appears that the level of Ni governs the formation of the Ni-bearing intermetallics during solidification even if there are differences in the concentration of other elements in the liquid and is a major determinant of phase selection. As is evident from the Al-Ni polythermal section in Fig. 3.2a, the equilibrium composition range of the different phases at low Ni levels are so narrow that a small change in Ni content results in the formation of different phases. For clarity, this polythermal section has been presented over two narrow temperature and Ni ranges in Figs. 3.2b-c. The solidification path of the Al-Si-Mg-Cu-Fe-Ni system under equilibrium conditions is also shown in Fig. 3.3.

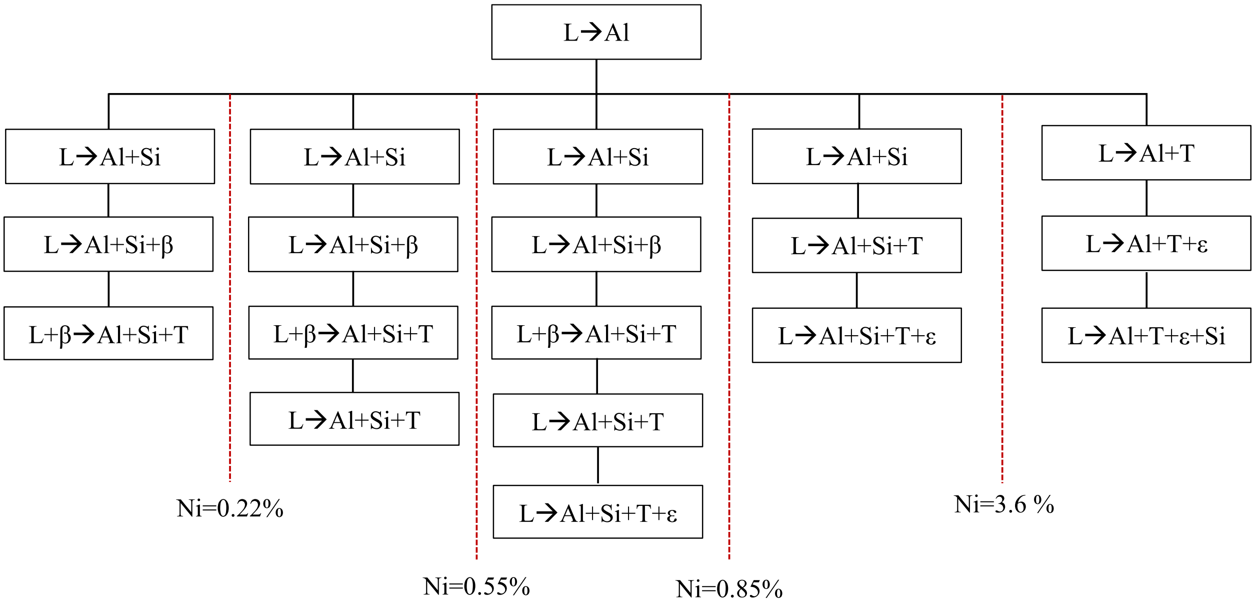

Fig. 3.3 Solidification path of Al-Si-Mg-Cu-Fe-Ni system under equilibrium conditions (0-7% Ni).

Based on the calculations, the solidification of alloys with less than 3.6% Ni starts with the formation of the dendritic α-Al phase followed by the α(Al)-Si eutectic mixture. Depending on the Ni level, subsequent reactions could be the formation of the T-Al_9FeNi or β-Al_5FeSi phase. At very low levels of Ni, solidification continues with the formation of the β-Al_5FeSi phase. Then, through a peritectic reaction, the liquid reacts with the β-Al_5FeSi phase forming the T-Al_9FeNi phase:

$$L + \beta \rightarrow Al + Si + T \tag{9}$$

Calculations show that at Ni less than 0.22% the T-Al_9FeNi and β-Al_5FeSi phases could coexist in equilibrium (Fig. 3.2c). However, in alloys to the right of the peritectic point, 0.22% Ni, the peritectic reaction completely transforms the β-Al_5FeSi phase into the T-Al_9FeNi phase. In the case of alloys with more than 0.56% Ni, solidification terminates according to reaction (2) discussed above. In these alloys, the T-Al_9FeNi phase is in equilibrium with the ε-Al_3Ni phase.

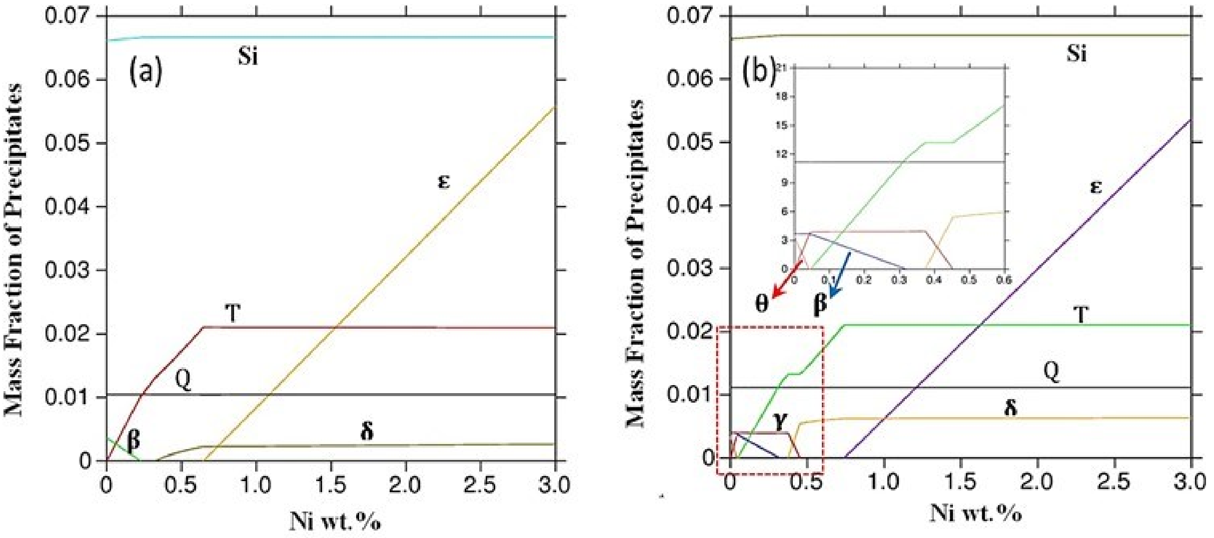

Fig. 3.4 Effect of Ni additions on the amount of different phases of the Al-7Si-0.5Cu-0.35Mg-0.1Fe alloy at (a) 300 °C and (b) 200 °C in equilibrium conditions. It is worth noting that a very small amount of Ni completely suppresses the formation of π phase in this alloy system.

Figs. 3.4a and 3.4b show the effect of Ni content on the mass fraction of the equilibrium phases in the Al-7Si-0.5Cu-0.35Mg-0.1Fe alloy at 300 °C and 200 °C, respectively. It was observed that at 300 °C, the equilibrium amount of phases in the alloy with no Ni were 0.4% β-Al_5FeSi, 1% Q-$Al_5Cu_2Mg_8Si_6$ and 6.6% Si. Ni addition leads to the suppression of the β-Al_5FeSi phase; Fe preferentially binds with Ni forming the T-Al_9FeNi phase rather than the β-Al_5FeSi phase. Ni in concentrations above 0.3% forms the δ-$Al_3(CuNi)_2$ phase. As the Ni level increases up to ~ 0.6%, progressively more T-Al_9FeNi and δ-$Al_3(CuNi)_2$ phases form. Further increase of Ni does not increase the amount of these phases; a nickel tri-aluminide, ε-Al_3Ni phase forms instead. At 200 °C, the γ-Al_7Cu_4Ni phase could be present at low levels of Ni up to 0.48%. It is also worth mentioning that the θ-Al_2Cu phase is present at trace levels of Ni at this temperature, however, it is rapidly suppressed with Ni additions. As shown by thermodynamic calculations, even though the presence of Ni decreases the amount of Cu in the matrix by forming the δ-$Al_3(CuNi)_2$ or γ-Al_7Cu_4Ni phase, the amount of Q phase is independent of the Ni level in these alloys and appears to be only a function of temperature.

3.3.2 Thermal analysis and the effect of Ni on pre-eutectic freezing range

Cooling curves of alloys containing 0.1-1% Ni are shown in Fig. 3.5a. The cooling curve analysis (CCA) revealed two thermal arrests during solidification of the alloys. The first one corresponds to the start of solidification with the formation of Al dendrites which occurred at an almost constant temperature (612 ºC) for all the alloys tested. Thermodynamic calculations also confirmed that the slope of the liquidus line in Al-Ni phase diagrams presented in Fig. 3.2c is negligible. Nonetheless, the temperature of the second thermal arrest which corresponds to the Al-Si eutectic reaction decreases with Ni. This indeed increases the pre-eutectic freezing range of the alloys from 41 ºC for Al-7Si-0.5Cu-0.35Mg-0.1Fe alloy to 57ºC for the Al-7Si-0.5Cu-0.35Mg-0.1Fe-1.0Ni alloy (Fig. 3.5b) which could lead to the increased amount of porosity. Microstructural investigation at low magnifications (Fig. 3.6) confirmed that the amount of porosity increased as a result of Ni addition. This may adversely affect the mechanical properties. The hot-tearing susceptibility of Al-Si alloys has been studied via constrained-rod castings as described elsewhere [26] where a direct relationship was determined between the non-equilibrium freezing range and the hot tear-sensitivity. Indeed Ni-containing alloys with increased freezing range also exhibited increased cracking. CCA was not sufficiently sensitive to detect the other phase transformations.

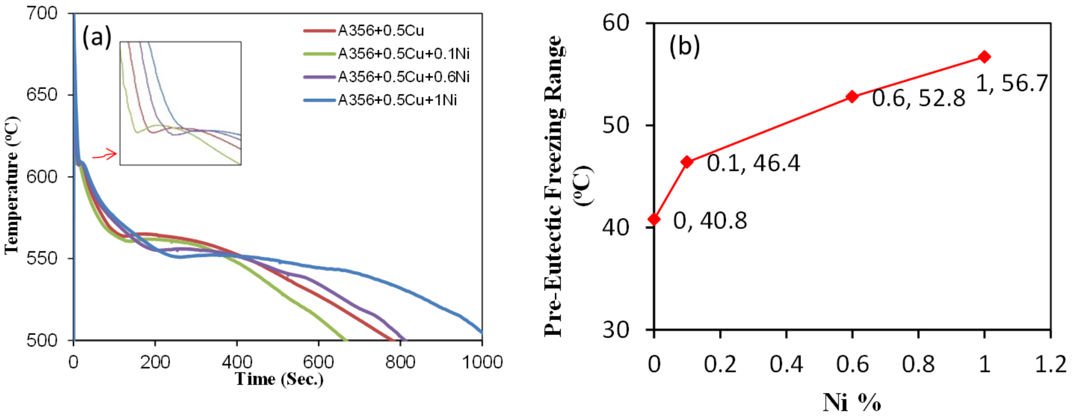

Fig. 3.5 Thermal analysis of the Al-7Si-0.5Cu-0.35Mg-0.1Fe alloys with 0.0-1.0%Ni (a) CCA (b) Pre-eutectic freezing range as a function of Ni.

3.3.3 Microstructure and phase analysis

Since thermodynamic calculations cannot simulate the metastable phases of as-cast and heat-treated structures, detailed microstructural investigations were carried out on the alloys. Representative as-cast, solutionized and aged microstructures of the Al-7Si-0.5Cu-0.35Mg-0.1Fe-1.0Ni and Al-7Si-0.5Cu-0.35Mg-0.1Fe alloys are shown in Figs. 3.7a-b. The secondary dendrite arm spacing (SDAS) of the different alloys was measured to be 29 ± 2 μm showing no relation with Ni in the alloys. Since the Sr level and the casting conditions are kept constant for all the alloys, no difference in SDAS was indeed expected, knowing that SDAS is only function of cooling rate or some trace elements such as Sr when the dendrite-arm growth is poisoned by the addition [27-30]. Fig. 3.8 shows SEM micrographs of alloys with different Ni levels in the as-cast condition. Phases formed within the microstructures have been identified using a combination of morphological, XRD, EDS and EPMA analyses. The compositional range and other properties of these phases are presented in Table 3.3.

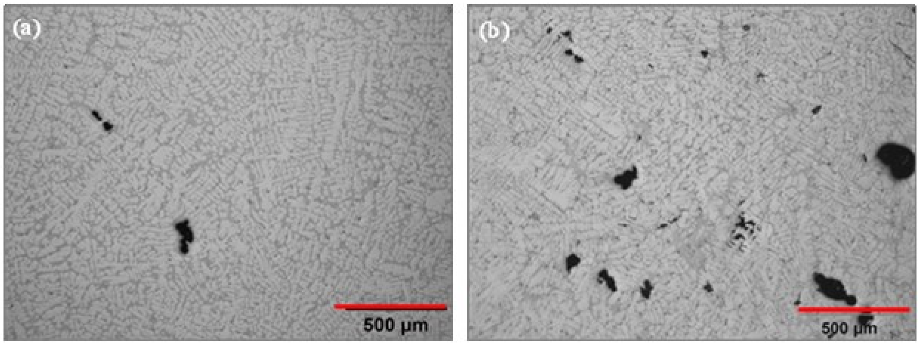

Fig. 3.6 Increased amount of porosity as a result of Ni addition in (a) Al-7Si-0.5Cu-0.35Mg-0.1Fe (b) Al-7Si-0.5Cu-0.35Mg-0.1Fe-1.0Ni; pores appear as black areas in the images.

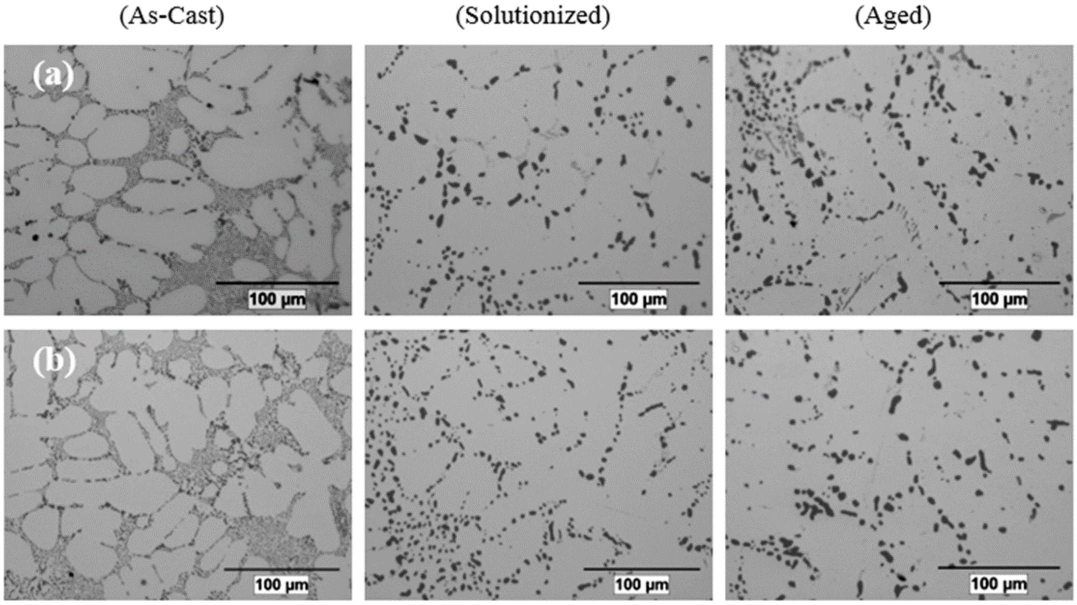

Fig. 3.7 Microstructure of the alloys in as-cast, solutionized and aged conditions (a) Al-7Si-0.5Cu-0.35Mg-0.1Fe-1.0Ni and (b) Al-7Si-0.5Cu-0.35Mg-0.1Fe.

Table 3.3 The intermetallic phases observed in the Al-Si-Cu-Mg-Fe-Ni system [16-18, 24, 31, 32]

Phase	Density (g/cm^3)	Composition range (wt.%)					Vickers hardness at 27 °C (GPa)	Microhardness at 300 °C (GPa)	Crystal structure	Space group	Lattice parameters
		Mg	Si	Cu	Ni	Fe					
Al_3Ni-ε	3.95				42		7-7.7	3.54	Orthorhombic	Pnma	$a = 6.611$, $b = 7.366$, $c = 4.90$
Al_3CuNi (Al_3Ni_2)-δ	4.76			0–31.2	29.2–60		−11	–	Hexagonal	$P\bar{3}ml$	$a = 4.036$, $c = 4.90$
									Rhombohedral[a]	R32, R3m or $R\bar{3}m$	$a = 13.5$, $\alpha = 17°27'$
Al_7Cu_4Ni-γ	5.48			38.7–50.7	11.8–22.2		9.87–10	5.8	Hexagonal	–	$a = 0.41–0.42$
									bcc	–	$a = 1.46$, $c = 0.497–0.503$
Al,FeNi-T	3.4				18–28	4.5–14	7.71	–	Monoclinic	$P2_1/c$	$a = 6.2$, $b = 6.3$, $c = 8.6$, $\alpha = 95°$
Mg_2Si-M	1.88	63.2	36.8				4.5	1.77	Cubic	Fm3m	6.35–6.4
Al_2Cu-θ	4.34			52.5–53.9			4–6	2	Tetragonal	I4/mcm	$a = 6.066$, $c = 4.874$
$Al_5Cu_2Mg_8Si_6$-Q	2.79	31.1	27	20.3			6.5	–	Hexagonal	–	$a = 10.32$, $c = 4.05$
Al_5FeSi-β	3.3		12–15			25–30	5.8	7.85	Monoclinic	–	$a = b = 6.12$, $c = 41.5$, $\alpha = 91°$
$Al_8FeMg_3Si_6$-π	2.82	14.1	32.9			10.9	6.85	3.76	Hexagonal	$p\bar{6}2m$	$a = 6.63.c = 7.94$

[a] Structure and lattice parameters varies with composition

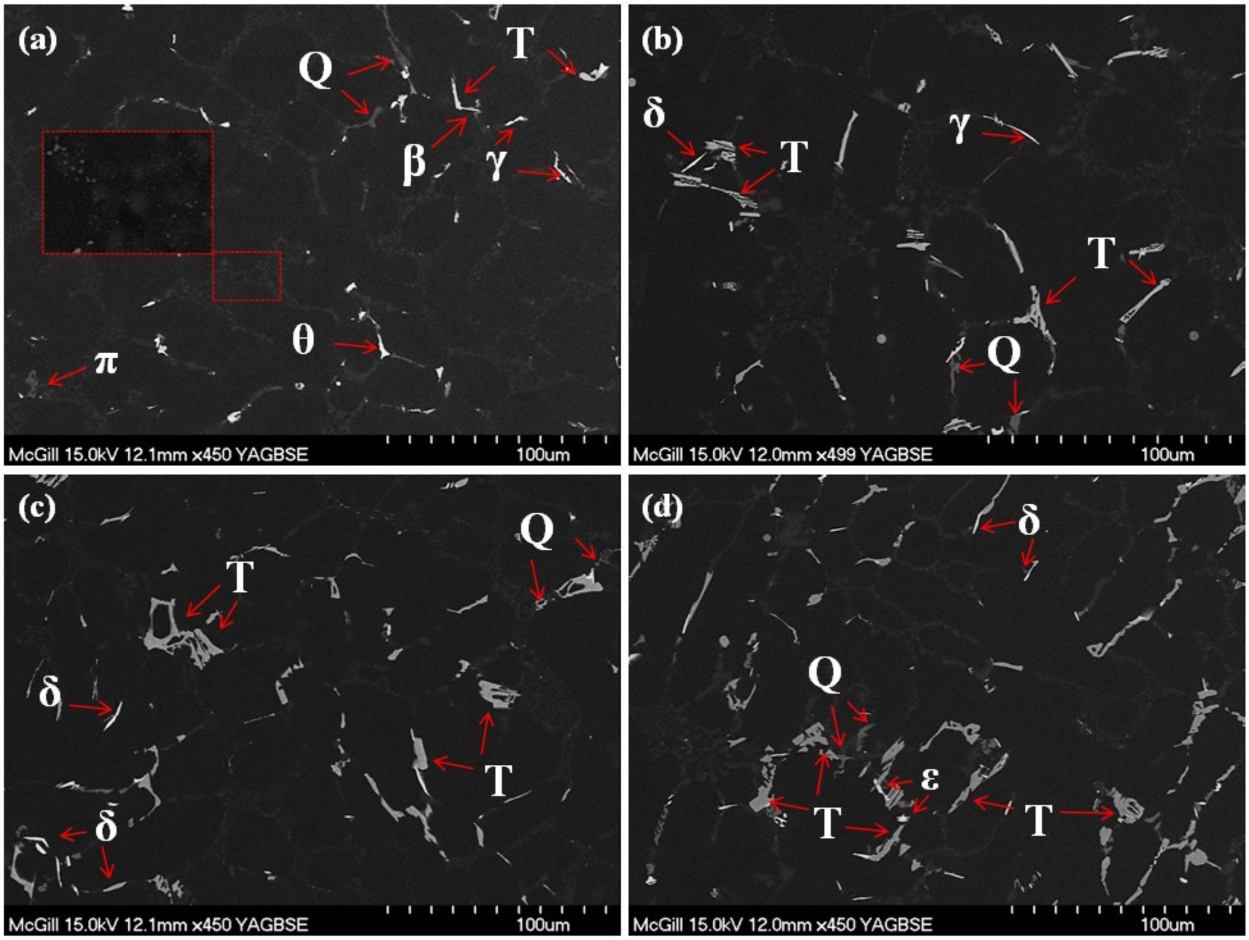

Fig. 3.8 Microstructure of the as-cast Al-7Si-0.5Cu-0.35Mg-0.1Fe with (a) 0.1Ni, (b) 0.3Ni, (c) 0.6Ni (d) 1.0Ni.

The T-Al$_9$FeNi phase

The T phase adopts a coarse Chinese-script morphology and appears as a gray intermetallic under SEM in backscattered mode. The EPMA results revealed a wide range of existence for this phase from 14.6%Fe, 17.6%Ni in the Al-7Si-0.5Cu-0.35Mg-0.1Fe-0.1Ni alloy to 4.97%Fe, 26.2%Ni in the Al-7Si-0.5Cu-0.35Mg-0.1Fe-1.0Ni alloy. It dissolves up to 1.2%Si and 1%Cu. The amount of this phase increases with increasing Ni (Figs. 3.8a-d). However, the composition deviates from the stoichiometric value: 15.6%Fe, 16.4%Ni [17]. According to the thermodynamic calculations (Fig. 3.4a) at 1%Ni, the microstructure consists predominantly (2.1%) of T phase at 300 ºC. This phase was also observed as fine precipitates (~1µm) in the interdendritic regions (Fig. 3.8a) in addition to the coarse eutectic ones. These small precipitates are formed through peritectic reaction (9) at the end of the solidification. It is worth mentioning that the amount of fine T phase decreases with an increase in Ni content as evidenced by microstructural analysis. It is clear from the isopleths in Fig. 3.2 that the T phase is a thermodynamically stable phase below the solidus. Therefore, after solution treatment (Fig. 3.9) it stays within the microstructure.

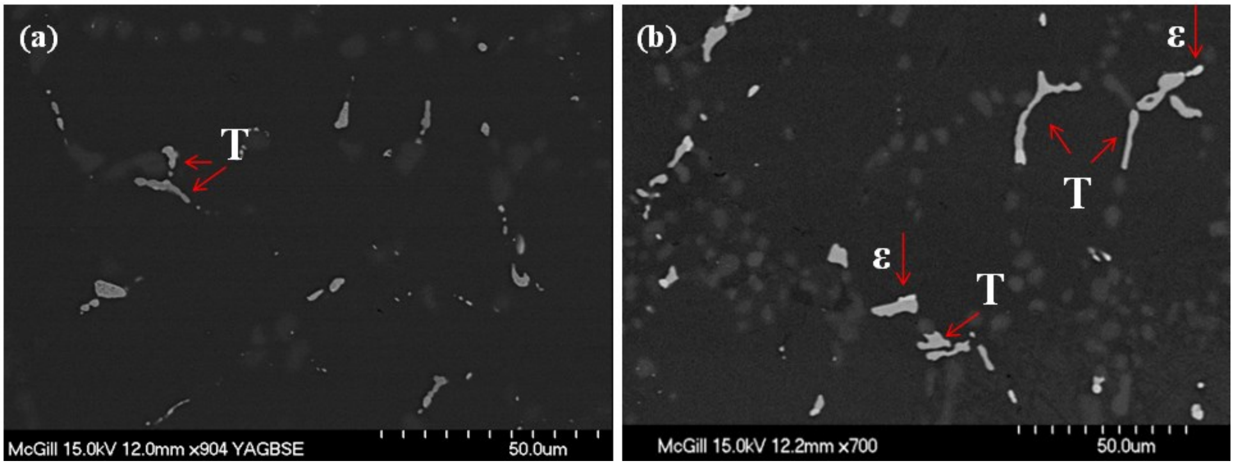

Fig. 3.9 Microstructure of the (a) Al-7Si-0.5Cu-0.35Mg-0.1Fe-0.3Ni and (b) Al-7Si-0.5Cu-0.35Mg-0.1Fe-1.0Ni alloys after solution treatment.

The γ-Al$_7$Cu$_4$Ni and δ-Al$_3$(CuNi)$_2$ phases

Having a blocky-shape, the **γ** and **δ** phases appear as bright-white precipitates and are barely distinguishable by image contrast and both have wide ranges of existence. The **γ** phase observed in the alloys with 0.1 and 0.3% Ni has a range of 32-38% Cu, 17-21% Ni and dissolves up to 2.4%Si and 0.5% Fe. The δ phase has a compositional range of 25-28% Cu, 29-30% Ni and dissolves not more than 0.2% Si and 0.1% Fe. This phase was observed in alloys with Ni contents more than 0.3% (Figs. 3.8b-d). The similar morphology and composition of these two phases make differentiation by WDS/EDS chemical analyses alone difficult.

To verify the results observed in the metallographic investigation, X-ray diffraction (XRD) phase analysis was carried out using a matrix extraction method. The Al matrix was dissolved in 20% NaOH solution and the insoluble intermetallics were collected by filtering in order to provide adequate volume fraction of the intermetallics for XRD analysis. The results are shown in Fig. 3.10 confirming the presence of Q, θ, β and π phases in our reference alloy; Al-7Si-0.5Cu-0.35Mg-0.1Fe and Q, T, γ and δ phases in Al-7Si-0.5Cu-0.35Mg-0.1Fe-0.3Ni alloy, which are in good agreement with the thermodynamic calculations and EPMA results. These two Ni- and Cu- bearing phases do not have significant high temperature stability. Calculations show that the γ phase above 290 °C and the δ phase above 333 °C are not thermodynamically stable (Fig. 3.2b). After solution treatment all these phases transform into the T and/or ε phases (Fig. 3.9).

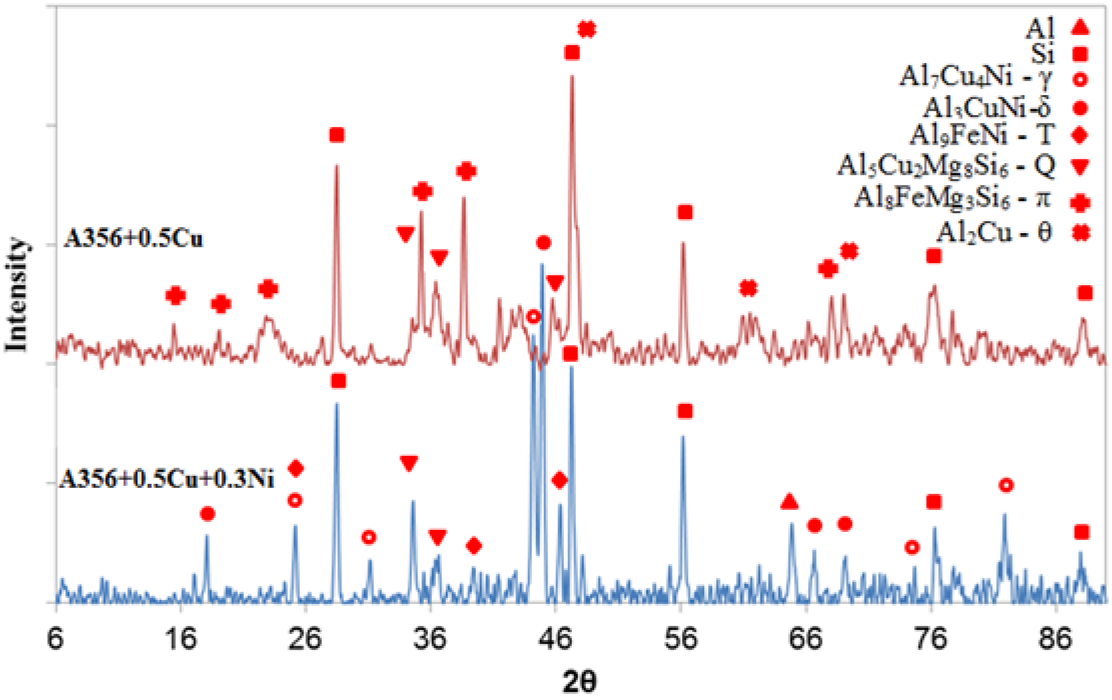

Fig. 3.10 XRD patterns of the extracted intermetallics from as-cast Al-7Si-0.5Cu-0.35Mg-0.1Fe and Al-7Si-0.5Cu-0.35Mg-0.1Fe-0.3Ni alloys.

The ε-Al_3Ni phase

This phase appears as a bright-white intermetallic with a blocky morphology and is always associated with the T phase (Fig. 3.8d). It forms via reaction (2) and has a very narrow compositional range from 37.6 to 38% Ni. The solubility of Cu in this phase is up to 2.6% and it dissolves less than 0.5% Si and 0.4% Fe. This phase has been observed in the Al-7Si-0.5Cu-0.35Mg-0.1Fe-1.0Ni alloy with the calculated amount of 0.85% at 300 °C. After solution treatment it remains unchanged (Fig. 3.9b). Calculations showed a wide temperature stability range (room temperature up to the solidus) for this compound.

The β-Al_5FeSi phase

The β phase has a plate-like morphology and forms along the interdendritic regions. It is usually associated with the metastable π phase. This phase was only observed in the Al-7Si-0.5Cu-0.35Mg-0.1Fe and in a reduced amount in the Al-7Si-0.5Cu-0.35Mg-0.1Fe-0.1Ni alloys. The β phase has a narrow range of 29% Fe, 15% Si to 29% Fe, 16% Si and dissolves up to 2.4% Ni. This phase is also thermodynamically stable at high temperatures and stays within the microstructure after heat treatment.

The Q-$Al_5Cu_2Mg_8Si_6$ and θ-Al_2Cu age-hardening precipitates

The quaternary Q phase appears as a dark-gray precipitate with Chinese-script morphology while the θ phase has a bright-white appearance with a blocky morphology. The amount of θ phase decreases rapidly by increasing the Ni level, obviously due to the consumption of Cu by Ni and the formation of the γ phase. This phase has been reported [19] to have a limited range of existence (Table 3.3). However, Ni broadens the compositional range from 44 to 48% Cu by dissolving in it up to 1.5%. The EPMA results also revealed the presence of dissolved Si, Mg and Fe up to 2.1, 0.5, 1.1%, respectively in this phase. The Q phase with a homogeneity range of 25-27% Si, 19.6-20.3% Cu, 25-29% Mg dissolves up to 4% Ni. These two precipitates, Q-$Al_5Cu_2Mg_8Si_6$ and θ-Al_2Cu are generally not considered thermally stable in aluminum alloys due to high diffusion rate of Cu and Mg at elevated temperatures which leads to Ostwald ripening. In this alloy system, the θ and Q phases are thermodynamically unstable above 280 °C and 440 °C, respectively.

The results of thermodynamic calculations and metallographic observations revealed that in this alloy system, for a given amount of Mg and Cu, a specific amount of the Q phase forms regardless of the Ni content. It should be mentioned that a negligible amount of π phase was observed in the as-cast Al-7Si-0.5Cu-0.35Mg-0.1Fe-0.1Ni alloy. This phase disappears after solution treatment and does not form during the aging process. Figs. 3.11a-f present the 3D morphologies of the extracted intermetallics. These particles have been identified by EDS analysis.

Notably, for some of the intermetallics, such as Q, the chemical analysis by EDS after matrix dissolution gives a value very close to the stoichiometric values of these phases.

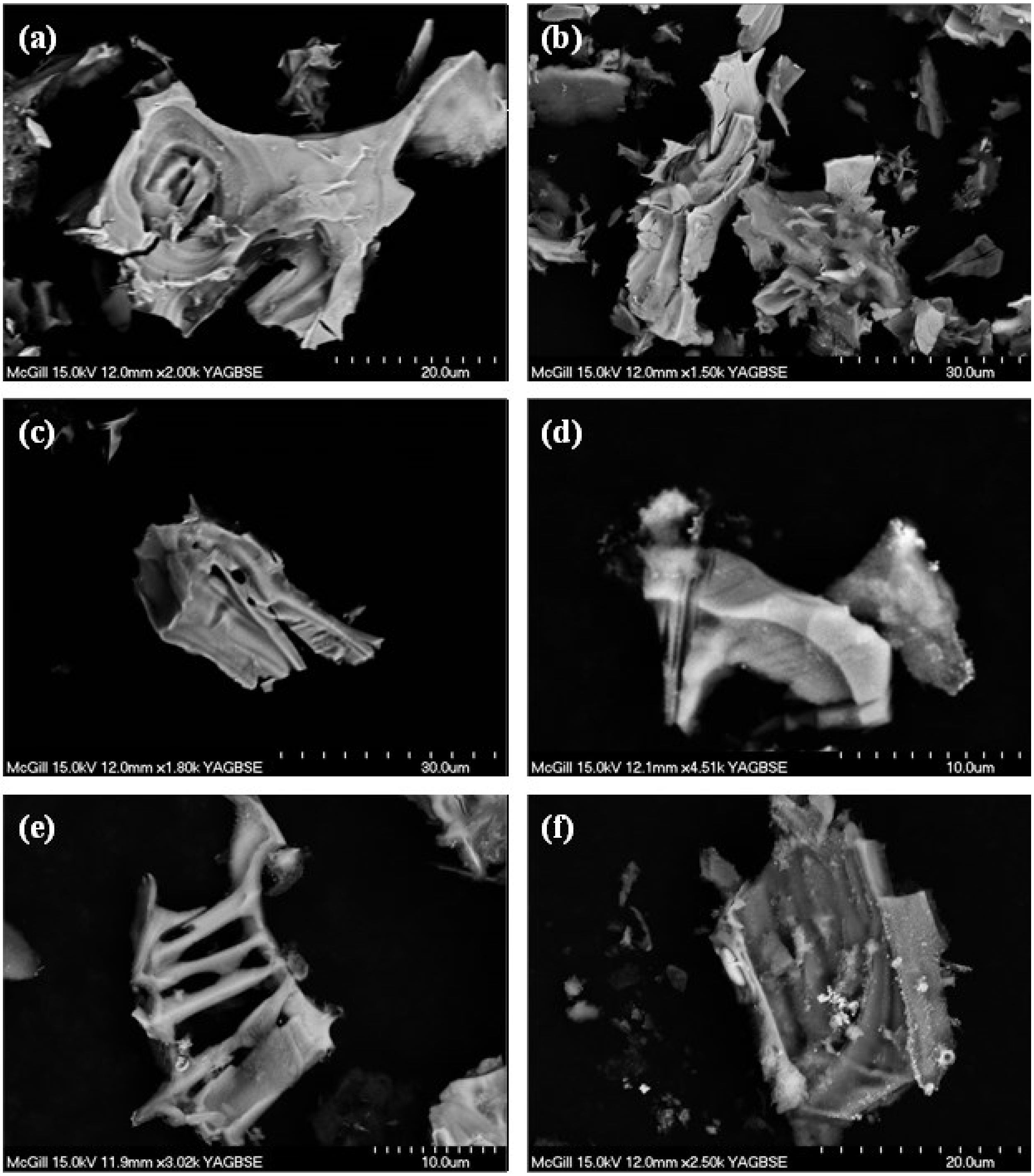

Fig. 3.11 Complex 3D morphology of the (a) δ (b) γ (c) T (d) ε (e) Q (f) π intermetallics extracted from as-cast Al-7Si-0.5Cu-0.35Mg-0.1Fe and Al-7Si-0.5Cu-0.35Mg-0.1Fe-(0.1-1)Ni alloys.

The θ and Q are age-hardening precipitates in the Al-Si-Cu-Mg alloy system. As mentioned previously, Ni addition suppresses the formation of the θ by forming δ and γ phases. While it has no effect on the amount of the Q precipitates (Figs. 3.4a-b). Obviously, suppression of θ precipitates could reduce age hardening of these alloys. During solution treatment at 540 °C, both the δ and γ phases are not thermodynamically stable and transform into T or ε phases and Cu present in the phases dissolves into the matrix. At the aging temperature (200 °C), due to the very low diffusivity and solid solubility of Ni in the aluminum matrix, the δ and γ phases which are thermodynamically stable at this temperature do not re-form even after 600 h of aging.

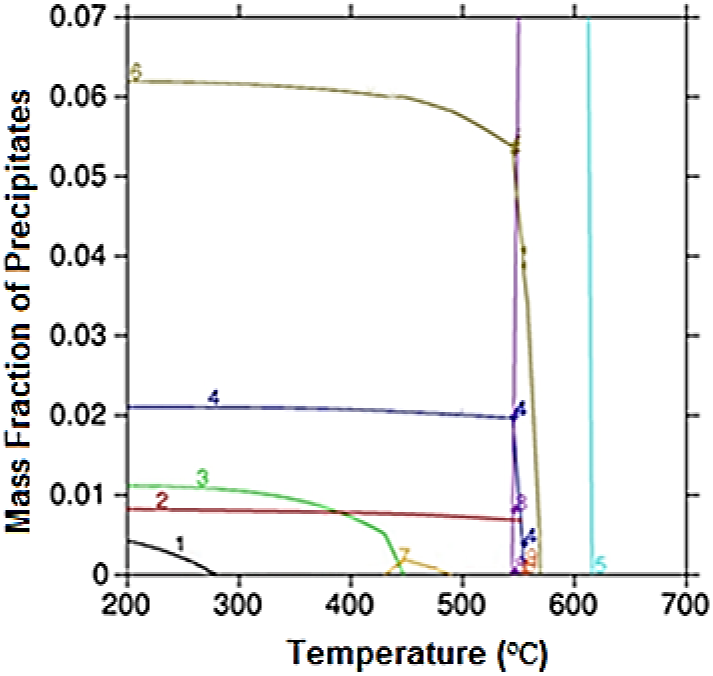

Fig. 3.12 Effect of excluding the δ and γ phases on the equilibrium phase formation of Al-7Si-0.5Cu-0.35Mg-0.1Fe-1.0Ni alloy (1 = θ, 2 = ε, 3 = Q, 4 = T, 5 = Al, 6 = Si, 7 = M).

Thermodynamic modeling was carried out in equilibrium conditions, this time without considering the formation of those two phases. Results are shown in Fig. 3.12 for the Al-7Si-0.5Cu-0.35Mg-0.1Fe-1.0Ni alloy. Excluding Ni and Cu bearing phases from the calculations revealed the presence of θ phase at the aging temperature. TEM analysis confirmed the calculation results. Fig. 3.13a presents the Q and θ precipitates formed on the (001) planes of the Al matrix after 170 hours of aging. These precipitates grow further by prolonging the aging process (Figs. 3.13b-d). It is worth noting that detailed TEM/SEM investigations revealed that no Ni-bearing precipitates formed during the different stages of the aging process. However, at 300 °C SEM-

EDS analysis confirmed that Cu diffuses into the T or ε transforming them into δ or γ phases. High temperatures and the wide existence range of theses precipitates facilitate this process.

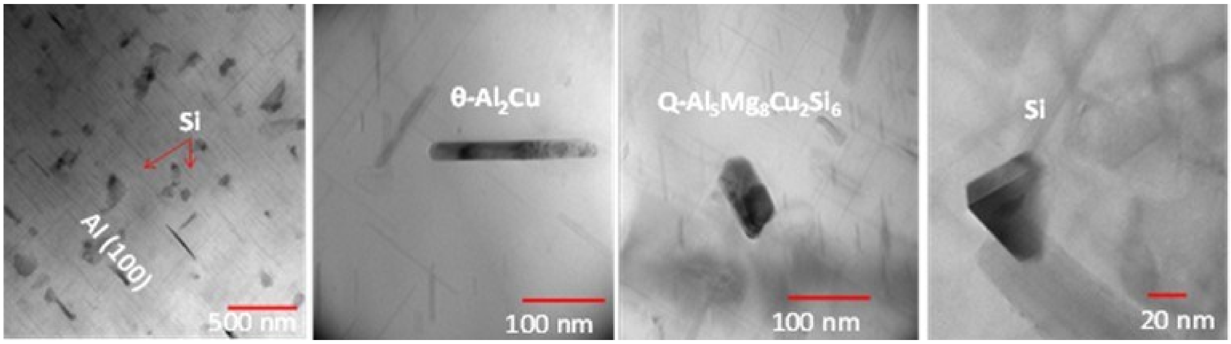

Fig. 3.13 TEM micrographs of the Al-7Si-0.5Cu-0.35Mg-0.1Fe-1.0Ni alloy after aging at 200 °C. (a) θ and Q precipitates formed on the (001) plane of Al after 170 h of aging, (b) θ, (c) Q and (d) Si precipitates after 600 h of aging.

Results of the metallographic observations and thermodynamic calculations are summarised in Table 3.4. As seen in this table, calculations at 300 °C are in good agreement with the experimental results. However, at 200 °C as previously mentioned, there is a discrepancy between the experimental and modeling results which originates from the low diffusivity of Ni in Al and slow kinetics of phase formation at this temperature. As shown previously, due to the negligible solid solubility of Ni in Al, the as cast microstructure of the alloys does not show a large departure from equilibrium. Hence, the calculated equilibrium microstructure at 200 °C can be a good representation of the as-cast microstructure.

Table 3.4 Precipitate phases in alloys under different conditions (experimental and calculated)

Alloy	Precipitate phases				
	As cast condition	Aged at 200 °C for 600 h	Calculated equilibrium at 200 °C	Soaked at 300°C for 100 h	Calculated equilibrium at 300 °C
R	θ, Q, β, π	θ, Q, β	θ, Q, β	Q, β	Q, β
R+0.1Ni	θ, Q, β, π,T, γ	θ, Q, β, T	Q, β, T, γ	Q, β, T	Q, β, T
R+0.3Ni	Q,T, γ, δ*	θ, Q,T	Q,T, γ	Q,T	Q,T
R+0.6Ni	Q,T, δ	θ, Q,T	Q,T, δ	Q,T, δ	Q,T, δ
R+1.0Ni	Q,T, δ, ε	θ, Q,T, ε	Q,T, δ, ε	Q,T, δ, ε	Q,T, δ, ε

* The amount is negligible.

Altering the Cu and Fe levels could significantly change the phase distribution. In order to study these effects, isothermal sections of the phase diagram were calculated and presented in Fig. 3.14. It is clear that for given amounts of Cu and Fe, Ni first binds with Fe forming the T phase. With increasing Ni, the amount of this phase increases until all the Fe is consumed by Ni. When the Ni is increased beyond that level, excess Ni binds with Cu forming γ or δ phases depending on the Ni:Cu ratio. At low Ni:Cu ratios the γ phase forms while at high Ni:Cu ratios formation of the δ phase becomes most probable. Further increase in Ni results in the formation of the ε phase. This trend applies for almost any given Cu and Fe amounts (Fig. 3.15). Based on this knowledge for the alloys with Cu and Ni contents more than 0.5%, the phase field distribution of Fig. 3.14b could be divided into three distinctive regions with two diagonal lines representing different Ni:Cu ratios. It can therefore be concluded that:

1) when the Ni:Cu is below 0.25, Ni and Cu form the γ phase,
2) at Ni:Cu > 0.25 the δ phase can co-exist,
3) and at Ni:Cu > 1.5 the ε phase can exist within the microstructure of these alloys.

It is worth noting that due to a strong affinity of Ni for Fe in this alloy system, increasing the Fe increases the amount of T phase. This decreases the Ni:Cu ratio and consequently affects the phase field distribution (Fig. 3.14a) according to the diagram in Fig. 3.15. It should also be pointed out that Ni:Fe ≈ 2 is the limit above which the formation of plate-like β phase is suppressed.

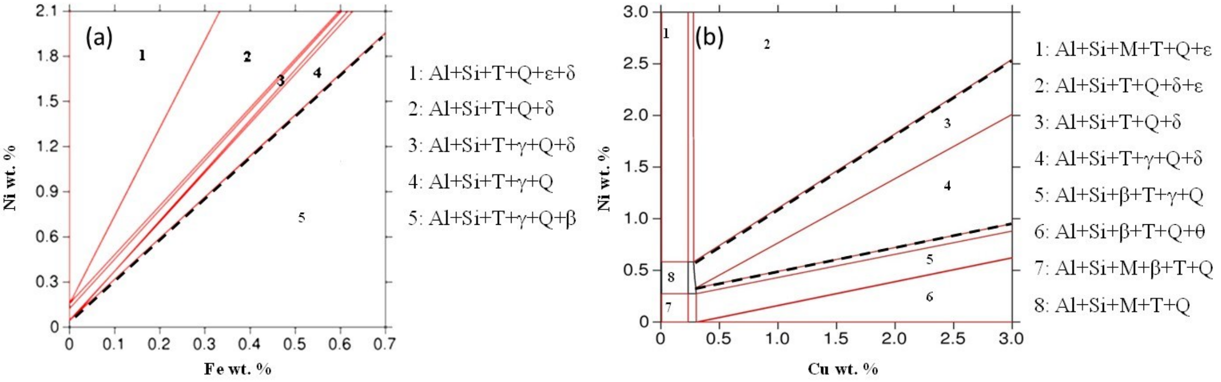

Fig. 3.14 Distribution of phase fields at 200 °C and fixed amounts of Al-7%Si-0.35%Mg (a) 0.5%Cu, (b) 0.1%Fe.

3.3.4 Contribution of the different phases to the overaged hardness

In order to understand the expected effect of different Ni bearing precipitates on mechanical properties, hardness measurements were taken on T7 (aged for 5 hours at 200 °C) samples after 300 hours of soaking at 300 °C (Table 3.5). The hardness of the Al-7Si-0.5Cu-0.35Mg-0.1Fe-0.1Ni alloy decreased 3.4% compared to the reference alloy. This might be because of the suppression of the β phase as a result of Ni addition. The Al-7Si-0.5Cu-0.35Mg-0.1Fe-0.3Ni alloy showed a 12.4% increase in hardness. Calculations show the presence of 1.2% T phase within the microstructure. The hardness of the Al-7Si-0.5Cu-0.35Mg-0.1Fe-0.6Ni alloy is 42.4% higher than the reference alloy when 2% T and 0.3% δ phase is calculated to be within the microstructure. The presence of 0.85% ε phase within the microstructure of the Al-7Si-0.5Cu-0.35Mg-0.1Fe-1.0Ni alloy did not contribute much to the hardness of this alloy. From the hardness testing results it can be concluded that the δ phase makes the most significant contribution to the hardness of the alloys among the Ni-bearing precipitates. Therefore, Ni and Cu additions must be controlled in a way that maximizes the amount of the δ phase (Ni:Cu ≈ 1.5).

Table 3.5 Hardness of alloys after 300 hours of soaking at 300 °C with calculated amounts of Ni bearing precipitates

Alloy	**Calculated amount of Ni-bearing precipitates at 300 °C**				**T7 hardness after 300 h soaking at 300 °C (HRF)**
	T	γ	δ	ε	
R	0.0	0.0	0.0	0.0	23.4
R+0.1Ni	0.5	0.0	0.0	0.0	22.6
R+0.3Ni	1.2	0.0	0.0	0.0	26.3
R+0.6Ni	2.0	0.0	0.3	0.0	33.3
R+1.0Ni	2.1	0.0	0.3	0.85	34.5

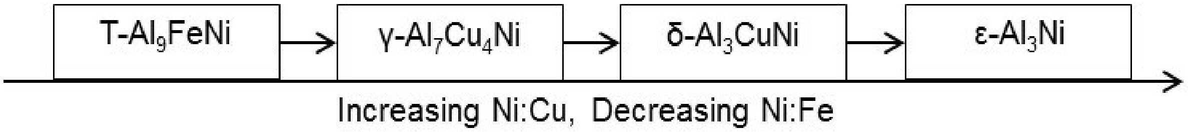

Fig. 3.15 Chart showing the effect of Ni:Cu and Ni:Fe ratios on the phase formation of Al-Si-Cu-Mg-Fe-Ni system in the range of engine alloys.

3.4 Conclusions

Thermodynamic modeling and experimental investigation have been carried out in combination to study the effects of Ni additions on the microstructure and phase formation of A356+0.5%Cu alloy.

1. Four different Ni bearing phases are formed as a result of Ni addition: T-Al_9FeNi, γ-Al_7Cu_4Ni, δ-Al_3CuNi and ε-Al_3Ni
2. EPMA results revealed wide range of existence for these intermetallics.

3. The analysis of phase field distribution showed that the Ni:Cu and Ni:Fe ratios determine which precipitate will form within the alloys. The γ phase forms at Ni:Cu < 0.25, when Ni:Cu > 0.25 the δ phase starts to form and, at Ni:Cu > 1.5, the formation of ε phase becomes most probable. Ni:Fe ≈ 2 could be considered as a limit above which the all of the Fe in the alloy is bound to Ni in T phase and the formation of plate-like β phase is suppressed.
4. CCA revealed that Ni addition increases the freezing range of the alloys and leads to high amounts of porosity.
5. TEM investigations showed no nano-scale Ni-bearing precipitates; however, the results confirmed the presence of θ and Q precipitates formed during the aging process.
6. Solution treatment dissolves all the δ and γ precipitates formed during solidification. These phases do not form during aging at 200 ^{o}C. Nevertheless, at an operating temperature of 300 ^{o}C these precipitates start to form again.
7. Equilibrium and non-equilibrium calculations, along with the experimental verifications, showed that phase selection in the as-cast microstructure of these alloys do not exhibit serious departure from the calculated equilibrium state.
8. For alloy design purposes, it can be noted that the δ-Al_3CuNi phase makes the most significant contribution to the T7 hardness of the alloys and leads to a significant increase in hardness (e.g. 40%) over the reference alloy, Al-7Si-0.5Cu-0.35Mg-0.1Fe. The amount of this phase is maximized at Ni:Cu ≈ 1.5.

3.5 Acknowledgments

This work was supported by the NSERC (Natural Sciences and Engineering Research Council) of Canada Strategic project grant with Rio Tinto Alcan (RTA). The financial support of REGAL (FQRNT Regroupement Aluminum Research Center) is also acknowledged. The authors thank Pierre Vermette of McGill University for his assistance in experimental work. Amir Rezaei Farkoosh would like to gratefully acknowledge financial support from McGill University through the MEDA (McGill Engineering Doctoral Award) program. Prof. Pekguleryuz sincerely thanks Dr Fred Major of RTA for valuable discussions at the inception of the NSERC project, and his intellectual contribution and support through the course of this research.

3.6 References

[1] O. El Sebaie, A.M. Samuel, F.H. Samuel, H.W. Doty, The effects of mischmetal, cooling rate and heat treatment on the hardness of A319.1, A356.2 and A413.1 Al–Si casting alloys, Mater. Sci. Eng., A, 486 (2008) 241-252.

[2] I. Polmear, Light alloys: from traditional alloys to nanocrystals, Butterworth-Heinemann, 2005.

[3] M. Garat, G. Laslaz, Improved Aluminum Alloys for Common Rail Diesel Cylinder Heads, in: AFS, IL, USA, 2007, pp. 1-8.

[4] H. Ye, An overview of the development of Al-Si-Alloy based material for engine applications, J. Mater. Eng. Perform., 12 (2003) 288-297.

[5] P. Sepehrband, R. Mahmudi, F. Khomamizadeh, Effect of Zr addition on the aging behavior of A319 aluminum cast alloy, Scripta Mater., 52 (2005) 253-257.

[6] J.Y. Yao, J.A. Taylor, Characterisation of intermetallic particles formed during solution treatment of an Al–7Si–0.4Mg–0.12Fe alloy, J. Alloys Compd., 519 (2012) 60-66.

[7] H. Ammar, A. Samuel, F. Samuel, E. Simielli, G. Sigworth, J. Lin, Influence of Aging Parameters on the Tensile Properties and Quality Index of Al-9 Pct Si-1.8 Pct Cu-0.5 Pct Mg 354-Type Casting Alloys, Metall. Mater. Trans. A, 43 (2012) 61-73.

[8] D.H. Xiao, J.N. Wang, D.Y. Ding, S.P. Chen, Effect of Cu content on the mechanical properties of an Al–Cu–Mg–Ag alloy, J. Alloys Compd., 343 (2002) 77-81.

[9] M. Zeren, Effect of copper and silicon content on mechanical properties in Al–Cu–Si–Mg alloys, J. Mater. Process. Technol., 169 (2005) 292-298.

[10] S. Wang, K. Matsuda, T. Kawabata, T. Yamazaki, S. Ikeno, Variation of age-hardening behavior of TM-addition Al–Mg–Si alloys, J. Alloys Compd., 509 (2011) 9876-9883.

[11] W. Kasprzak, D. Emadi, M. Sahoo, M. Aniolek, Development of Aluminium Alloys for High Temperature Applications in Diesel Engines, in, Materials Science Forum, 2009, pp. 595-600.

[12] X. Hu, F. Jiang, F. Ai, H. Yan, Effects of rare earth Er additions on microstructure development and mechanical properties of die-cast ADC12 aluminum alloy, J. Alloys Compd., 538 (2012) 21-27.

[13] F.J. Feikus, Optimisation of AlSi Cast-Alloys for Cylinder Head Applications, in: AFS, Georgia, USA, 1998, pp. 1-21.

[14] Y. Li, S. Brusethaug, A. Olsen, Influence of Cu on the mechanical properties and precipitation behavior of AlSi7Mg0. 5 alloy during aging treatment, Scripta Mater., 54 (2006) 99-103.

[15] L. Heusler, F.J. Feikus, M.O. Otte, Alloy and Casting Process Optimization for Engine Block Application, in: AFS Trans, 2001, pp. 215-223.

[16] V.S. Zolotorevskiĭ, N.A. Belov, M.V. Glazoff, Casting aluminum alloys, Elsevier Science Ltd, 2007.

[17] N.A. Belov, D.G. Eskin, N.N. Avxentieva, Constituent phase diagrams of the Al–Cu–Fe–Mg–Ni–Si system and their application to the analysis of aluminium piston alloys, Acta Mater., 53 (2005) 4709-4722.

[18] Z. Asghar, G. Requena, E. Boller, Three-dimensional rigid multiphase networks providing high-temperature strength to cast AlSi10Cu5Ni1-2 piston alloys, Acta Mater., 59 (2011) 6420-6432.

[19] L.F. Mondolfo, Aluminum alloys: structure and properties, Butterworths London, 1976.

[20] S.S. Sreeja Kumari, R.M. Pillai, B.C. Pai, A study on the structural, age hardening and mechanical characteristics of Mn and Ca added Al–7Si–0.3Mg–0.6Fe alloy, J. Alloys Compd., 453 (2008) 167-173.

[21] Z. Qian, X. Liu, D. Zhao, G. Zhang, Effects of trace Mn addition on the elevated temperature tensile strength and microstructure of a low-iron Al–Si piston alloy, Mater. Lett., 62 (2008) 2146-2149.

[22] C.L. Chen, R. Thomson, The combined use of EBSD and EDX analyses for the identification of complex intermetallic phases in multicomponent Al–Si piston alloys, J. Alloys Compd., 490 (2010) 293-300.

[23] C.L. Chen, A. Richter, R.C. Thomson, Investigation of mechanical properties of intermetallic phases in multi-component Al–Si alloys using hot-stage nanoindentation, Intermetallics, 18 (2010) 499-508.

[24] V. Raghavan, Al-Cu-Fe-Mg-Ni-Si (Aluminum-Copper-Iron-Magnesium-Nickel-Silicon), Journal of Phase Equilibria and Diffusion, 28 (2007) 223-225.

[25] J. Andersson, T. Helander, L. Höglund, P. Shi, B. Sundman, Thermo-Calc & DICTRA, computational tools for materials science, Calphad, 26 (2002) 273-312.

[26] M.O. Pekguleryuz, S. Lin, E. Ozbakir, D. Temur, C. Aliravci, Hot tear susceptibility of aluminium-silicon binary alloys, Int. J. Cast Met. Res., 23 (2010) 310-320.

[27] M. Flemings, Solidification processing, Metall. Mater. Trans. B, 5 (1974) 2121-2134.

[28] S. Hegde, K.N. Prabhu, Modification of eutectic silicon in Al–Si alloys, J. Mater. Sci., 43 (2008) 3009-3027.

[29] A.K.P. Rao, K. Das, B.S. Murty, M. Chakraborty, Al–Ti–C–Sr master alloy—A melt inoculant for simultaneous grain refinement and modification of hypoeutectic Al–Si alloys, J. Alloys Compd., 480 (2009) L49-L51.

[30] Y.-C. Tsai, C.-Y. Chou, S.-L. Lee, C.-K. Lin, J.-C. Lin, S.W. Lim, Effect of trace La addition on the microstructures and mechanical properties of A356 (Al–7Si–0.35Mg) aluminum alloys, J. Alloys Compd., 487 (2009) 157-162.

[31] C.L. Chen, A. Richter, R.C. Thomson, Mechanical properties of intermetallic phases in multi-component Al–Si alloys using nanoindentation, Intermetallics, 17 (2009) 634-641.

[32] Y. Li, Y. Yang, Y. Wu, L. Wang, X. Liu, Quantitative comparison of three Ni-containing phases to the elevated-temperature properties of Al-Si piston alloys, Mater. Sci. Eng., A, 527 (2010) 7132-7137.

CHAPTER 4

THE EFFECTS OF MANGANESE ON THE T-PHASE AND CREEP RESISTANCE IN AL-SI-CU-MG-NI ALLOYS

The work on the Ni additions continued with a study on the mechanical behavior of the Ni-containing alloys. This chapter presents the effects of minor Ni additions on the strength and creep resistance of Al-7Si-0.5Cu-0.3Mg. The mechanical performance has been related to the microstructural features of the as-cast alloys discussed in Chapter 4 as well as the microstructure evolved after creep and tensile testing. This chapter has been published as a journal article: *A.R. Farkoosh, M. Pekguleryuz, The effects of manganese on the T-phase and creep resistance in Al–Si–Cu–Mg–Ni alloys, Mater. Sci. Eng., A, 582 (2013) 248-256.*

ABSTRACT

Al-7Si-0.5Cu-0.3Mg-(0.3-1)Ni alloys were investigated for elevated temperature performance. It was found that while the yield strength of the overaged alloys at 300 ^{o}C increased with Ni, the creep resistance decreased. Microstructural observations revealed that the brittle interdendritic T-Al_9FeNi intermetallics undergo severe cracking in the early stages of creep deformation, which weakens the interdendritic regions and leads to a decrease in creep resistance. This study shows that Mn additions modify the T-phase preventing cracking during creep and increase the creep resistance.

Keywords: Aluminum alloys; Casting; Creep properties; Nickel addition; Aluminum engine alloys

4.1 Introduction

Even though aluminum casting alloys have been used for powertrain applications (engine blocks and cylinder heads) over the past fifteen years due to their high specific strength, castability and superior corrosion resistance, their low creep resistance now limits their use in new Diesel engines which operate under severe conditions of temperatures and stress [1-7]. The design of the Diesel engine alloy requires an interpretation of the operating conditions in relationship to material properties. During operation, engine start-stop cycles introduce cyclic compressive and tensile loading stemming from the restriction of thermal expansion and contraction in the narrow bridges between the valves of the engine block. At the high end of the temperature range (~300 ^{o}C), the material tries to expand but the restriction by the bulk generates compressive stresses (20-30 MPa) placing the material under compressive creep loading [2]. During cool-down, the restriction to contraction induces tensile stresses at mid-cycle temperatures; since the temperature is moderate (<150 ^{o}C) in engine cool-down, creep is not significantly activated but tensile properties become critical. Furthermore, cyclic plastic damage that occurs during engine operation leads to crack initiation reducing fatigue life. On the basis of the foregoing, the ideal engine alloys should have creep resistance (300 ^{o}C, 20 MPa) and offer adequate ductility to accommodate the tensile stresses plastically to avoid crack propagation and catastrophic failures; the alloy microstructure should also exhibit metallurgical stability at engine working temperatures.

In 1998 Feikus [3] introduced the A356 + 0.5% Cu alloy which gained certain market share in Diesel engines in Europe. The alloy is heat-treatable via the Cu- and Mg-bearing aging precipitates, Q-$Al_5Mg_8Cu_2Si_6$ and θ-Al_2Cu [8] and showed improved creep resistance and strength at 250 °C over the base alloy, A356. However, mechanical properties drop drastically at 300 °C; due to the high solid solubility and diffusivity of Cu and Mg in Al, rapid coursing of the age hardening precipitates occurs at elevated temperatures which leads to matrix softening and significant drop in strength.

Research to improve the elevated temperature properties of this alloy has led in 2006 [2] to the second generation of alloys with Zr additions to the A356 + 0.5% Cu alloy to provide thermally stable Al-Si-Zr dispersoids for enhanced creep resistance and high temperature strength. Another route in designing aluminum alloys for strength at high temperatures is the addition of Ni to Al-Si alloys, which were first developed as piston alloys with substantial amounts of Ni (e.g. Al12Si1Cu1Mg2Ni) [9]. A new Diesel engine alloy, Al-7Si-0.4Mg-0.4Cu-0.5Ni-0.4Fe was presented by Heusler et al. [10], showing 20% increase in fatigue strength and some improvement in tensile strength over the A356 + 0.5% Cu alloy. Ni is added to Al to form thermally stable nickel aluminides; the thermal stability of the intermetallics stem from the large driving force for compound formation between Al and Ni, and the low solid solubility and diffusivity of Ni in Al. Ni forms different thermally stable intermetallics in this multi-component alloy system depending on the Ni:Cu and Ni:Fe ratios [9, 11-13]: ε-Al_3Ni, δ-Al_3CuNi, γ-Al_7Cu_4Ni, T-Al_9FeNi, all of which make contribution to elevated temperature strength.

Research has been conducted to investigate the strengthening mechanisms activated by Ni addition. Asghar et al. [11] have proposed that Ni aluminides formed through a eutectic reaction increase the degree of interconnectivity of the hard eutectic network in piston alloys. This enhance the load transfer to hard and thermally stable phase when matrix softens as age hardening precipitates ripen and lose their strengthening effect at high temperatures. Stadler et al. [14] have also shown that the load transfer mechanism is effective even after solution treatment of different grades of Al-Si-Cu-Mg-Ni alloys.

Despite the positive effects of Ni intermetallics on strength, their presence adversely affects the ductility. The creep behaviour of these alloys is not known and no work has been conducted to improve the ductility. In the present work, (i) the effect of varying Ni levels (0.3-1 wt.%) and the influence of Ni-intermetallics on creep resistance and high temperature strength are investigated and (ii) the alloy is further modified with Mn to improve creep resistance.

4.2 Experimental procedures

The alloys were prepared in a high frequency NORAX Canada induction furnace using commercial grade A356 alloy (supplied by Rio Tinto Alcan Inc.). Cu, Ni and Mn were added to the melt from a set of master alloys at 760 °C, holding for 15 min to dissolve. To modify the eutectic Si morphology, all the alloys were modified with 150 ppm Sr just prior to degassing. Inductively coupled plasma (ICP) technique was used to determine the chemical compositions of the alloys. According to the Ni and Mn contents, the alloys studied were designated as MG3R03N, MG3R06N, MG3R10N and MG3R10N03M. The chemical compositions of the alloys are presented in Table 4.1. All compositions are given in wt.% hereafter, unless otherwise specified.

Table 4.1 The chemical compositions of the alloys

Alloy	**Chemical Composition (wt.%)**								
	Si	Mg	Cu	Ni	Fe	Ti	Mn	Sr	Al
MG3R03N	6.64	0.36	0.58	0.31	0.13	0.11	<0.01	0.013	Bal.
MG3R06N	6.50	0.31	0.53	0.62	0.10	0.10	<0.01	0.015	Bal.
MG3R10N	6.94	0.32	0.57	1.02	0.13	0.10	<0.01	0.017	Bal.
MG3R10N03M	6.80	0.30	0.53	0.98	0.13	0.10	0.32	0.013	Bal.

Cylindrical bars, 30 mm diameter, were cast into a pre-heated (400 °C) permanent mold at 730 °C. Cylindrical creep specimens, 50mm in gauge length and 12.7 mm in diameter were machined from the castings according to ASTM E8 standard. To avoid probable incipient melting, solution annealing was carried out in two stages; 4 hours at 500 °C followed by 10 hours at 545 °C. The samples were then quenched in water at room temperature and aged at 200 °C up to 600 hours.

Based on the performance requirements for Diesel engine applications, tensile creep tests were conducted at 300 ^{o}C in air under constant load corresponding to 20 MPa stress. Utilizing two extensometers (error (ε) < 0.0001 mm/mm), gauge length displacement was measured. A K-Type (Chromel-Alumel) thermocouple with an error of ± 1 ^{o}C was attached to the specimen to control the temperature. Compression test was performed with a strain rate of 0.01 s^{-1} on cylindrical specimens (6mm in diameter, 9 mm in height) to determine the yield strength of the alloys at room temperature, 150 and 300 ^{o}C. Tensile testing was carried out at room temperature and 300 ^{o}C at a deformation rate of 0.01 s^{-1}. In all elevated temperature tests, samples were soaked 100 hours at temperature prior to testing. Vickers macro-hardness was measured using a Buehler hardness testing machine with a load of 20 kg.

Samples for microstructural investigation were taken from the castings and ground with a series of SiC papers and polished on porous neoprene polishing cloth with Al_2O_3 solution. Final polishing was done using a Buehler vibratory polisher with a colloidal silica solution. A Hitachi S-4700 field emission gun scanning electron microscope (FEG-SEM) equipped with an Oxford INCA energy dispersive spectroscopy (EDS) detector was utilized for metallographic examinations. Accelerating voltage was 15 kV and a beam current of 10 μA was chosen. Electron probe microanalyzer (EPMA) coupled with wavelength dispersive spectroscopy (WDS) detectors was used for quantitative analysis performed by a JEOL-8900 EPMA instrument, operating at 20 kV. Thin foils for transmission electron microscopy (TEM) were prepared by mechanical grinding and jet polished using a Struers Tenupol 5 jet polisher. A solution of 10% Nitric acid in methanol was used at -40 ^{o}C. The TEM images were acquired via Philips CM200 microscope operated at 200 kV. The EDS spectra were obtained by EDAX detector connected to the column.

4.3 Results and discussion

4.3.1 Microstructural analysis

Ni-containing alloys possess various complex Ni-bearing intermetallics (Table 4.2) which makes the analysis of this alloy system a challenging task. Therefore, different characterization techniques were utilized to identify the precipitates formed within the alloys. Detailed characterization methods have been explained in our previous study [15].

Table 4.2 Precipitates formed in the alloys in as cast and heat treated conditions

Alloys	**MG3R03N**	**MG3R06N**	**MG3R10N**	**M3GR10N03M**
Precipitates in as cast condition	Q-$Al_5Mg_8Cu_2Si_6$ δ-Al_3CuNi[a] γ-Al_7Cu_4Ni T-Al_9FeNi	Q-$Al_5Mg_8Cu_2Si_6$ δ-Al_3CuNi γ-Al_7Cu_4Ni[a] T-Al_9FeNi	Q-$Al_5Mg_8Cu_2Si_6$ ε-Al_3Ni δ-Al_3CuNi T-Al_9FeNi	Q- $Al_5Mg_8Cu_2Si_6$ ε-Al_3Ni δ-Al_3CuNi T-Al_9FeNi α-$Al_{15}(FeMn)_3Si_2$
Precipitates after solution annealing	T-Al_9FeNi	T-Al_9FeNi	T-Al_9FeNi ε-Al_3Ni	T-Al_9FeNi ε-Al_3Ni α-$Al_{15}(FeMn)_3Si_2$
Precipitates after 600 hours of aging at 200 ºC	Q-$Al_5Mg_8Cu_2Si_6$ θ-Al_2Cu T-Al_9FeNi	Q-$Al_5Mg_8Cu_2Si_6$ θ-Al_2Cu T-Al_9FeNi	Q-$Al_5Mg_8Cu_2Si_6$ θ-Al_2Cu T-Al_9FeNi ε-Al_3Ni	Q-$Al_5Mg_8Cu_2Si_6$ θ-Al_2Cu ε-Al_3Ni T-Al_9FeNi α-$Al_{15}(FeMn)_3Si_2$
Precipitates at 300 ºC	Q-$Al_5Mg_8Cu_2Si_6$ γ-Al_7Cu_4Ni T-Al_9FeNi	Q-$Al_5Mg_8Cu_2Si_6$ T-Al_9FeNi δ-Al_3CuNi	Q-$Al_5Mg_8Cu_2Si_6$ T-Al_9FeNi δ-Al_3CuNi ε-Al_3Ni	Q-$Al_5Mg_8Cu_2Si_6$ ε-Al_3Ni δ-Al_3CuNi T-Al_9FeNi α-$Al_{15}(FeMn)_3Si_2$

[a] The amount is negligible

Solidification microstructures

The microstructures of as-solidified alloys (Fig. 4.1) consist of primary aluminum dendrites with the eutectic Si particles and various interdendritic intermetallics. The secondary dendrite arm spacing (SDAS) of the different alloys was measured to be 29 ± 2 µm showing no relation with the Ni level in the alloys. The SDRS is known to depend solely on cooling rate [16] or some trace elements such as Sr which poison the dendrite arm growth [17]. As the Sr level and cooling rates are kept constant in all the castings, no difference was expected.

Ni-containing alloys and intermetallic phase selection: Our previous study has shown that phase selection in this alloy system strongly depends on the Cu:Ni ratio [15]. The precipitate phases observed in the alloys are listed in Table 4.2. The MG3R03N alloy with the lowest level of Ni, 0.3%Ni, (Fig. 4.1a) forms the T-Al_9FeNi, Q-$Al_5Mg_8Cu_2Si_6$ and two Ni- and Cu-bearing precipitates (γ-Al_7Cu_4Ni and δ-Al_3CuNi). The T-Al_9FeNi with a coarse Chinese-script morphology is the predominant phase and appears darker than the other Ni-bearing intermetallics. Having a blocky shape, the γ-Al_7Cu_4Ni and δ-Al_3CuNi phases appear as bright-white precipitates. The θ-Al_2Cu, π-$Al_8FeMg_3Si_6$ and β-Al_5FeSi phases which usually exist in Al-Si-Cu-Mg alloy system [15] are not found in this alloy. As the Ni content increases, going from Fig. 4.1a to 4.1c, the amount of T-Al_9FeNi phase increases. The MG3R06N alloy with 0.6% Ni (Fig. 4.1b), contains T-Al_9FeNi, δ-Al_3CuNi and Q-$Al_5Mg_8Cu_2Si_6$ phases. The γ-Al_7Cu_4Ni phase in this alloy exists in negligible amounts. As the Ni content further increases to 1% (MG3R10N alloy), in addition to the T-Al_9FeNi and δ-Al_3CuNi phases, Ni forms the ε-Al_3Ni phase which is usually associated with the T-Al_9FeNi phase (Fig. 4.1c).

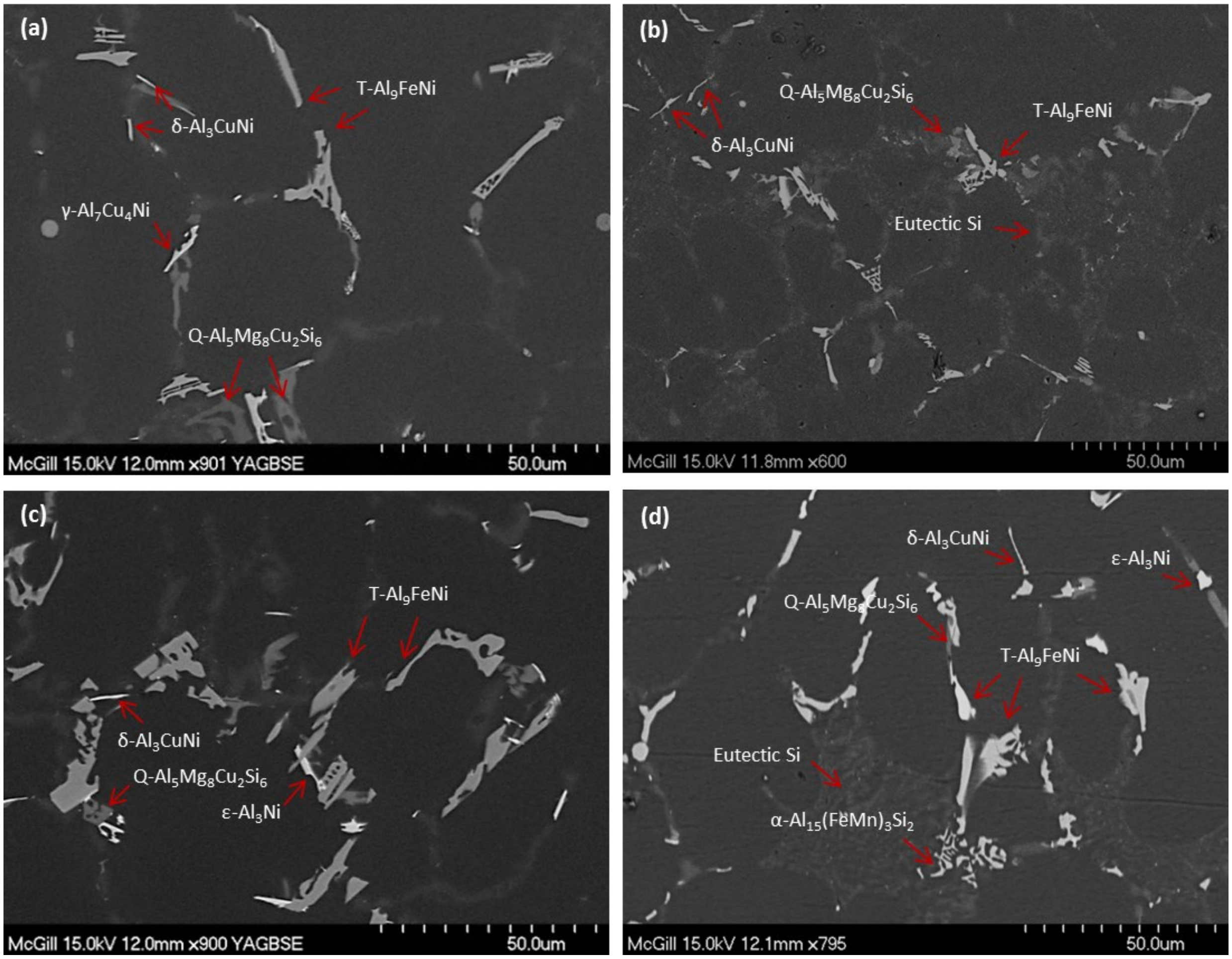

Fig. 4.1 The microstructure of the (a), MG3R03N, (b) MG3R06N, (c) MG3R10N and (d) M3GR10N03M alloys in as cast condition. Different Ni intermetallics are formed depending on the Ni content.

Ni- and Mn-containing alloy: The MG3R10N03M alloy (Fig. 4.1d) with 1%Ni and 0.3%Mn contains the α-$Al_{15}(FeMn)_3Si_2$ precipitate in addition to the precipitates that exist in the MG3R10N alloy. This phase with skeletal morphology appears as a gray precipitate within the microstructure and is usually present with Mn alloying [18, 19]. Our WDS analysis shows that Mn does not transform the T-Al_9FeNi intermetallic, but dissolves in it (up to 2%) broadening the composition range; this would increase the ductility of these intermetallics [20, 21]. This alloy has lower amount of T-Al_9FeNi phase because of the formation of the α-$Al_{15}(FeMn)_3Si_2$ precipitate (Fig. 4.1d compared to Fig. 4.1c) which leaves a lower amount of Fe to bind with Ni. The WDS analysis confirms that Mn also dissolves up to 2% in the *δ-*Al_3CuNi phase, however, it does not seem to influence the dissolution or precipitation kinetics of this phase: δ-Al_3CuNi, with some dissolved Mn, decomposes at the solutionizing temperature just as it does in the Ni-containing alloy, MG3R10N.

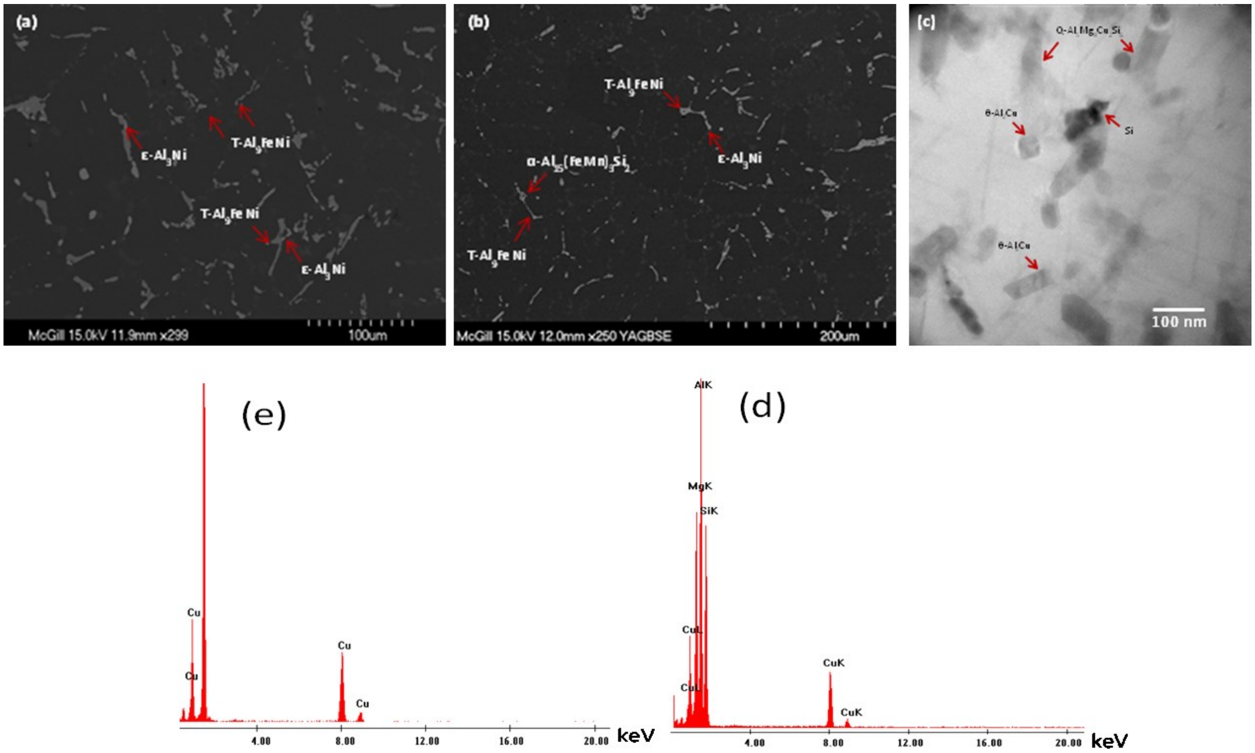

Fig. 4.2 The SEM micrographs of the (a) MG3R10N, (b) MG3R10N03M alloys after 600 hours of aging at 200 ºC. The Cu- or Mg-containing precipitates are dissolved during solution treatment. The bright field (BF) TEM micrograph of (c) MG3R10N alloy showing the θ-Al_2Cu and Q-$Al_5Mg_8Cu_2Si_6$ precipitates. No fine Ni precipitates were observed in intradendritic regions of the alloy. The EDS spectra of the (d) Q-$Al_5Mg_8Cu_2Si_6$ and (e) θ-Al_2Cu precipitates.

Heat-treated microstructures

Al-Si-Cu-Mg alloys are heat-treatable and are usually used in overaged condition. The microstructural evolution of Ni-containing alloys were investigated after solution treatment and ageing. In all Ni levels investigated, solution heat treatment dissolves all the Cu- or Mg-bearing precipitates (Table 4.2), but the T-Al_9FeNi, ε-Al_3Ni and α-$Al_{15}(FeMn)_3Si_2$ phases which are thermodynamically stable at the solution treatment temperatures remain unaffected. Aging at 200 ^{o}C for 600 hours does not induce any morphological change in these intermetallics. No Ni- or Mn-bearing phases re-form as seen in the SEM micrographs of the MG3R10N and MG3R10N03M alloys given in Figs. 4.2a-b.

An interesting feature of the microstructural evolution in Ni-containing alloys is the precipitation of the θ-Al_2Cu phase during ageing, which was not present in the as-solidified condition: TEM analysis reveals that in at all Ni levels investigated, both the θ-Al_2Cu and the Q-$Al_5Mg_8Cu_2Si_6$ precipitates form and grow during the aging process (Table 4.2). Fig. 4.2c shows the TEM micrograph of the MG3R10N alloy, showing that these precipitates have ripened after 600 hours of aging at 200 ^{o}C. The formation of the θ-Al_2Cu precipitates in the alloys with Ni addition can be attributed to the dissolution of the δ-Al_3CuNi and γ-Al_7Cu_4Ni phases during solution treatment releasing Cu into the matrix to maintain equilibrium: interestingly δ-Al_3CuNi and γ-Al_7Cu_4Ni do not re-form even after 600 hours of aging at 200 ^{o}C, due to the low diffusivity and low solid solubility of Ni in the aluminum matrix and the excess Cu at this temperature forms both of the aging precipitates, θ-Al_2Cu and Q-$Al_5Mg_8Cu_2Si_6$ instead. It is noteworthy that Ni phases do not participate in the age hardening process; no Ni-bearing precipitates were observed with TEM (Fig. 4.2c). This can be explained by the limited solid solubility of Ni in aluminum (especially in the presence of 7% Si). The Ni addition, therefore, does not significantly influence the age hardening precipitation at 200 ^{o}C.

TEM investigation of the MG3R10N03M alloy shows no Mn dispersoids in the microstructure; Mn usually forms small amounts of Fe and Mn dispersoids in Al-Si-Cu-Mg during solutionizing [22-24] but it seems that in the presence of Ni such dispersoids do not form; this can be attributed to the formation of large amounts of T-Al_9FeNi and α-$Al_{15}(FeMn)_3Si_2$ intermetallics which significantly decreases the Fe and Mn in the Al matrix .

Synopsis on microstructural evolution

Our microstructural observations show that Ni addition results in the formation of four different phases: ε-Al_3Ni, δ-Al_3CuNi, γ-Al_7Cu_4Ni and T-Al_9FeNi, all of which are interdendritic precipitates (Table 4.2, Fig. 4.1). However, after solution treatment, the δ-Al_3CuNi and γ-Al_7Cu_4Ni intermetallics transforms into the T-Al_9FeNi or ε-Al_3Ni phases and do not re-form during aging at 200 ^{o}C. Moreover, SEM and TEM analyses show no dispersed Ni-bearing precipitates in the intradendritic regions that could lead to Orowan dispersion hardening. Mn mainly forms α-$Al_{15}(FeMn)_3Si_2$ intermetallics and dissolves in the T phase which does not undergo any subsequent morphological change.

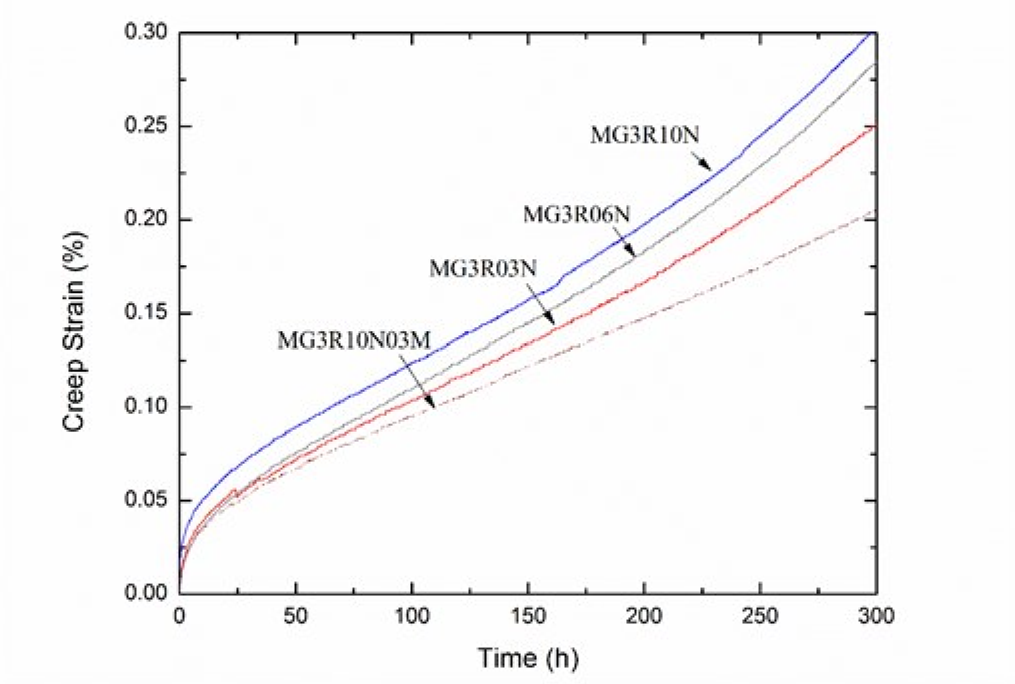

Fig. 4.3 Tensile creep curves of the alloys tested at 300 °C under stress of 20 MPa; alloys have been aged for 600 hours at 200 °C and soaked for 100 hours at the test temperature prior to testing. Mn modified alloy shows the lowest creep strain.

4.3.2 Creep performance

Creep behaviour and the effect of the T-Phase

Fig. 4.3 shows typical creep curves of the alloys tested at 300 °C under a tensile stress of 20 MPa, exhibiting all three stages of creep (primary, secondary and tertiary) within the test duration (300 hours). It is noted that creep deformation increases with increasing Ni. The minimum creep rate (steady state creep rate in the secondary creep stage, Fig. 4.4a) is $1.75 \times 10^{-7}\ s^{-1}$ for the MG3R03N alloy, and increases to $1.95 \times 10^{-7}\ s^{-1}$ for the MG3R06N alloy. Fig. 4.3 shows that the Ni additions accelerate the creep deformation from the early stages of primary creep. Figs. 4.4b and 4.4c also show the strain to tertiary creep and time to tertiary creep, respectively; with increasing Ni content, the amount of deformation before the onset of tertiary creep increases while the time to reach the tertiary creep decreases. This indicates that the creep deformation has been accelerated and dominated by the primary and tertiary stages at higher Ni levels. The microstructure of the creep-tested MG3R10N alloy (Fig. 4.5a) exhibits the ε-Al_3Ni, δ-Al_3CuNi and the cracked T-Al_9FeNi intermetallics (Fig. 4.5b). Decohesion at the interface of the T-phase and the matrix and cavity formation at an interdendritic triple point are also detected, which are evidence for deformation accumulation and the onset of tertiary creep stage (Fig. 4.5b).

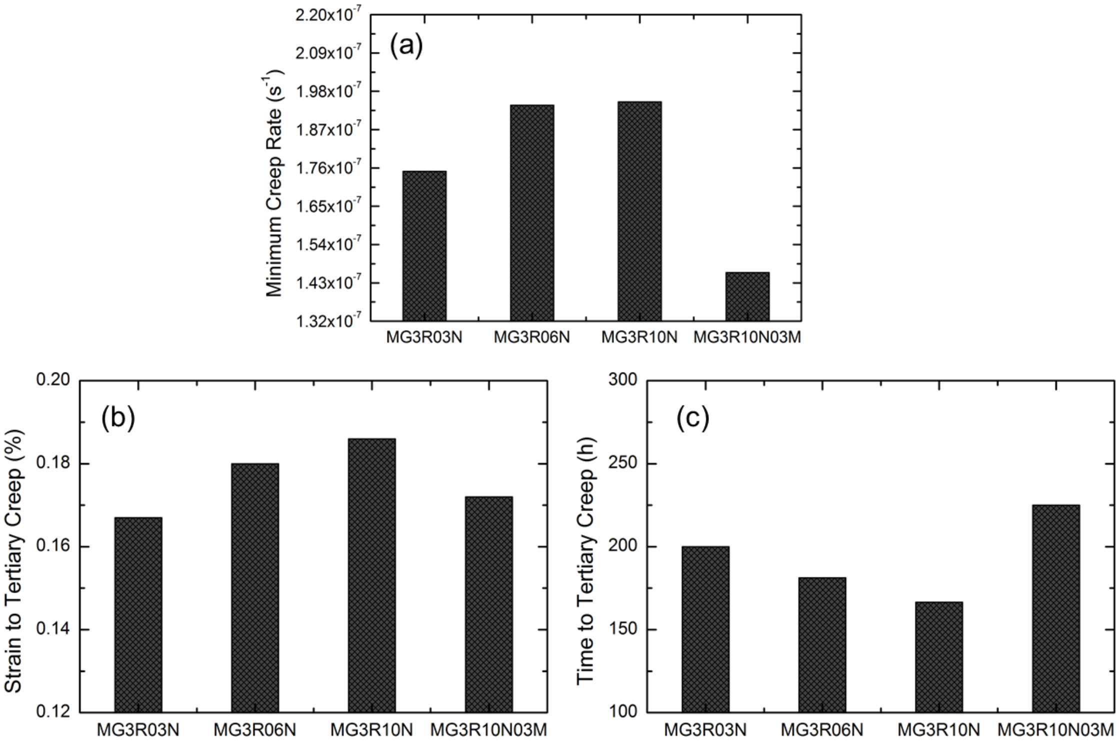

Fig. 4.4 (a) Minimum creep rate, (b) strain to tertiary creep and (c) time to tertiary creep obtained from the creep curves of Fig. 4.3.

The early onset of tertiary creep (Fig. 4.4c) in the alloys studied can be related to the effect of Ni on the Cu solubility in Al. Microstructural analysis shows that the δ-Al_3CuNi or γ-Al_7Cu_4Ni phases are re-formed (Table 4.2, Fig. 4.5a) during the soaking at the temperature prior to testing and also during the course of creep loading (due to increased diffusivity of solute atoms at this temperature), leading to a decrease in the Cu concentration of the α-Al. EDS analysis after 100 hours of soaking at 300 ^{o}C prior to creep testing reveals that the Cu in α-Al decreases from 0.28% to 0.25% in the MG3R10N alloy. This obviously reduces the amount of the Cu-bearing aging precipitates leading to a reduction in dispersion strengthening. The TEM micrograph of Fig. 4.6 shows that the volume fraction of the age hardening precipitates is noticeably low at this temperature; precipitates are coarse and the inter-particle distances are large. The volume fraction of Cu precipitates is deemed to decrease over the course of creep loading when more δ-Al$_3$CuNi phase forms. Dislocation pile-up in the interdendritic regions in the early stages of creep leading to intermetallic cracking is usually observed in metallic alloys when the dendrite interiors cannot pin the dislocations. A decrease in the Cu precipitates in Ni-containing alloys would certainly accelerate slip and dislocation pile-up in the interdendritic regions. This phenomenon has been recently reported for the creep deformation of Mg-Mn based alloys [25]. Dislocation pile up at the interface of the T-phase and the matrix can generate sufficiently large stresses to initiate cracks in the intermetallic [26, 27]. Since the T-Al$_9$FeNi precipitates are large and very brittle, cracks generated propagate easily and lead to material instability. A similar phenomenon has also been reported by Jaglinski et al. [28] where, the poor creep resistance of hyper-eutectic Al-Si die-cast alloys is attributed to the brittle fracture of large primary Si particles in the primary creep stage.

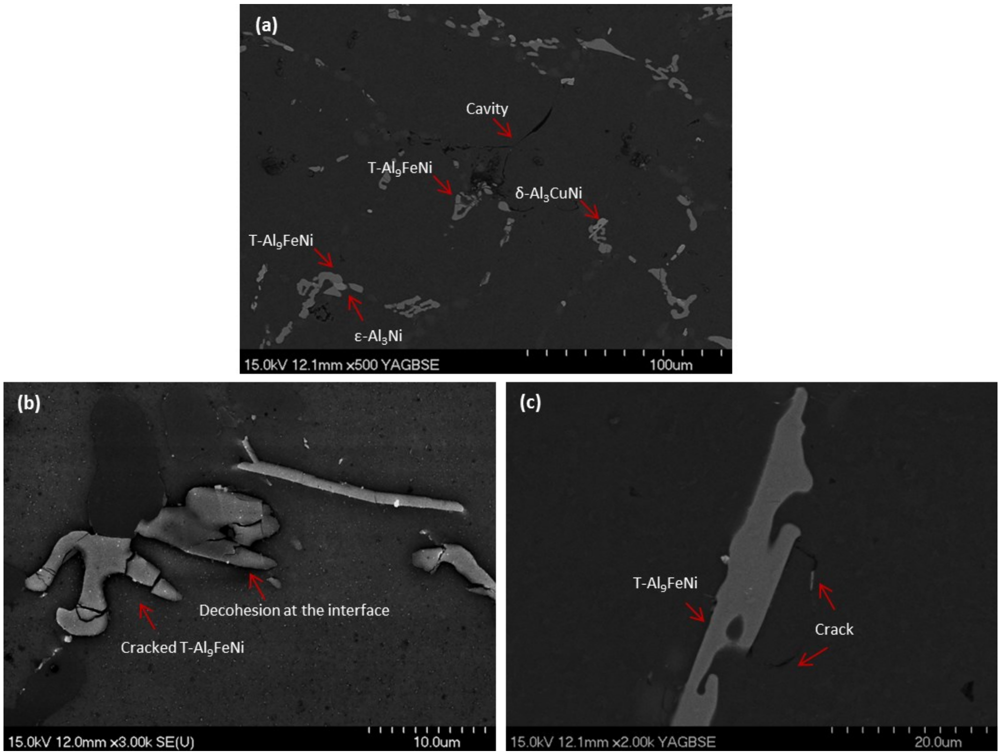

Fig. 4.5 The microstructure of the alloys after 300 hours of creep at 300 °C, 20 MPa. (a) MG3R10N alloy, cavity formation at an interdendritic triple point; the δ-Al3CuNi precipitates are formed at this temperature. (b) Cracked T-Al$_9$FeNi intermetallics in the MG3R10N alloy at higher magnification; decohesion is seen at the matrix-intermetallic interface. (c) MG3R10N03M alloy, the T-Al$_9$FeNi intermetallic remains undamaged after creep testing. The crack in the Al matrix arrested at the intermetallic.

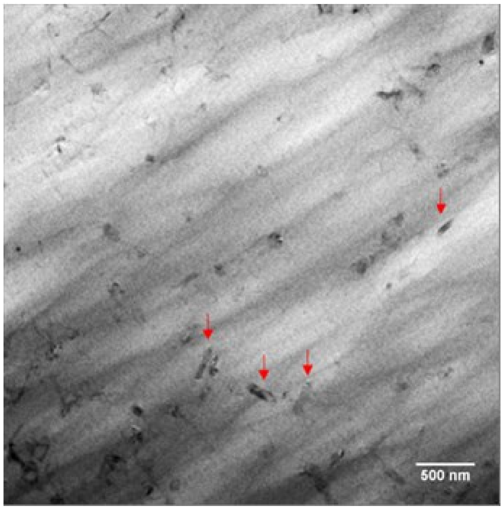

Fig. 4.6 The BF-TEM micrograph of the MG3R10N alloy showing coarse Q-$Al_5Mg_8Cu_2Si_6$ precipitates after 100 hours of soaking at 300 °C.

The existence of the brittle T-phase has an important effect on the creep behaviour of the Ni-containing alloys. As the Ni content in the alloys increases, the amount of the interdendritic T-Al_9FeNi phase increases; the T-Al_9FeNi suffers from cracking evidenced by the triple-point cracking and the displacement of the broken T-Al_9FeNi particles (Fig. 4.5b). Consequently, creep deformation is accelerated and the time to reach tertiary creep is shortened. In such situation, the creep curve is dominated by the primary and tertiary stages as can be seen in the MG3R10N alloy. Macro-hardness analysis after creep deformation (Fig. 4.7) shows that the strength of the alloys is significantly affected by the cracked T-Al_9FeNi intermetallics; the strength of the alloys decreases as the Ni content increases.

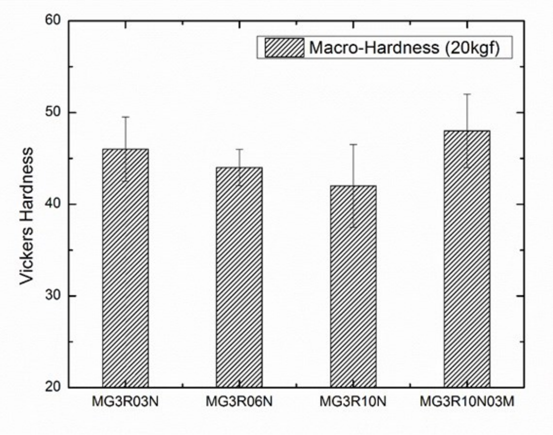

Fig. 4.7 The Vickers macro-hardness of the alloys after 300 hours of creep at 300 °C, 20 MPa.

The effect of Mn

Interestingly, the addition of 0.3% Mn to the MG3R10N alloy with 1% Ni leads to an improvement in creep resistance. The minimum creep rate decreases from 1.95×10^{-7} s^{-1} in the MG3R10N alloy to 1.45×10^{-7} s^{-1} in the MG3R10N03M alloy (Fig. 4.4a). Fig. 4.5c shows the creep-tested MG3R10N03M where the T-Al_9FeNi intermetallic within the microstructure exhibits no cracking. Due to the lack of dislocation pinning, dislocation pile up at the T-phase has not been eliminated but the crack is generated in the Al matrix rather than within the intermetallic. This indicates that the T-Al_9FeNi phase in the Mn modified alloy is less brittle. The T-Al_9FeNi phase dissolves up to ~2% Mn which would impart ductility to the intermetallic; intermetallics that exist over a composition range (which are not stoichiometric compounds) are known to exhibit some ductility due to partial metallic bonding. The T-Al_9FeNi phase has a monoclinic crystal structure of space group $P2_1/c$ [29], which is crystallographically an ordering of hexagonal close-packed layers (prototype AuCd). Mn is known to substitute for Fe in intermetallics, however, it is not known at this stage if it also alters the short range ordering in the crystal structure, forming a homologous compound to T-Al_9FeNi with the same short range order parameters (α_1 and α_2) and closely related unit cells but different chemistry [30]. Further work on this intermetallic itself should be carried out and its mechanical properties should be determined.

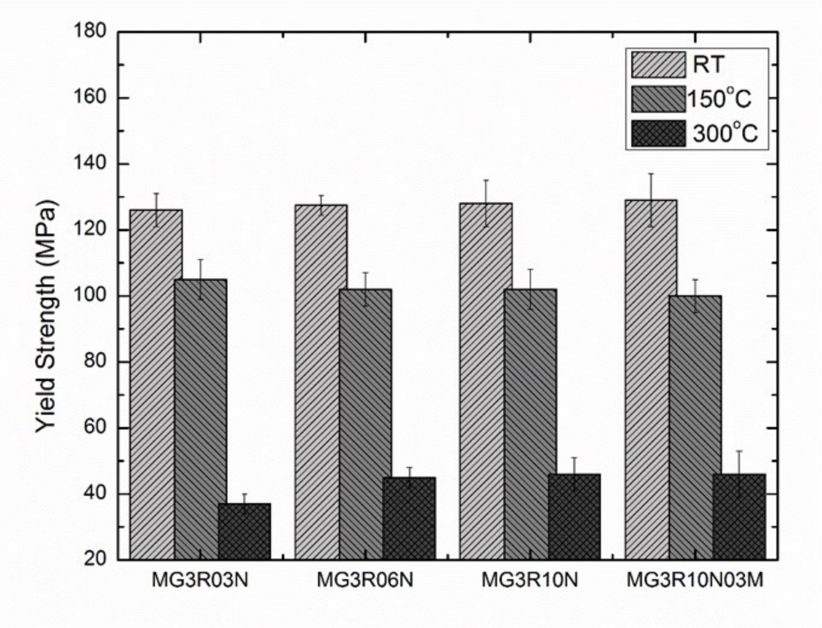

Fig. 4.8 The yield strength of the alloys tested at different temperatures obtained from compression tests.

The creep properties of the MG3R10N03M alloy show that the creep resistance increases by Mn modification of the T-Al_9FeNi; Mn dissolution in the T-Al_9FeNi prevents crack formation. Decreased amount of the T-Al_9FeNi intermetallics in the MG3R10N03M alloy is another reason for the improved creep resistance of this alloy over the MG3R10N alloy.

4.3.3 The effects of the intermetallic phases on compressive and tensile properties

Both compressive and tensile tests were conducted on the alloys. Tensile tests were performed for determining the the ductility of the alloys and the fracture modes.

Yield strength

Fig. 4.8 shows the compressive yield strength of the alloys at different temperatures. Notably, the Ni level does not influnce the yield strength (YS) of the alloys up to 150 ^oC; this is because the main strengthening in the alloys is provided by the very fine and coherent θ-Al_2Cu and Q-$Al_5Mg_8Cu_2Si_6$ precipitates and the Ni precipitates, T-Al_9FeNi and/or ε-Al_3Ni (Table 4.2), have only negligible contribution to the strength of the alloys. At 300^{o}C, however, the compressive yield strength increases noticeably with Ni > 0.6% (MG3R06N and MG3R10N). The MG3R06N alloy shows 30% increase in yield strength at 300 ^{o}C. Further increase in Ni contents (MGR10N) has minor effect on the yield strength. These findings at 300 ^{o}C can be related to the phase selection in the alloys. SEM analysis shows that during soaking at 300 ^{o}C the γ-Al_7Cu_4Ni phase forms in the MG3R03N alloy and the δ-Al_3CuNi phase forms in the MG3R06N and the MG3R10N alloy (Table 4.2). It can be concluded that the δ-Al_3CuNi phase plays an important role in the elevated temperature strength when the age hardening precipitates have lost their strengthening effect (Fig. 4.6). This is consistent with the results obtained by Y. Li et al. [31] on Ni piston alloys. They have shown that of all the Ni precipitates, the δ-Al_3CuNi phase makes the most significant contribution to the elevated temperature strength of aluminum piston alloys. It is also seen that increasing the Ni level from 0.6 to 1% increases the amount of the T-Al_9FeNi phase while the amount of the δ-Al_3CuNi phase remains the same.

Ductility

Tensile tests conducted on the MG3R10N and MG3R10N03M alloys shows that Ni-containing alloys have rather low ductility (~ 2.2%) at room temperature (Fig. 4.9a), due to the brittleness of the intermetallics, especially the T-Al_9FeNi phase. The examination of the fracture surface of the alloys after static tensile test at room temperature (Fig. 4.10) reveals that the alloys show mixed cellular fracture mode which has been described by Warmuzek [32] as having both brittle and ductile fracture features. The brittle mode is due to the fracture of brittle phases which crack or sometimes lead to decohesion at the interfaces between the second phase and the matrix.

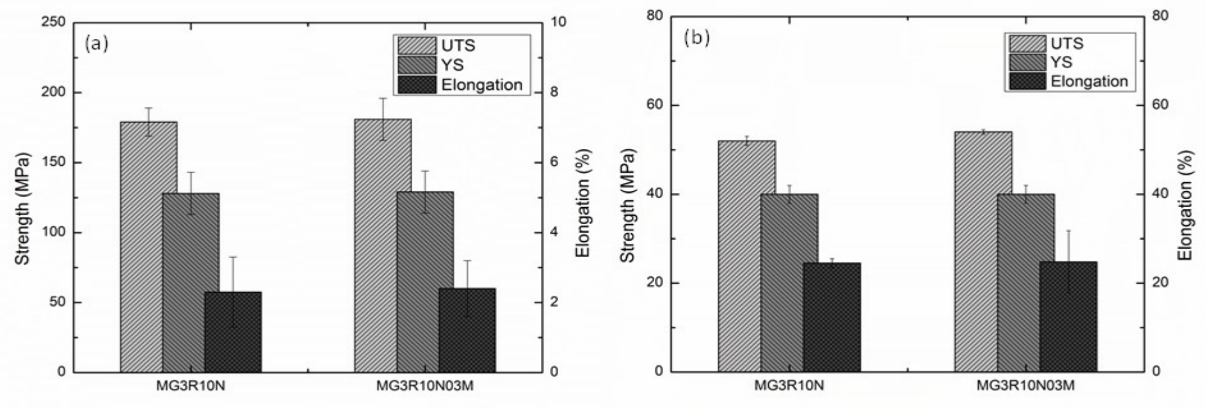

Fig. 4.9 Tensile properties of the selected alloys tested at (a) room temperature and (b) 300 °C.

The fracture surface of the MG3R10N alloy exhibits mixed (ductile-brittle) fracture with cracked brittle T-Al$_9$FeNi phase (EDS analysis, Fig. 4.10a); The continuity in the boundary between the T-Al$_9$FeNi intermetallics and the soft Al matrix is not preserved. Decohesion at different places are indicated by arrows in Fig. 4.10a. Secondary cracks also exist in the T-Al$_9$FeNi intermetallics which are the indications of high level of brittleness. The tear ridges of the deformed Al matrix do not completely surround the brittle, coarse intermetallics. The river patterns formed by parallel cleavage facets of the T-Al$_9$FeNi intermetallics are visible.

The fracture surface of the MG3R10N alloy after tensile test at 300 °C also exhibits a mixed-cellular fracture (Fig. 4.10c). Cracked T-Al$_9$FeNi intermetallics are present inside the cells of the deformed Al matrix; the cracks have propagated on several cleavage planes and decohesion zones can be observed at the matrix/precipitate interface confirming that these intermetallics are very brittle even at 300 °C. The fracture surface of the MGR10N03M alloy also shows the features of the cellular fracture very similar to the MGR10N alloy (Fig. 4.10d). These results indicate that the T-phase is a key factor in the low ductility of the alloys.

The effect of Mn

Eventhough Mn addition improves the creep resistance, the overall effect of 0.3% Mn addition (MG3R10N03M alloy) on compressive YS (Fig. 4.8) and tensile properties (Figs. 4.9a-b) is not significant. Mn decreases the amount of the brittle T-Al_9FeNi intermetallics and improves its ductility but forms a considerable amount of the brittle α-$Al_{15}(FeMn)_3Si_2$ intermetallics. The fracture surface of the MG3R10N03M alloy (Fig. 4.10b) is similar to the MG3R10N alloy; cleavage facets with secondary cracks are visible in the T-Al_9FeNi and some of the α-$Al_{15}(FeMn)_3Si_2$ intermetallics. The shear edges of the ductile Al matrix are present around the T-Al_9FeNi intermetallics where decohesion took place at the interface of the Al matrix and the T-Al_9FeNi intermetallics. It can be postulated that adjusting the Mn content to lower levels ($Mn < 0.3\%$), to decrease the T-Al_9FeNi but also form a lower amount of brittle α-$Al_{15}(FeMn)_3Si_2$ intermetallics could have positive effects on mechanical properties. It should be noted that the Mn-modified T-phase which does not crack at low strain (~ 0.1%) during creep does crack under high strain (~ 20%) during the tensile test. This is similar to the behaviour of the eutectic Si particles during creep and tensile testing.

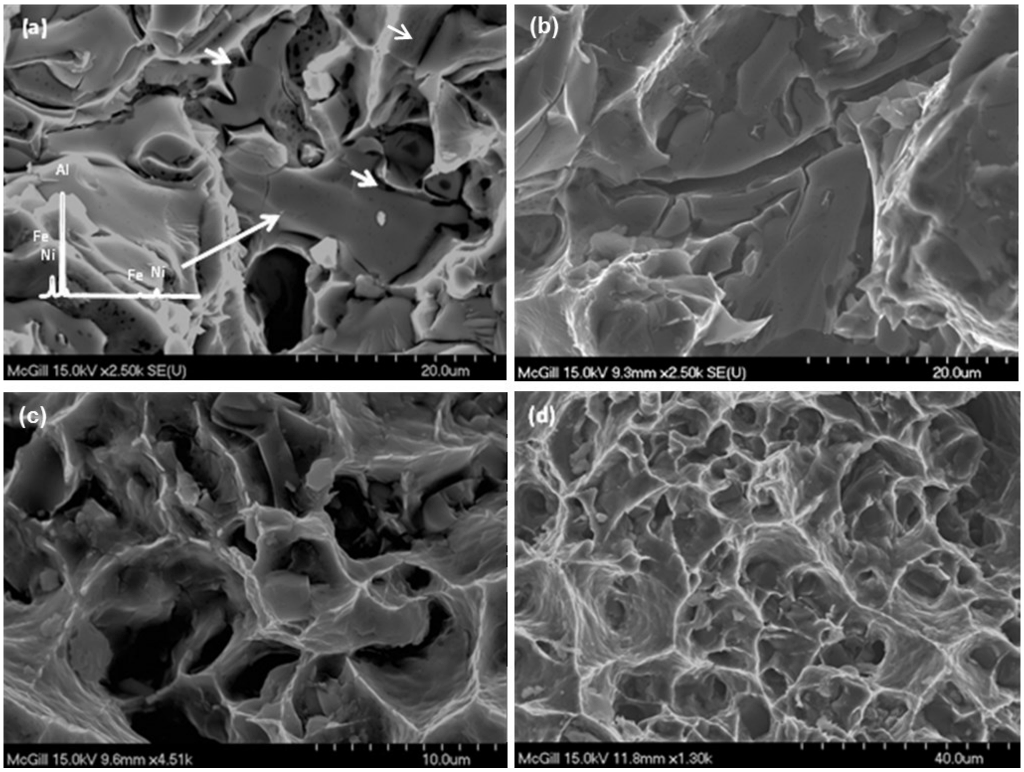

Fig. 4.10 Fracture surface of the (a) MG3R10N with the inset showing the EDS spectrum of T-Al_9FeNi, (b) MG3R10N03M alloy, after 600 hours of aging at 200 °C, fracture after static tensile test at room temperature, (c) MG3R10N and (d) MG3R10N03M alloys after 600 hours of aging at 200 °C and soaking for 100 hours at the test temperature, fracture after static tensile test at 300 °C.

4.4 Concluding remarks

The microstructure and the elevated temperature properties (strength, creep resistance) of Al7Si0.5Cu0.3Mg(0.3-1)Ni alloys have been investigated. The mechanical performance has been related to the microstructural features.

Microstructure and Phase Selection: Ni, depending on the chemical composition of the alloy, forms the T-Al_9FeNi, δ-Al_3CuNi, γ-Al_7Cu_4Ni and ε-Al_3Ni intermetallics in interdendritic regions during solidification. After solution annealing the δ-Al_3CuNi and γ-Al_7Cu_4Ni phases decompose and do not form during aging at 200 ^oC. Aged microstructures mainly consist of coarse T-Al_9FeNi intermetallics and Si particles in interdendritic regions as well as the θ-Al_2Cu and Q-$Al_5Mg_8Cu_2Si_6$ precipitates.

Creep and the Effect of T-Al_9FeNi: The T-Al_9FeNi intermetallics are very brittle even at 300 ^oC and undergo cracking when exposed to creep deformation. Crack formation in the T-Al_9FeNi intermetallics occurs at the very early stage of creep deformation and deteriorates the creep resistance of these alloys. The creep resistance decreases as the amount of the T-Al_9FeNi intermetallics increases with increasing Ni. The δ-Al_3CuNi and γ-Al_7Cu_4Ni phases form slowly at 300 ^oC by consuming the Cu contents of the alloys, during creep process which may hasten the creep deformation.

Strength: Thermally stable Ni intermetallics increase the yield strength of these alloys at 300 ^oC. However, this effect is negligible at low temperatures.

The Effect of Mn: Mn dissolves in T-Al_9FeNi phase and eliminates its adverse effects on creep resistance by preventing its early cracking during creep loading. Furthermore, Mn imparts ductility to the T-Al_9FeNi intermetallics the investigation of which is of future interest.

4.5 Acknowledgment

This work was supported by the NSERC (Natural Sciences and Engineering Research Council) of Canada Strategic project grant with Rio Tinto Alcan (RTA). The authors thank Pierre Vermette of McGill University for his assistance in experimental work. Amir Rezaei Farkoosh would like to gratefully acknowledge the financial support of McGill University through MEDA (McGill Engineering Doctoral Award) program. A part of the research presented in this paper was financed by the Fonds québécois de la recherche sur la nature et les technologies by the intermediary of the Aluminium Research Centre – REGAL. In addition, we are grateful for the help and assistance of Prof. H. Vali and Dr. Xue-Dong Liu (TEM).

4.6 References

[1] A.M.A. Mohamed, F.H. Samuel, S.A. kahtani, Microstructure, Tensile Properties and Fracture Behavior of High Temperature Al-Si-Mg-Cu Cast alloys, Mater. Sci. Eng., A.

[2] M. Garat, G. Laslaz, Improved Aluminum Alloys for Common Rail Diesel Cylinder Heads, in: AFS, IL, USA, 2007, pp. 1-8.

[3] F.J. Feikus, Optimisation of AlSi Cast-Alloys for Cylinder Head Applications, in: AFS, Georgia, USA, 1998, pp. 1-21.

[4] F. Stadler, H. Antrekowitsch, W. Fragner, H. Kaufmann, E.R. Pinatel, P.J. Uggowitzer, The effect of main alloying elements on the physical properties of Al–Si foundry alloys, Mater. Sci. Eng., A, 560 (2013) 481-491.

[5] M. Okayasu, Y. Ohkura, S. Takeuchi, S. Takasu, H. Ohfuji, T. Shiraishi, A study of the mechanical properties of an Al–Si–Cu alloy (ADC12) produced by various casting processes, Mater. Sci. Eng., A, 543 (2012) 185-192.

[6] T. Gao, D. Li, Z. Wei, X. Liu, Evolution, microhardness of ZrAlSi intermetallic and its impact on the elevated-temperature properties in Al–Si alloys, Mater. Sci. Eng., A, 552 (2012) 523-529.

[7] H.A. Elhadari, H.A. Patel, D.L. Chen, W. Kasprzak, Tensile and fatigue properties of a cast aluminum alloy with Ti, Zr and V additions, Mater. Sci. Eng., A, 528 (2011) 8128-8138.

[8] Y. Li, S. Brusethaug, A. Olsen, Influence of Cu on the mechanical properties and precipitation behavior of AlSi7Mg0. 5 alloy during aging treatment, Scripta Mater., 54 (2006) 99-103.

[9] V.S. Zolotorevskiĭ, N.A. Belov, M.V. Glazoff, Casting aluminum alloys, Elsevier Science Ltd, 2007.

[10] L. Heusler, F.J. Feikus, M.O. Otte, Alloy and Casting Process Optimization for Engine Block Application, in: AFS Trans, 2001, pp. 215-223.

[11] Z. Asghar, G. Requena, E. Boller, Three-dimensional rigid multiphase networks providing high-temperature strength to cast AlSi10Cu5Ni1-2 piston alloys, Acta Mater., 59 (2011) 6420-6432.

[12] N.A. Belov, D.G. Eskin, N.N. Avxentieva, Constituent phase diagrams of the Al–Cu–Fe–Mg–Ni–Si system and their application to the analysis of aluminium piston alloys, Acta Mater., 53 (2005) 4709-4722.

[13] L.F. Mondolfo, Aluminum alloys: structure and properties, Butterworths London, 1976.

[14] F. Stadler, H. Antrekowitsch, W. Fragner, H. Kaufmann, P.J. Uggowitzer, Effect of main alloying elements on strength of Al-Si foundry alloys at elevated temperatures, Int. J. Cast Met. Res., 25 (2012) 215-224.

[15] A.R. Farkoosh, M. Javidani, M. Hoseini, D. Larouche, M. Pekguleryuz, Phase formation in as-solidified and heat-treated Al–Si–Cu–Mg–Ni alloys: Thermodynamic assessment and experimental investigation for alloy design, J. Alloys Compd., 551 (2013) 596-606.

[16] M. Flemings, Solidification processing, Metall. Mater. Trans. B, 5 (1974) 2121-2134.

[17] H. Liao, Y. Sun, G. Sun, Correlation between mechanical properties and amount of dendritic α-Al phase in as-cast near-eutectic Al–11.6% Si alloys modified with strontium, Mater. Sci. Eng., A, 335 (2002) 62-66.

[18] J.Y. Hwang, H.W. Doty, M.J. Kaufman, The effects of Mn additions on the microstructure and mechanical properties of Al–Si–Cu casting alloys, Mater. Sci. Eng., A, 488 (2008) 496-504.

[19] L. Lu, A. Dahle, Iron-rich intermetallic phases and their role in casting defect formation in hypoeutectic Al−Si alloys, Metall. Mater. Trans. A, 36 (2005) 819-835.

[20] N. Stoloff, Toughening mechanisms in intermetallics, Metall. Mater. Trans. A, 24 (1993) 561-567.

[21] R.A. Varin, M.B. Winnicka, Plasticity of structural intermetallic compounds, Mater. Sci. Eng., A, 137 (1991) 93-103.

[22] S.P. Chen, N.C.W. Kuijpers, S. van der Zwaag, Effect of microsegregation and dislocations on the nucleation kinetics of precipitation in aluminium alloy AA3003, Mater. Sci. Eng., A, 341 (2003) 296-306.

[23] H.Y. Kim, T.Y. Park, S.W. Han, H.M. Lee, Effects of Mn on the crystal structure of α-Al(Mn,Fe)Si particles in A356 alloys, J. Cryst. Growth, 291 (2006) 207-211.

[24] H.Y. Kim, S.W. Han, H.M. Lee, The influence of Mn and Cr on the tensile properties of A356–0.20Fe alloy, Mater. Lett., 60 (2006) 1880-1883.

[25] M. Celikin, A.A. Kaya, M. Pekguleryuz, Effect of manganese on the creep behavior of magnesium and the role of α-Mn precipitation during creep, Mater. Sci. Eng., A, 534 (2012) 129-141.

[26] D. Hull, D.J. Bacon, Introduction to dislocations, Butterworth-Heinemann, 2011.

[27] I.L. Mogford, The deformation and fracture of two-phase materials, Metallurgical Reviews, 12 (1967) 49-68.

[28] T. Jaglinski, R. Lakes, Creep behavior of Al-Si die-cast alloys, TRANSACTIONS-AMERICAN SOCIETY OF MECHANICAL ENGINEERS JOURNAL OF ENGINEERING MATERIALS AND TECHNOLOGY, 126 (2004) 378-383.

[29] P. Villars, L.D. Calvert, Pearson's handbook of crystallographic data for intermetallic phases, ASM International, Materials Park, OH, 1991.

[30] J.H. Westbrook, R.L. Fleischer, Crystal structures of intermetallic compounds, in, Wiley, Chichester; New York, 2000.

[31] Y. Li, Y. Yang, Y. Wu, L. Wang, X. Liu, Quantitative comparison of three Ni-containing phases to the elevated-temperature properties of Al-Si piston alloys, Mater. Sci. Eng., A, 527 (2010) 7132-7137.

[32] M. Warmuzek, Aluminum-silicon casting alloys: atlas of microfractographs, Asm Intl, 2004.

CHAPTER 5

DISPERSOID STRENGTHENING OF A HIGH TEMPERATURE AL-SI-CU-MG ALLOY VIA MO ADDITION

Molybdenum has been identified in the alloy strategy of this doctoral work for its potential for dispersoid formation. Mo was of interest because of its low diffusivity in Al and some but limited solid and liquid solubility at the peritectic reaction temperature. One of the initial stages of this work was a study on the behavior of Mo in Al-Si alloys to generate fundamental knowledge on the precipitation of the Mo-containing dispersoids and their effect on mechanical properties at elevated temperatures. This chapter has been accepted for publication: *A.R. Farkoosh, X.-G. Chen, M. Pekguleryuz, Dispersoid Strengthening of a High Temperature Al-Si-Cu-Mg Alloy via Mo Addition, Mater. Sci. Eng., A, 620 (2014) 181-189.*

ABSTRACT

The influence of Mo addition on the microstructure and mechanical properties of an Al-7Si-0.5Cu-0.3Mg alloy (wt.%) was investigated. The Mo-containing alloy exhibited significant improvement in creep resistance over the base alloy. At 300 °C and 30 MPa, the minimum creep rate decreased by 95% while creep time-to-fracture was increased by 2 orders of magnitude, from 50 min to 1500 min. The tensile yield strength at 300 °C was also increased by 25%. These effects were attributed to the formation of novel Al-(Fe,Mo)-Si dispersoids during solution treatment in the grain interiors (intradendritic regions). Unlike the age-hardening precipitates, which coarsened resulting in loss of strength, these dispersoids were thermally stable and retained their strengthening effect at 300 °C. TEM investigations showed that the dislocation motions were effectively hindered by these fine dispersoids, leading to the reduction in the minimum creep rate. The onset of the tertiary creep stage was delayed by postponing the dislocation pile-up at the interdendritic Si particles. It was found that Mo addition suppressed the formation of the brittle plate-like β-Al_5FeSi intermetallics and formed a blocky Al-(Fe,Mo)-Si phase in the cast microstructure, which resulted in 34% increase in elongation at 300 °C.

Keywords: Al-Si alloys; Mo addition; Creep resistance; High temperature mechanical properties; Dispersoid strengthening; TEM

5.1 Introduction

Al-Si alloys offer significant weight advantages for Diesel engines. To improve the fuel efficiency and performance of Diesel engines, the operation temperature and pressure of the engines are progressively increased, which necessitates developing new creep resistant Al alloys. Under the Diesel engine operating conditions (300 °C, 20-30 MPa) the creep mechanisms that are rate controlling in Al are dislocational (dislocation climb, pipe diffusion, movement of dislocation with solute atmospheres) [1-3]. Effective dislocation pinning via fine and stable second phases, and high temperature solutes with low mobility are important in impeding these creep mechanisms [3]. Age-hardening precipitates in Al alloys (mainly Cu- and/or Mg-containing) are widely used to improve strength at room temperature, however, they can only be effective for strength and creep resistance at temperatures below 250 °C [1, 4-6]. At higher temperatures, precipitate coarsening (Ostwald ripening) leads to severe loss of strength, therefore their use for the Diesel engine, which reaches 300 °C during engine heat-up, is not possible. Alloy development activities in high temperature Al alloys can follow two routes: (i) slowing down the coarsening kinetics of the age hardening precipitates by trace additions of e.g. In, Ce and Ge [7-9], and (ii) designing thermally stable precipitates (dispersoids), which retain their effectiveness up to much higher temperatures [10].

Solutes as dispersoid formers in Al: Effective dispersoids for improved creep resistance need to be thermally stable and of high volume fraction and uniform distribution. A combination of all three attributes is difficult to attain in Al alloys. The *thermal stability* of the dispersoids depends on the low solid solubility and diffusivity of the constituent solute atoms in the Al matrix. Transition metals (TMs) and rare earth (RE) elements [11] are potential candidates as dispersoid formers, since they are slow diffusers in Al, and their solid solubility in Al is often limited. However, low solubility gives rise to low volume-fraction of the dispersoids. Al-Si casting alloys usually have high silicon (*Si)* levels to ensure good castability. Si, however, has certain adverse effects on dispersoid formation in Al. In the Al-Si-TM systems, Si, at high levels, lower the peritectic and eutectic temperatures as well as the solid solubility of the alloying elements in the Al matrix [12] and decreases their ability to form dispersoids. Furthermore, Si may incorporate in the structure of the trialuminides (Al_3M, M = Sc, Zr, Er, Hf, Nb, Ti) and, thereby decrease their coarsening resistance [11, 13].

Scandium (Sc) forms coherent Al_3M type dispersoids in wrought Al alloys [14-18], however, because of its high cost, its use in Al alloys is limited. *Zirconium* (*Zr)* also forms coherent Al_3M type dispersoids in Al [19-21], albeit with very low strengthening efficiency in the Al-Si casting alloys [22]. *Chromium (Cr)* forms face centered cubic (FCC) α-AlCrSi dispersoids, incoherent or semicoherent, in wrought and casting alloys [23]. Mn addition, single or in combination with Cr, forms α-Al(Mn,Cr,Fe)Si intermetallics [24-28]. The Mn and Cr [25, 27, 29-35] dispersoids in Al alloys exhibit various chemical compositions and complex crystal structures (quasicrystals). These dispersoids are reported to have an incoherent or semicoherent interface with the Al matrix [27] and the strengthening efficiency is low.

Molybdenum (Mo) as a dispersoid former: In search for a promising dispersoid forming solute for Al-Si casting alloys, the authors have determined that Mo can potentially form a large amount of metallurgically stable dispersoids in Al-Si casting alloys even when added at low levels. Importantly, the low diffusivity of Mo in Al (2.3×10^{-26} m^2s^{-1} at 300 °C) [36] along with the limited solid solubility of this element in Al (~ 0.25 wt.% at peritectic temperature, 660 °C), which decreases rapidly with decreasing temperature (Fig. 5.1), makes it an interesting candidate as dispersoid former for Al. Mo has not received much attention previously for use in Al alloys, because the dispersoid phase does not readily form under the conditions of conventional casting and low solutionizing temperatures. The only use of Mo is limited to certain rapidly solidified (RS) powder metallurgy alloys [37-41]. Reliable data on the phase selection and precipitation of Mo-containing alloys are scarce. The Al-rich region of the Al-Mo phase diagram (Fig. 5.1) shows a series of consecutive peritectic reactions and the formation of different Al_XMo intermetallics [42-47]. The BCC $Al_{12}Mo$ phase is the last phase that forms through a peritectic reaction at slightly above the melting point of pure Al (Fig. 5.1b).

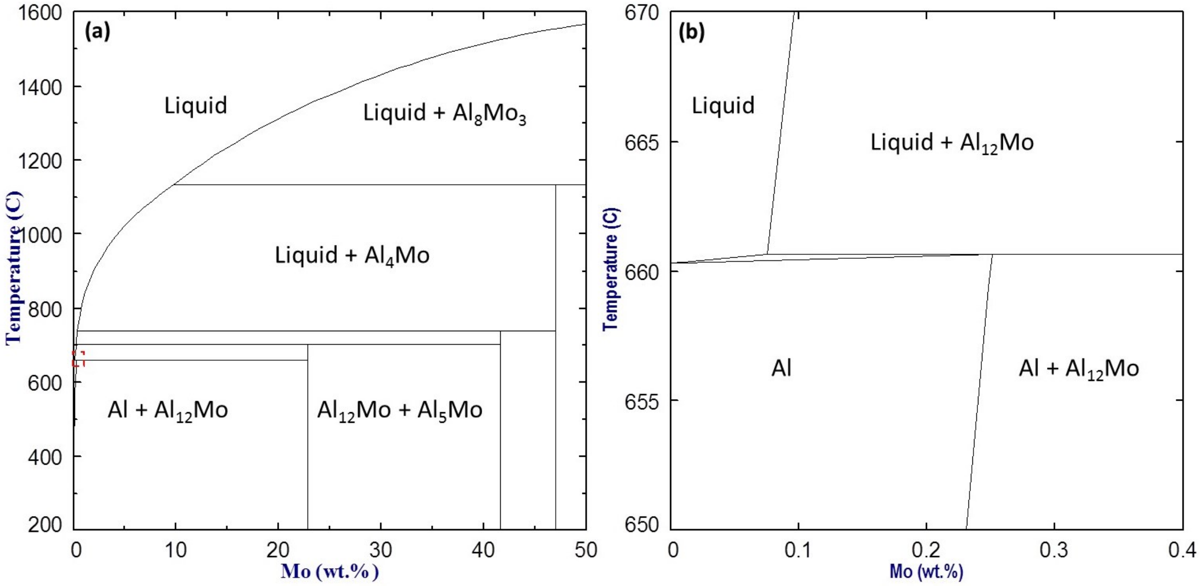

Fig. 5.1 (a) Al-Mo binary phase diagram and (b) enlarged view of the Al-rich corner (calculated using FactSage software).

This paper investigates the possibility of forming a large amount of thermally stable dispersoids via Mo addition in an Al-7Si alloy through conventional casting process and subsequent high temperature heat treatment. The effect of Mo and its dispersoids on the microstructure and creep resistance as well as tensile properties at elevated temperatures (300 ^{o}C) was studied and compared to the base alloy containing no Mo.

5.2 Experimental procedures

The Al7Si0.5Cu0.3Mg (reference alloy, designated as MG3R) and Al7Si0.5Cu0.3Mg0.3Mo (designated as MG3R3M) alloys were synthesized in an induction furnace (NORAX Canada Inc.) and cast into a preheated (400 ^{o}C) permanent mold to obtain cylindrical bars of 30 mm diameter. A commercial grade A356 alloy supplied by Rio Tinto Alcan Inc. was used and the Cu and Mo levels were adjusted by the addition of the Al-33 wt.% Cu and Al-10 wt.% Mo master alloys at 760 ^{o}C. All the alloys were modified with 150 ppm Sr. The chemical composition of the alloys were determined by inductively coupled plasma (ICP) analysis (Table 5.1). All alloy compositions in this paper are given in wt.%, unless otherwise specified. All cast samples were solutionized at two stages to avoid possible incipient melting: 4 hours at 500 ^{o}C followed by 1-10 hours at 540 ^{o}C, in an electrically heated, air-circulating chamber furnace. The samples were immediately quenched in water at room temperature and aged at 200 ^{o}C for 5 hours (T7).

Table 5.1 Chemical composition of the alloys

Alloy	Chemical Composition (wt.%)							
	Si	Cu	Mg	Fe	Ti	Mo	Sr	Al
MG3R	6.94	0.58	0.30	0.11	0.10	< 0.01	0.014	Balance
MG3R03M	6.97	0.57	0.29	0.10	0.09	0.27	0.013	Balance

Tensile creep test specimens with a diameter of 12.7 mm and a gauge length of 50 mm were machined from the cast samples according to the ASTM E8 standard. Compressive creep test samples with a diameter of 20 mm and a length of 30 mm were machined from the castings. Creep testing was conducted at 300 ^{o}C under constant load corresponding to 30 MPa. Temperature was monitored with a thermocouple with an error of ± 0.1 ^{o}C attached to the specimen. The gauge length displacement was measured with two high precision extensometers with a resolution of 5 μm. Tensile test was performed according to ASTM E8 at a strain rate of 0.01 s^{-1}. All elevated temperature tests were conducted in air and samples were soaked at 300 ^{o}C, 100 hours prior to testing. Vickers microhardness measurements (a minimum of 10 measurements for each sample) were carried out on polished samples using a Clark CM100AT hardness testing machine with a load of 10 g. The macrohardness was measured using a Buehler hardness testing machine.

Specimens for microstructural characterization were prepared by grinding with a series of SiC papers. They were polished on a porous neoprene polishing cloth with the Al_2O_3 (5 and 0.3 μm) solutions. Final polishing was performed with a Buehler vibratory polisher using a 0.06 μm colloidal silica suspension. A field emission gun scanning electron microscope (FEG-SEM, Hitachi S-4700) and a conventional scanning electron microscope (SEM, Hitachi SU3500) were used for microstructural investigation. The accelerating voltage was 15 kV and a beam current of 10 μA was chosen for all SEM observations. Thin foils for transmission electron microscopy (TEM) were prepared by mechanical grinding and jet polished using a Struers Tenupol 3 jet polisher with a solution of 10% Nitric acid in methanol at -40 ºC. The TEM images were acquired using a Philips CM200 microscope operating at 200 kV. The EDS spectra were obtained by EDAX detector connected to the column.

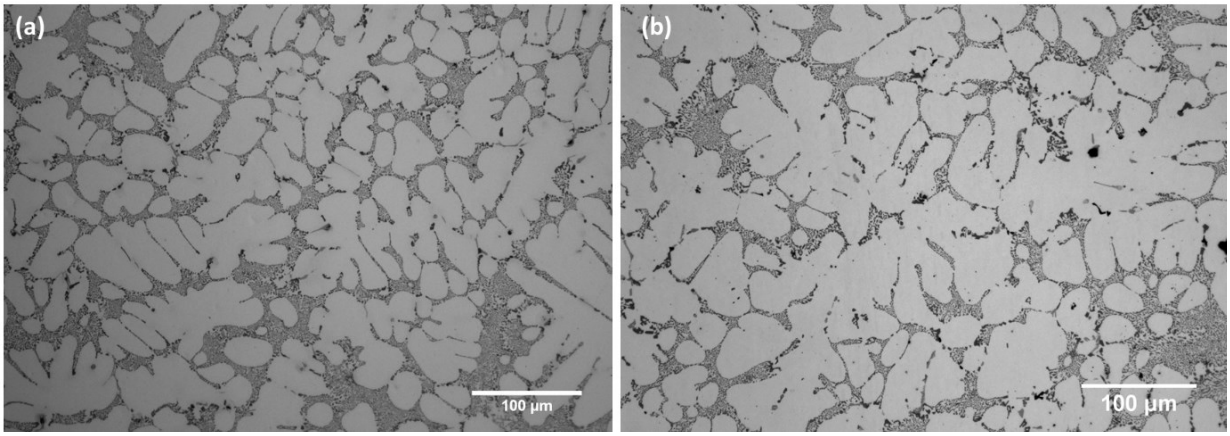

Fig. 5.2 The as-cast microstructures of the (a) MG3R and (b) MG3R3M alloy.

5.3 Results and discussion

5.3.1 Alloy microstructures

As-cast microstructures

The as-cast microstructures of both alloys (the base and the Mo-containing alloys) consist of α-Al dendrites with various intermetallic phases and eutectic Si particles in the interdendritic regions (Fig. 5.2). For both alloys, the secondary dendrite arm spacing (SDAS) was measured to be 30 ± 5 μm, showing no significant change following Mo addition. The as-cast MG3R alloy (Fig. 5.3.a) contains two Fe-containing intermetallics (β-Al_5FeSi and π-$Al_8FeMg_3Si_6$) and two Cu-containing intermetallics (θ-Al_2Cu and Q-$Al_5Cu_2Mg_8Si_6$). The brittle β-Al_5FeSi platelets (Fig. 5.3b) are a concern for ductility and fracture toughness. These platelets are known to form at the end of solidification; they can impede interdendritic feeding giving rise to the shrinkage pores as seen in Fig. 5.3b. The addition of 0.3%Mo (MG3R3M alloy) results in the formation of a new Al-(Fe,Mo)-Si intermetallic phase with bulky morphology (Fig. 5.3c). The 0.1%Fe in the alloy seems to be completely consumed by Mo in forming the Al-(Fe,Mo)-Si phase, and the formation of the β-Al_5FeSi and π-$Al_8FeMg_3Si_6$ intermetallic phases are suppressed.

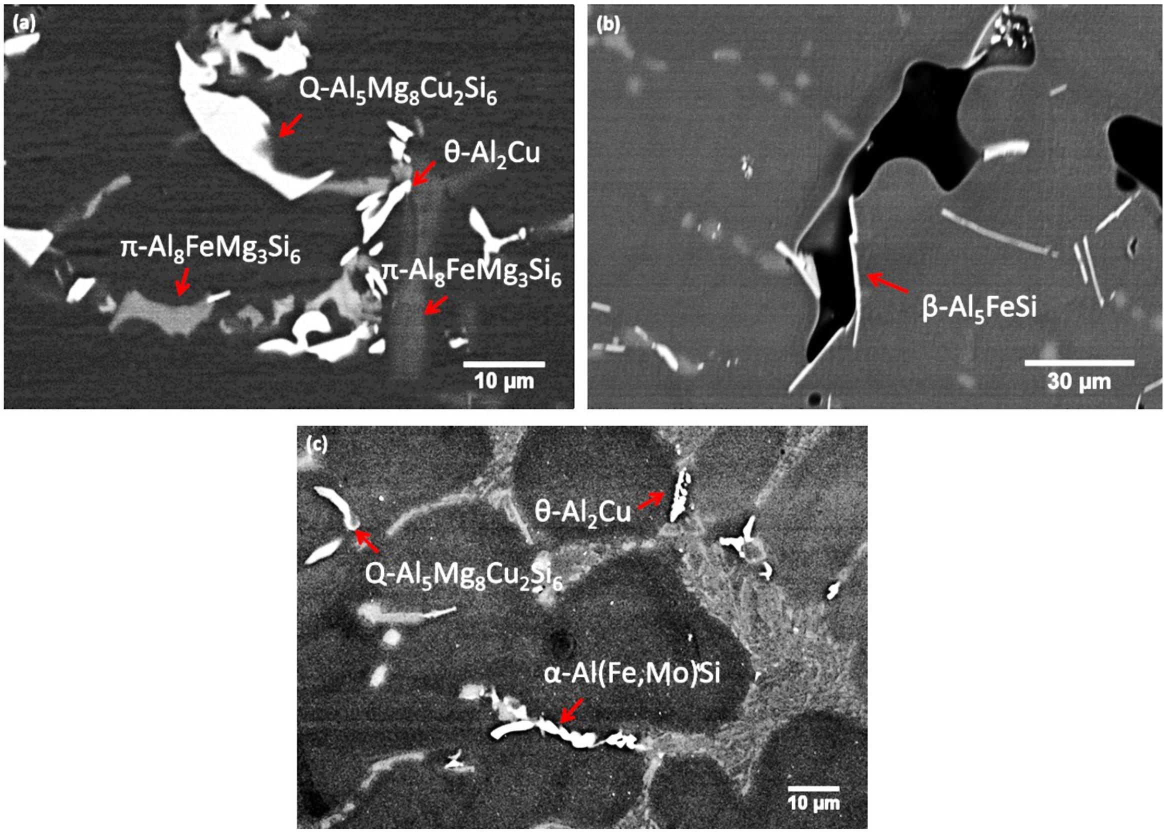

Fig. 5.3 Backscattered SEM micrographs showing (a) the intermetallics formed in the as-cast MG3R, (b) the β-Al_5FeSi platelets formed in the as-cast MG3R blocking the interdendritic feed path and (c) the intermetallics formed in the as-cast MG3R3M.

Solution-treated microstructures

The π-$Al_8FeMg_3Si_6$ phase (with Chinese script morphology), present in the as-solidified microstructure of MG3R, decomposed during solution treatment and is not seen in the solution-treated microstructure (Fig. 5.4a). The β-Al_5FeSi phase of the MG3R alloy is thermodynamically stable at the solutionizing temperature and does not undergo decomposition during solution treatment (Fig. 5.4a). In the MG3R3M alloy, all the phases formed during solidification are dissolved except for the Al-(Fe,Mo)-Si phase (Fig. 5.4b).

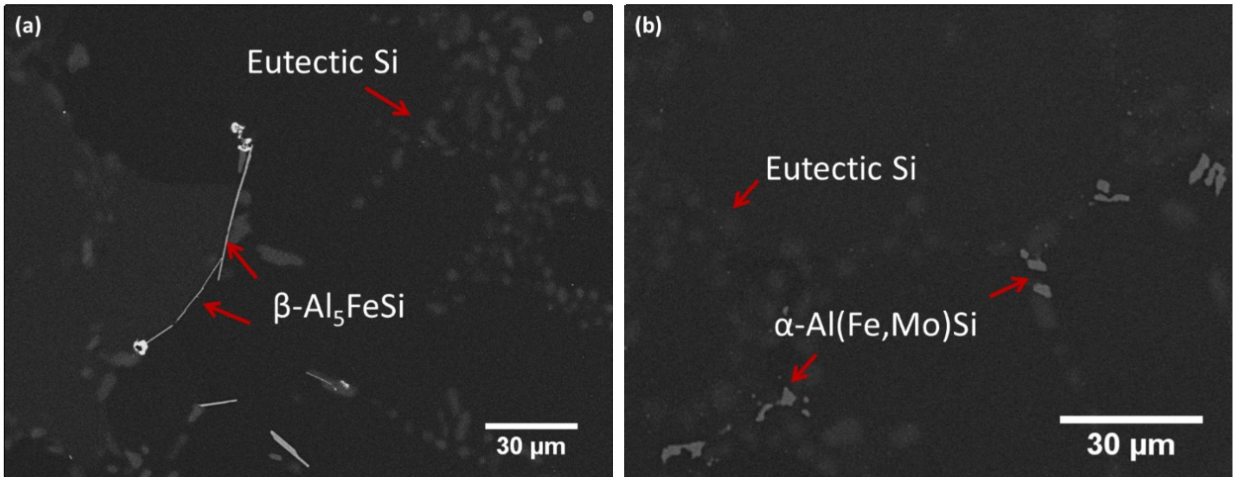

Fig. 5.4 Backscattered SEM micrographs showing the solution treated (4 h at 500 ºC and 10 h at 540 ºC) microstructures of the (a) MG3R and (b) MG3R3M alloy.

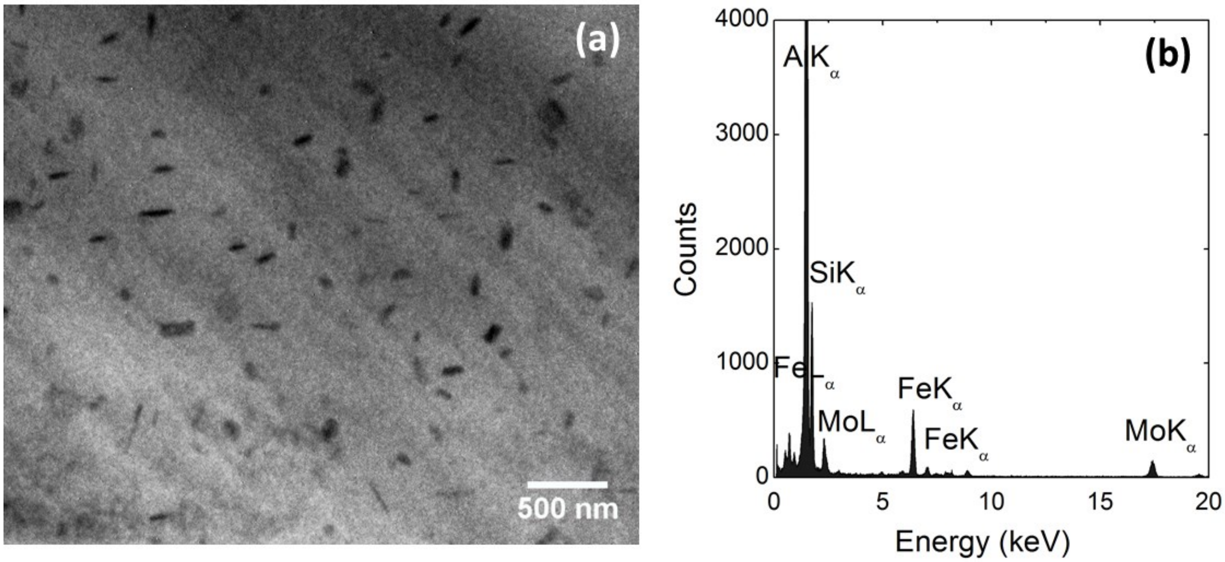

Fig. 5.5 (a) Bright field TEM micrograph showing the α-Al-(Fe,Mo)-Si dispersoids in the intradendritic regions of the MG3R3M alloy formed after 10 h of solution treatment at 540 ºC. (b) EDS spectrum of the Al-(Fe,Mo)-Si dispersoids.

TEM analysis (Fig. 5.5a) performed after solution treatment (4 hours at 500 ºC and 10 hours at 540 ºC) of the MG3R3M alloy shows that a substantial amount of fine Mo-containing dispersoids with an average size of $\langle D \rangle = 120\ nm$ are found in the intradendritic regions. The formation of the intradendritic dispersoids can be explained by the Al-Mo binary phase diagram

(Fig. 5.1), according to which, the partition coefficient, k_0 is greater than unity. The peritectic nature of the alloy system leads to Mo supersaturation of the dendrite cores as a result of micro-segregation during non-equilibrium solidification. Upon thermal exposure (solution treatment), fine dispersoids are precipitated in the Mo-supersaturated Al cores. Because of the low diffusivity of Mo in Al, however, the formation of the Mo dispersoids requires high temperatures close to the solidus. EDS analysis (Fig. 5.5b) showed that the dispersoids are a quaternary Al-(Fe,Mo)-Si phase.

5.3.2 Age hardening response of the alloys

Fig.5. 6 shows the age hardening curves of the MG3R and MG3R3M alloys. The peak hardness of both alloys are synchronous (t = 100 min). However, a moderately higher value of the peak hardness was observed for the Mo-containing alloy. After prolonged ageing over a period of four weeks, the Mo-containing alloy displays clearly higher hardness values than that of the base alloy. The microstructural evolution of the aged alloys was investigated via TEM analysis.

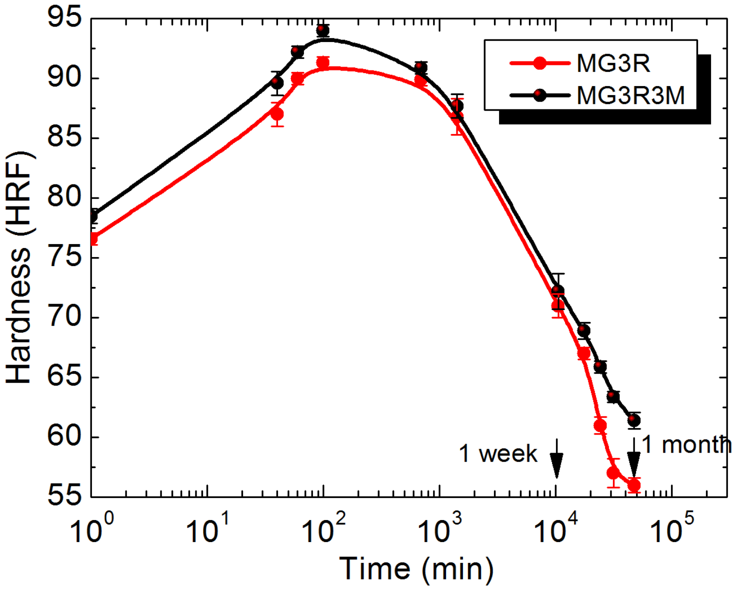

Fig. 5.6 HRF hardness evolution of the MG3R and MG3R3M alloys during artificial ageing at 200 °C.

Al7Si0.5Cu0.3Mg (MG3R)

Figs. 5.7a-c show the microstructural evolution of the MG3R alloy during artificial ageing at 200 °C. It can be seen that overageing leads to the coarsening and ripening of the θ-Al_2Cu and Q-

$Al_5Cu_2Mg_8Si_6$ precipitates (Figs. 5.7b and c), which results in the loss of their strengthening effect as observed in the age-hardening curve (Fig. 5.6). This is related to the high diffusion rates of Cu and Mg in Al and substantial solid solubility of these elements in the Al matrix, which lead to Ostwald ripening. At 300 ^oC (Fig. 5.7d), TEM investigations show that only the coarse Q-$Al_5Cu_2Mg_8Si_6$ precipitates are present within the microstructure; the θ-Al_2Cu precipitates are dissolved because of their thermodynamic instability at this temperature.

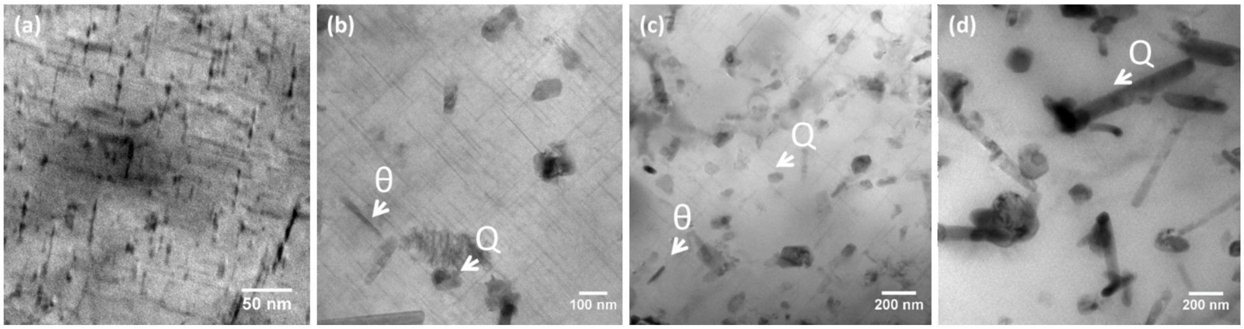

Fig. 5.7 Bright field TEM micrographs of the microstructure of the MG3R alloy after solution treatment and (a) 12 hours (b) 170 hours (c) 500 hours of ageing at 200 ^oC, showing the θ and Q precipitates, (d) T7 (5 h at 200 ^oC) followed by 240 hours of soaking at 300 ^oC, showing only the coarsened Q precipitates.

Al7Si0.5Cu0.3Mg0.3Mo (MG3R3M)

Figs. 5.8a-b shows the microstructures of MG3R3M during artificial ageing at 200 ^oC. After 12 hours of ageing (Fig. 5.8a), the θ-Al_2Cu and Q-$Al_5Cu_2Mg_8Si_6$ precipitates as well as the Mo-containing dispersoids coexist in the aluminum matrix. It is seen that the Mo-containing dispersoids (indicated by arrows) remain unchanged during the prolonged ageing, while both θ-Al_2Cu and Q-$Al_5Cu_2Mg_8Si_6$ precipitates become coarsened (Fig. 5.8b). In the peak ageing, as understood, both alloys are mainly strengthened by the θ-Al_2Cu and Q-$Al_5Mg_8Cu_2Si_6$ precipitates and the Al-(Fe,Mo)-Si dispersoids in MG3R3M exert additional strengthening (Fig. 5.6). After prolonged ageing times at 200 ^oC (overageing), the hardness decreases rapidly for the MG3R alloy, while the decrease of the hardness is slower for the MG3R3M alloy yielding higher hardness values, particularly for a long overageing time of few weeks (Fig. 5.6). At 300 ^oC, the strengthening effect of the Al-(Fe,Mo)-Si dispersoids is expected to become more significant, because of the stability of the dispersoids at this temperature and further coarsening of the Q-$Al_5Cu_2Mg_8Si_6$ precipitates (Fig. 5.8c).

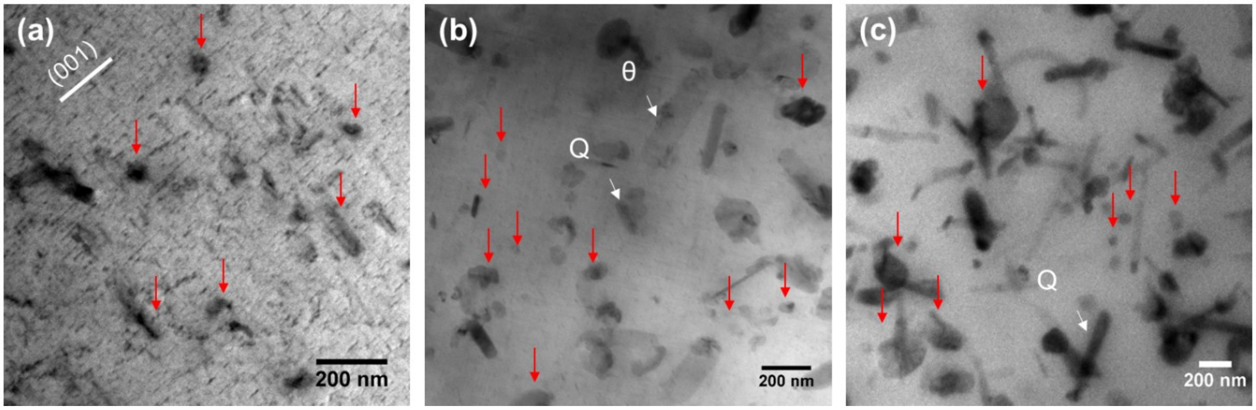

Fig. 5.8 Bright field TEM micrographs showing the evolution of the precipitates after (a) 12 h and (b) 600 h of ageing at 200 ºC and (c) T7 (5 h at 200 ºC) followed by 240 hours of soaking at 300 ºC, showing no coarsening of the α-Al(Fe,Mo)Si dispersoids. The α-Al(Fe,Mo)Si dispersoids are indicated by red arrows.

Vickers microhardness measurements were carried out to study the strengthening effect of the dispersoids on the matrix of the MG3R3M alloy. The alloy was first soaked at 500 ºC for 4 hours to dissolve all the Cu- and/or Mg-bearing intermetallics. The samples were then held isothermally at 540 ºC for various times up to 16 hours. After each time interval, the samples were quenched in water at room temperature and the precipitation of the dispersoids was monitored via microhardness measurements at room temperature (Fig. 5.9). The Vickers microhardness of the as-cast alloy was found to be 65 ± 3 HV, which remains almost constant during soaking at 500 ºC, indicating the occurrence of no precipitation after 4 hours. At 540 ºC, the microhardness of the alloy increases to its peak value, 83 ± 1 HV after 1 hour, then starts to decrease and reaches 72 ± 3 HV after 10 hours and 68 ± 2 HV after 16 hours. This indicates that compared to 500 ºC, soaking at 540 ºC induces higher mobility to the Mo solutes enabling the precipitation of the dispersoids. The decline in microhardness after prolonged solution treatment is attributed to the coarsening of the dispersoids.

5.3.3 Creep behavior of the alloys

Tensile and compressive creep tests were conducted at 300 ºC and 30 MPa. All creep specimens were solution-treated for 4 hours at 500 ºC and 1 hour at 540 ºC, followed by a soaking of 100 hours at 300 ºC prior to creep testing, to obtain maximum dispersion strengthening in the Mo-containing alloy (Fig. 5.10). The same treatment was applied to the base alloy. Fig. 5.10a compares the tensile creep behavior of the MG3R and MG3R3M alloys. The deformation rate, $\dot{\varepsilon}(= d\varepsilon/dt)$ of the MG3R3M alloy, possessing fine Mo-containing dispersoids, starts to deviate from that of the MG3R alloy at the very early stages of creep deformation. In the secondary creep stage, a significant ~ 95% reduction in the minimum creep rate of the Mo-containing alloy is observed. The creep time-to-fracture increases from 50 min for the MG3R alloy to 1500 min for the MG3R3M alloy.

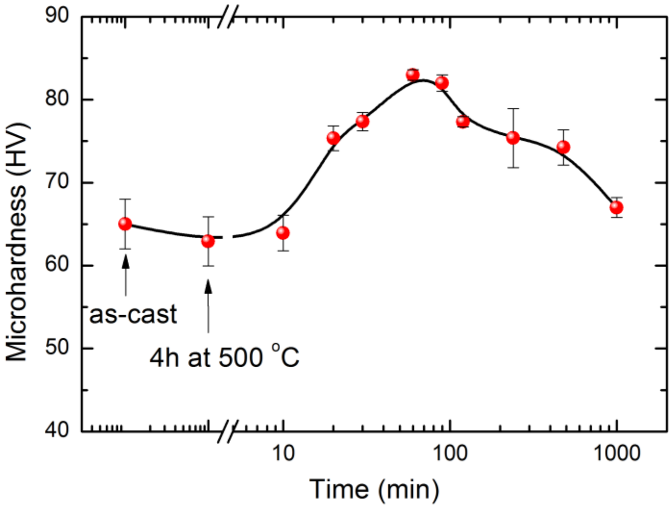

Fig. 5.9 Microhardness evolution of the Al matrix of the MG3R3M alloy at 540 °C.

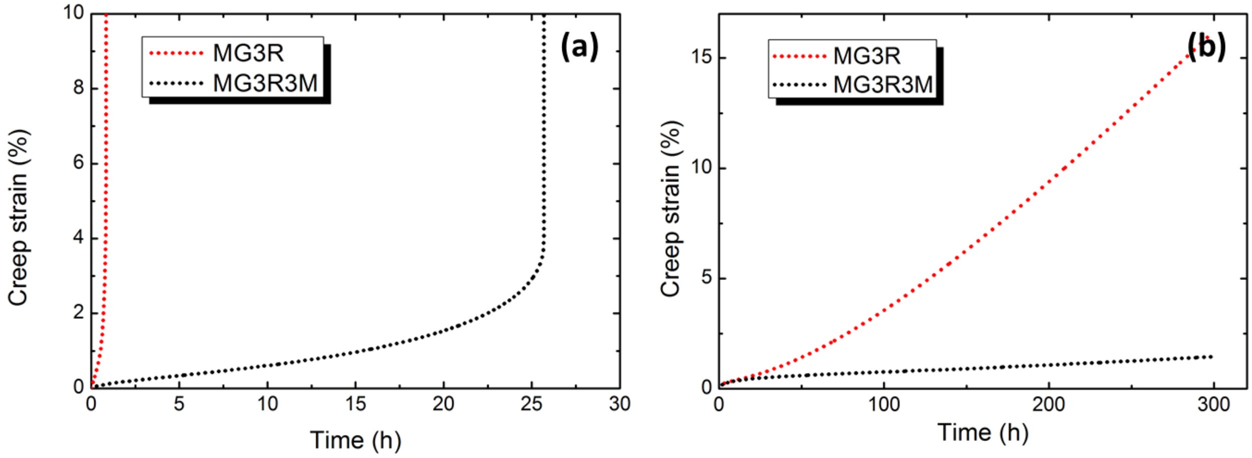

Fig. 5.10 Creep deformation vs. time at 300 °C and 30 MPa under (a) tensile and (b) compressive loading. Solution treated at 540 °C for 1 h, aged at 200 °C for 5 hours and soaked at the test temperature for 100 hours prior to testing.

The investigation of the creep deformation of the alloys under relatively longer (300 h) compressive creep further confirms the results obtained from the tensile creep tests. The compressive creep rate of the MG3R3M alloy was ~ 90% lower than the base alloy (Fig. 5.10b).

TEM investigations of the creep tested samples (Fig. 5.11, 300 hours of compressive creep at 300 °C and 30 MPa) demonstrate dislocation arrangements in both alloys. Fig. 5.11a shows the interaction of the dislocations with the large Q-$Al_5Mg_8Cu_2Si_6$ precipitates in the MG3R alloy. In the case of the MG3R3M alloy, the dislocation motions are mostly hindered by the fine dispersoids (Fig. 5.11b).

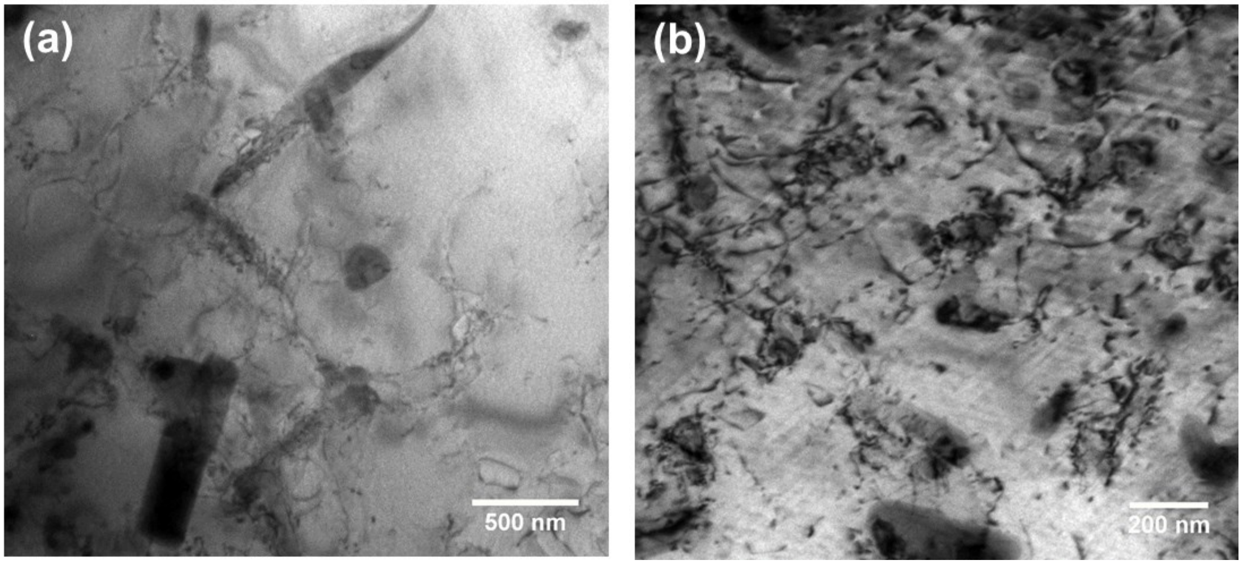

Fig. 5.11 Bright field TEM micrographs showing dislocation/precipitate interactions in the intradendritic regions of the (a) MG3R and (b) MG3R3M alloy after 300 hours of compressive creep at 300 °C and 30 MPa.

The very low creep rate of the Mo-containing alloy during a long thermal exposure period (100 hours soaking and 300 hours creep at 300 °C) indicates that the Mo-containing dispersoids are thermally stable at 300 °C. The coarsening rate constant, K, of the precipitates can be estimated using [48]:

$$K \propto \frac{\gamma D C_m}{RT} \tag{1}$$

where γ = interfacial free energy; D = diffusivity of the rate-controlling solute atoms, C_m = solubility limit of the rate-controlling solute atoms; and RT has its usual meaning. K value for Mo–containing dispersoids (MG3R3M alloy) at 300 °C is in the order of ~10^{-33} mol.s^{-1}, which is almost negligible compared to the K value for Cu-bearing precipitates at this temperature, ~10^{-22} mol.s^{-1}. Parameters used to estimate the K values are given in Table 5.2.

Table 5.2 Parameters used to estimate the K value at 300 °C [10, 53], C_m values were calculated using FactSage software.

Phase	γ (mJ.m^{-2})	D_o (m^2.s^{-1})	Q (kJ.mol^{-1})	C_m (wt.%)	K (mol.s^{-1})
Ageing precipitates (Cu-containing)	~200	6.54×10^{-5}	136	0.42	$\sim 10^{-22}$
Dispersoids (Mo-containing)	~500	1.4×10^{-3}	250	1.81E-3	$\sim 10^{-33}$

5.3.4 Tensile creep fracture mechanism at 300 °C and the effect of dispersoids

The SEM investigations of the alloys after tensile creep testing at 300 °C and 30 MPa reveals that both alloys fail in a ductile interdendritic mode. Fig. 5.12a shows that voids, indicated by arrows, form at the Si particles in the interdendritic regions of the MG3R alloy, after 30 min of tensile creep testing at 300 °C and 30 MPa. By contrast, the void formation was significantly delayed in the MG3R3M alloy and no void was observed with SEM analysis even after 10 hours of tensile creep (Fig. 5.12b). TEM investigation was conducted to elucidate the differences between two alloys. It is seen that in the MG3R alloy (Fig. 5.13), pile-up of dislocations occurred at large Si particles in the interdendritic regions, which results in a local stress build-up as the material creeps further [49, 50]. On reaching a critical value, these stresses can lead to the particle cracking or decohesion at the particle/matrix interface, thereby resulting in the void formation. The delayed void formation in the MG3R3M alloy can be attributed to the presence of the fine dispersoids that effectively pin the dislocations (Fig. 5.11b). Dislocations, if not properly pinned in the dendrite interiors (i.e. the MG3R alloy, Fig. 5.11a), can readily reach the interdendritic regions and pile up at Si or intermetallic particles that are located in the interdendritic boundaries.

By comparing these two alloys, MG3R3M with fine dispersoids and MG3R, it is evident that the void formation is controlled by dislocation creep. Voids nucleated grow in tension as the material creeps further. It was seen (Fig. 5.14a), however, that after certain amount of creep strain, deformation localizes between primary large pores (present in the solidification structure) that are located close to the maximum shear direction (at ~ 45° to the load axis). The flow localization bands between pores, arrowed in Fig. 5.14a, can be clearly seen on the gauge length surface of the creep specimens. The localization of the creep strain changes the void growth rate; voids located on the bands grow faster in shear and tension (void growth in shear and tension is been explained in [51]) as creep rate is higher in these regions. Because of the high stress sensitivity of the creep rate (measured by apparent stress exponent, n_a, which is usually high (4.4-40) in dispersion strengthened Al alloys) and small work hardening during creep, inhomogeneous void growth tends to be stabilized till the voids on the flow localization path, coalesce and give the fracture path.

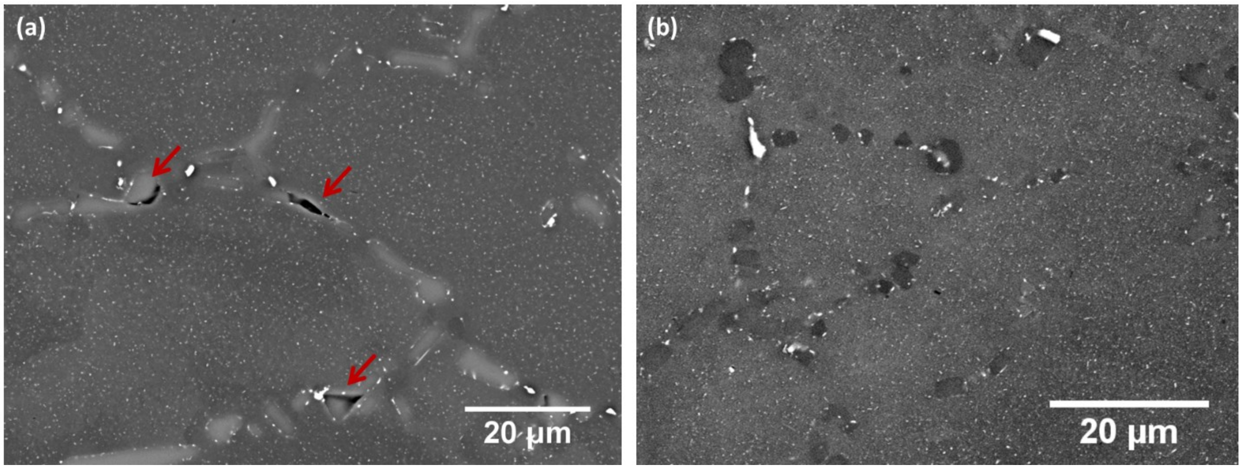

Fig. 5.12 SEM mixed images (SE + BSE) showing the microstructure of the alloys after tensile creep testing at 300 ºC and 30 MPa (a) MG3R after 30 min, and (b) MG3R3M after 10 h. Cavitation can be seen in the interdendritic regions of the MG3R alloy at the Si/matrix, while no cavity is seen in the microstructure of the MG3R3M alloy.

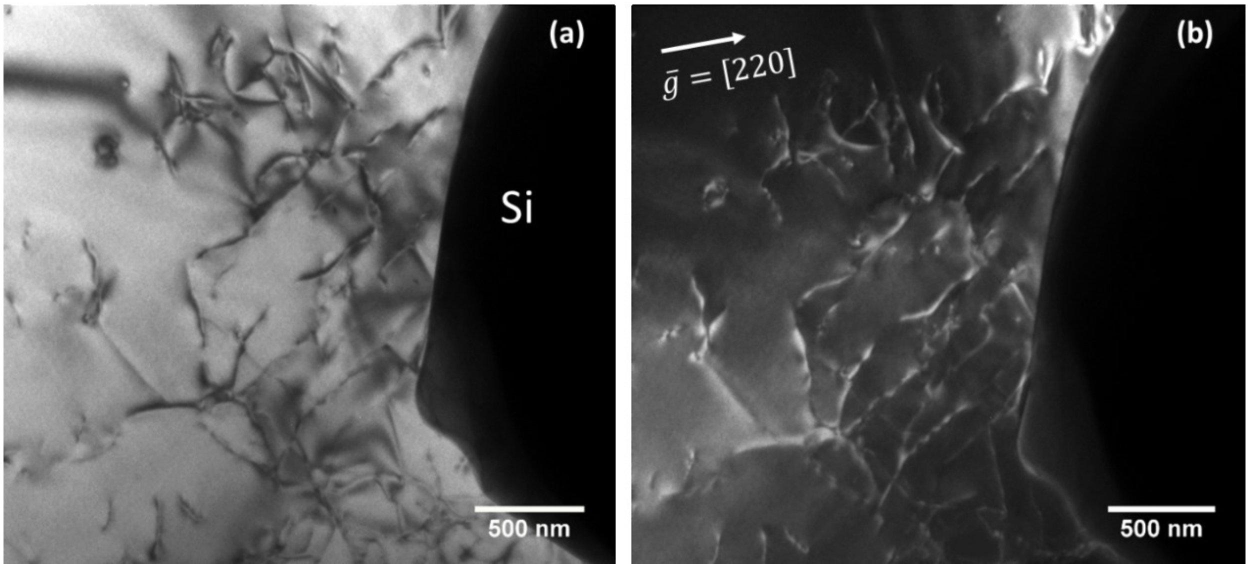

Fig. 5.13 (a) Bright field TEM and (b) dark field TEM micrographs of the interdendritic regions of the MG3R alloy at the early stage of creep deformation at 300 ºC and 30 MPa, showing dislocation pile-up at the Si/matrix interface.

On the basis of the foregoing discussion, the fracture process can be assumed to occur in three distinct stages: i) void nucleation and growth, ii) flow localization between primary larger pores and accelerated void growth and iii) void coalescence along the flow localization path. It is evident that, by postponing the void formation (stage i), the dispersoid strengthening by Mo addition can significantly delay the time-to-fracture. Figs. 5.14b-c show the fracture surface of the MG3R alloy. Dimples, typical of ductile fracture and cavitation process, can be seen on the surface (Fig. 5.14c); Si particle are often observed at the bottom of the dimples. Similar features are also seen on the fracture surface of the MG3R3M alloy (Fig. 5.14d).

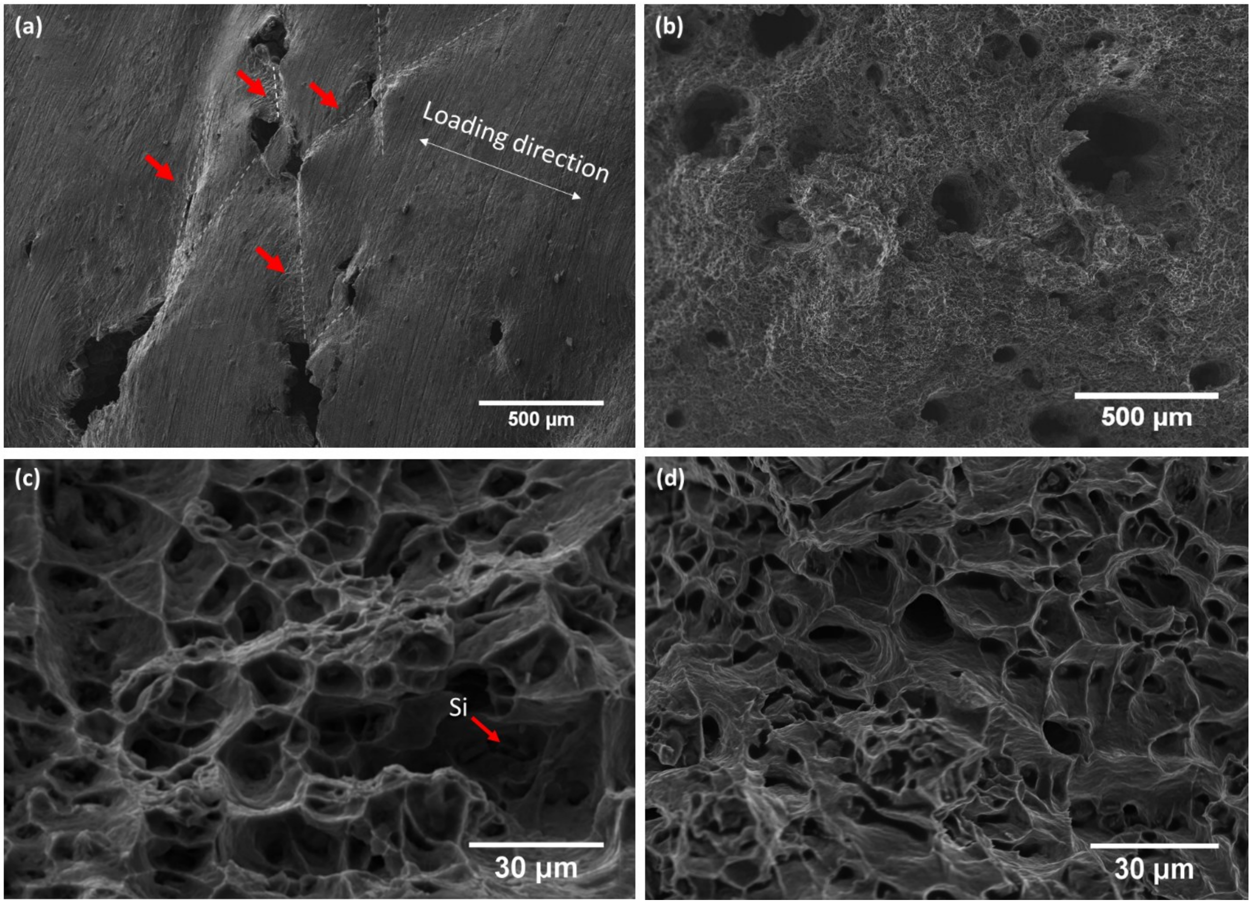

Fig. 5.14 The MG3R alloy (a) to (c), tensile creep tested to fracture at 300 °C and 30 MPa: (a) gage length surface showing the flow localization between pores (b) fracture surface, showing the pores and shear dimples, characteristic of ductile fracture (c) fracture surface at higher magnifications, showing the dimples with Si particle at the bottom of the dimples, and (d) fracture surface of the MG3R3M alloy, tensile creep tested to fracture at 300 °C and 30 MPa, showing similar dimple structure.

5.3.5 Tensile properties at 300 °C

The tensile properties of the MG3R and MG3R3M alloys at 300 °C are presented in Fig. 5.15. The yield strength (YS), ultimate tensile strength (UTS) and elongation (El) of the MG3R3M alloy are increased by approximately 25, 15 and 35% respectively, compared to the MG3R alloy. The improvement in the strength at this temperature is attributed to the presence of the thermally stable

Al-(Fe,Mo)-Si dispersoids in the Al matrix. These nano-scale dispersoids are effective in Orowan strengthening at high temperature. As mentioned above, at 300 °C only the coarse Q-$Al_5Cu_2Mg_8Si_6$ precipitates remain in the Al matrix and the contribution of such precipitates to the strength was weak. The presence of a substantial amount of thermally stable Al-(Fe,Mo)-Si dispersoids played a dominant role in the high temperature strength. The increase in ductility is one of the benefits of the Mo addition because of the elimination of the brittle β-Al_5FeSi platelets. In Al-Si casting alloys, the β-Al_5FeSi platelets formed during solidification act as crack nucleation sites that lower the ductility of these alloys even at elevated temperatures [52]. The replacement of the brittle β-Al_5FeSi platelets (often associated with pores) by bulky Al-(Fe,Mo)-Si intermetallics, as a result of Mo addition, certainly improves the elongation.

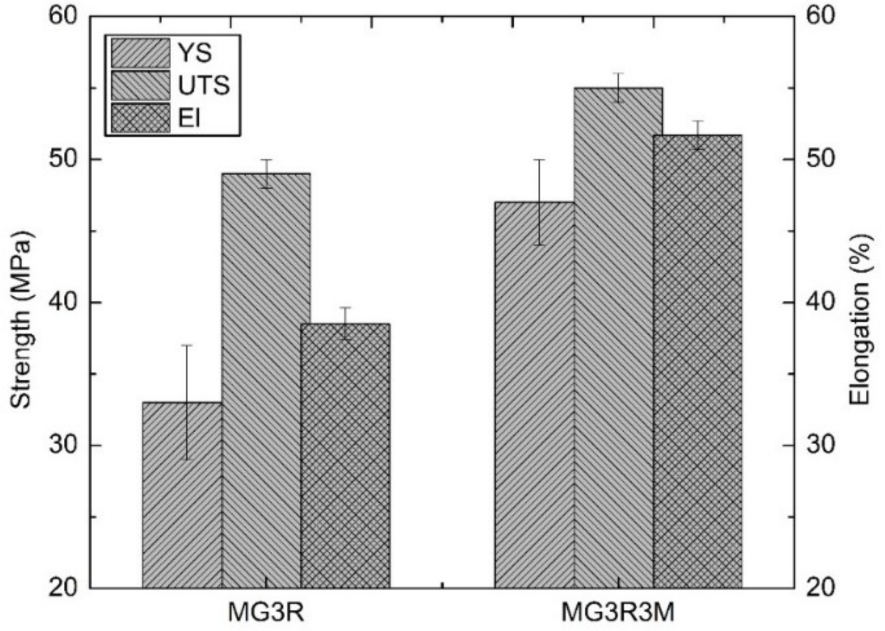

Fig. 5.15 Tensile properties of the alloys at 300 °C. Solution treated at 540 °C for 10 h, aged at 200 °C for 5 hours and soaked at 300 °C for 100 hours.

The present study demonstrated that a low level Mo addition to the Al-Si-Cu-Mg alloys can significantly increase the creep resistance and mechanical properties at elevated temperature, which can promote the wide use of the Al casting alloys in more severe operating conditions such as the Diesel engine application. The precipitation of the Al-(Fe,Mo)-Si dispersoids via Mo addition can be expected to occur in other aluminum alloy systems, which can potentially lead to the enhanced the elevated temperature strength, creep and recrystallization resistance without impairing the ductility.

5.4 Conclusions

The effect of Mo addition at a low level (0.3%) on the microstructure and elevated temperature mechanical properties of an Al-7Si-0.5Cu-0.3Mg alloy has been described in this study. The following conclusions can be drawn:

1. With Mo addition, a substantial amount of nano-scale Al-(Fe,Mo)-Si dispersoids precipitated during solution treatment in the Al-7Si-0.5Cu-0.3Mg alloy, which were thermally stable after sustained exposure to elevated temperature and retained their strengthening effect.
2. The Mo-containing alloy exhibited significant improvement in the creep properties at 300 °C and 30 MPa; the minimum creep rate decreased ~ 95% and the creep time-to-fracture increased from 50 min to 1500 min compared to the base alloy.
3. YS, UTS and El at 300 °C of the Mo-containing alloy were increased by ~ 25, 15 and 35% respectively, compared to the base alloy.
4. TEM investigations revealed that the Al-(Fe,Mo)-Si dispersoids effectively hindered the dislocation motions, leading to a significant increase in the elevated temperature strength and creep resistance.
5. SEM analysis of the alloys after creep testing at 300 °C and 30 MPa revealed that both alloys fracture in a ductile manner, exhibiting three stages: i) void nucleation and growth, ii) flow localization between primary larger pores and accelerated void growth and iii) void coalescence along the flow localization path.
6. The Al-(Fe,Mo)-Si dispersoids, by effectively pinning the dislocations in the dendrite grain interiors, delay the void nucleation and growth and increase the creep time-to-failure during tensile creep process.
7. Mo addition suppressed the formation of the brittle β-Al_5FeSi intermetallic phase and promoted the formation of a blocky Al-(Fe,Mo)-Si intermetallic phase in the cast microstructure, thereby improving the tensile elongation at 300 °C by 34%.

5.5 Acknowledgment

This work was supported by the NSERC (Natural Sciences and Engineering Research Council of Canada) strategic project grant with Rio Tinto Alcan (RTA). The authors thank Pierre Vermette (McGill University) and Martin Bouchard (University of Québec at Chicoutimi) for their assistance in experimental work. Amir Rezaei Farkoosh would like to gratefully acknowledge the financial support of McGill University through MEDA (McGill Engineering Doctoral Award) program and research support through the NSERC/Rio Tinto Alcan Research Chair at University of Québec at Chicoutimi.

5.6 References

[1] M. Garat, G. Laslaz, Improved Aluminum Alloys for Common Rail Diesel Cylinder Heads, in: AFS, IL, USA, 2007, pp. 1-8.
[2] F.R.N. Nabarro, Creep in commercially pure metals, Acta Mater., 54 (2006) 263-295.
[3] F.R.N. Nabarro, F. De Villiers, Physics of creep and creep-resistant alloys, CRC press, 1995.
[4] A.R. Farkoosh, M. Javidani, M. Hoseini, D. Larouche, M. Pekguleryuz, Phase formation in as-solidified and heat-treated Al–Si–Cu–Mg–Ni alloys: Thermodynamic assessment and experimental investigation for alloy design, J. Alloys Compd., 551 (2013) 596-606.
[5] A.R. Farkoosh, M. Pekguleryuz, The effects of manganese on the T-phase and creep resistance in Al–Si–Cu–Mg–Ni alloys, Mater. Sci. Eng., A, 582 (2013) 248-256.
[6] M. Javidani, D. Larouche, Application of cast Al–Si alloys in internal combustion engine components, Int. Mater. Rev., 59 (2014) 132-158.
[7] S.P. Ringer, K.S. Prasad, G.C. Quan, Internal co-precipitation in aged Al–1.7Cu–0.3Mg–0.1Ge (at.%) alloy, Acta Mater., 56 (2008) 1933-1941.
[8] D.H. Xiao, J.N. Wang, D.Y. Ding, H.L. Yang, Effect of rare earth Ce addition on the microstructure and mechanical properties of an Al–Cu–Mg–Ag alloy, J. Alloys Compd., 352 (2003) 84-88.
[9] G. Wang, Q. Sun, L. Shan, Z. Zhao, L. Yan, Influence of Indium Trace Addition on the Precipitation Behavior in a 357 Cast Aluminum Alloy, J. Mater. Eng. Perform., 16 (2007) 752-756.

[10] K.E. Knipling, D.C. Dunand, D.N. Seidman, Criteria for developing castable, creep-resistant aluminum-based alloys-A review, Zeitschrift fur Metallkunde, 97 (2006) 246.

[11] K.E. Knipling, Development of a nanoscale precipitation-strengthened creep-resistant aluminum alloy containing trialuminide precipitates, PhD Thesis, Northwestern University, Ann Arbor, 2006.

[12] L.F. Mondolfo, Aluminum alloys : structure and properties, Butterworths, London; Boston, 1976.

[13] N.Q. Vo, D.C. Dunand, D.N. Seidman, Improving aging and creep resistance in a dilute Al–Sc alloy by microalloying with Si, Zr and Er, Acta Mater., 63 (2014) 73-85.

[14] E.A. Marquis, D.N. Seidman, Nanoscale structural evolution of Al3Sc precipitates in Al(Sc) alloys, Acta Mater., 49 (2001) 1909-1919.

[15] M.J. Jones, F.J. Humphreys, Interaction of recrystallization and precipitation: The effect of Al3Sc on the recrystallization behaviour of deformed aluminium, Acta Mater., 51 (2003) 2149-2159.

[16] S. Iwamura, Y. Miura, Loss in coherency and coarsening behavior of Al3Sc precipitates, Acta Mater., 52 (2004) 591-600.

[17] M.E. Krug, D.N. Seidman, D.C. Dunand, Creep properties and precipitate evolution in Al–Li alloys microalloyed with Sc and Yb, Mater. Sci. Eng., A, 550 (2012) 300-311.

[18] K.E. Knipling, R.A. Karnesky, C.P. Lee, D.C. Dunand, D.N. Seidman, Precipitation evolution in Al–0.1Sc, Al–0.1Zr and Al–0.1Sc–0.1Zr (at.%) alloys during isochronal aging, Acta Mater., 58 (2010) 5184-5195.

[19] K.E. Knipling, D.C. Dunand, D.N. Seidman, Precipitation evolution in Al–Zr and Al–Zr–Ti alloys during aging at 450–600 °C, Acta Mater., 56 (2008) 1182-1195.

[20] K.E. Knipling, D.C. Dunand, D.N. Seidman, Precipitation evolution in Al–Zr and Al–Zr–Ti alloys during isothermal aging at 375–425 °C, Acta Mater., 56 (2008) 114-127.

[21] J.D. Robson, P.B. Prangnell, Modelling Al3Zr dispersoid precipitation in multicomponent aluminium alloys, Mater. Sci. Eng., A, 352 (2003) 240-250.

[22] T. Gao, D. Li, Z. Wei, X. Liu, Evolution, microhardness of ZrAlSi intermetallic and its impact on the elevated-temperature properties in Al–Si alloys, Mater. Sci. Eng., A, 552 (2012) 523-529.

[23] L. Lodgaard, N. Ryum, Precipitation of chromium containing dispersoids in Al–Mg–Si alloys, Mater. Sci. Technol., 16 (2000) 599-604.

[24] A.M.F. Muggerud, Y. Li, R. Holmestad, Composition and orientation relationships of constituent particles in 3xxx aluminum alloys, Philosophical Magazine, 94 (2013) 556-568.

[25] Y.J. Li, L. Arnberg, Quantitative study on the precipitation behavior of dispersoids in DC-cast AA3003 alloy during heating and homogenization, Acta Mater., 51 (2003) 3415-3428.

[26] Y.J. Li, A.M.F. Muggerud, A. Olsen, T. Furu, Precipitation of partially coherent α-Al(Mn,Fe)Si dispersoids and their strengthening effect in AA 3003 alloy, Acta Mater., 60 (2012) 1004-1014.

[27] L. Lodgaard, N. Ryum, Precipitation of dispersoids containing Mn and/or Cr in Al–Mg–Si alloys, Mater. Sci. Eng., A, 283 (2000) 144-152.

[28] K. Matsuda, S. Taniguchi, K. Kido, Y. Uetani, S. Ikeno, Effects of Cu and transition metals on the precipitation behaviors of metastable phases at 523 K in Al-Mg-Si alloys, Materials Transactions-JIM, 43 (2002) 2789-2795.

[29] J.A. Walsh, K.V. Jata, E.A. Starke Jr, The influence of Mn dispersoid content and stress state on ductile fracture of 2134 type Al alloys, Acta Metall., 37 (1989) 2861-2871.

[30] P. Ratchev, B. Verlinden, P. Van Houtte, Effect of preheat temperature on the orientation relationship of (Mn,Fe)Al6 precipitates in an AA 5182 Aluminium—Magnesium alloy, Acta Metall. Mater., 43 (1995) 621-629.

[31] S.P. Chen, N.C.W. Kuijpers, S. van der Zwaag, Effect of microsegregation and dislocations on the nucleation kinetics of precipitation in aluminium alloy AA3003, Mater. Sci. Eng., A, 341 (2003) 296-306.

[32] R.A. Jeniski Jr, Effects of Cr addition on the microstructure and mechanical behavior of 6061-T6 continuously cast and rolled redraw rod, Mater. Sci. Eng., A, 237 (1997) 52-64.

[33] H.Y. Kim, S.W. Han, H.M. Lee, The influence of Mn and Cr on the tensile properties of A356–0.20Fe alloy, Mater. Lett., 60 (2006) 1880-1883.

[34] O. Engler, Z. Liu, K. Kuhnke, Impact of homogenization on particles in the Al–Mg–Mn alloy AA 5454 – Experiment and simulation, J. Alloys Compd., 560 (2013) 111-122.

[35] G. Timelli, A. Fabrizi, S. Capuzzi, F. Bonollo, S. Ferraro, The role of Cr additions and Fe-rich compounds on microstructural features and impact toughness of AlSi9Cu3(Fe) diecasting alloys, Mater. Sci. Eng., A, 603 (2014) 58-68.

[36] N. van Chi, D. Bergner, Diffusion of Mo and W in Al, in: F.J. Kedves, D.L. Beke (Eds.) DIMETA-82: Diffusion in Metals and Alloys, Trans Tech Publications, Switzerland, 1983, pp. 334-337.

[37] P. Li, H. Yu, S. Chai, Y. Li, Microstructure and properties of rapidly solidified powder metallurgy Al–Fe–Mo–Si alloys, Scripta Mater., 49 (2003) 819-824.

[38] D. Shenglong, L. Dabo, W. Tianzhen, L. Chunyu, Damping behaviour and mechanical properties of rapidly solidified Al–Fe–Mo–Si/Al alloys, J Mater. Sci, 33 (1998) 2227-2231.

[39] F. Carreño, M. Torralba, M. Eddahbi, O.A. Ruano, Elevated temperature creep behavior of three rapidly solidified Al-Fe-Si materials containing Cr, Mn, or Mo, Mater. Sci. Eng., A, 230 (1997) 116-123.

[40] V.K. Vasudevan, H.L. Fraser, The microstructures of rapidly solidified and heat-treated Al-8Fe-2Mo-Si alloys, Mater. Sci. Eng., 98 (1988) 131-136.

[41] V. K. Vasudevan, H. L. Fraser, Identification of precipitates in rapidly solidified and heat-treated Al-8Fe-2Mo-Si alloys, Scripta Metall., 21 (1987) 1105-1110.

[42] M. Eumann, G. Sauthoff, M. Palm, Re-evaluation of phase equilibria in the Al-Mo system, Int. J. Mater. Res., 97 (2006) 1502-1511.

[43] B. Grushko, S.B. Mi, A study of the Al-rich region of the Al–Cu–Mo alloy system, J. Alloys Compd., 509 (2011) L30-L33.

[44] Z. Du, C. Guo, C. Li, W. Zhang, Thermodynamic Description of the Al-Mo and Al-Fe-Mo Systems, J. Phase. Equilib. Diffus., 30 (2009) 487-501.

[45] H. Okamoto, Al-Mo (Aluminum-Molybdenum), J. Phase. Equilib. Diffus., 31 (2010) 492-493.

[46] V. Raghavan, Al-Fe-Mo (Aluminum-Iron-Molybdenum), J. Phase. Equilib. Diffus., 30 (2009) 372-374.

[47] V. Raghavan, Al-Mo-Si (Aluminum-Molybdenum-Silicon), J. Phase. Equilib. Diffus., 33 (2012) 329-333.

[48] H. Calderon, P. Voorhees, J. Murray, G. Kostorz, Ostwald ripening in concentrated alloys, Acta Metall. Mater., 42 (1994) 991-1000.

[49] M.E. Kassner, 10 - Creep Fracture, in: Fundamentals of Creep in Metals and Alloys (Second edition), Elsevier, Amsterdam, 2008, pp. 221-246.

[50] M. Ashby, C. Gandhi, D. Taplin, Overview No. 3 Fracture-mechanism maps and their construction for fcc metals and alloys, Acta Metall., 27 (1979) 699-729.

[51] N.A. Fleck, J.W. Hutchinson, Void Growth in Shear, P Roy Soc Lond A Mat, 407 (1986) 435-458.

[52] C.M. Dinnis, J.A. Taylor, A.K. Dahle, As-cast morphology of iron-intermetallics in Al–Si foundry alloys, Scripta Mater., 53 (2005) 955-958.

[53] D.A. Porter, K.E. Easterling, Phase Transformations in Metals and Alloys, (Revised Reprint), CRC press, 1992.

CHAPTER 6

PRECIPITATION OF COHERENT ALPHA-AL(FE,MO)SI DISPERSOIDS IN AN AL-SI-CU-MG CAST ALLOY VIA MO ADDITION

The positive effect of Mo additions to the base alloy was evident in the initial phase of the study. The next phase of the work on Mo additions focused on an in-depth characterization of the Mo-containing dispersoids. This chapter presents the results of the study on the formation and evolution of nanoscale Mo-containing dispersoid phase during solution treatment of Al-7Si-0.5Cu-0.3Mg-0.3Mo; the study been conducted largely via TEM and HRTEM. The chemical composition, crystal structure, orientation relationship and coherency of the dispersoids have been determined. The structural correlation between the dispersoid phase and the Al matrix has been explained. This chapter has been submitted for peer-review: *A.R. Farkoosh, X.-G. Chen, M. Pekguleryuz, Precipitation of coherent α-Al(Fe,Mo)Si dispersoids in an Al-Si-Cu-Mg cast alloy via Mo addition, submitted to Journal of Alloys and Compounds, (2014).*

ABSTRACT

Molybdenum (Mo) addition at a low level (0.3 wt.%) forms a substantial amount of nanoscale α-Al(Fe,Mo)Si dispersoids in the intradendritic regions during the solution treatment of an Al-7Si-0.5Cu-0.3Mg cast alloy. In the present study, the crystal structure and coherency of these dispersoids were investigated by transmission electron microscopy (TEM) and high-resolution transmission electron microscopy (HRTEM). Quantitative EDS analysis showed that the dispersoids have the approximate stoichiometric formula of $Al_{22}(Fe_{6\text{-}8}Mo)Si_4$. Their crystal structure, determined by selected area electron diffraction (SAED) analysis, is body centered cubic (BCC) with lattice parameter of $a_0 = 12.54 \pm 0.03\ \mathring{A}$ and space group of Im3. A systematic SAED analysis revealed that a large number of the dispersoids have a strong orientation relationship with the Al matrix given as: $\langle 001\rangle_d // \langle 001\rangle_m$ and $\{350\}_d // \{002\}_m$. HRTEM investigations and crystal structure simulations showed that there is a coherency of the atomic planes at the interface between the dispersoids and the Al matrix, which is related to the structural correlation between these two phases.

Keywords: Aluminum alloys; Dispersion hardening; Interface structure; Orientation relationship; Mo addition

6.1 Introduction

Aluminum alloys are generally strengthened by precipitation (age) hardening at low temperatures. However, at elevated temperatures, age-hardening precipitates are prone to Ostwald ripening and loss of their strengthening effect, limiting the wide use of these alloys in high temperature applications (e.g. 300 ^oC of the Diesel engine operation). One important approach towards improving the high temperature performance of Al alloys is to introduce thermally stable fine dispersoids into the Al matrix [1-3]. Here, developing high temperature cast alloys faces several challenges in generating a large amount of effective dispersoids. In particular, there are thermodynamic limitations in creating large volume fractions of the dispersoids because of the low solid solubility of the dispersoid-forming solutes in the Al matrix, especially in the case of the Al-Si cast alloys [4]. Additionally, a lack of coherency at the dispersoid/matrix interface usually leads to a low strengthening efficiency. In order to achieve a highly desirable dispersoid/matrix coherency (each plane of the matrix have one corresponding plane from the dispersoid so that the two lattices are continuous across the interface), a similarity between the crystal structure of the dispersoid and the Al matrix must be present. This similarity increases the probability of having dispersoid/matrix interfaces with identical atomic configuration in both phases, which is required for the coherency of the interface [5, 6]. Crystal structure similarity can also facilitate nucleation of the dispersoids (increasing the number density) and increase coarsening resistance at elevated temperatures.

On the basis of their crystal structures, the dispersoids found in Al alloys can be categorized into two main groups of intermetallics: 1- trialuminides (Al_3M) with cubic $L1_2$ or tetragonal $D0_{22}$ and $D0_{23}$ structures (e.g. Al_3Sc, Al_3Zr, Al_3Hf and Al_3Er) and 2- quasicrystals or their approximants (e.g. AlMnSi and AlCrSi). Trialuminides are known to be coherent dispersoids, because of possessing crystal structures similar to Al [7-10]. Quasicrystals and their approximants, on the other hand, are generally believed to form incoherent precipitates/dispersoid with low strengthening efficiency [11]. These dispersoids are commonly formed through addition of alloying elements such as Cr and Mn [12, 13]. Single addition of Cr forms a face centered cubic (FCC) α-AlCrSi dispersoid phase ($a_0 = 10.9$ A°); these dispersoids have an incoherent or semicoherent interface with the Al matrix, and the strengthening efficiency is low [11]. Mn addition, single or in combination with Cr, forms Mn- and/or Cr-containing dispersoids referred to as α-Al(Mn,Cr,Fe)Si intermetallics [13, 14]. The crystal structure of this phase is simple cubic (SC) or body centred cubic (BCC) depending on the chemical composition (Mn:Fe ratio [15] and the presence of trace elements such as B [16]) and has a large lattice parameter, a_0 in the range of 12.5–12.7 A°. Recently, Li et al. [17] have shown that in an Al-Mn-Si-Fe system, it is possible to achieve significant dispersoid strengthening by precipitation of partially coherent α-Al(Mn,Fe)Si approximant phase. A one dimensional (1-D) coherency between the $(23\bar{5})$ planes of the dispersoids and the $\{020\}$ planes of the matrix was reported.

The authors have been studying the behaviour of Mo in Al-Si cast alloys for the purpose of improving the creep resistance and mechanical properties of these alloys at elevated temperatures [4]. It is found that Mo addition at a low level (0.3 wt.%) can form a large amount of metallurgically stable Al-(Fe,Mo)-Si dispersoids in the intradendritic regions. We have determined experimentally that these fine quaternary dispersoids significantly improve the creep resistance and the tensile strength at 300 °C [4]. Through the effective interaction of the dispersoids with dislocations, the minimum creep rate of the Al-7Si-0.5Cu-0.3Mg-0.3Mo alloy at 300 °C, 30 MPa decreased by 90-95% compared to the base alloy (Al-7Si-0.5Cu-0.3Mg). However, the exact nature of the Mo-containing dispersoids is unknown. The previous use of Mo in Al alloys was limited mostly to the rapidly solidified (RS) powder metallurgy alloys [18-20]. Li et al. [20] have reported the presence of Mo-containing dispersoids in a RS Al-Fe-Mo-Si alloy, which form directly from the liquid phase during rapid solidification. These have been identified as α-AlFeSi phase assuming that Mo atoms substitutes for Fe atoms ($Al_{12}(Fe,Mo)Si_3$) in the crystal structure. Vasudevan et al. [18] also have identified similar dispersoids having a BCC structure with a lattice parameter of $a_0 = 12.63 \pm 0.03$ A° and space group Im3 in a RS Al-8Fe-2Mo-Si alloy [18].

This paper reports on the crystal structure of the Al(Fe,Mo)Si dispersoids formed in the Al-7Si-0.5Cu-0.3Mg-0.3Mo alloy during high temperature solution treatment and the structural similarity between this complex quasicrystal approximant phase and Al. The orientation relationship and interfacial structures are studied. The possibility of having coherent interfaces between the dispersoids and Al matrix has been discussed.

6.2 Experimental procedures

The Al7Si0.5Cu0.3Mg0.3Mo (MG3R3M) was synthesized in a high frequency NORAX Canada induction furnace using the commercial grade A356 alloy supplied by Rio Tinto Alcan Inc., Al-20 wt.% Mo and Al-33 wt.% Cu master alloys. During melting, the alloy was modified by the addition of 150 ppm Sr using Al-10 wt.% Sr master alloy. Degassing was carried out at 720 °C using high purity argon gas prior to pouring. Cylindrical bars of 30 mm diameter were cast in a pre-heated (400 °C) permanent mold at 730 °C. The chemical composition of the alloy was determined by inductively coupled plasma (ICP) technique, and presented in Table 6.1. Hereafter, all compositions in this paper are given in wt.%. The solution treatment comprised two stages to avoid probable incipient melting; 4 hours of holding at 500 °C followed by 1-10 hours at 540 °C. The samples were immediately quenched in water at room temperature.

Specimens for microstructural characterization were cut using a low speed diamond saw, ground with a series of SiC papers and polished on a porous neoprene polishing cloth with Al_2O_3

solution. Final polishing was performed with a Buehler vibratory polisher using a colloidal silica solution. For transmission electron microscopy (TEM) studies, thin foils were prepared by mechanical grinding and jet polished using a Struers Tenupol 5 jet polisher. A solution of 10% Nitric acid in methanol was used at -40 ^{o}C. Ar ion milling at a very low angle was performed on the polished samples in a Gatan Precision Ion Polishing System (PIPS) to remove the oxide layer. Conventional TEM investigations and corresponding selected area electron diffraction pattern (SAED) analysis were performed with a Philips CM200 microscope operated at 200 kV. The EDS spectra were obtained by EDAX detector connected to the column. High-resolution TEM (HRTEM) imaging was performed on a field emission microscope, the FEI TecnaiG2 F20, operating at 200 kV. To enhance the image contrast, Fourier mask filtering was performed using DigitalMicrograph^{TM} software; Fourier transform was applied to the image acquired and then by filtering the fast Fourier transform (FFT) pattern with a mask and reversing the processing (inverse-FFT), final image is obtained with enhanced contrast. Dispersoid diameter and particle size distribution (PSD) were determined by image analysis of the TEM micrographs. Dispersoids (a minimum of 100 measurements per sample) were manually traced and the dimensions were determined using ImageJ software. The diameter of an area-equivalent circle was reported as dispersoid size. Jmol program was used for the 3D visualization of the crystal structures.

Table 6.1 Chemical compositions of the alloy

Alloy	Chemical Composition (wt.%)							
	Si	Mg	Fe	Ti	Cu	Mo	Sr	Al
MG3R3M	6.97	0.29	0.10	0.09	0.57	0.27	0.013	Balance

6.3 Results and discussion

6.3.1 Formation of the Mo-containing dispersoids during solution treatment

A two-stage solution treatment at 500 ^{o}C and 540 ^{o}C respectively, were used to form the dispersoids. The micro-hardness (Table 6.2) after 4 hours of solutionizing at 500 ^{o}C is the same as the as-cast value of 63 HV showing no significant precipitation at this temperature. At 540 ^{o}C, the microhardness increases to a peak value of 83 HV after 60 min of solutionizing. Fig. 6.1a shows that in this condition, a substantial amount of fine Mo-containing dispersoids appear in the intradendritic regions with an average equivalent diameter of ~ 20 nm. The formation of the dispersoids upon solutionizing of the as-cast alloy is due to the decomposition of the supersaturated solid solution of Mo in the Al matrix. Because of the peritectic nature of the Al-Mo system (solid-liquid partition coefficient, $k_0 > 1$), micro-segregation during non-equilibrium solidification leads to the Mo supersaturation of the dendrite centers. It is noted that some of the dispersoids are heterogeneously nucleated on dislocations. Figs. 6.1b-c show that the dispersoids coarsen with increasing solutionizing time and the average size increases to ~ 35 and 120 nm after 150 and 600 min, respectively, resulting in decrease in microhardness (Table 6.2).

Table 6.2 Vickers micro-hardness of the as-quenched alloy with different solution treatments

Vickers micro-hardness (HV)					
As-cast	240 min @ 500	20 min @ 540	60 min @ 540	150 min @ 540	600 min @ 540
65 ± 3	63 ± 5	65 ± 2	83 ± 1	81 ± 2	72 ± 3

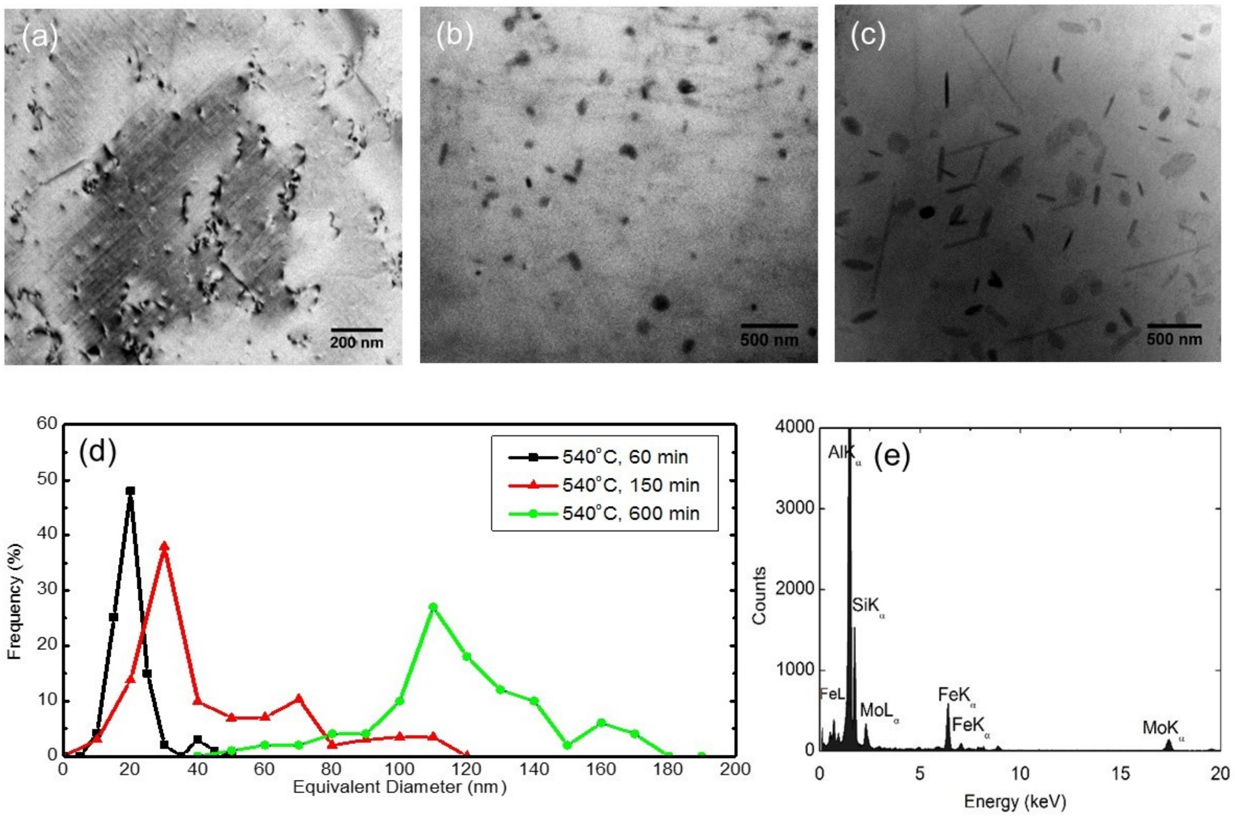

Fig. 6.1 Bright field TEM micrographs showing the evolution of precipitate size and morphology at 540 ºC after (a) 60, (b) 150 and (c) 600 minutes in intradendritic regions, along with (d) the particle size distribution of the dispersoids (histogram) and (e) EDS spectrum of the dispersoids.

The PSD is slightly bimodal after 60 min at 540 °C (Fig. 6.1d), but it broadens with increasing soaking time. This behavior can be attributed to the concurrent coarsening and partial dissolution of the dispersoids during high temperature heat treatment. Rapid pipe diffusion along the dislocation cores is another factor which can account for the bimodal PSD; the dispersoids located on the dislocations can grow faster because of the easy diffusion path between them [8]. The dispersoids with sizes less than 50 nm exhibit quasi-circular morphology, which develop into rhomboidal dispersoids as their size increases (Fig. 6.1c). The evolution of the morphology during coarsening is interesting; the quasi-circular (quasi-spherical) morphology indicates that the high misfit strain at the interface leads the dispersoid to surface-area minimization. As the interface energy relaxes during coarsening via the incorporation of the dislocations, the dispersoid assumes a rhomboidal shape surrounded likely with slow growing faces during its facetted growth. The interface structure will be discussed in details in section 5.3.5.

Quantitative TEM-EDS analysis yields the approximate stoichiometric formula of $Al_{22}(Fe_{6-8}Mo)Si_4$ for the dispersoids (Fig. 6.1e). It is noted that the Mo content in the dispersoids is much lower than the Fe content (Fe:Mo = 8, after 10 h at 540 °C), however, it increases slightly with increasing the solutionizing time (Fe:Mo = 6, after 24 h at 540 °C), indicating that more Mo atoms likely substitute for Fe atoms. This is slightly different from the stoichiometry ($Al_{12}(Fe,Mo)_3Si$) reported by Li et al. [20] in an RS Al-Fe-Mo-Si alloy; in their case the Mo dispersoids form directly from the liquid phase during rapid solidification (RS).

The results of the two-step solutionizing show that the formation of the dispersoids requires high temperatures, which is mainly due to the low diffusivity of Mo in Al (1.8×10^{-20} m^2s^{-1} at 500 °C, orders of magnitude lower than Fe and Si) [21]. However the diffusivity of Fe also plays a role; because of the low solid solubility of Fe in Al (0.04 wt.% max at the eutectic temperature, 654 °C in equilibrium conditions) [22], long-distance diffusion of Fe is required either from the adjacent matrix or large particles in the interdendritic regions to form the dispersoids. At 540 °C, close to the solidus, the diffusivity of Mo and Fe increases (1.2×10^{-19} m^2s^{-1} for Mo and 4.9×10^{-15} m^2s^{-1} for Fe at 540 °C) [21] and the dispersoid formation is enhanced.

6.3.2 Crystal structure of the dispersoids

Intradendritic dispersoids formed during the solution treatment (4 h at 500 °C and 10 h at 540 °C) were analyzed via SAED to determine their crystal structure. Fig. 6.2 shows the SAED patterns recorded along different zone axes of an individual dispersoid (Fig. 6.2a) within the [001]-[011]-[111] streographic triangle. Each pattern was indexed on the basis of a BCC lattice with reflections satisfying $h + k + l = 2n$. The lattice parameter was determined to be $a_0 = 12.54 \pm 0.03\ \mathring{A}$, which is similar to that of the BCC dispersoid identified by Vasudevan et al. [18, 19] in a rapidly solidified Al-8Fe-2Mo-Si alloy. From the symmetry elements observed in the diffraction patterns, the space group is deduced to be Im3. The dispersoid therefore is isomorphous with the α-AlFeSi intermetallic [23] with similar atomic arrangement (138 atoms per BCC unit cell: 100 Al, 14 Si and 24 Fe atoms and $\alpha_0 = 12.56\ A^{\circ}$). This phase is a structure with a Mackay icosahedron (MI) [24, 25] as a space-filling unit (Fig. 6.4a).

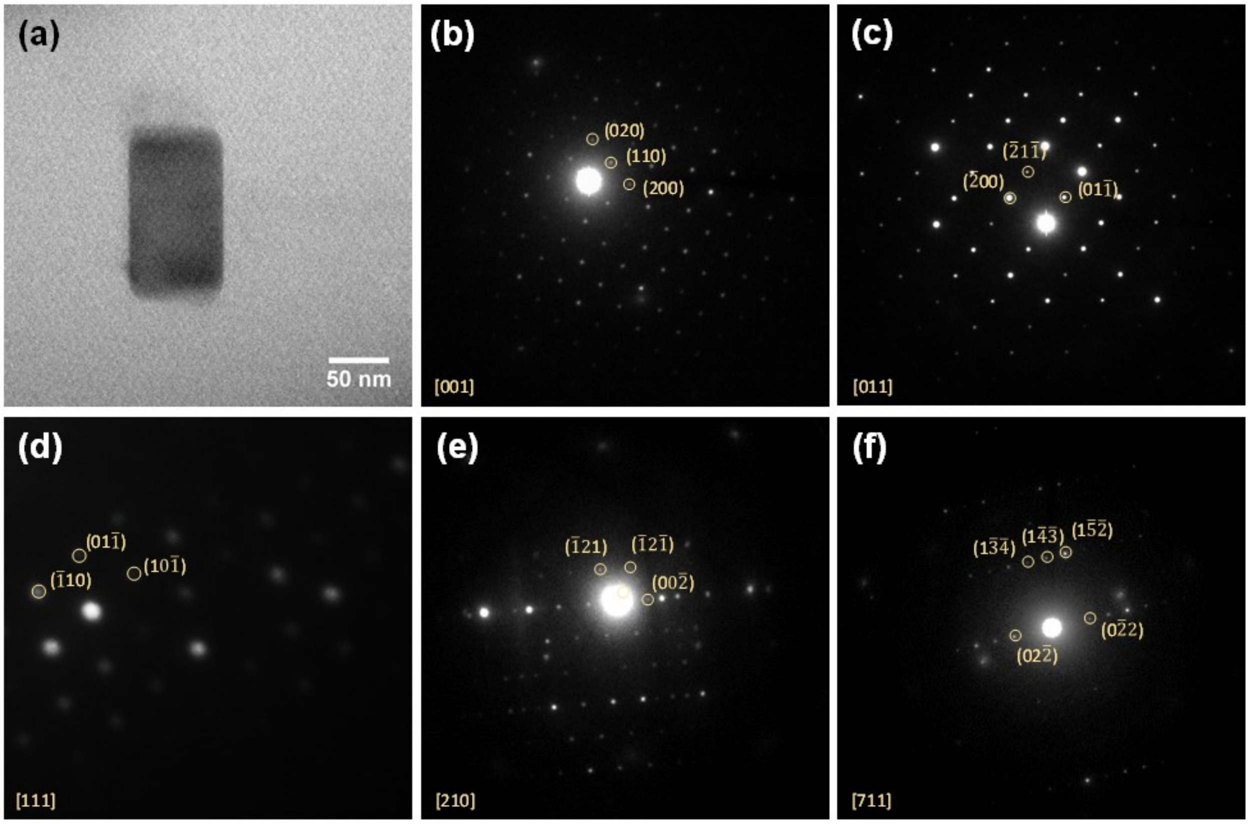

Fig. 6.2 (a) Bright field TEM image from an individual α-Al(Fe,Mo)Si dispersoids formed in intradendritic regions during solution treatment (4 h at 500 ºC and 10 h at 540 ºC) and the corresponding selected area electron diffraction patterns recorded along (b) [001], (c) [011], (d) [111], (e) [210] and (f) [711] zone axis within the [001]-[011]-[111] streographic triangle.

Fig. 6.3 (column 2) shows the experimental HRTEM lattice images of the individual dispersoids taken along the [110], $[1\bar{2}\bar{3}]$ and [203] zone axis as shown by the corresponding FFTs (column 1). The interplanar spacings measured using the HRTEM images are in close agreement with calculated interplanar spacings. However, from the experimental images it was not possible to comment on the position of the constituent atoms. Therefore, HRTEM image simulation was performed using the QSTEM multislice software [26]. The structural model proposed by Cooper [23] has been modified by substituting some of the Fe atoms with Mo atoms (to give the experimentally measured stoichiometry) and the experimentally determined lattice constant $\alpha_0 = 12.54\ A°$ was used.

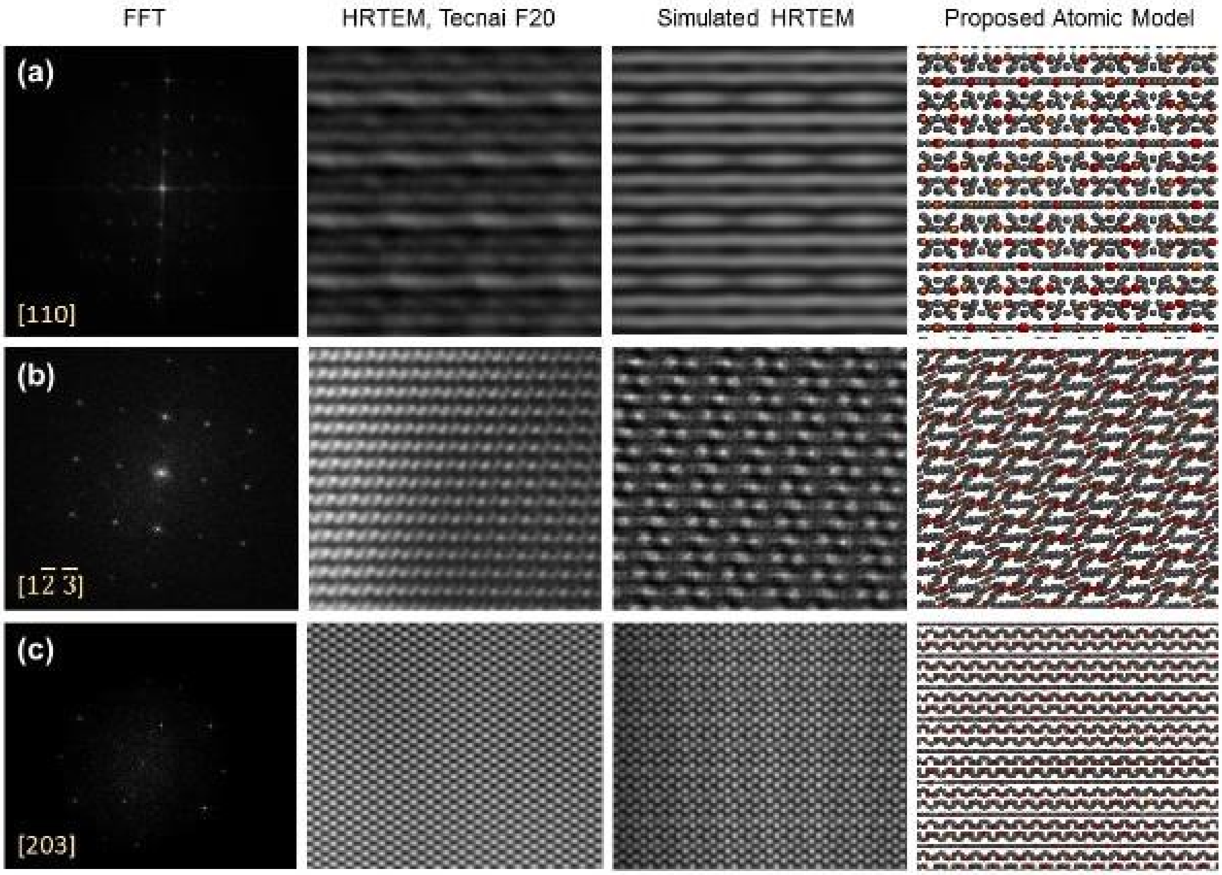

Fig. 6.3 Comparison between the experimental HRTEM images (second column from left) taken along (a) [110] (b) $[1\bar{2}\bar{3}]$ (c) [203] zone axes of the dispersoids (corresponding FFTs are shown in the first column) and the HRTEM computer simulations of the corresponding zone axes (third column). Projections of the proposed atomic model used to obtain the simulated images along the zone axis are presented in the fourth column. The simulation parameters: beam energy = 200 kV, C_S = 1.1 mm, C_C = 1 mm, vibration x = y = z = 2 pm, defocus = -59.5 nm, and thickness = 80 nm. The experimentally determined lattice constant $\alpha_0 = 12.54\ A°$ is used.

Three different atomic models were developed to determine the position of the Mo atoms within the crystal structure: in *Model I,* the Mo atoms were substituted for Fe atoms sitting on the second icosahedron (IC) layer of the MI cluster (Fig. 6.4a). In *Model II,* the Mo atoms were substituted for Fe atoms sitting on the third layer (glue atomic sites), and, in *Model III*, the Mo atoms were randomly substituted for Fe atoms within the unit cell. Simulation results revealed that the position of the Mo atoms did not have significant influence on the image simulation output (likely because of the low amounts of the Mo atoms within the crystal) therefore Model III was chosen. Atomistic simulations such as DFT [27] analyses may give more insight into the lattice position of the Mo atoms. Simulated HRTEM images are presented in Fig. 6.3 (column 3) along with the projections of the proposed model (column 4). It can be seen that the simulation results correspond closely with the images obtained experimentally, confirming that the model correctly represents the dispersoid structure.

6.3.3 Structural correlation between the BCC dispersoids and the FCC Al

Structural correlation between the dispersoid and the matrix is an important factor which governs the interface coherency and the nucleation of the precipitate in a solid matrix. If the structures are closely correlated, dispersoid/matrix coherency is more likely, the nucleation barrier is reduced and the precipitation is facilitated. We can analyze the correlation of the BCC dispersoids and the FCC aluminum with the aid of MI as a space-filling unit.

BCC α-Al(Fe,Mo)Si dispersoids

The MI depiction of the Mo-substituted BCC intermetallic is given in Fig. 6.4a. Jmol program [28] was used for the 3D visualization using the atomic coordinates given for the α-AlFeSi intermetallic by Cooper [23]. The inner shell of the MI possess 12 Al/Si atoms on the vertices of an icosahedron with 20 close-packed {111} faces. The center of the icosahedron is vacant. The second shell consist of 12 Fe/Mo atoms on the vertices of a larger icosahedron, and 30 Al/Si atoms have occupied the mid-edge sites. This assembly, comprised of a cluster of 54 (Al, Si, Fe and Mo) atoms is called MI icosahedron [29, 30]. MI clusters can fill the space with "glue" atoms in between them when packed in a BBC lattice. The orientation of the MI is such that its two-fold, three-fold and five-fold symmetry axes are parallel to the $\langle 001\rangle$, $\langle 111\rangle$ and $\langle 035\rangle$ directions of the BCC lattice, respectively, giving rise to the Im3 space group of the crystal. Kinematically simulated electron diffraction patterns of the α-phase along the [001], [111] and [530] zone axes (Fig. 6.5) confirm the two-fold, three-fold and pseudo-five-fold symmetry of the BCC crystal, respectively.

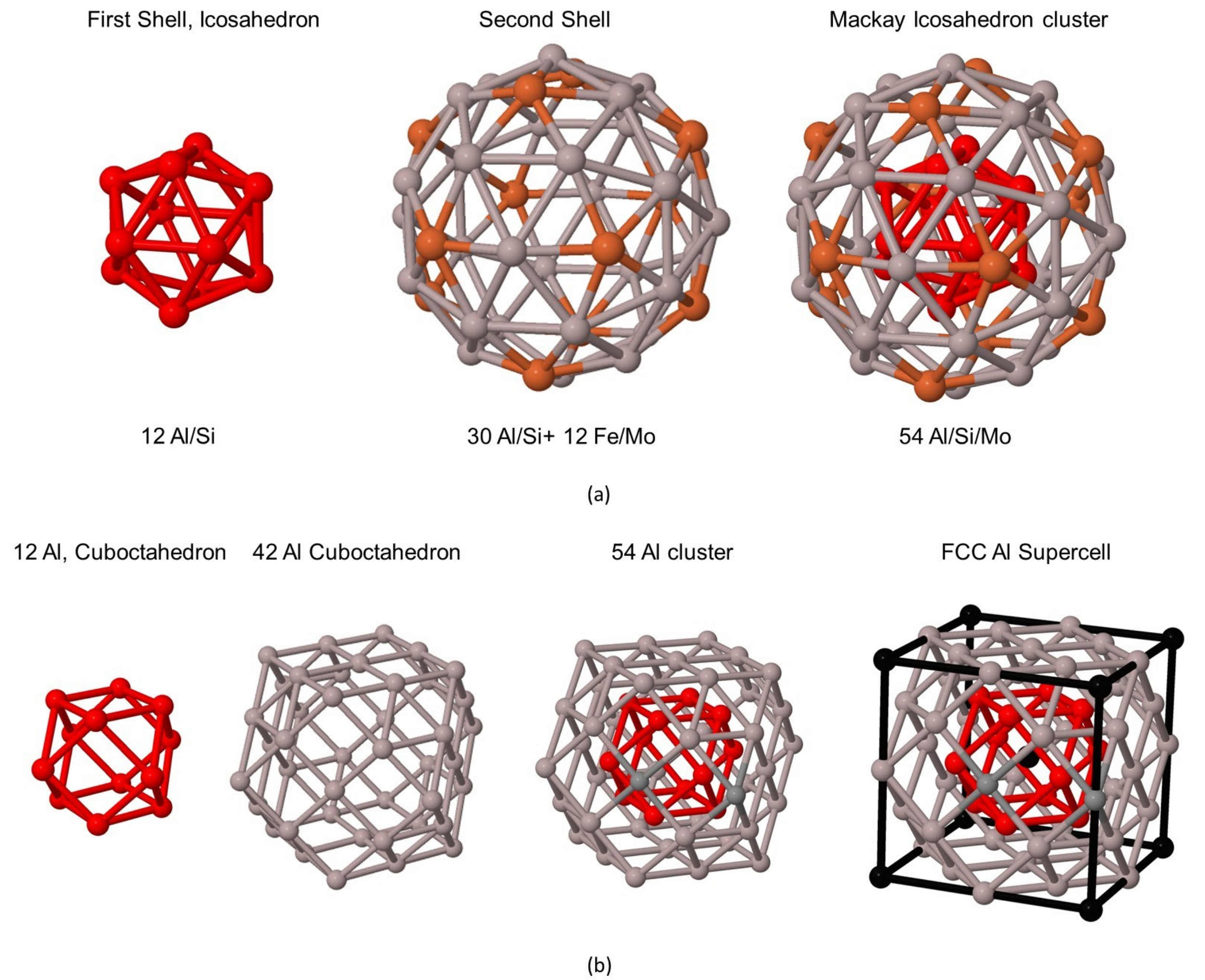

Fig. 6.4 (a) Mackay Icosahedron cluster as a space-filling unit of the 1-1 approximants of the Al-based icosahedral quasicrystals, red and gray being Al/Si and orange being Fe/Mo atoms. (b) 2×2×2 Al supercell. Al structure considered as different concentric cuboctahedral shells with 6 {001} and 8 {111} faces. Each of the cuboctahedrons can be easily distorted into an icosahedron.

FCC aluminum

Fig. 6.4b depicts the Al matrix as a 2×2×2 Al (FCC). By removing one atom from the center and 4 atoms from the vertices (the black atoms) a 54 cluster of atoms remains which consist of 2 concentric cuboctahedral shells. Both the inner (12 red atoms) and outer (42 gray atoms) shells have 6 {001} and 8 {111} faces. Each of the cuboctahedrons can be distorted into an icosahedron by a small uniform contraction of the vertices towards the center of the cuboctahedron. This splits the {001} faces into two equilateral {111} triangles. Therefore, when some of the Al atoms of the outer cuboctahedron are substituted by Mo and Fe atoms, with high valence-electron density, the cuboctahedral clusters can be easily transformed into the icosahedral clusters forming the dispersoids.

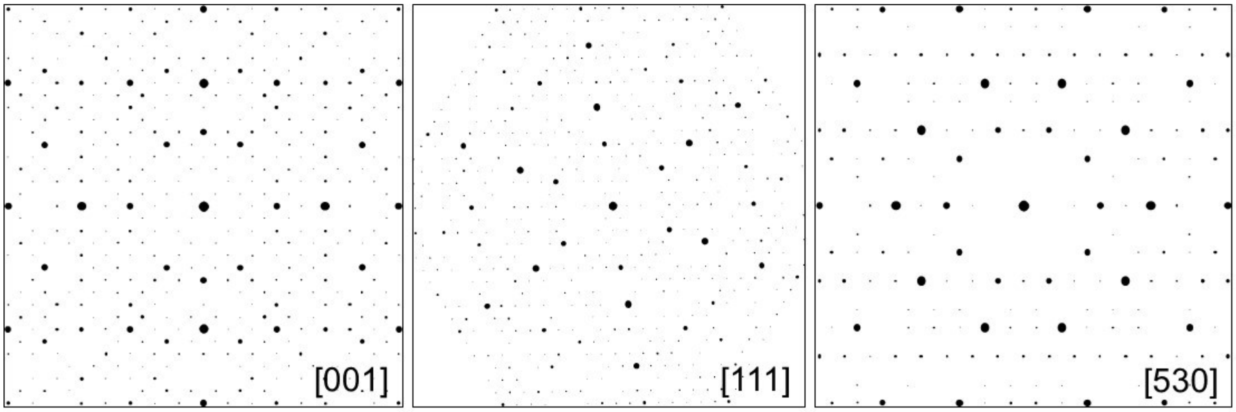

Fig. 6.5 Kinematically simulated electron diffraction patterns of the α-phase along the [001], [111] and [530] zone axes showing two-fold, three-fold and pseudo-five-fold symmetry, respectively. Model III was used.

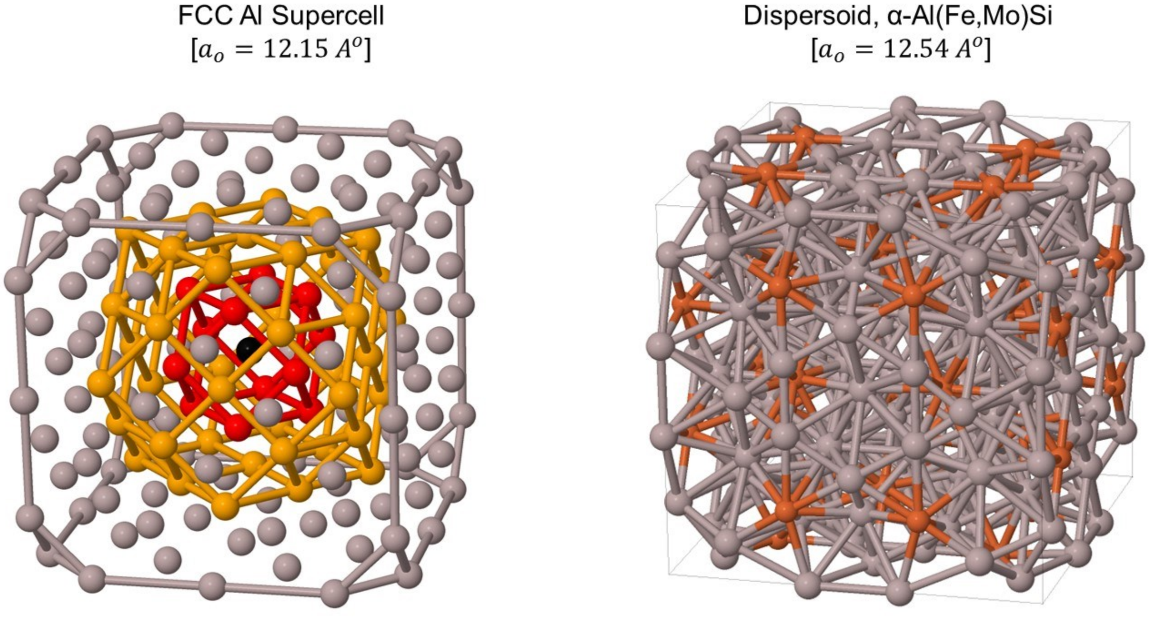

FCC Al Supercell
$[a_o = 12.15\ A^o]$

Dispersoid, α-Al(Fe,Mo)Si
$[a_o = 12.54\ A^o]$

Fig. 6.6 Comparison of a 3×3×3 Al (FCC) supercell (left) with the unit cell of the dispersoids (right).

Correlation of the BCC α-Al(Fe,Mo)Si dispersoids to the FCC Al Matrix

Fig. 6.6 compares a 3×3×3 Al (FCC) supercell with the unit cell of the dispersoids. A difference of ~ 3% has been noted between the lattice constants. Since the structures of the matrix and the dispersoids are similar, orientational epitaxy of the dispersoids is expected. This, along with the large lattice parameter and quasi-icosahedral symmetry of the dispersoid phase, makes it possible to have a large number of crystallographic planes matching the matrix planes. To verify this hypothesis and predict the possible orientation relationships, the interplanar spacings of the low index Al planes ({111}, {002}, {022} and {113}) have been compared with the calculated interplanar spacings of the closely matching (for misfit, $\varepsilon < 15\%$) planes of the dispersoids (Table 6.3). The misfit of the parallel planes was calculated using $\varepsilon = |d_m - d_d|/d_m$, where d_m and d_d are the interplanar spacings of the matrix and dispersoid, respectively. It can be seen from Table 6.3 that there are many different sets of well matching planes of the dispersoid and the matrix. However, the existence of these geometrically possible plane pairs depends on how these configurations lower the total energy of the system.

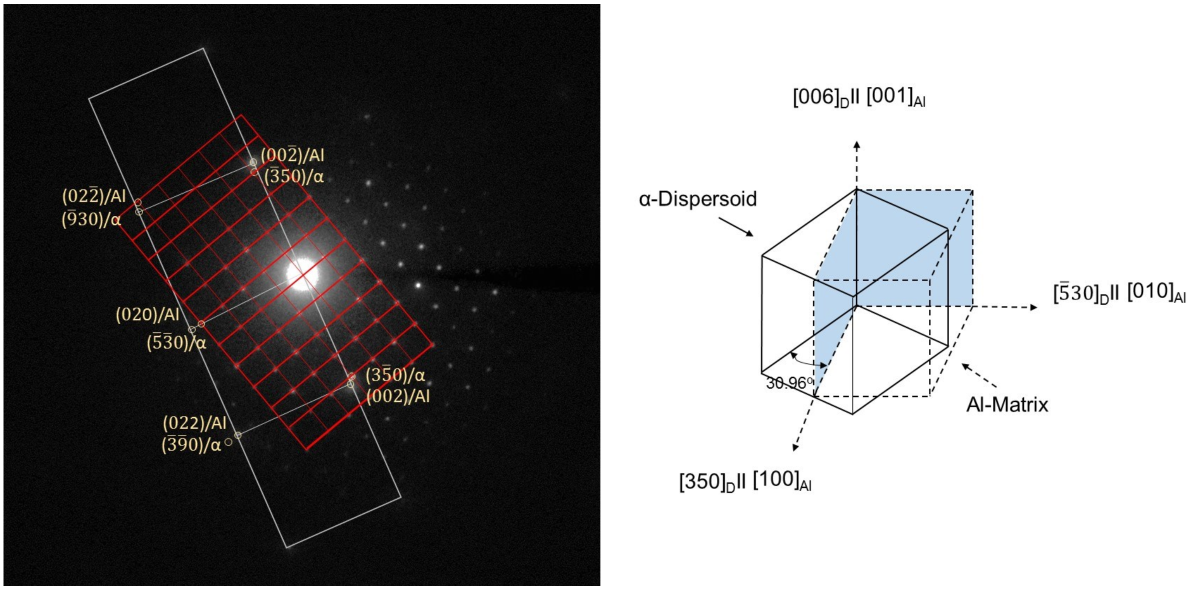

Fig. 6.7 Common orientation relationship between the dispersoids and the matrix $[100]_{d,}\,[100]_m$.

6.3.4 Orientation relationship between the dispersoid and the Al matrix

Fig. 6.7 shows a SAED taken with $B = [001]_d$ from a single dispersoid. It can be seen that the {350} and {390} planes of the dispersoid are nearly parallel to the {002} and {022} planes of the matrix, respectively. This is the most common orientation relationship that was observed, and can be given as:

$$\langle 001\rangle_d // \langle 001\rangle_m \tag{OR1}$$

$$\{350\}_d // \{002\}_m$$

The resulting orientation relationship and the misfit of the parallel planes are given in Table 6.4. Fig. 6.8a shows TEM micrograph of the dispersoids formed at 540 °C after 120 min. The centered dark field image on the $(\bar{3}50)$ reflection of a dispersoid following the OR1 is also given in Fig. 6.8b. The image contains the dispersoids that have the OR1 with the matrix. By comparing the two images of Fig. 6.8 (bright field with centered dark field), it can be seen that OR1 is the most frequent OR.

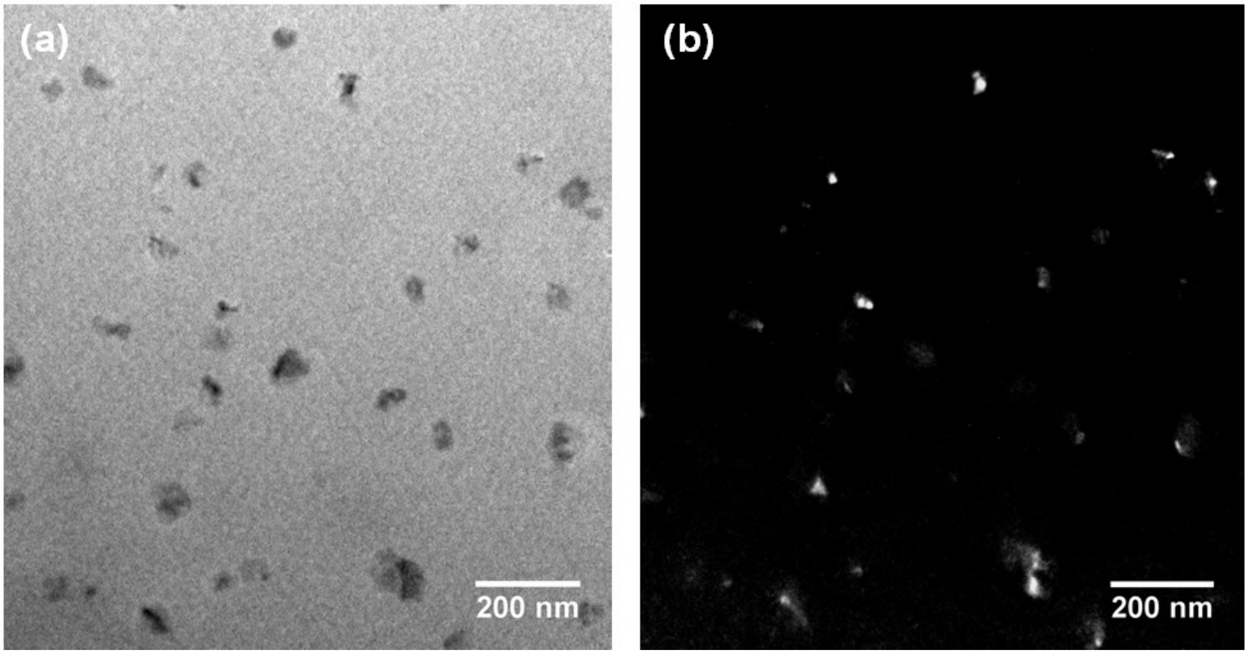

Fig. 6.8 (a) Bright field TEM micrograph showing the dispersoids formed at 540 °C after 120 min and (b) centered dark field micrograph of the same region as (a) using the $(\bar{3}50)$ reflection of the α-Al(Fe,Mo)Si.

It is noted that only a fraction of the predicted (see Table 6.3) closely matching plane pairs was observed experimentally. To further investigate the observed common OR (Fig. 6.7) and consider possible explanations for the selection of this OR by the system, a kinematical simulation of the electron diffraction patterns of the dispersoid embedded in the Al matrix (following OR1) was performed (Fig. 6.9) using CaRIne Crystallography software.

The selection of a specific OR by the system is mainly attributed to the system's tendency to minimize interfacial energy and reduce the nucleation barrier [5, 31]. The controlling factors can be categorized into chemical factors such as the nature of the atomic bonds at the interface and structural (or geometrical) factors such as the elastic misfit strains or misfit dislocations. Hence, the system attempts to minimize the total energy with respect to these two factors. It is noteworthy that in the reciprocal lattice space, the intensity of the diffraction spots can be a measure of the electron density of the corresponding planes in real space. Therefore, the planes with high mass and electron density (high structure factor) show diffraction spots with high intensities. These are the planes that give rise to Bragg peaks, and the atomic density is averagely distributed on such planes. These planes are listed in Table 6.3 for the α-phase. On the basis of the foregoing argument, the coincidence of two points in reciprocal lattice space can be considered as an interface in real space and the energy of such interface is inversely proportional to the total intensity of the overlapping diffraction points [32, 33]. In other words, the preferred OR (having well-matching plane pairs) should maximize the total intensity of all the overlapping diffraction points.

Table 6.3 Matching crystallographic planes of the Al matrix and the α-Al(Fe,Mo)Si phase

Al			**α-Al(Fe,Mo)Si***			**Misfit, ε (%)**
hkl	Interplanar spacing (A^o)	XRD I/I_o	Hkl	Interplanar spacing (A^o)	XRD I/I_o	
111	2.338	100	**134, 510**	2.46	11.3	5.2
			125	2.29	7.2	2.1
			530	2.15	52.3	8.0
			600	2.09	26.5	10.6
			532	2.03	100	13.2
002	2.024	46.9	**125**	2.29	7.2	13.1
			530	2.15	52.3	6.2**
			600	2.09	26.5	3.3**
			532	2.03	100	0.3**
			602	1.98	11.4	2.2
022	1.432	26.4	**835**	1.27	26.3	11.3
			10 0 0	1.25	8	12.7
311	1.221	23.4	**835**	1.27	26.3	4
			10 0 0	1.25	8	2.4

* The interplanar spacing of the planes with the structure factures above 7% of the maximum (i.e. for {532}) and misfit < 15% have been calculated using $a_0 = 12.54\ A^o$.

** Observed experimentally

SAED simulations provided further understanding of the different coincident planes in three dimensional real space by virtually allowing us to investigate the overlapping diffraction points along different zone axes. In Fig. 6.9 the simulation results are shown along three different zone axes. Fig. 6.9a shows the SAED along the $[001]_d$ which is in good agreement with experimental SAED in Fig. 6.7. The $[\bar{3}50]_d$ and $[530]_d$ zone axes views reveal more information about the coinciding planes. From these SAED simulations and stereographic analysis we can conclude that the dispersoid phase is oriented such that its three mutually perpendicular high density (high structure factor) planes, $(\bar{3}50)$, (530) and (006) are parallel to the {002} planes of the Al matrix.

Table 6.4 Orientation relationship observed experimentally and the misfit of the coinciding planes

Parallel directions	Parallel planes	Misfit, ε (%)
$\langle \mathbf{001} \rangle_d // \langle \mathbf{001} \rangle_m$	$\{350\}_d // \{002\}_m$	6.22
$\langle \mathbf{001} \rangle_d // \langle \mathbf{001} \rangle_m$	$\{390\}_d // \{022\}_m$	7.67
$\langle \mathbf{001} \rangle_d // \langle \mathbf{001} \rangle_m$	$\{006\}_d // \{002\}_m$	3.26

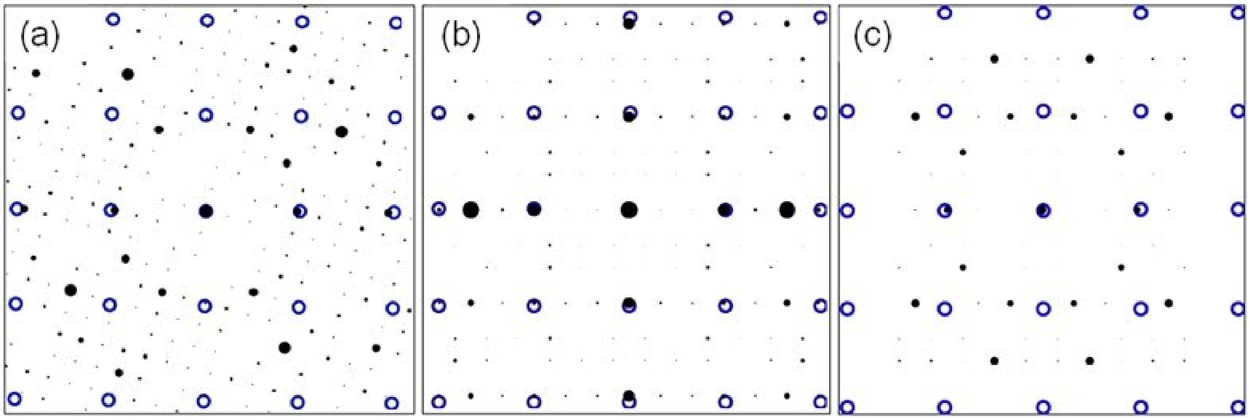

Fig. 6.9 Kinematically simulated electron diffraction patterns of the dispersoid and the Al matrix following the experimentally determined orientation relationship (Fig. 6.7) viewed along (a) $[001]_d$, (b) $[\bar{3}50]_d$ and (c) $[530]_d$. Solid black circles and open blue circles are the Al and the α-phase (dispersoid) reflections respectively.

The mutual perpendicularity of these high density planes makes it possible to have coherent or semicoherent interfaces with the three mutually perpendicular {002} planes of the Al matrix, which leads to a low total interface energy in the system. In the case of the $(350)_d$ type planes, these planes match face to face with the {002}m planes (identical atomic configuration in both phases is highly desirable for coherent interfaces). This is also predictable from the $[\bar{3}50]_d$ zone axis view (Fig. 6.9b). To further illustrate the identical atomic configuration in both planes, in Fig. 6.10, the simulated HRTEM images of the dispersoid and the matrix are shown along the $[350]_d$ and $[001]_m$ zone axes, respectively. From the atomic model projections along these zone axes (which only show the position of the atoms, Fig. 6.10 middle column), it is not very clear that these two planes perfectly match. However, because of the similarity in the periodicity of the electron density on the $(002)_{Al}$ and $(350)_{d}$ planes, which gives rise to the identical HRTEM images, it can be seen that these two planes closely match face-to-face (compare Fig. 6.10a with b); a comparison of the plane spacing (Table 6.3) confirms that the $(006)_{d}$ and the $\{002\}_{m}$ planes can be coherent if an ~ 3% strain is allowed along the interface over a few hundred angstroms, and the $\{350\}_{d}$ type planes could be coherent with the $\{002\}_{m}$ planes of the matrix with an ~ 6% misfit strain. As the Al matrix is softer in <100> directions [5], accommodation of the large misfits in these directions are more probable and easier than any other direction.

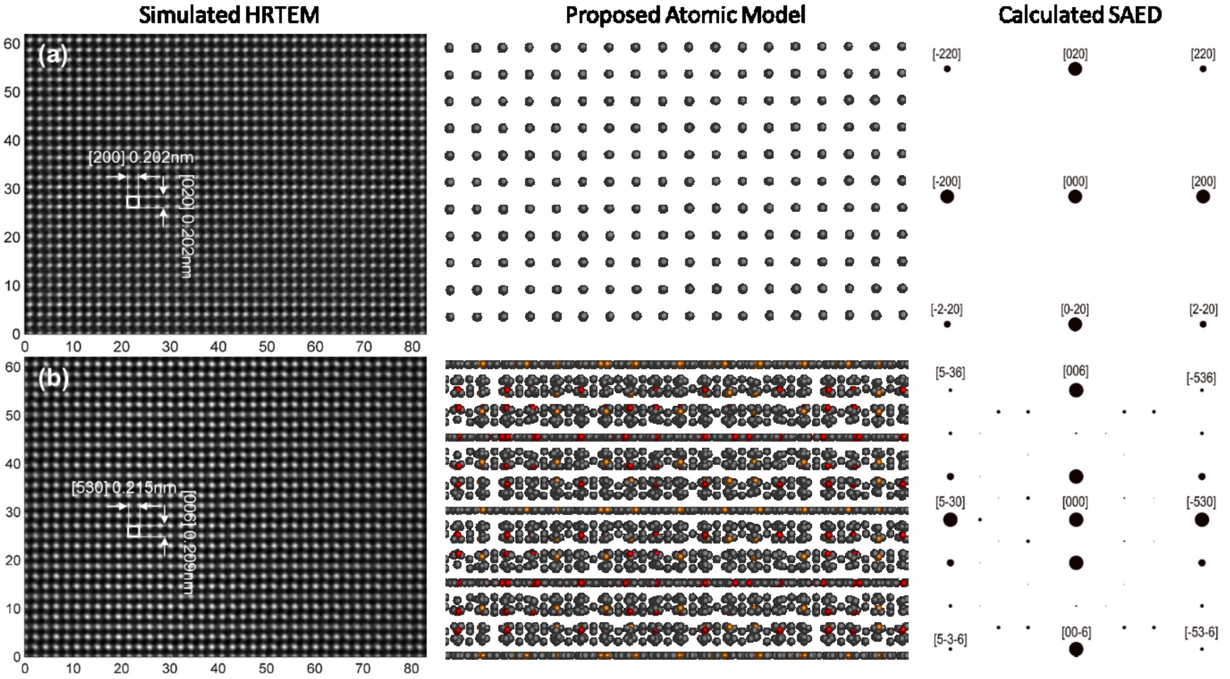

Fig. 6.10 HRTEM computer simulations along the (a) [001] zone axis of Al and (b) [350] zone axis of the dispersoid phase.

6.3.5 Interfacial structure and the coherency of the dispersoids

In order to study the atomic structure of the dispersoid/matrix interface in details, HRTEM images of the interface were simulated. A bicrystal supercell (containing Al and dispersoid unit cells following the common OR) was generated by the QSTEM Model Builder software [26], which can be saved in a standard CFG file for direct high resolution image simulations by QSTEM. A rigid lattice (unrelaxed) model of the interface was used, which does not allow any displacement (elastic relaxation) along the interface except for the thermal vibrations. The supercell thickness (in direction normal to the interface) was chosen sufficiently large (t = 200 A°) to avoid artifacts originated from the artificial periodic arrangement of the atoms close to the interface.

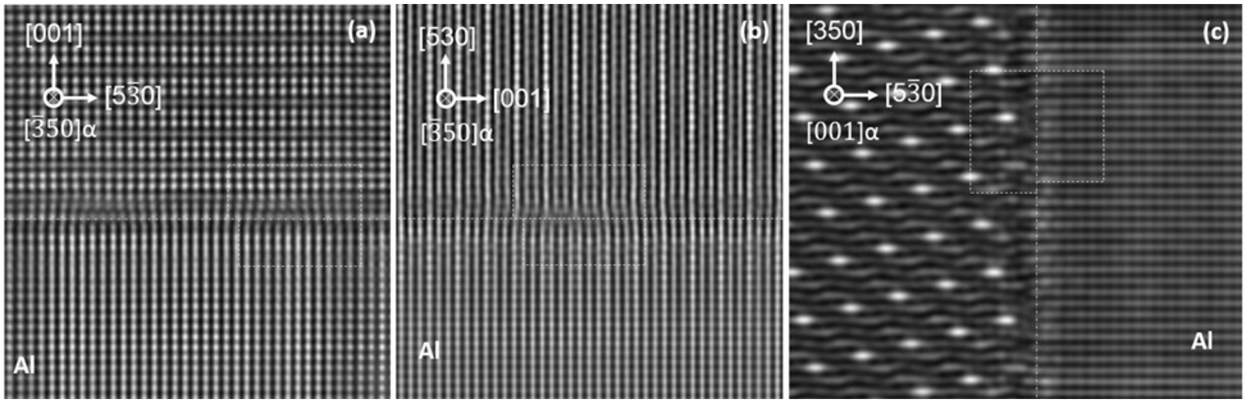

Fig. 6.11 Computer simulated HRTEM images of the interface between the Al matrix and the dispersoid phase viewed along the (a) and (b) $[\bar{3}50]_d$ and (c) $[001]_d$ zone axes.

Fig. 6.11 shows the simulated HRTEM images of the dispersoid/Al interface along the three mutually perpendicular $[\bar{3}50]_d$ and $[001]_d$ zone axes. These directions are chosen to study the predicted interfaces. Figs. 6.11a-b show the interfaces viewed along the $[\bar{3}50]_d$ direction. It can be seen that the unrelaxed interface model predicts regions of good lattice match in which the $(530)_d$ planes match the $(020)_m$ planes (Fig. 6.11a), and the $(006)_d$ planes match the $(200)_m$ planes (Fig. 6.11b). In regions of poor lattice match, misfit dislocations are visible. The Burgers circuits drawn around the misfit dislocations gives a Burgers vector ($\vec{b} = 1/2a_{Al} < 001 >$) parallel to the interface. It can be seen that every 16 $(530)_d$ planes correspond to every 18 $(020)_m$ planes, and every 40 $(006)_d$ planes correspond to every 41 $(200)_m$ planes, which is in good agreement with the geometrically expected spacing of the misfit dislocations ($D = |\vec{b}|/\varepsilon$). It is worth mentioning that although no relaxation is allowed along the interface (hypothetical case), however, even in this case, good commensurate regions between the periodically distributed misfit dislocations are predicted. No attempt has been made to relax the interface in this model. However, it is clear that by factoring in the relaxation it is possible to have a fully coherent interface for fine dispersoids (if 6% and 3.2% strains are allowed along the interfaces for the Fig. 6.11a and Fig. 6.11b respectively). The $[001]_d$ view of the dispersoid/Al interface is also shown in Fig. 6.11c. The commensurate regions where the $(350)_d$ planes match the $(002)_m$ planes can be seen as well as the misfit dislocations. Should the interfaces be the same as these planes, then the geometry necessitates that the dispersoid phase grow into a cuboid-shaped phase (with faces being the $(\bar{3}50)_d$, $(530)_d$ and $(001)_d$ planes parallel to the <001>$_{Al}$ directions). The TEM observations (Fig. 6.2a) confirmed the existence of the rectangular shaped dispersoids within the microstructure frequently. It should be mentioned that the interfaces are not always the same as these planes. This is due to the structural similarity and the existence of the different coincident plane pairs between the dispersoids phase and the Al matrix (Table 6.3), which make the growth along a number of different directions energetically possible. Some examples of these interface structures are observed experimentally.

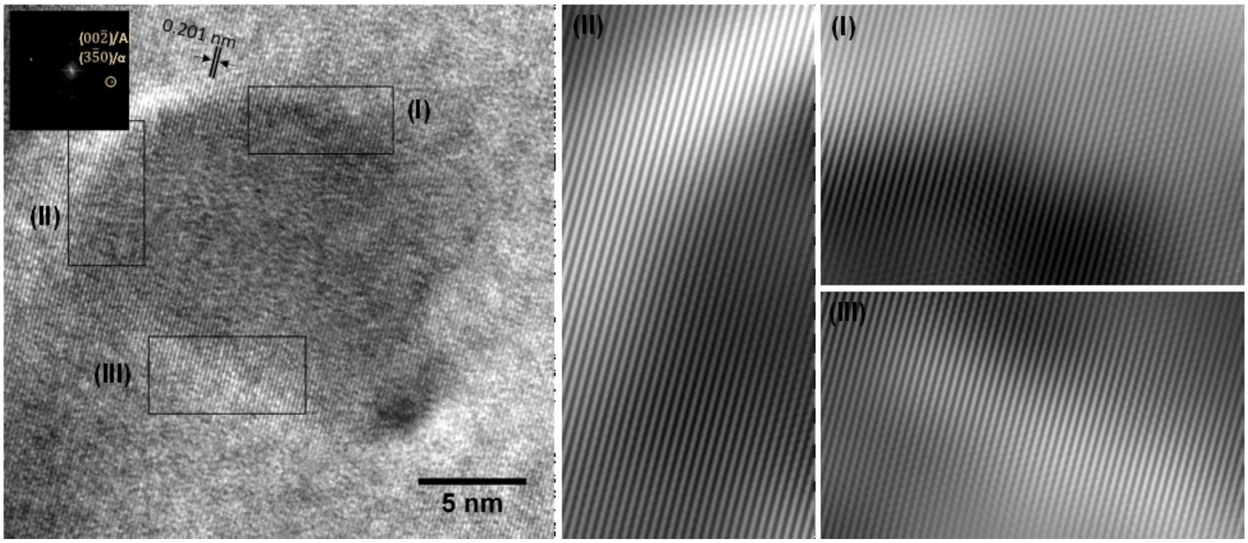

Fig. 6.12 HRTEM micrograph showing a coherent dispersoid formed after 60 min at 540 °C that exhibits the OR1. FFT filtering was performed on the black-framed areas around the interface using the two coinciding reflections of $\{002\}_m$ and $\{350\}_d$. A perfect coherency of the atomic planes at the interface can be seen.

Fig. 6.12 shows the HRTEM image of a dispersoid with OR1; it is ~15 nm in size and formed after 60 min at 540 °C. The lattice fringes corresponding to the $(00\bar{2})$ planes of the matrix and $(3\bar{5}0)$ planes of the dispersoid are visible. FFT filtering was performed to reduce the noise and reveal the continuity of the atomic planes using the two coinciding reflections of $\{002\}_m$ and $\{350\}_d$. The enlarged FFT filtered images, corresponding to the black-framed areas around the interface are shown on the right-hand side of the figure; there is a coherency of the atomic planes at the interface associated with the elastic misfit strain, and no misfit dislocation is observed. Fig. 6.13 shows a dark field TEM micrograph of a larger dispersoid with a more clear Ashby-Brown strain field contrast.

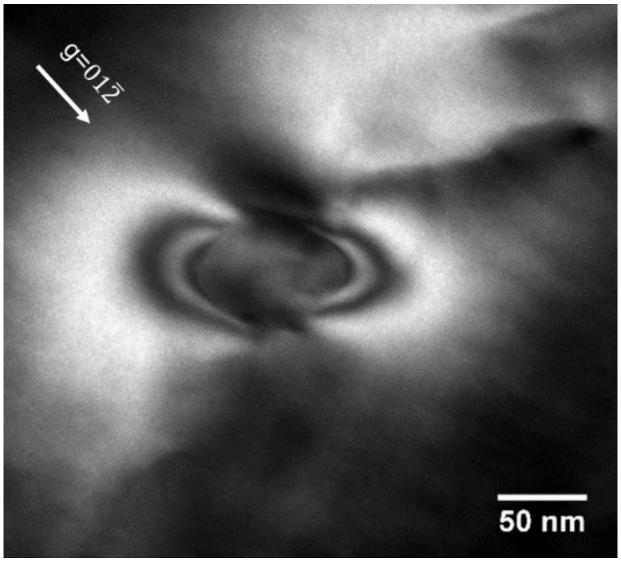

Fig. 6.13 Dark field-TEM micrograph of a misfitting coherent dispersoid with D ~ 60 nm formed after 120 min at 540 °C, showing the strain field developed around the dispersoid.

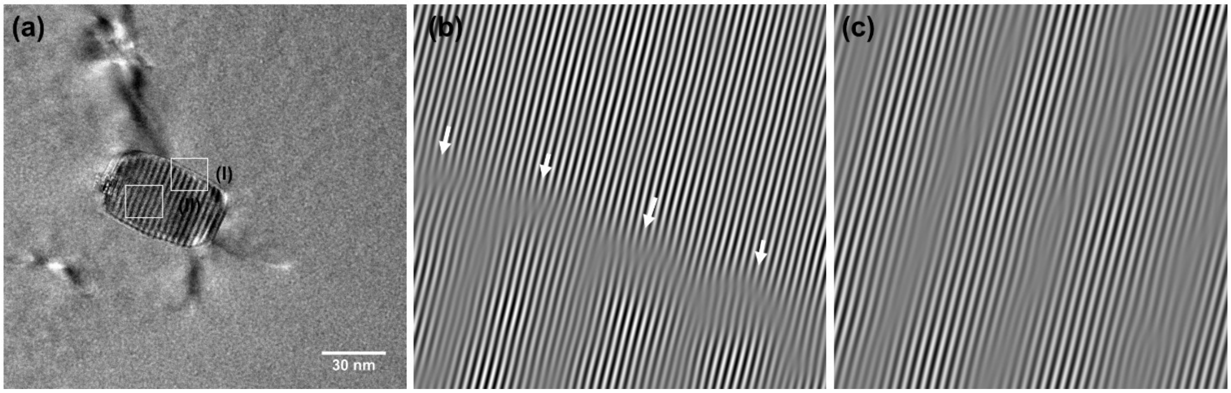

Fig. 6.14 (a) Moiré fringes in a dispersoid precipitate located on a dislocation indicating the presence of misfit dislocations at the dispersoid/matrix interface, (b) and (c) FFT filtered images from the regions marked I and II. Misfit dislocations are indicated by white arrows.

Fig. 6.14a shows a single dispersoid nucleated on a dislocation. Moiré fringes can be seen on the dispersoid, which are generally generated as a result of the superposition of two lattices with slightly different lattice parameters or with a small relative rotation [34, 35]. After FFT filtering, the (Fig. 6.14b) misfit dislocations are revealed at the interface. These dislocations with burgers vector, $\vec{b} = 1/2\mathrm{a}_m < 001 >$ are periodically distributed at the interface to accommodate the misfit strain. It can be seen that the number of the misfit dislocations is closely equal to the number of the Moiré fringes. Every 14d$\{002\}$ of matrix a misfit dislocation is located to relax the interfacial strain, which is in good agreement with the geometrically expected spacing of the misfit dislocations ($|\vec{b}|/\varepsilon$) [5]. The dispersoids also showed orientation relationships different from OR1 (the most frequent orientation relationship). Parallel plane pairs such as $\{532\}_d//\{002\}_m$were quite often observed. Fig. 6.15a shows a HRTEM image of a dispersoid (~ 60 nm) seen after 150 min of solutionizing at 540 ^{o}C. The image was taken with electron beam slightly off the [001] zone axis of the matrix. The {532} planes of the dispersoid are parallel to the {002} planes of the matrix. As can be seen from the enlarged FFT filtered images (two reflections of the matrix, (002) and (020) are used for filtering) corresponding to the white-framed areas (Figs. 6.15b-e), the dispersoid is not coherent at the entire interface. The facets marked I and II (Figs. 6.15b-c) are coherent with matrix, whereas, the facets marked III and IV (Figs. 6.15d-e) show misfit dislocations (arrowed in the corresponding images) at the interface.

Table 6.5 Fe-containing dispersoids formed in Al alloys

Phase	Crystal Structure	Common OR	Average Coherency Strain (%)	Lattice Parameters (A^o)	Space Group	Comments	Ref.
α-Al(FeMn)Si	SC	$<1\bar{1}1>$p//$<1\bar{1}1>$m $\{5\bar{2}\bar{7}\}$p//{011}m	~1	$a = 12.65$	Pm3	Mn:Fe>>1 found as dispersoids in A3xxx alloys	[17]
α-Al(Cr,Fe)Si	SC or BCC	-	NC*	$a = 12.6$	Pm3 or Im3	-	[13]
Al6(Fe,Mn)	Orthorhombic	(001)p//($3\bar{1}5$)m [$\bar{1}10$]p//[$21\bar{1}$]m	~1	$a = 7.50$, $b = 6.50$, $c = 8.84$	Cmcm	Plate-like found in AA5182 and Direct Chill-cast 3xxx with low Si	[40, 43, 44]
α-Al(Fe,Mn)Si	SC	-	NC	$a = 12.6$	Pm3	Rhomboidal, found in AA5182,	[43]

*Non-coherent

As seen, fine dispersoids may be coherent with the Al matrix, if they are small enough. The critical size, above which dispersoids gradually loss their coherency and the associated strain, depends on a number of factors such as modulus of elasticity of the two phases, crystallographic orientation, temperature, chemistry of the interface and misfit [36, 37]. However, at room temperature it can roughly be estimated as [5]:

$$D_{cr} \approx 2|\vec{b}|/\varepsilon \tag{1}$$

Assuming ε in the range of 3-6% and $|\vec{b}| = 0.2\ nm$, equation (1) predicts dispersoid size of ~ 7-14 nm for fully coherent dispersoids. However, the dispersoids form at 540 ^{o}C, and because of the higher lattice thermal expansion of Al compared to the intermetallics (thermal expansion coefficient of Al is ~ 2.4×10^{-5} K^{-1}, which is one order of magnitude higher than common intermetallic compounds), misfit is expected to decrease with temperature [37]. Moreover, a significant decrease in the modulus of elasticity of Al with temperature (from ~ 70 GPa at room temperature to ~ 45 GPa at 540 °C), allows more strain accumulation at the interface. Therefore, at 540 °C (precipitation temperature), D_{cr} can be much higher than the values estimated by equation (1). Further investigation of the coherency loss and the underlying mechanisms might lead to a deeper understanding of the growth and coarsening of the dispersoids.

6.3.6 Comparison to other dispersoid phases

Fe-containing dispersoids form in Al alloys when alloying elements such as Cr and Mn are added [13, 14, 38, 39]. These dispersoids are either incoherent (e.g. Cr-containing dispersoids) [40, 41] or semicoherent with low misfit strains (~ 1%) (see Table 6.5). Incoherent precipitates are only effective strengtheners when they form very fine and in large quantities, which are usually hard to attain. Mo-containing dispersoids unlike other Fe-containing dispersoids in Al alloys are unique because they are coherent and the misfit strain is considerably higher (~ 6%). A comparison can be made between the Mo-containing dispersoid in this study and the Mn-containing dispersoid, α-Al(Fe,Mn)Si, that forms in certain Al alloys. In particular:

1. The Mn-containing dispersoid which is isomorphous with the α-AlMnSi phase [25] coarsens due to the relatively high solid solubility of Mn in Al (1.25% at 658 °C, ~ 0.1% at 300 °C) and its relatively high diffusivity (9.5×10^{-22} m^2s^{-1} at 300 °C) [21]. As such, the Mn dispersoids would coarsen when exposed to elevated temperatures (300 °C) for applications such as engine block over a long period of time. The coarsening rates of common precipitates/dispersoids in Al alloys are given in appendix A. Depending on the alloy, the Mn dispersoids may be partially coherent [17, 42-44] with misfit strains ~1% or incoherent [13, 45], which have a low strengthening efficiency.
2. On the other hand, the average misfit strains for the Mo dispersoid, BCC α-Al(Fe,Mo)Si is considerably high (~ 6%); therefore it is expected to be more potent in matrix strengthening. Furthermore, low solid solubility (~ 0.25% at the peritectic temperature, 661 °C) and low diffusivity of the Mo atoms in the Al matrix (2.3×10^{26} m^2s^{-1} at 300 °C) provide excellent thermal stability to the α-Al(Fe,Mo)Si dispersoids at elevated temperatures. However, during thermal treatments such as high temperature solutionizings, the coherent Mo-dispersoids would

eventually reach a critical size where the introduction of dislocations at the dispersoid/matrix interface is energetically more favorable than the increase in the matrix strain. Therefore, the dispersoids become semicoherent and eventually non-coherent with the matrix. To circumvent this change in dispersoid properties, solutionizing of the alloys should be stopped before the critical dispersoid size is attained.

6.4 Conclusions

Nano-scale α-Al(Fe,Mo)Si dispersoid phase which formed during the solution treatment of an Al-Si-Cu-Mg cast alloy has been studied via conventional and high-resolution TEM. The main conclusions are:

1. Mo addition at a low level (0.3%) can form a substantial amount of fine Mo-bearing dispersoids in the intradendritic regions upon solutionizing the as-cast alloy.
2. The dispersoids have the approximate stoichiometric formula of $Al_{22}(Fe_{6-8}Mo)Si_4$ with the Mo content being much lower than the Fe. Their crystal structure (determined by SAED analysis) is body centered cubic (BCC) with lattice parameter of $a_0 = 12.54 \pm 0.03\ \mathring{A}$ and space group of Im3.
3. Structural analysis reveals that the BCC dispersoids are strongly correlated with the FCC Al matrix.
4. A systematic SAED analysis revealed that most of dispersoids precipitated in the present alloy have strong orientation relationship with the Al matrix determined as: $\langle 001\rangle_d // \langle 001\rangle_m$ and $\{350\}_d // \{002\}_m$.
5. HRTEM analysis along with the interfacial structure simulations showed that these dispersoids may be coherent with the Al matrix.

6.5 Acknowledgment

This work was supported by the NSERC (Natural Sciences and Engineering Research Council) of Canada Strategic Project grant with Rio Tinto Alcan (RTA) as well as a team grant from FQRNT (Fonds Québécois de la Recherche sur la Nature et les Technologies) and FQRNT Network REGAL Grant. The authors thank Pierre Vermette (McGill University) and Martin

Bouchard (Université du Québec à Chicoutimi) for their assistance in experimental work. Amir Rezaei Farkoosh would like to gratefully acknowledge the financial support of McGill University through MEDA (McGill Engineering Doctoral Award) program and research support provided through the NSERC/RTA Industrial Research Chair in Metallurgy of Aluminum Transformation at University of Québec at Chicoutimi. We wish to also acknowledge Dr. Xue-Dong Liu of McGill FEMR (Facility for Electron Microscopy Research) for fruitful discussions.

6.6 References

[1] K.E. Knipling, D.C. Dunand, D.N. Seidman, Criteria for developing castable, creep-resistant aluminum-based alloys–A review, Zeitschrift für Metallkunde, 97 (2006) 246-265.

[2] A.R. Farkoosh, M. Pekguleryuz, The effects of manganese on the T-phase and creep resistance in Al–Si–Cu–Mg–Ni alloys, Mater. Sci. Eng., A, 582 (2013) 248-256.

[3] A.R. Farkoosh, M. Javidani, M. Hoseini, D. Larouche, M. Pekguleryuz, Phase formation in as-solidified and heat-treated Al–Si–Cu–Mg–Ni alloys: Thermodynamic assessment and experimental investigation for alloy design, J. Alloys Compd., 551 (2013) 596-606.

[4] A.R. Farkoosh, X.-G. Chen, M. Pekguleryuz, Dispersoid Strengthening of a High Temperature Al-Si-Cu-Mg Alloy via Mo Addition, submitted to Materials Science and Engineering: A, (2014).

[5] D.A. Porter, K.E. Easterling, Phase Transformations in Metals and Alloys, (Revised Reprint), CRC press, 1992.

[6] A.P. Sutton, R.W. Balluffi, Interfaces in Crystalline Materials, OUP Oxford, 2006.

[7] K.E. Knipling, R.A. Karnesky, C.P. Lee, D.C. Dunand, D.N. Seidman, Precipitation evolution in Al–0.1Sc, Al–0.1Zr and Al–0.1Sc–0.1Zr (at.%) alloys during isochronal aging, Acta Mater., 58 (2010) 5184-5195.

[8] K.E. Knipling, D.C. Dunand, D.N. Seidman, Precipitation evolution in Al–Zr and Al–Zr–Ti alloys during isothermal aging at 375–425 °C, Acta Mater., 56 (2008) 114-127.

[9] C. Booth-Morrison, D.N. Seidman, D.C. Dunand, Effect of Er additions on ambient and high-temperature strength of precipitation-strengthened Al–Zr–Sc–Si alloys, Acta Mater., 60 (2012) 3643-3654.

[10] D.N. Seidman, E.A. Marquis, D.C. Dunand, Precipitation strengthening at ambient and elevated temperatures of heat-treatable Al(Sc) alloys, Acta Mater., 50 (2002) 4021-4035.

[11] L. Lodgaard, N. Ryum, Precipitation of chromium containing dispersoids in Al–Mg–Si alloys, Mater. Sci. Technol., 16 (2000) 599-604.

[12] D. Tsivoulas, P.B. Prangnell, The effect of Mn and Zr dispersoid-forming additions on recrystallization resistance in Al–Cu–Li AA2198 sheet, Acta Mater., 77 (2014) 1-16.

[13] L. Lodgaard, N. Ryum, Precipitation of dispersoids containing Mn and/or Cr in Al–Mg–Si alloys, Mater. Sci. Eng., A, 283 (2000) 144-152.

[14] H.Y. Kim, S.W. Han, H.M. Lee, The influence of Mn and Cr on the tensile properties of A356–0.20Fe alloy, Mater. Lett., 60 (2006) 1880-1883.

[15] P. Donnadieu, G. Lapasset, T.H. Sanders, Manganese-induced ordering in the α-(Al-Mn-Fe-Si) approximant phase, Philos. Mag. Lett., 70 (1994) 319-326.

[16] J.G. Zheng, R. Vincent, J.W. Steeds, Crystal structure determination of an Al-Fe-Si-Be phase by convergent-beam electron diffraction, Philos. Mag. A, 79 (1999) 2725-2733.

[17] Y.J. Li, A.M.F. Muggerud, A. Olsen, T. Furu, Precipitation of partially coherent α-Al(Mn,Fe)Si dispersoids and their strengthening effect in AA 3003 alloy, Acta Mater., 60 (2012) 1004-1014.

[18] V.K. Vasudevan, H.L. Fraser, The microstructures of rapidly solidified and heat-treated Al-8Fe-2Mo-Si alloys, Mater. Sci. Eng., 98 (1988) 131-136.

[19] V. K. Vasudevan, H. L. Fraser, Identification of precipitates in rapidly solidified and heat-treated Al-8Fe-2Mo-Si alloys, Scripta Metallurgica, 21 (1987) 1105-1110.

[20] P. Li, H. Yu, S. Chai, Y. Li, Microstructure and properties of rapidly solidified powder metallurgy Al–Fe–Mo–Si alloys, Scripta Mater., 49 (2003) 819-824.

[21] K.E. Knipling, D.C. Dunand, D.N. Seidman, Criteria for developing castable, creep-resistant aluminum-based alloys-A review, Zeitschrift fur Metallkunde, 97 (2006) 246.

[22] L.F. Mondolfo, Aluminum alloys: structure and properties, Butterworths London, 1976.

[23] M. Cooper, The crystal structure of the ternary alloy [alpha](AlFeSi), Acta Crystallographica, 23 (1967) 1106-1107.

[24] A. Goldman, R. Kelton, Quasicrystals and crystalline approximants, Reviews of modern physics, 65 (1993) 213-230.

[25] H.A. Fowler, B. Mozer, J. Sims, Triple-shell symmetry in α-(Al,Si)-Mn, Physical Review B, 37 (1988) 3906-3913.

[26] C.T. Koch, Determination of core structure periodicity and point defect density along dislocations, in, Arizona State University, Ann Arbor, 2002, pp. 214-214 p.

[27] X. Gonze, J.M. Beuken, R. Caracas, F. Detraux, M. Fuchs, G.M. Rignanese, L. Sindic, M. Verstraete, G. Zerah, F. Jollet, M. Torrent, A. Roy, M. Mikami, P. Ghosez, J.Y. Raty, D.C. Allan, First-principles computation of material properties: the ABINIT software project, Computational Materials Science, 25 (2002) 478-492.

[28] R. Hanson, Jmol - a paradigm shift in crystallographic visualization, J. Appl. Crystallogr., 43 (2010) 1250-1260.

[29] U. Mizutani, M. Inukai, H. Sato, E. Zijlstra, Hume-Rothery stabilization mechanism and e/a determination for RT-and MI-type 1/1-1/1-1/1 approximants studied by FLAPW-Fourier analyses, Chem. Soc. Rev., 41 (2012) 6799-6820.

[30] W. Steurer, S. Deloudi, Fascinating quasicrystals, Acta Crystallographica Section A, 64 (2008) 1-11.

[31] M.X. Zhang, P.M. Kelly, Edge-to-edge matching and its applications: Part II. Application to Mg–Al, Mg–Y and Mg–Mn alloys, Acta Mater., 53 (2005) 1085-1096.

[32] A.R.S. Gautam, J.M. Howe, A method to predict the orientation relationship, interface planes and morphology between a crystalline precipitate and matrix. Part I. Approach, Philosophical Magazine, 91 (2011) 3203-3227.

[33] M.H. Braun, J. Merwe, Reciprocal-space formulation and prediction of misfit accommodation in rigid and strained epitaxial systems, Metallurgical and Materials Transactions A, 33 (2002) 2485-2494.

[34] P. Dou, A. Kimura, T. Okuda, M. Inoue, S. Ukai, S. Ohnuki, T. Fujisawa, F. Abe, Polymorphic and coherency transition of Y–Al complex oxide particles with extrusion temperature in an Al-alloyed high-Cr oxide dispersion strengthened ferritic steel, Acta Mater., 59 (2011) 992-1002.

[35] J. Ribis, Y. de Carlan, Interfacial strained structure and orientation relationships of the nanosized oxide particles deduced from elasticity-driven morphology in oxide dispersion strengthened materials, Acta Mater., 60 (2012) 238-252.

[36] S. Iwamura, Y. Miura, Loss in coherency and coarsening behavior of Al3Sc precipitates, Acta Mater., 52 (2004) 591-600.

[37] J. Røyset, N. Ryum, Some comments on the misfit and coherency loss of Al3Sc particles in Al–Sc alloys, Scripta Mater., 52 (2005) 1275-1279.

[38] Q. Du, W.J. Poole, M.A. Wells, N.C. Parson, Microstructure evolution during homogenization of Al–Mn–Fe–Si alloys: Modeling and experimental results, Acta Mater., 61 (2013) 4961-4973.

[39] O. Engler, Z. Liu, K. Kuhnke, Impact of homogenization on particles in the Al–Mg–Mn alloy AA 5454 – Experiment and simulation, J. Alloys Compd., 560 (2013) 111-122.

[40] P. Ratchev, B. Verlinden, P. Van Houtte, Effect of preheat temperature on the orientation relationship of (Mn,Fe)Al6 precipitates in an AA 5182 Aluminium—Magnesium alloy, Acta Metall. Mater., 43 (1995) 621-629.

[41] G.E. Totten, D.S. MacKenzie, Handbook of Aluminum: Vol. 1: Physical Metallurgy and Processes, CRC Press, 2003.

[42] Y.J. Li, L. Arnberg, Quantitative study on the precipitation behavior of dispersoids in DC-cast AA3003 alloy during heating and homogenization, Acta Mater., 51 (2003) 3415-3428.

[43] Y.J. Li, W.Z. Zhang, K. Marthinsen, Precipitation crystallography of plate-shaped Al6(Mn,Fe) dispersoids in AA5182 alloy, Acta Mater., 60 (2012) 5963-5974.

[44] A.M.F. Muggerud, Y. Li, R. Holmestad, Composition and orientation relationships of constituent particles in 3xxx aluminum alloys, Philosophical Magazine, 94 (2013) 556-568.

[45] I. Nikulin, A. Kipelova, S. Malopheyev, R. Kaibyshev, Effect of second phase particles on grain refinement during equal-channel angular pressing of an Al–Mg–Mn alloy, Acta Mater., 60 (2012) 487-497.

CHAPTER 7

AL-SI-CU-MG-MO ALLOY STRENGTHENED BY THERMALLY STABLE COHERENT DISPERSOIDS: CREEP RESISTANCE AND MECHANISMS AT 300-350 ^{O}C

This chapter presents the results of a detailed creep investigation of the Al-7Si-0.5Cu-0.3Mg-0.3Mo alloy possessing nanoscale Mo-containing dispersoids. The creep mechanisms are explained and the activation energies are determined. A new method of determining activation energies in dispersoid-strengthened alloys is discussed. This chapter has been submitted for peer-review: *A.R. Farkoosh, X.-G. Chen, M. Pekguleryuz, Al-Si-Cu-Mg-Mo alloy strengthened by thermally stable coherent dispersoids: Creep resistance and mechanisms at 300-350 °C, submitted to Materials Science and Engineering: A, (2014).*

ABSTRACT

The creep behavior of a novel Al-Si-Cu-Mg-Mo alloy containing nanoscale coherent dispersoids was studied over the temperature range of 300-350 °C. Three distinct creep deformation regions have been identified on the basis of the stress exponents obtained from the creep data, and transmission electron microscopy (TEM) observations. A low stress region with stress exponent ~ 1.5 (region I) was identified as the diffusion creep region. At higher stresses (> ~18 MPa, region II), the stress exponent value was elevated (~20) and varied with applied stress. High activation energies for creep in the range of 445-568 kJ/mol (typical of dispersion strengthened alloys) were determined using the power law relationship. TEM analysis showed effective dislocation pinning by the coherent dispersoids. Threshold stress approach yielded activation energy values in the range of 145-185 kJ/mol that slightly overestimate the dislocation climb mechanism. At very high stress levels, region III was identified, in which Orowan bowing was found to be the deformation mechanism. It was shown that the size and coherency of dispersoids have significant influence on the stress level at which the transition to region III occurs.

Keywords: Creep; Al alloys; Dispersoid; Activation energy; TEM; Deformation mechanism

7.1 Introduction

Age-hardened Al alloys exhibit poor creep resistance because of the thermal and metallurgical instabilities of the ageing precipitates at elevated temperatures [1-3]. One route towards improving the creep resistance of such alloys is to introduce thermally stable dispersoids, which impede the movement of dislocations at elevated temperatures where age hardening precipitates lose their strengthening effect [4, 5]. Depending on their size, coherency, misfit strain and orientation relationship with the Al matrix, these dispersoids enhance the creep resistance with varying degrees of effectiveness [4, 6]. It has been reported that the creep resistance imparted by these dispersoids is insignificant in Al-Si alloys [7]. We have previously reported that the Al-Si-Cu-Mg-

Mo alloy system contains thermally stable dispersoids [8, 9], which are coherent with the matrix, and the high coherency strain (up to ~ 6%) at the dispersoid/matrix interface has a significant influence on the creep resistance [10]. At 300 ºC, 30 MPa, a 90-95% decrease in the minimum creep rate was observed, and the creep time-to-fracture increased from 50 to 1500 min by postponing the onset of the tertiary creep stage. The activation energies for creep in dispersoid strengthened alloys are usually associated with very high apparent activation energies, which cannot be explained by common creep mechanisms [11]. This complication has been addressed by the introduction of the notion of the threshold stress, which is defined as a lower limiting stress below which dislocation creep is not measurable. The analysis still yields only an approximation to the creep micro-mechanisms.

This article presents a detailed analysis of the creep behavior of the Al-7Si-0.5Cu-0.3Mg-0.3Mo alloy. Activation energies are determined and the creep micro-mechanisms are discussed. Overall, the present work provides a basis for understanding the creep deformation in the Al-Si-Cu-Mg-Mo alloy system, and may guide the development of a new class of creep resistant Al alloys which could meet operating demands under severe conditions. This alloy system could be used for lightweighting in automotive industry for high stress-temperature applications such as Diesel engine blocks developed recently.

7.2 Experimental procedures

An alloy with nominal compositions (in wt.%) of Al-7Si-0.5Cu-0.3Mg-0.3Mo (MG3R3M) was synthesized in a high frequency NORAX Canada induction furnace using commercial grade A356 alloy supplied by Rio Tinto Alcan Inc., Al-33 wt.% Cu and Al-10 wt.% Mo master alloys. All alloys were modified with 150 ppm Sr, using Al-10 wt.% Sr master alloy. Cylindrical bars of 30 mm diameter were cast in a pre-heated (400 ºC) permanent mold at 730 ºC. The chemical compositions of the alloys were determined by the inductively coupled plasma (ICP) technique, and presented in Table 7.1. All the compositions are given in wt.% hereafter, unless otherwise specified. Degassing was carried out at 730 ºC using high purity argon gas prior to pouring.

Creep test specimens with cylindrical gauge length and diameter of 50 and 12.7 mm were machined from the castings according to the ASTM E8 standard. Test samples were given a T7 heat treatment in an electrically heated, air-circulating chamber furnace comprising a two-step solution treatment (4 hours at 500 ^{o}C followed by 1 hour and 10 hours at 540 ^{o}C to avoid probable incipient melting), water quench at room temperature immediately after solution treatment and ageing at 200 ^{o}C for 5 hours. Tensile creep testing was conducted at 300-350 ^{o}C under step loadings; at each step, after the establishment of the steady-state deformation the load was increased. Gauge length displacement was measured with two high precision extensometers with a resolution of 5μm. Temperature was monitored with a thermocouple with an error of ± 0.1 ^{o}C attached to the specimen. All elevated temperature tests were conducted in air and samples were soaked at 300 ^{o}C, 100 hours prior to testing. In these tests, when the steady state was reached, the applied load was increased and the minimum creep rate, $\dot{\varepsilon}_m (= d\varepsilon/dt)_{min}$ obtained from the slope of these curves was plotted versus the applied stress, σ, on a double-logarithmic scale. Maximum five data points were obtained from each specimen and the total strain was less than 2%.

Microstructural characterization was performed on as-cast and heat-treated alloys. Specimens were cut using a low speed diamond saw and ground with a series of SiC papers, then polished on a porous neoprene polishing cloth with an Al_2O_3 solution. Final polishing was performed with a Buehler vibratory polisher using a colloidal silica solution. A Hitachi S-4700 field emission gun scanning electron microscope (FEG-SEM) equipped with an Oxford INCA energy dispersive spectroscopy (EDS) detector was used at 15kV with a beam current of 10 μA to study the microstructure. For transmission electron microscopy (TEM), creep-tested samples were prepared by mechanical grinding and electropolished (Struers Tenupol 5 jet polisher) to electron transparency using a solution of 10% nitric acid in methanol at -40 ^{o}C. TEM analysis was performed utilizing a Philips CM200 microscope operating at 200 kV.

Table 7.1 The chemical composition of the alloy (in wt.%)

Si	Mg	Cu	Fe	Ti	Mo	Sr	Al
6.49	0.31	0.53	0.11	0.10	0.29	0.014	Bal.

7.3 Results and discussion

7.3.1 Microstructure

The microstructure of the MG3R3M alloy in the as-cast condition consists of the α-Al dendrites with various intermetallic phases and eutectic Si particles in the interdendritic regions (Fig. 7.1a). The details of the microstructures and the microstructural evolution during solutionizing and ageing of the alloy have been reported in our previous study [8, 9] and are summarized in Table 7.2. Two solution treatments at 540 °C were used (1h and 10h) which give different dispersoid sizes and distributions (Fig. 7.2).

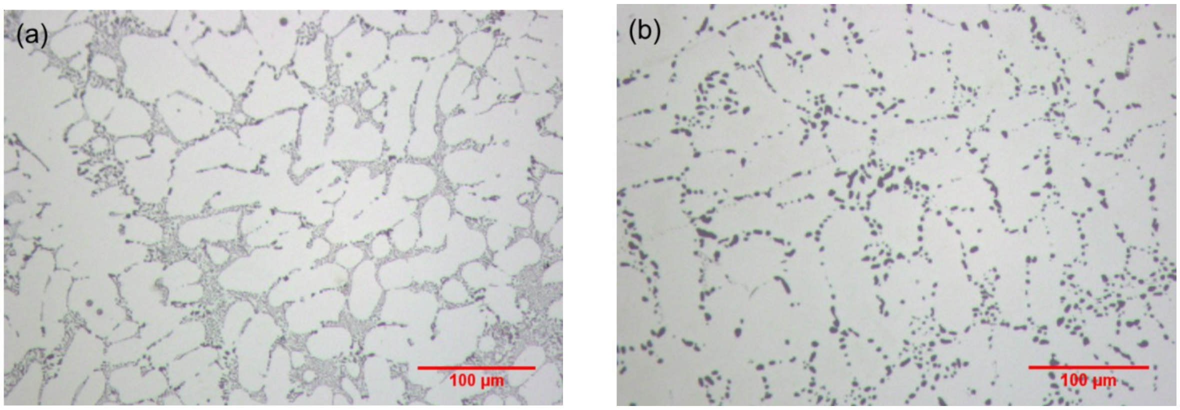

Fig. 7.1 The (a) as-cast and (b) heat-treated microstructure of the alloy.

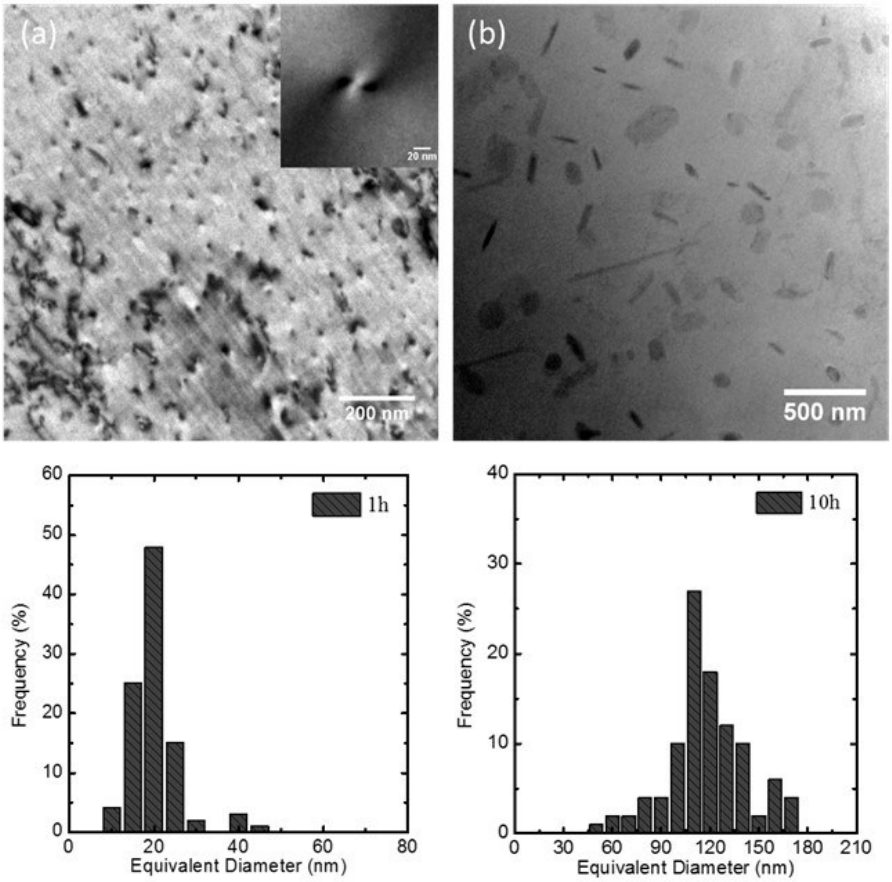

Fig. 7.2 BF-TEM microstructures and the particle size distribution of the dispersoids after (a) 1 hour and (b) 10 hours of solution treatment at 540 °C. Finer dispersoids of the micrograph (a) show coherency strain contrast confirming their coherency with the matrix.

Table 7.2 Precipitate phases present in the alloy in different conditions

As-cast	T7 (5 h at 200 °C)	300 °C, soaked for 100 h
α-Al-(Fe,Mo)-Si Q-$Al_5Cu_2Mg_8Si_6$, θ-Al_2Cu	α-Al-(Fe,Mo)-Si Q-$Al_5Cu_2Mg_8Si_6$, θ-Al_2Cu	α-Al-(Fe,Mo)-Si Q-$Al_5Cu_2Mg_8Si_6$

7.3.2 Creep behaviour

Fig. 7.3 shows typical creep curves at T = 300 °C, σ = 20 - 28 MPa. A short primary stage is followed by a well-defined steady-state region. Minimum creep rate, $\dot{\varepsilon}_m(= d\varepsilon/dt)_{min}$ versus the applied stress, σ, plotted on a double-logarithmic scale are presented in Fig. 7.4. Three distinct regions are clearly seen in this figure.

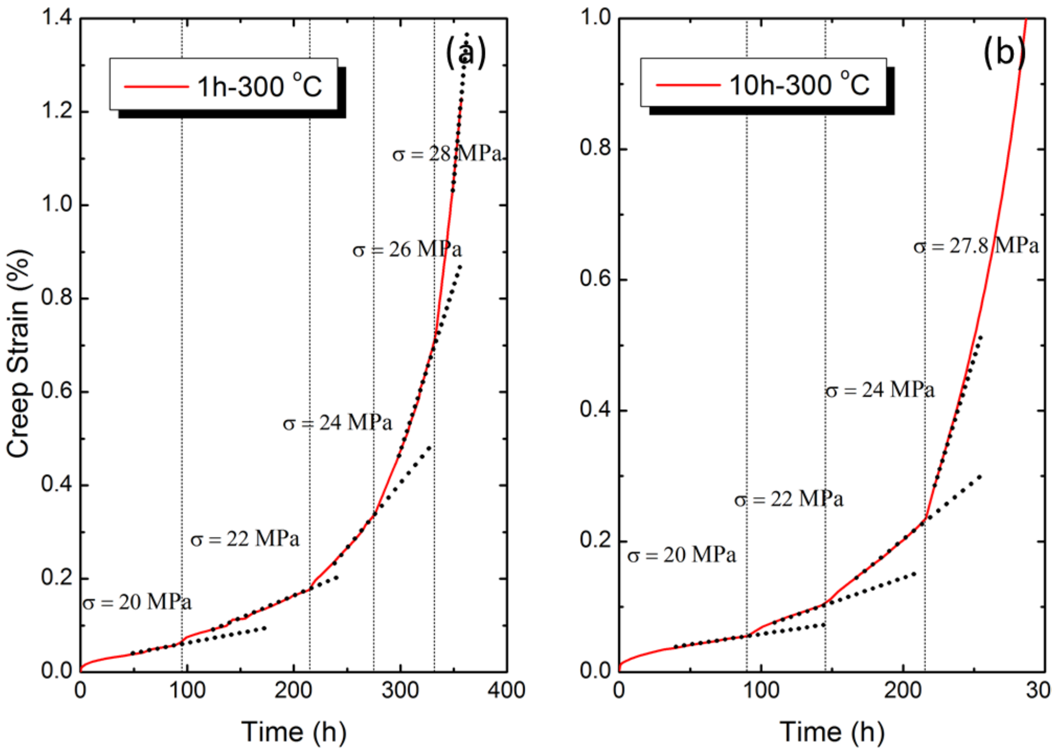

Fig. 7.3 Typical tensile creep deformation vs. time for the (a) 1h and (b) 10h alloys at 300 °C for different stress levels.

Power-Law Relationship

The three regions in the $\dot{\varepsilon}_m$ vs. σ plot of Fig. 7.4 were analyzed using the power-law relationship (the dependence of the minimum creep rate on temperature and stress) [12]:

$$\dot{\varepsilon}_m = A\sigma^{n_a}\exp\left(-\frac{Q_a}{RT}\right) \quad (1)$$

where, A is a constant, n_a is the apparent stress exponent, Q_a is the apparent activation energy and RT has its usual meaning.

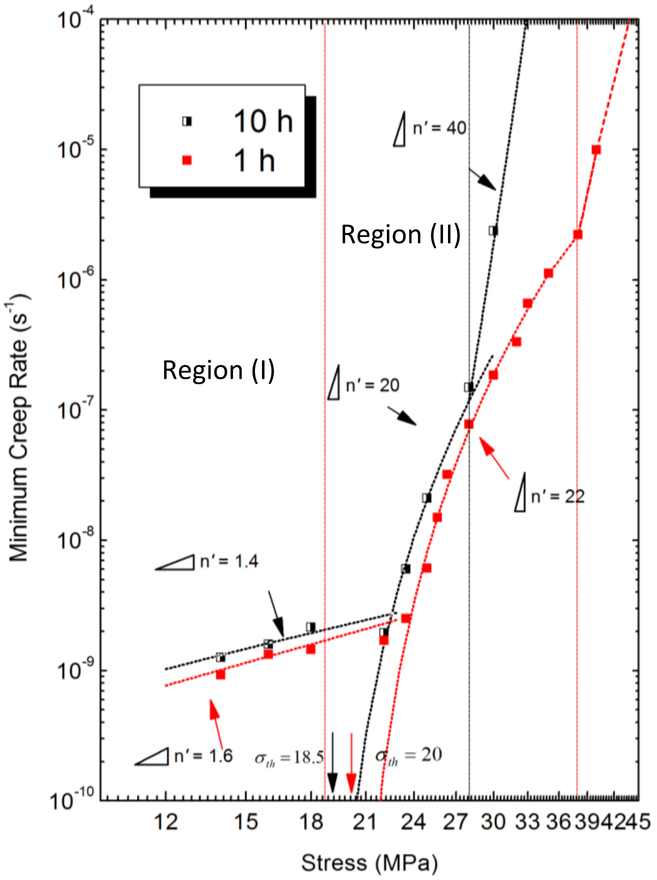

Fig 7.4. Minimum creep rate, $\dot{\varepsilon}_m$ at 300 °C vs. applied stress, σ for the alloys with 1h and 10h heat treatment plotted on a double-logarithmic scale.

Creep behaviour in region I

In region I, the apparent stress exponent, $n_a(= \partial \ln \dot{\varepsilon}_m / \partial \ln \sigma)$, is 1.4 for the 10h and 1.6 for the 1h alloy with minimum strain rates in the order of 10^{-9} s^{-1}. The experimental data in this region with n ~ 1-2 (Newtonian viscous flow) are indications of diffusional (Nabarro-Herring, Coble or Harper-Dorn) creep [13, 14]. As expected, the heat treatment and the dispersoid size does not appear to have a significant influence on the creep deformation rate in this region.

Fig. 7.5 shows bright-field (BF) and centered dark field (CDF) TEM micrographs of the microstructure of the 10h alloy after creep testing at 300 °C, 16.9 MPa for 140 hours (region I of Fig. 7.4). Attempts have been made to tilt the specimen for examinations under $g.b \neq 0$ conditions for the possible dislocations. As can be seen, there is no evidence of substantial dislocation activity confirming that diffusion creep processes occur in region I, consistent with the experimentally determined stress exponents.

Creep behaviour in region II

The plot of Fig. 7.4 shows a transition from $n_a \sim 1.5$ at low stresses (< 18 MPa) to $n_a \sim 20$ (region II) at higher stresses (the exponent decreases with applied stress; the $\dot{\varepsilon}_m$vs. σ plot shows curvature in this region), implying a change in creep deformation mechanism. It can be seen that the resistance to dislocation creep of the 1h alloy with an average dispersoids size $< D > \sim 20$ nm is considerably higher than that of the 10h alloy with $< D > \sim 120$ nm. [15]. The region II is further analyzed later in the text.

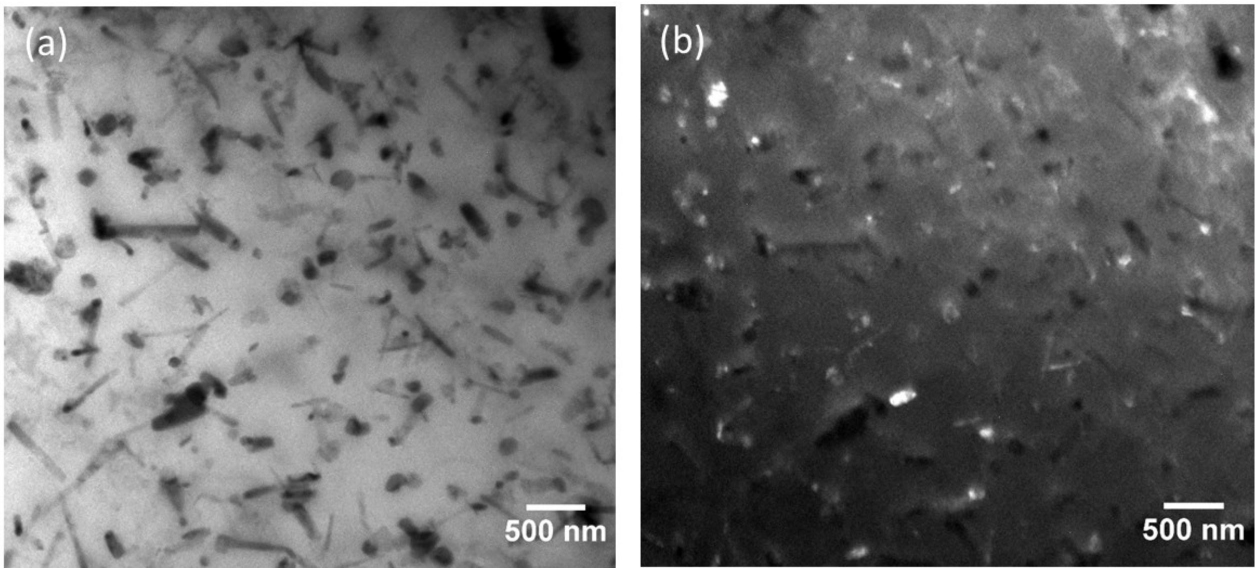

Fig. 7.5 BF-TEM (a) and CDF-TEM (b) microstructure of the 10h alloy after creep testing at 300 ºC and 16.9 MPa for 140 hours (Region I of Fig. 7.4, diffusional creep), little or no dislocation activities were observed.

Creep behaviour in region III

In region III, with an increase in the stress level (>27.8 MPa for the 10h and >37.5 MPa for the 1h alloy), there is an abrupt jump in the stress exponents and strain rates. It was noted that at high stress levels, the steady-state stage is of a short duration and the tertiary stage begins shortly after (Fig. 7.6 for the 1h alloy). Fig. 7.6a shows the measured strain rate vs. time for three different stress levels in 1h alloy. It is evident that at 20 MPa the steady state stage is very well established and of a long duration. By increasing the stress level to 30 MPa, the duration of the steady-state stage decreases. At higher stresses, 40 MPa (in region III) there is only a minimum in the strain rate rather than a well-established steady-state creep region, and in fact, true steady-state condition does not establish. This short-duration minimum is clearly demonstrated by re-plotting the strain rate vs. strain in Figs. 7.6b-d. The steady-state creep can be established if the work hardening rate is balanced by the work softening rate. Stress in this region seems to be sufficiently high (close to yield strength = 60 MPa) to disturb this equilibrium by operating other deformation mechanisms such as Orowan bowing. It is seen that the transition to region III occurs at higher stresses for the 1h alloy (possessing finer dispersoids), which results in significantly higher creep resistance for this alloy at high stress levels; fine and closely-spaced dispersoids increase the stress required for dislocation bowing between the dispersoids.

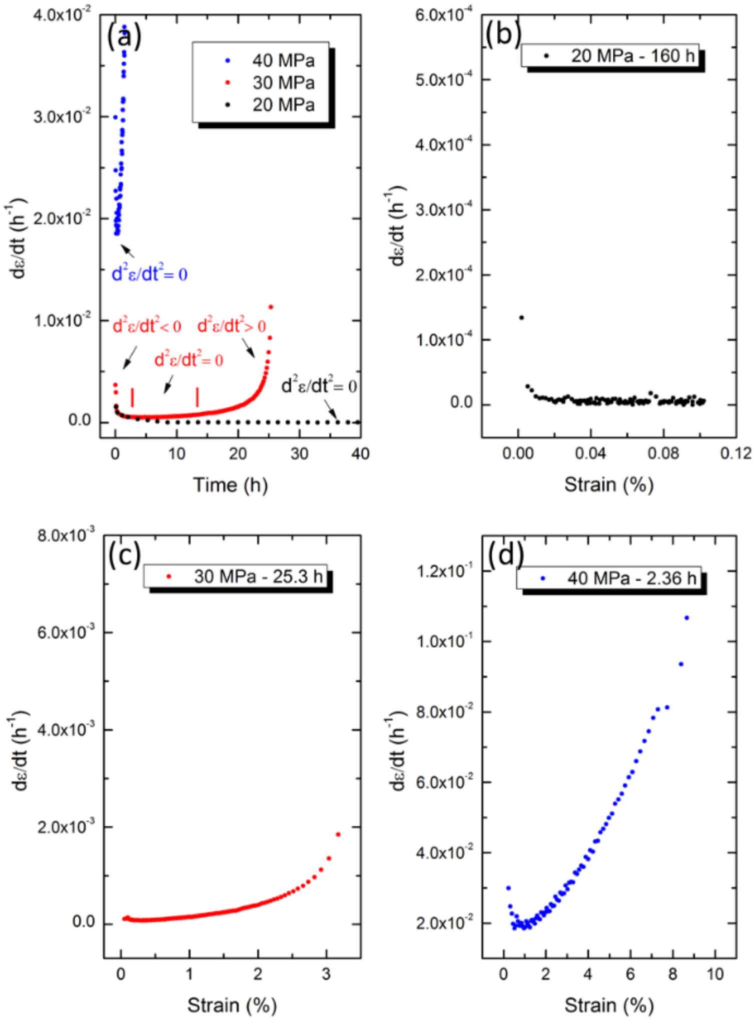

Fig. 7.6 (a) Strain rate vs. time for the 1h alloy at 300 °C, 20-40 MPa, and corresponding strain rate vs. strain at (b) 20 MPa, (c) 30 MPa and (d) 40 MPa.

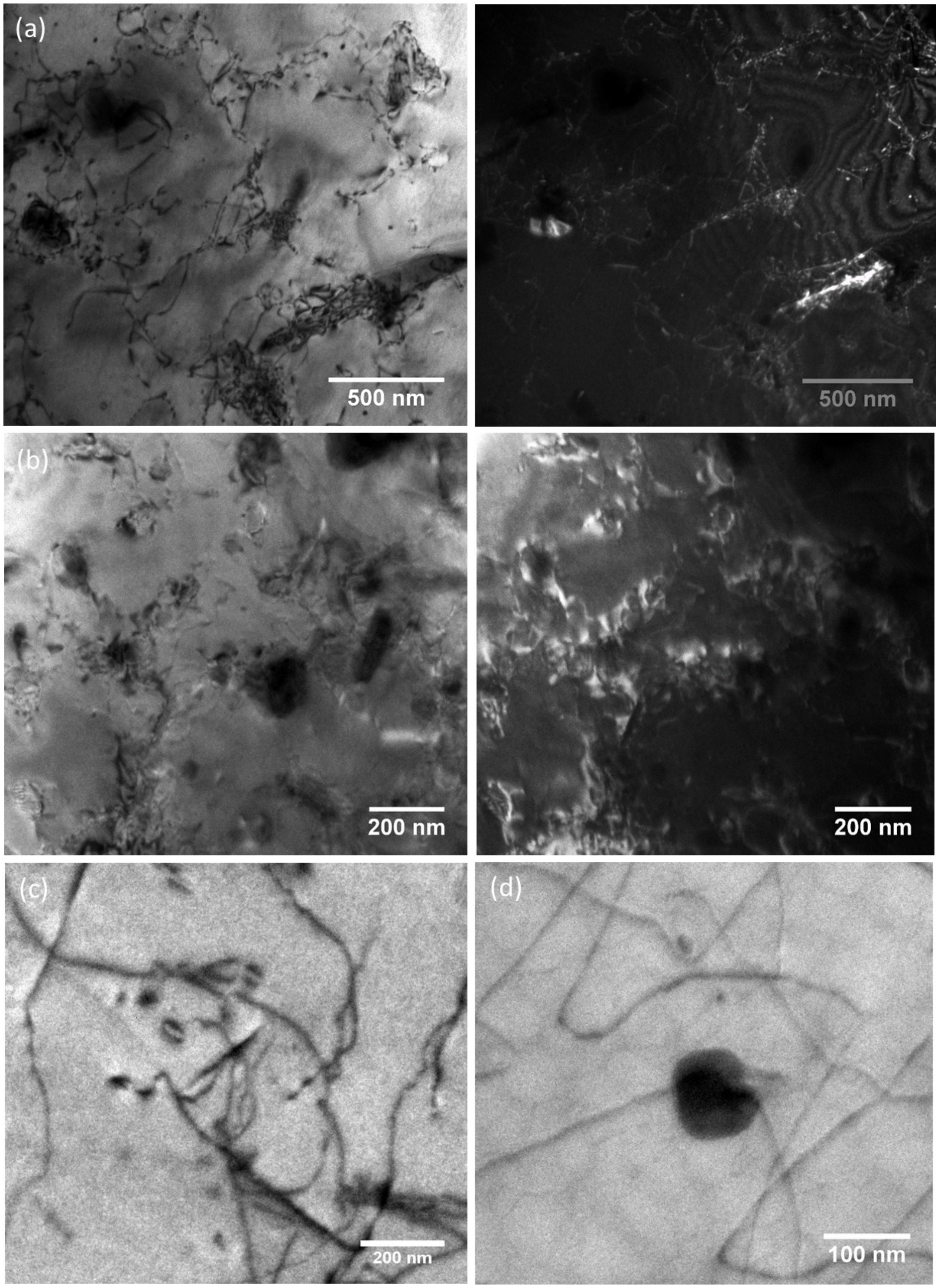

Fig. 7.7 BF- and CDF-TEM microstructures of the (a) 1h and (b) 10h alloys after creep testing at 300 ºC and 25.65 MPa for 300 hours (region II of Fig. 7.4, dislocation creep). The dislocation arrangement in both alloys provides evidence for the dislocation/dispersoid interaction mechanism. This is shown at higher magnifications for the (c) 1h and (d) 10h alloys.

There is evidence for the increase in dislocation density and dislocation/dispersoid interaction at higher stresses, in region II, as seen in Fig. 7.7. For instance, Figs. 7.7a-b show the microstructures of the 1h and 10h alloys after 300 hours of creep testing at 300 ºC, 25.65 MPa (region II of Fig. 7.4). The dislocation arrangements in both alloys indicate dislocation/dispersoid interaction. In the case of the 1h alloy, it seems that the dislocations are hindered in their motion mostly by the fine dispersoids. This is shown at a higher magnification in Fig 7.7c. Details of the dislocation/dispersoid interaction in this alloy were difficult to observe because of the overlapping strain field contrast from the coherent dispersoids [16] and the dislocations. A clear example of these interactions is shown in Fig. 7.7d for a larger dispersoid in the 10h alloy; a segment of the dislocation seems to be at the stage of climb over the dispersoid. No attempt has been made to measure the dislocation density, however, general qualitative TEM investigations at higher stress levels in region II (Fig. 7.8) show that the dislocation density increases with applied stress. There is no indication of the dislocations cutting the dispersoids even at high stress levels.

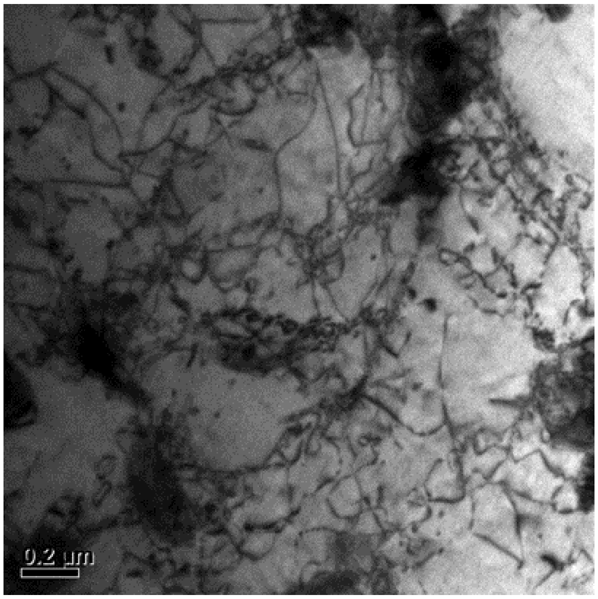

Fig. 7.8 BF-TEM microstructures of the 1h alloy after creep testing at 300 ºC and 30 MPa for 10 hour. The dislocation density is increased compared to Fig. 7.7a.

Threshold stress, σ_{th}

For dispersion strengthened alloys, the concept of threshold stress has been introduced to address the anomalously high and variable n_a and Q values. Introduction of the threshold stress, σ_{th}, below which dislocation creep is not significant, into equation (1) and modulus corrections gives [17, 18]:

$$\dot{\varepsilon}_m = A'\left(\frac{\sigma-\sigma_{th}}{G}\right)^n \exp\left(-\frac{Q}{RT}\right) \tag{2}$$

where, G is the shear modulus, n is stress exponent of the matrix and A' is a constant. The experimental data for the region II (dislocation creep) of Fig. 7.4 have been re-examined via equation (2) and assuming that the σ_{th} is independent of the applied stress. The threshold stress was estimated by plotting $\dot{\varepsilon}^{1/n}$ vs. σ on a double linear scale (Fig. 7.9a), and by extrapolating the data to $\dot{\varepsilon} = 0$ [19]. The stress exponent, $n = 4.4$ for the dislocation creep of Al [12, 20] was used, which yielded the best linear fit ($R^2 = 0.98$). Results show that $\sigma_{th} = 20$ MPa for the 1h and $\sigma_{th} = 18.5$ MPa for the 10h alloy; these values are indicated by arrows in Fig. 7.4. To validate this approach, in Fig. 7.9b, the minimum creep rate vs. effective stress, $(\sigma - \sigma_{th})$ was plotted on a double-logarithmic scale using the σ_{th} values obtained from Fig. 7.4, where the data points for both alloys fall on a straight line with a slope ~ 4.4.

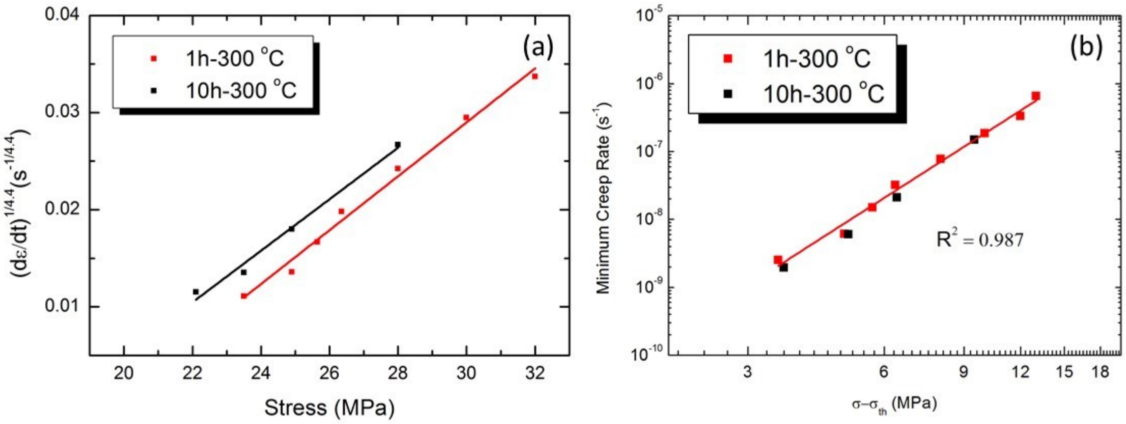

Fig. 7.9 (a) Plot of $\dot{\varepsilon}_m{}^{1/n}$ vs. stress using n = 4.4 for dislocation creep region of Fig. 7.4 and (b) double-logarithmic plot of the minimum creep rate, $\dot{\varepsilon}_m$vs. effective stress, $(\sigma - \sigma_{th})$ using the σ_{th} values obtained from Fig. 7.4.

Fig. 7.10 shows the effect of temperature (300-350 °C) on the steady-state creep rate of the 1h alloy. Only the dislocation creep (region II) has been plotted. The values of the threshold stress at higher temperatures are determined from Fig.7.10 and presented in Fig. 7.11a. The experimentally determined threshold stresses are strongly temperature-dependant even after normalizing by the shear modulus (Fig. 7.11b). The relationship between the threshold stress, σ_{th}(MPa) and temperature, T (K) is described by a quadratic function as:

$$\sigma_{th} = 1024 - 3.2T + 0.0025T^2 \tag{3}$$

It is expected from equation (3) that the threshold stress disappears at high temperatures (above 370 ºC). Others [21, 22] have proposed an exponential decay of the threshold stress with temperature in some metal matrix composites and have associated an energy term with the processes that gives rise to threshold stress [23]. However, our calculations show that because of the linear variation of the σ_{th}/G with reciprocal temperature (Fig. 7.11b), the exponential decay of the threshold stress yields a constant activation energy, which contradicts the experimental results and cannot be accounted for if equation (2) holds true.

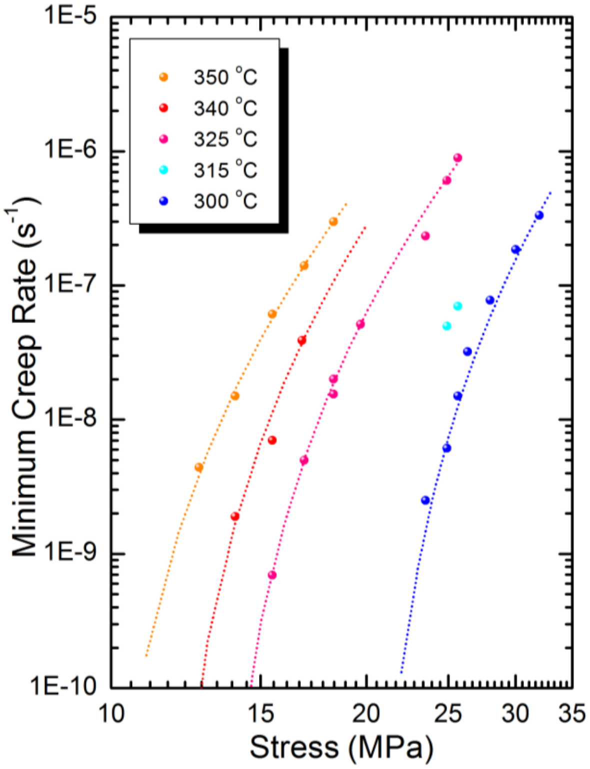

Fig. 7.10 Minimum creep rate vs. applied stress for the 1h alloy at 300-350 ºC plotted on a double-logarithmic scale.

The existence of the threshold stress has been disputed for many years and its origin is not fully understood. Several models have been proposed to explain the presence of a threshold stress for alloys possessing coherent and incoherent precipitates. It has been shown that for the non-shearable precipitates, the threshold stress may be due to the interaction of the dislocations with the precipitates during climb and bypass (slowing down the kinetics of dislocation climb) [24] or the operation of Orowan mechanism. The models based on the elastic dislocation/precipitate interaction have been supported by direct TEM observations [11]. Recently, Krug et al. [6] have developed a model that considers the elastic interaction of the dislocations and coherent precipitates during the climb process and have shown that in the alloys strengthened by coherent precipitates, elastic interactions facilitate the dislocation climb process, however, dislocations are trapped after climb at the departure side, which results in threshold stress.

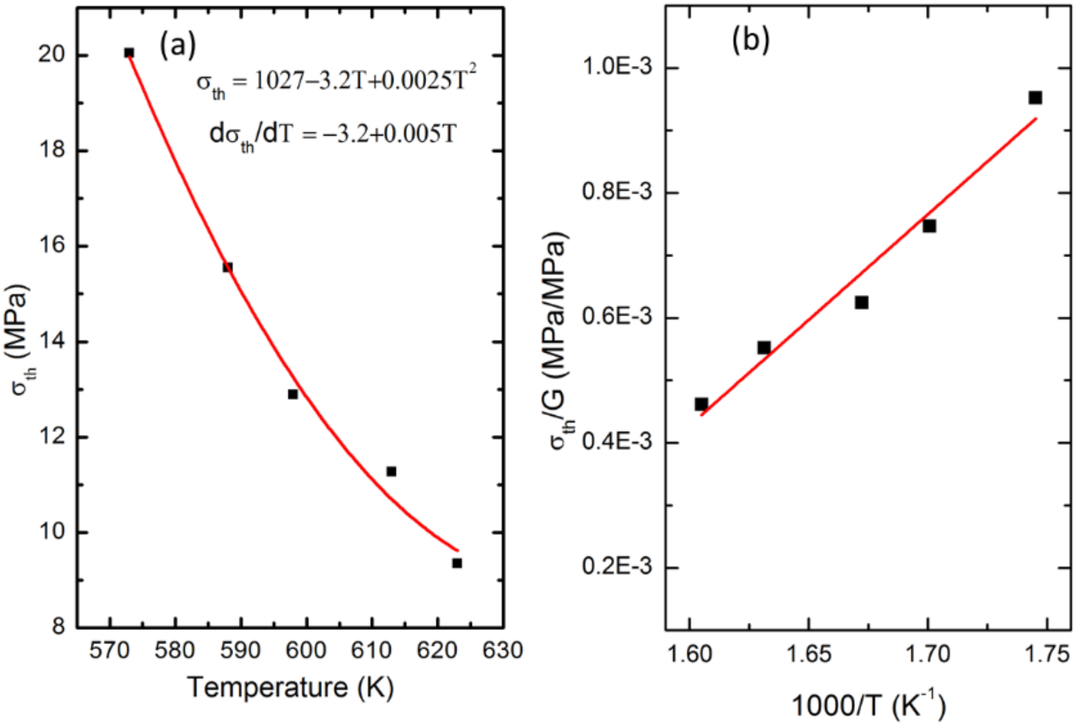

Fig. 7.11 (a) Variation of the threshold stress obtained from Fig. 7.10 with temperature and (b) linear dependence of the normalized threshold stress on T^{-1}.

7.3.3 Activation energy

The apparent activation energy

The apparent activation energy for creep deformation is defined as:

$$Q_a = -R\frac{\partial \ln \dot{\varepsilon}_m}{\partial\left(\frac{1}{T}\right)}|_{\sigma}. \quad (4)$$

Q_a for the 1h alloy can be determined from Fig. 7.12 where $ln\ (\dot{\varepsilon}_m)$ has been plotted against reciprocal temperature at constant stresses using the data obtained from Fig. 7.10. Even though the variation of the apparent activation energy for creep with temperature and applied stress has been well documented in previous creep studies [15, 21, 25], however, to obtain the apparent activation energies, the variation of $ln(\dot{\varepsilon}_m)$ with reciprocal temperature at constant stress levels has been estimated by most of the researchers [26] to be linear in a limited temperature range, which yields a constant activation energy. Here, a correction has been made by applying a logarithmic function for curve fitting, the derivative of which gives $-Q_a/R$ at different temperatures. Because of the linear variation of σ_{th}/G with reciprocal temperature (Fig. 7.11b), and referring to equation (2), it is trivial that the variation of $ln(\dot{\varepsilon}_m)$ with reciprocal temperature is of logarithmic nature.

Table 7.3 Activation energies estimated from the experimental data (Q_a) and the calculations (Q)

Applied Stress (MPa)	**Temperature (K)**	**Qa (kJ/mol)**	**Correction term (kJ/mol)** $nRT^2\left\{\left(\frac{d\sigma_{th}}{dT}\right)\left(\frac{1}{\sigma-\sigma_{th}}\right)+\left(\frac{dG}{dT}\right)\left(\frac{1}{G}\right)\right\}$	**Q (kJ/mol)**
15.5	588	567.76	388.25	179.51
16.9	588	444.80	292.04	152.76
24.9	613	515.47	330.66	184.81
25.65	613	453.11	307.91	145.20

As shown in Table 7.3, the apparent activation energy for the creep of this alloy (e.g. 515 kJ/mol at 613 K and 24.9 MPa) is much higher than that for self-diffusion of Al (143.4 kJ/mol) [27] and decreases with the applied stress and increases with temperature. Similar behaviour has been reported for different Al alloys strengthened by precipitates/dispersoids or incoherent particles (e.g. Al-Si-Cu-Mg [22], Al-4Mg-10vol%SiC [28], rapidly solidified Al-Fe-V-Si [29], Al-Si [21], Al-Sc-X, and Al-Zr-X [19, 30, 31] alloys).

Threshold stress approach to determine the activation energy

Taking equation (2) as the governing equation for dislocation creep, the activation energy for creep of our alloy can be calculated using:

$$Q = Q_a + nRT^2\left[\left(\frac{d\sigma_{th}}{dT}\right)\frac{1}{\sigma-\sigma_{th}} + \left(\frac{dG}{dT}\right)\frac{1}{G}\right] \tag{5}$$

Calculation results are shown in Table 7.3. For the shear modulus of pure Al, $G\ (MPa) = 3.022 \times 10^4 - 16T(K)$ is used [32] and the variation of the threshold stress with temperature is obtained from equation (3) as: $d\sigma_{th}/dT\ (MPaK^{-1}) = 0.005T\ (K) - 3.2$.

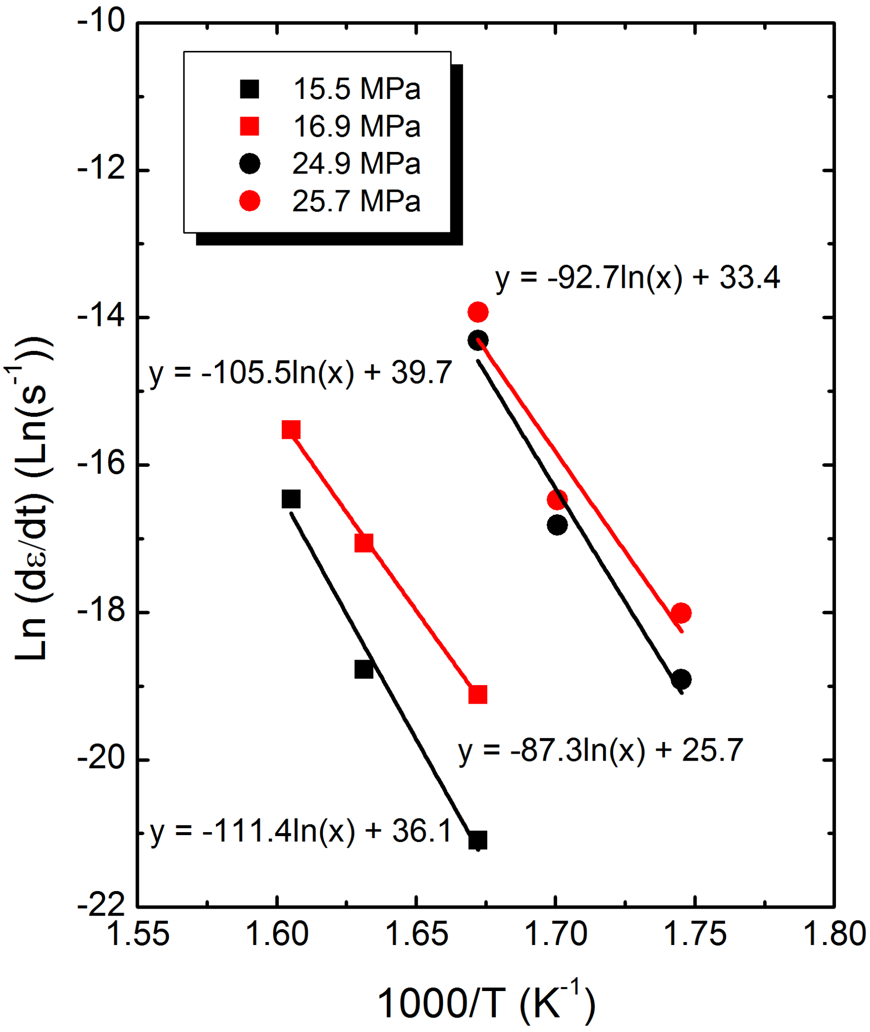

Fig. 7.12 Variation of the $ln\ (\dot{\varepsilon}_m)$ with reciprocal temperature for the 1h alloy. A logarithmic function is chosen to describe the dependency; $y = ln\ (\dot{\varepsilon}_m)$ and $x = 1000/T$.

Equation (5) has two correction terms between square brackets: $(d\sigma_{th}/dT)(1/(\sigma - \sigma_{th}))$ for the threshold stress and $(dG/dT)(1/G)$ for the modulus corrections, which are multiplied by nRT^2. After applying these corrections, the activation energy values are in the range of activation energies for the metallurgical phenomena (i.e. diffusion based). The Q values are in the range of 145-185 kJ/mol. However, this approach overestimates the activation energy value, which if the diffusion of the Al atoms (or vacancies) were the main rate-controlling process for the climb of the dislocations, this value would be very close to the activation energy for the lattice self-diffusion of Al. This overestimation cannot be attributed to the occurrence of Ostwald ripening or continuous precipitation because of the very high thermal stability of the dispersoids and the fact that the ageing precipitates are already coarsened and reach their stable size (creep specimens are soaked at 300 ^{o}C for 100 hour prior to testing). While the threshold stress approach and the modulus corrections do not explain the fine nuances in the creep mechanisms, direct estimation of activation energies may help elucidate creep micro-mechanisms as described below.

Estimation of apparent activation energy

Dislocation creep may have different mechanisms ranging from *climb* to *movement of dislocations with jogs* or *movement of dislocations with solute atmospheres*. The micro-mechanisms for these processes are also varied (self-diffusion, creation of jogs, solute-diffusion). Table 7.4 summarizes the activation energies for mechanisms and micro-mechanisms of dislocation creep. In most cases, one of these mechanisms is rate-controlling. In an alloy with slow-diffusing solutes and coherent dispersoids, the rate-controlling step for creep could be described as a dislocation process that involves multiple mechanisms in series: moving of solutes away from the dislocation segments and then the climb of dislocation segments (involving jog creation) in the strain field of the dispersoids. Furthermore, solute diffusion from the dislocation atmosphere can occur in series. When mechanisms occur in parallel the slowest process would be rate-controlling, however, when in series they can be cumulative. Sherby et al. [33] have estimated the apparent activation energy for creep in pure Al in the low temperature range assuming four discrete creep mechanisms acting in parallel and using a weight factor for each process. In a complex alloy such as the Al-Si-Mg-Cu-Mo alloys possessing coherent dispersoids and slow-moving solutes (Mo, Ti, Si, Cu, Fe), three discrete creep mechanisms can be considered to operate in series: movement of solute atmospheres → dislocation climb (jog creation → self-diffusion).

(1) The solute atmosphere of the dislocations would change with increasing temperature as solutes become mobile; solutes dissipated into the matrix near the vicinity of the dislocations would compete with Al atoms for the vacancies either interfering or slowing down climb processes. *The activation energy for this mechanism is the activation energy for solute diffusion,* $\boldsymbol{Q_S}$;

(2) Once the dislocations lose their solute atmosphere they would undergo climb with the activation energy approximated by jog creation and self-diffusion;

(3) However closely spaced nanoscale dispersoids would produce obstacles to dislocation motion in the slip and also the climb planes; the dislocations would then be forced into the dispersoid stress fields in a mechanism similar to a dislocation intersection involving jog creation. The activation energy for this mechanism is related [34] to the activation energy for jog creation in the strain field of the dispersoid ($\boldsymbol{q}$) and energy change due to the applied stress ($-w$).

The activation energy for the combined mechanism,$\boldsymbol{Q_C}$, can be written as:

$$\boldsymbol{Q_C} = \boldsymbol{Q_S} + \boldsymbol{Q_{Al}} + (\boldsymbol{q} - \boldsymbol{w}). \qquad (6)$$

The energy change due to stress ($-w$) in dispersoid (Orowan) strengthening can be expressed as $-w = -\tau b^2 l$, where τ = applied shear stress, b = Burger's vector and l = length of dislocation that moves between the dispersoids (inter-particle spacing). The jog creation energy in the strain field of the dispersoid ($\boldsymbol{q}$) can be estimated as [35] $\boldsymbol{q} = \lambda G b^3$, where λ is a constant and depends on the strain field of the dispersoids. It can be seen that, $\boldsymbol{Q_C}$ is a function of temperature, applied stress and inter-particle spacing. At a constant temperature $\boldsymbol{Q_C}$ decreases with the applied stress, which is in agreement with the experimental results (Table 7.3). $\boldsymbol{Q_C}$ calculated for the 1h alloy at 613 K and 25.65 MPa without assigning any weighting factors to the three discrete mechanisms ($\lambda = 1$) is ~ 410 kJ/mol, which is close to 453.11 kJ/mol, the value obtained experimentally. Although this is a crude estimation, it can shed light on the micro-mechanisms of the complex creep deformation of the alloy in this stress and temperature range. Undoubtedly applying appropriate weighting factors can lead to a closer approximation of the activation energies. Correct assignment of the weighting factors requires knowledge of the type and the amount of the solute atoms that segregate to the dislocation cores. Atom probe tomography or atomistic simulations based on the molecular dynamics or phase field crystal methods can be a useful means of determining these values. The effect of the coherency strain on the jog creation energy is neglected ($\lambda = 1$) in these calculations, which also require an in-depth examination in future studies. Determining the components of the complex creep deformation mechanisms in dispersion strengthened alloys would have an important contribution to further alloy design.

Table 7.4 Activation energies for creep mechanisms [34-40]

Mechanism	Micro-mechanisms	Net activation energy, Q
Dislocation intersection	Dislocation is forced through the stress field of another dislocation, involves jog or kink creation ($\boldsymbol{q_o}$) and the energy change due to stress ($\boldsymbol{-w}$).	$\boldsymbol{Q} = \boldsymbol{q_o} - \boldsymbol{w}$; $\boldsymbol{w} = \tau b^2 l$, $\boldsymbol{q_o} = \alpha G b^3$, where τ = applied shear stress, b = Burger's vector, l = length of the free segment of the dislocation, α = constant, G = shear modulus
Movement of Dislocations with Jogs	A back stress acts on the jog, which restricts its motion; the jog continues to move if a vacancy forms (q_f) and moves away (q_m).	$\boldsymbol{Q} = \boldsymbol{q_f} + \boldsymbol{q_m} = \boldsymbol{Q_{Al}}$, The activation energy for the process is equal to the energy for vacancy formation (q_f) and the energy to move it away (q_m). The sum of these values is the activation energy for self-diffusion: $\boldsymbol{Q_{Al} = 143\ kJ/mol}$
Dislocation Climb	Jog formation ($\boldsymbol{q_o}$), vacancy formation (q_f) and migration (q_m).	$\boldsymbol{Q} = q_f + q_m + \boldsymbol{q_o} = \boldsymbol{Q_{Al}} + \boldsymbol{q_o} \sim \boldsymbol{Q_{Al}}$, approximated by self-diffusion when no elastic interactions are involved or thermal jogs are present.
Movement of Dislocation Atmospheres	Movement of the solute atoms away from the dislocation	$\boldsymbol{Q_S}$ = activation energy for diffusion of solute atoms $\boldsymbol{Q_{Al}} =$ **143 kJ/mol;** $\boldsymbol{Q_{Mo}} =$ **250 kJ/mol;** $\boldsymbol{Q_{Ti}} =$ **260 kJ/mol** $\boldsymbol{Q_{Cu}} =$ **136 kJ/mol;** $\boldsymbol{Q_{Si}} =$ **150 kJ/mol;** $\boldsymbol{Q_{Fe}} =$ **221 kJ/mol**
Activated Cross Slip	A screw dislocation dissociates into a pair of partial dislocations with a connecting layer of stacking fault.	Activation energy for cross-slip is related to the stacking fault energy (SFE) ~ $\boldsymbol{160 - 200\ mJ/m2}$. Because of high SFE in Al, this mechanism is not assumed to be rate-controlling.
Cumulative mechanism	Movement of dislocation atmospheres, dislocation climb and interaction with dispersoid	$\boldsymbol{Q_C} = \boldsymbol{Q_S} + \boldsymbol{Q_{Al}} + (\boldsymbol{q} - \boldsymbol{w})$, $\boldsymbol{w} = \tau b^2 l$ τ = applied shear stress, b = Burger's vector, l = inter-particle spacing $\boldsymbol{q}$ = energy barrier for the dispersoid/dislocation interaction = jog formation and interaction with the strain field of the dispersoids ~ $\lambda G b^3$, λ = constant

7.4 Conclusions

Creep tests were conducted on an Al-7Si-0.5Cu-0.3Mg-0.3Mo alloy fabricated by conventional ingot metallurgy technique to determine the underlying deformation mechanism and the origin of high creep resistance in this alloy. The following conclusions have been drawn:

1. Three distinct creep regions have been identified in the double-logarithmic plot of minimum creep rate vs. applied stress on the basis of the dramatic stress exponent changes and TEM investigations.
2. Region I was identified as a diffusion creep region with exceptionally low strain rates of the order of 10^{-9} s^{-1} and stress exponent ~ 1.5.

3. Region II was identified as a dislocation creep region with high and variable stress exponent (~ 20) and activation energy (445-568 kJ/mol) values.
4. Threshold stress approach was introduced to rationalize these experimentally determined values leading to stress exponent ~ 4.4 and activations energy for creep in the range of 145-185 kJ/mol, which are consistent with the dislocation climb controlled mechanism.
5. TEM observations revealed the dislocation/dispersoid interaction in this region demonstrating that the mobile dislocations are effectively pinned by the dispersoids.
6. The resistance to dislocation creep of the alloy with fine ($< D > \sim 20nm$) and coherent dispersoids is considerably higher than that of the alloy possessing relatively coarse dispersoids.
7. In region III, exceptionally high creep rates are observed at the highest stress levels (close to yield stress), which is accounted for by the Orowan bowing mechanism.
8. It was seen that decreasing the dispersoid size help delay the transition to this region by promoting the Orowan strengthening.

7.5 Acknowledgments

This work was supported by the NSERC (Natural Sciences and Engineering Research Council) of Canada strategic project grant with Rio Tinto Alcan (RTA) as well as a team grant from FQRNT (Fonds Québécois de la Recherche sur la Nature et les Technologies). The authors thank Pierre Vermette (McGill University) and Martin Bouchard (Université du Québec à Chicoutimi) for their assistance in experimental work. Amir Rezaei Farkoosh would like to acknowledge the financial support of McGill University through MEDA (McGill Engineering Doctoral Award) program and research support provided through the NSERC/RTA Industrial Research Chair in Metallurgy of Aluminum Transformation at University of Québec at Chicoutimi. Thanks also to Dr. Xue-Dong Liu of McGill FEMR (Facility for Electron Microscopy Research) for fruitful discussions.

7.6 References

[1] A.R. Farkoosh, M. Javidani, M. Hoseini, D. Larouche, M. Pekguleryuz, Phase formation in as-solidified and heat-treated Al–Si–Cu–Mg–Ni alloys: Thermodynamic assessment and experimental investigation for alloy design, J. Alloys Compd., 551 (2013) 596-606.

[2] A.R. Farkoosh, M. Pekguleryuz, The effects of manganese on the T-phase and creep resistance in Al–Si–Cu–Mg–Ni alloys, Mater. Sci. Eng., A, 582 (2013) 248-256.

[3] X.Y. Liu, Q.L. Pan, X.L. Zhang, S.X. Liang, F. Gao, L.Y. Zheng, M.X. Li, Creep behavior and microstructural evolution of deformed Al–Cu–Mg–Ag heat resistant alloy, Mater. Sci. Eng., A, 599 (2014) 160-165.

[4] F.R.N. Nabarro, F. De Villiers, Physics of creep and creep-resistant alloys, CRC press, 1995.

[5] E. Arzt, Creep of dispersion strengthened materials: a critical assessment, (2009).

[6] M.E. Krug, D.C. Dunand, Modeling the creep threshold stress due to climb of a dislocation in the stress field of a misfitting precipitate, Acta Mater., 59 (2011) 5125-5134.

[7] M. Garat, G. Laslaz, Improved Aluminum Alloys for Common Rail Diesel Cylinder Heads, in: AFS, IL, USA, 2007, pp. 1-8.

[8] A.R. Farkoosh, X.G. Chen, M. Pekguleryuz, The effects of MG, MO and CR on the microstructure and elevated temperature mechanical properties of an AL-SI-CU-MG alloy, in, Montreal, QC, 2013, pp. 1220-1227.

[9] A.R. Farkoosh, X.-G. Chen, M. Pekguleryuz, Dispersoid Strengthening of a High Temperature Al-Si-Cu-Mg Alloy via Mo Addition, submitted to Materials Science and Engineering: A, (2014).

[10] A.R. Farkoosh, X.-G. Chen, M. Pekguleryuz, Precipitation of coherent α-Al(Fe,Mo)Si dispersoids in an Al-Si-Cu-Mg cast alloy via Mo addition, submitted to J. Alloys. Comp., (2014).

[11] S.P. Deshmukh, R.S. Mishra, I.M. Robertson, Investigation of creep threshold stresses using in situ TEM straining experiment in an Al–5Y2O3–10SiC composite, Mater. Sci. Eng., A, 527 (2010) 2390-2397.

[12] K.E. Knipling, D.C. Dunand, Creep resistance of cast and aged Al–0.1Zr and Al–0.1Zr–0.1Ti (at.%) alloys at 300–400 °C, Scripta Mater., 59 (2008) 387-390.

[13] T.G. Langdon, P. Yavari, An investigation of Harper-Dorn creep—II. The flow process, Acta Metall., 30 (1982) 881-887.

[14] F.R.N. Nabarro, Creep in commercially pure metals, Acta Mater., 54 (2006) 263-295.

[15] Y. Li, T. Langdon, Fundamental aspects of creep in metal matrix composites, Metall. Mater. Trans. A, 30 (1999) 315-324.

[16] R.A. Stevens, P.E.J. Flewitt, The dependence of creep rate on microstructure in a γ′ strengthened superalloy, Acta Metall., 29 (1981) 867-882.

[17] H. Watanabe, H. Tsutsui, T. Mukai, M. Kohzu, S. Tanabe, K. Higashi, Deformation mechanism in a coarse-grained Mg–Al–Zn alloy at elevated temperatures, Int. J. Plast., 17 (2001) 387-397.

[18] S. Spigarelli, Interpretation of creep behaviour of dispersion-strengthened Al–Fe–V–Si alloys in terms of detachment mechanisms: an overview, Mater. Sci. Eng., A, 337 (2002) 306-314.

[19] S.P. Deshmukh, R.S. Mishra, K.L. Kendig, Creep behavior and threshold stress of an extruded Al–6Mg–2Sc–1Zr alloy, Mater. Sci. Eng., A, 381 (2004) 381-385.

[20] S. Mitra, Elevated temperature deformation behavior of a dispersion-strengthened Al-Fe,V,Si alloy, Metall. Mater. Trans. A, 27 (1996) 3913-3923.

[21] L. Kloc, S. Spigarelli, E. Cerri, E. Evangelista, T. Langdon, An evaluation of the creep properties of two Al-Si alloys produced by rapid solidification processing, Metall. Mater. Trans. A, 27 (1996) 3871-3879.

[22] L. Kloc, S. Spigarelli, E. Cerri, E. Evangelista, T.G. Langdon, Creep behavior of an aluminum 2024 alloy produced by powder metallurgy, Acta Mater., 45 (1997) 529-540.

[23] F.A. Mohamed, K.-T. Park, E.J. Lavernia, Creep behavior of discontinuous SiC□Al composites, Mater. Sci. Eng., A, 150 (1992) 21-35.

[24] E.A. Marquis, D.C. Dunand, Model for creep threshold stress in precipitation-strengthened alloys with coherent particles, Scripta Mater., 47 (2002) 503-508.

[25] L. Kloc, E. Cerri, S. Spigarelli, E. Evangelista, T.G. Langdon, Significance of continuous precipitation during creep of a powder mettallurgy aluminum alloy, Mater. Sci. Eng., A, 216 (1996) 161-168.

[26] J. Čadek, H. Oikawa, V. Šustek, Threshold creep behaviour of discontinuous aluminium and aluminium alloy matrix composites: An overview, Mater. Sci. Eng., A, 190 (1995) 9-23.

[27] Y. Li, T.G. Langdon, Creep behavior of a reinforced Al-7005 alloy: Implications for the creep processes in metal matrix composites, Acta Mater., 46 (1998) 1143-1155.

[28] J. Čadek, K. Kuchařová, S. Zhu, Creep behaviour of an oxide dispersion strengthened Al–5Mg alloy reinforced by silicon carbide particulates—an oxide dispersion strengthened Al–5Mg–30SiC composite, Mater. Sci. Eng., A, 272 (1999) 45-56.

[29] Z.Y. Ma, S.C. Tjong, High-temperature creep behavior of SiC particulate reinforced Al-Fe-V-Si alloy composite, Mater. Sci. Eng., A, 278 (2000) 5-15.

[30] D.N. Seidman, E.A. Marquis, D.C. Dunand, Precipitation strengthening at ambient and elevated temperatures of heat-treatable Al(Sc) alloys, Acta Mater., 50 (2002) 4021-4035.

[31] M.E. van Dalen, D.N. Seidman, D.C. Dunand, Creep- and coarsening properties of Al–0.06 at.% Sc–0.06 at.% Ti at 300–450 °C, Acta Mater., 56 (2008) 4369-4377.

[32] Y. Li, T.G. Langdon, Creep behavior of an Al-6061 metal matrix composite reinforced with alumina particulates, Acta Mater., 45 (1997) 4797-4806.

[33] O.D. Sherby, J.L. Lytton, J.E. Dorn, Activation energies for creep of high-purity aluminum, Acta Metall., 5 (1957) 219-227.

[34] R.E. Reed-Hill, R. Abbaschian, Physical metallurgy principles, (1973).

[35] D. Hull, D.J. Bacon, Introduction to dislocations, Butterworth-Heinemann, 2011.

[36] M.O. Pekguleryuz, A.A. Kaya, Creep resistant magnesium alloys for powertrain applications, Adv. Eng. Mater., 5 (2003) 866-878.

[37] Y. Du, Y.A. Chang, B. Huang, W. Gong, Z. Jin, H. Xu, Z. Yuan, Y. Liu, Y. He, F.Y. Xie, Diffusion coefficients of some solutes in fcc and liquid Al: critical evaluation and correlation, Mater. Sci. Eng., A, 363 (2003) 140-151.

[38] K.E. Knipling, D.C. Dunand, D.N. Seidman, Criteria for developing castable, creep-resistant aluminum-based alloys-A review, Zeitschrift fur Metallkunde, 97 (2006) 246.

[39] J. Weertman, Steady-State Creep through Dislocation Climb, J. Appl. Phys., 28 (1957) 362-364.

[40] J. Weertman, Theory of Steady-State Creep Based on Dislocation Climb, J. Appl. Phys., 26 (1955) 1213-1217.

CHAPTER 8

INTERACTION BETWEEN MOLYBDENUM AND MANGANESE TO FORM EFFECTIVE DISPERSOIDS IN AN AL-SI-CU-MG ALLOY AND THEIR INFLUENCE ON CREEP RESISTANCE

The results obtained via microstructural investigation, in-depth characterization of the dispersoids via TEM and HRTEM (Chapters 5-7) and thermodynamic calculations by FactSage^{TM} software, led to a key phase of this doctoral study, the use of combined additions of Mo and Mn to further increase the volume fraction of the dispersoids, which resulted in the development of highly creep-resistant Al-Si-Cu-Mg-Mo-Mn alloys. Mn was of interest because of its low diffusivity and relatively high solid solubility in the Al matrix and its opposite partitioning behavior ($k_{Mn} < 1$ vs. $k_{Mo} > 1$) during non-equilibrium solidification. Mn is also known to form icosahedral phase, which is structurally similar to the Mo-containing dispersoids. This chapter has been submitted for peer-review: *A.R. Farkoosh, X.-G. Chen, M. Pekguleryuz, Interaction between molybdenum and manganese to form effective dispersoids in an Al-Si-Cu-Mg alloy and its influence on creep resistance, accepted by Materials Science and Engineering: A, (2014).*

ABSTRACT

The present work investigates the effect of adding Mo and Mn to an Al-Si-Cu-Mg alloy on the formation of thermally stable dispersoids. Mo and Mn in combination formed a large volume fraction of uniformly distributed dispersoids within the Al matrix, because of the opposite partitioning behavior ($k_{Mo} > 1\ vs.\ k_{Mn} < 1$) during the non-equilibrium solidification. Mo (without Mn) formed coherent α-Al(Fe,Mo)Si dispersoids with a BCC lattice, which were mostly located within intradendritic regions. Subsequent addition of Mn increased the amount of the dispersoids by substituting the Fe atoms. The combined addition also led to a more uniform dispersoid distribution by eliminating the interdendritic dispersoid-free zones (DFZs). Consequently, creep resistance in the temperature range of 300-350 °C improved significantly. At 300 °C and 30 MPa, the minimum creep rate decreased, and creep time-to-fracture and strain-to-fracture each increased with increasing Mn up to 0.5 wt.%. Further addition of Mn resulted in increased presence of the eutectic intermetallics in the interdendritic regions, which deteriorated the ductility of the alloy leading to a shorter creep-life time.

Keywords: Dispersoid; Al alloy; Creep; Manganese; Molybdenum; TEM

8.1 Introduction

Dispersion hardening resulting from a large volume fraction of uniformly dispersed fine dispersoids within the matrix is difficult to achieve in Al because of the low solid solubility of the dispersoid-forming elements [1]. In our previous studies [2, 3], it was shown that Mo can form a considerable amounts of metallurgically stable dispersoids in Al-Si cast alloys even when added at a low level. The Al matrix, supersaturated with Mo during non-equilibrium conventional solidification (casting), forms α-Al-(Fe,Mo)-Si dispersoids in the intradendritic regions during high temperature solution heat treatment. We have confirmed via selected area electron diffraction (SAED) analysis that the dispersoids possess a BCC crystal structure with a space group of Im3, and the lattice parameter of $a_0 = 12.54 \pm 0.03\ \overset{\circ}{A}$. The dispersoid phase was found to be structurally isomorphous with the α-AlFeSi intermetallic, having an approximate stoichiometric formula of $Al_{22}(Fe_{6-8}Mo)Si_4$. Structural analysis revealed that the BCC dispersoids are strongly correlated with the FCC Al matrix [3]. HRTEM studies have shown that, unlike the common dispersoids formed in commercial Al alloys, e.g. Al-Cr, these dispersoids are coherent with the matrix and the high coherency strain (up to ~ 6%) at the dispersoid/matrix interface has a significant influence on the creep resistance in the Al-6.5Si-0.5Cu-0.3Mg-(Mo) alloy system in the temperature range of 300-350 ºC [2, 4]. A large number of dispersoids were shown to have $\langle 001\rangle_d // \langle 001\rangle_m$ and $\{350\}_d // \{002\}_m$ orientation relationship with the matrix.

In the present work, thermodynamic calculations and experimental investigation were carried out to study the influence of Mn addition (in combination with Mo) on the dispersoid formation in the Al-7Si-0.5Cu-0.3Mg alloy and its effect on creep resistance. Mn was selected because of its: (i) low diffusivity in Al, (ii) substantial solubility in Al, (iii) ability to replace the Mo or Fe atoms in the α-Al(Fe,Mo)Si dispersoid phase or form structurally similar dispersoids and (iv) opposite partitioning behavior ($k_{Mo} > 1\ vs.\ k_{Mn} < 1$) during non-equilibrium solidification to form uniformly distributed dispersoids.

8.2 Thermodynamic simulation

Phase equilibria in the Al-6.5Si-0.5Cu-0.3Mg-0.1Fe-0.3Mo-(0.1-1.0)Mn multicomponent alloy systems were thermodynamically calculated to elucidate the phase selection and dispersoid formation in the Mo-containing alloys.

Al-Mo system [5-8]: The Al-rich region of the Al-Mo phase diagram (Fig. 8.1a) shows a series of consecutive peritectic reactions and the formation of different Al_XMo intermetallics. The BCC $Al_{12}Mo$ phase of $Al_{12}W$ type with the space group of Im3 [8] is the last phase that forms through a peritectic reaction from Al_5Mo at slightly above the melting point of pure Al (660.3 ºC). The occurrence of this terminal peritectic reaction at temperatures approaching the melting point of pure Al results in a very narrow freezing range for alloys with low amounts of Mo and a positive solidus and liquidus slopes. The maximum solid solubility is about 0.25% Mo at peritectic temperature (661 ºC), which decreases rapidly with temperature [5]. Our previous studies of the phase selection [2] show that in the Al-7Si-0.5Cu-0.3Mg system with low Mo and Fe levels, α-Al(Fe,Mo)Si is the only Mo-containing phase that forms during the solidification and high temperature heat treatments.

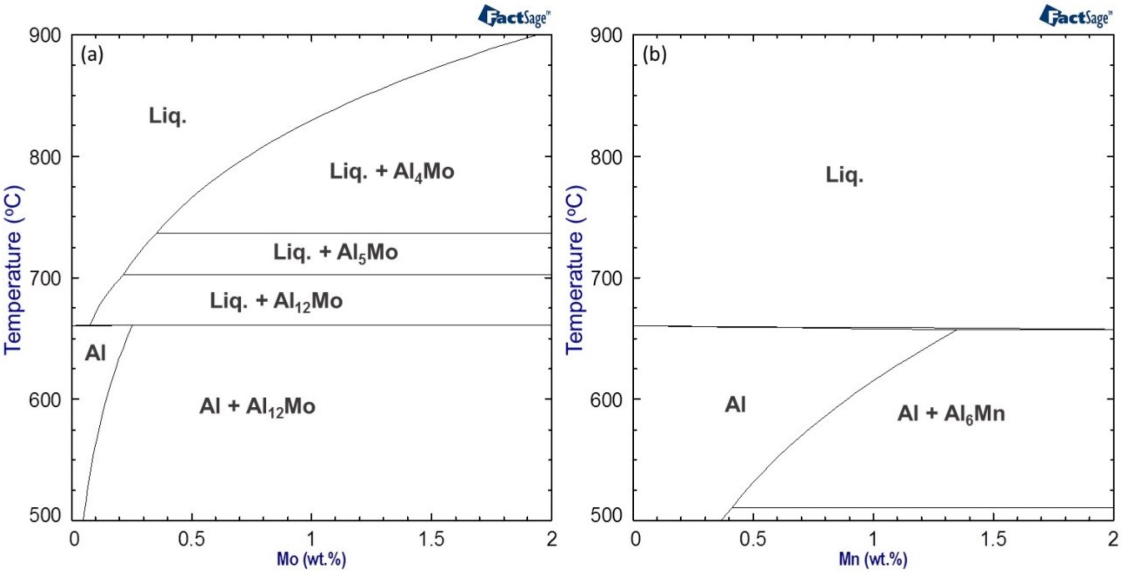

Fig. 8.1 (a) Al-Mo and (b) Al-Mn binary phase diagram, calculated by FactSage.

Al-6.5Si-0.5Cu-0.3Mg-0.1Fe-0.3Mo-(Mn) system: Manganese is of interest as an alloying addition to the Al-Si-Cu-Mg-Fe-Mo system, since it has relatively high solid solubility in Al (1.25% at 658 °C, ~0.1% at 300 °C) [9]. Mn is reported to form the α-Al(Fe,Mn)Si phase in certain Al alloys [10-16], which is structurally close to the α-Al(Fe,Mo)Si dispersoid phase [3]. Additionally, having a solid-liquid partition coefficient, $k_0 = C_S/C_L$ less than unity (Mn forms a terminal eutectic with Al, Fig. 8.1b [5]), Mn segregates towards the interdendritic regions, while Mo as a peritectic element segregates inversely to the dendrite cores. These opposite solute distribution profiles can yield a more uniform distribution of the dispersoids and eliminate dispersoid-free zones (DFZs).

Thermodynamic calculations were carried out using FactSage software (using FTlight data base) on an alloy system of Al-7Si-0.5Cu-0.3Mg-0.1Fe-0.3Mo with Mn additions in the range of 0.0-1.0%. Fig. 8.2a shows a calculated isopleth of the Al-7Si-0.5Cu-0.3Mg-0.1Fe-0.3Mo-(0.1-1.0)Mn system (M3R3M-Mn). The amounts of the phases that form at different temperatures in one of the alloys in the system, the Al-7Si-0.5Cu-0.3Mg-0.1Fe-0.3Mo-0.5Mn alloy (shown with the dashed line in Fig. 8.2a), are given in Fig. 8.2b. The solidus and the liquidus do not change with Mn concentration and Mn less than 0.75% has no significant influence on the freezing range

(Fig. 8.2a). Below 0.75% Mn, solidification starts with the formation of the primary Al phase (615 ^{o}C) followed by the precipitation of the secondary α-Al(Fe,Mo,Mn)Si intermetallic phase. The Al-Si eutectic mixture begins to form at 574 ^{o}C and continues to precipitate along with the α-Al(Fe,Mo,Mn)Si phase as the temperature decreases to 556 ^{o}C, at which point the solidification terminates. Above 0.75% Mn, solidification occurs with the formation of the primary α-Al(Fe,Mo,Mn)Si intermetallic phase; because of the direct formation of these primary intermetallics from the liquid phase, they are expected to be very coarse and bulky, which can adversely affect the ductility of the alloy.

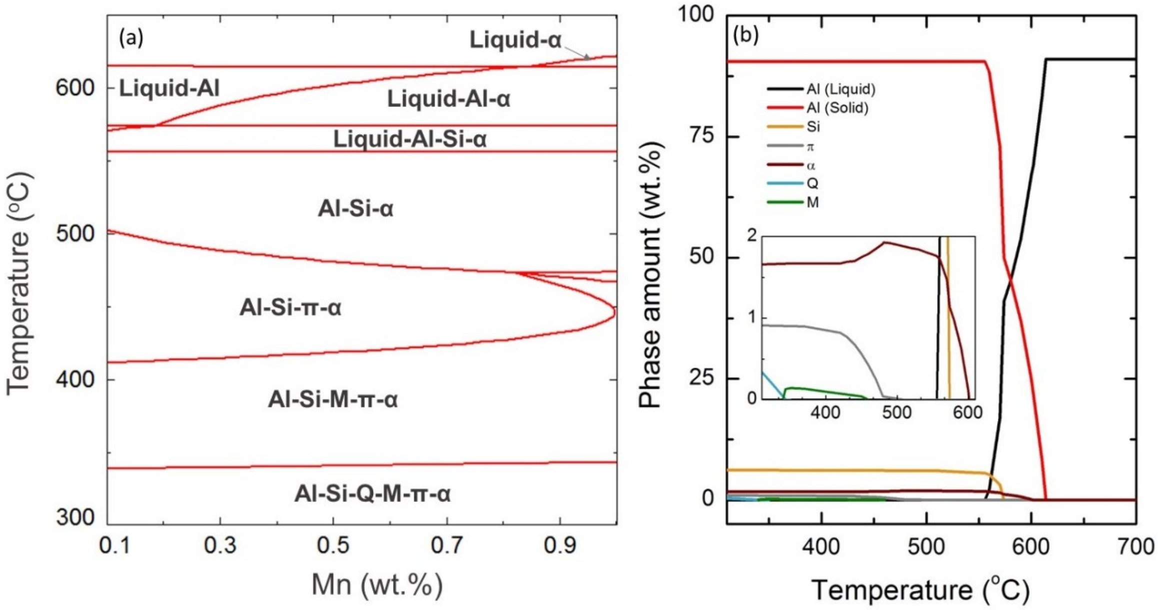

Fig. 8.2 (a) Calculated Al-7Si-0.5Cu-0.3Mg-0.1Fe-0.3Mo-(Mn) phase diagram, (b) the amount of the different phases as a function of temperature (equilibrium cooling conditions) for the Al-7Si-0.5Cu-0.3Mg-0.1Fe-0.3Mo-0.5Mn alloy (Mn = 0.5%). α-Al(Fe,Mo,Mn)Si, π-Al$_8$FeMg$_3$Si$_6$, Q-Al$_5$Cu$_2$Mg$_8$Si$_6$, M-Mg$_2$Si.

Scheil simulation: We have reported in our previous work that [3] the α-Al$_{22}$(Fe$_{6\text{-}8}$Mo)Si$_4$ dispersoid phase in the Al-6.5Si-0.5Cu-0.3Mg-0.1Fe-0.3Mo alloy precipitates from the supersaturated Al matrix during solution treatment of the cast alloys. Scheil cooling calculations have been performed to simulate the as-cast microstructures and determine the amount of the Mn trapped in the Al matrix during the non-equilibrium solidification. Scheil solidification assumes that no solute back diffusion occurs in the solid phase and that the local concentration of the solid remains constant during the solidification [17]. Also, the liquid phase is assumed to have a uniform concentration because of complete mixing. Calculations (Fig. 8.3a) show that the Mn concentration in the cast Al matrix, C_{Mn} increases with Mn up to C_{Mn} ~ 0.12%, in the alloy with 0.5% Mn (Al-7Si-0.5Cu-0.3Mg-0.1Fe-0.3Mo-0.5Mn). However, Mn > 0.5% does not change the degree of supersaturation. The amount of the α-Al(Fe,Mo,Mn)Si intermetallic phase formed during solidification (Fig. 8.3b, Table 8.1) increases from 0.34% in the Al-7Si-0.5Cu-0.3Mg-0.1Fe-0.3Mo alloy (with no Mn) to 3.28% in the Al-7Si-0.5Cu-0.3Mg-0.1Fe-0.3Mo-1Mn alloy (with 1% Mn). To calculate the amount of the dispersoids formed during solution treatment at 540 ^{o}C, equilibrium calculations were conducted using the matrix concentrations obtained from the Scheil cooling calculations. The calculated amount of the dispersoid phase at 540 ^{o}C (Fig. 8.3c) is directly proportional to C_{Mn} (Fig. 8.2a); it is noted that the amount of the dispersoid phase can increase to maximum 0.27% with the addition of 0.5% Mn. Increasing Mn beyond 0.5% specifically increases the amount of the primary α-Al(Fe,Mo,Mn)Si phase, which may be detrimental to the ductility of the alloy and cause feeding problems during the solidification.

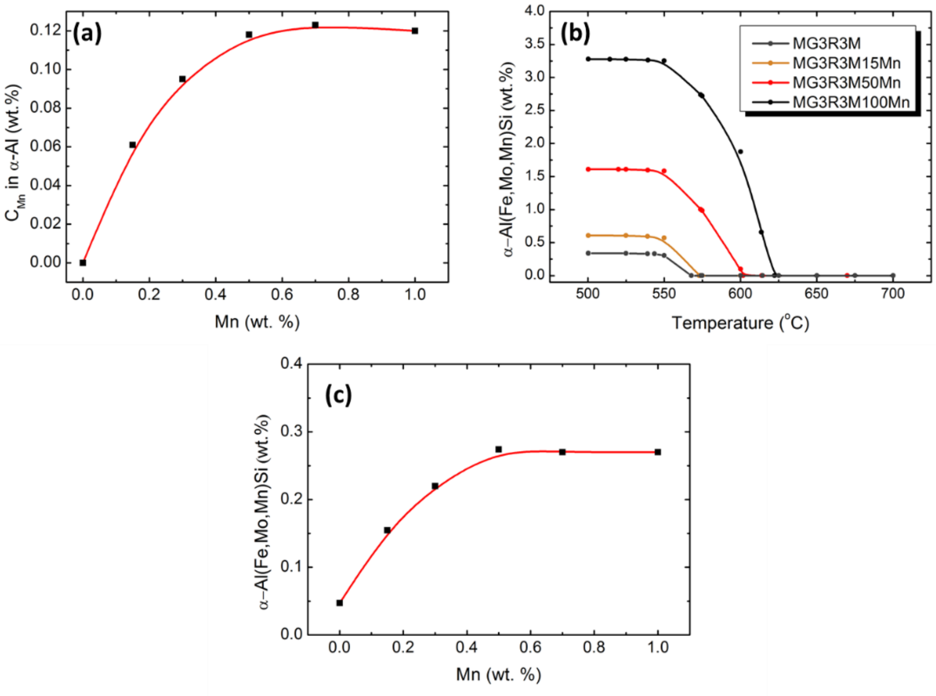

Fig. 8.3 Calculated (Scheil cooling) amount of (a) Mn in the Al matrix, C_{Mn} after solidification as a function of the Mn content of the alloy and (b) the α-Al(Fe,Mo,Mn)Si phase formed during solidification, (c) calculated (equilibrium) amount of the α-Al(Fe,Mo,Mn)Si dispersoid phase formed after solution treatment at 540 ^{o}C.

Table 8.1 Calculated amount of the different intermetallic phases formed during solidification (Scheil cooling)

Alloy	Phase amount (wt.%)			
	π	Q	θ	A
MG3R3M	0.15	0.35	0.35	0.34
MG3R3M15Mn	N*	0.27	0.27	0.62
MG3R3M50Mn	N	0.23	0.22	1.61
MG3R3M100Mn	N	0.23	0.23	3.28

N* = negligible

8.3 Experimental procedures

Commercial grade A356 alloy supplied by Rio Tinto Alcan Inc. was melted in a silicon carbide crucible using a high frequency NORAX Canada induction furnace. Cu, Mo and Mn were added to the melt from a set of master alloys (Al-33 wt.% Cu, Al-10 wt.% Mo and Al-25 wt.% Mn) at 760 ^{o}C, holding for 15 minutes to dissolve. All the alloys are modified with 150 ppm Sr, using Al-10 wt.% Sr master alloy. After 3 minutes of degassing with high purity argon gas at flow rate of 1 L/min, the alloys were cast into a pre-heated (400 ^{o}C) permanent mold at 730 ^{o}C to obtain cylindrical bars with diameter of 30 mm. The chemical compositions of the alloys are determined by the inductively coupled plasma (ICP) technique and are presented in Table 2; alloys are designated according to their Mn content. In this study, all compositions are given in wt.% hereafter, unless otherwise specified.

Table 8.2 Chemical compositions of the alloys

Alloy	Chemical Composition (wt.%)								
	Si	Mg	Cu	Fe	Ti	Mo	Mn	Sr	Al
MG3R3M	6.49	0.31	0.53	0.11	0.10	0.29	<0.01	0.014	Bal.
MG3R3M15Mn	6.66	0.36	0.56	0.13	0.11	0.34	0.18	0.014	Bal.
MG3R3M30Mn	6.75	0.29	0.53	0.10	0.11	0.31	0.27	0.016	Bal.
MG3R3M50Mn	6.81	0.30	0.50	0.12	0.10	0.27	0.51	0.015	Bal.
MG3R3M100Mn	6.54	0.35	0.55	0.12	0.11	0.29	0.95	0.015	Bal.

Creep test specimens with a cylindrical gauge length and diameter of 50 and 12.7 mm were machined from the castings according to the ASTM E8 standard and given a T7 heat treatment in an electrically heated, air-circulating chamber furnace. To avoid probable incipient melting, the solution treatment was carried out in two stages; 4 hours at 500 ^{o}C followed by 1 hour at 540 ^{o}C. The samples were then quenched in water at room temperature and aged at 200 ^{o}C for 5 hours (T7). Tensile creep testing was conducted at 300 and 350 ^{o}C under constant load corresponding to stresses in the range of 12-30 MPa. Temperature was monitored using a thermocouple with an error of ± 0.1 °C attached to the specimen. The gauge length displacement was measured with two high precision extensometers with a resolution of 5 μm. All elevated temperature tests were conducted in air and samples were soaked at 300 °C, 100 hours prior to testing. Specimens for microstructural characterization were cut from the castings using a low speed diamond saw and ground with a series of SiC papers. Specimens were then polished on a porous neoprene polishing cloth with Al_2O_3 solution. Final polishing was performed with a Buehler vibratory polisher using a colloidal silica solution. A Hitachi SU-3500 scanning electron microscope (SEM) equipped with a silicon drift detector (SDD) - X-Max^N was used for detailed second-phase observations. The accelerating voltage was 15 kV and a beam current of 10 μA was chosen. For transmission electron microscopy (TEM) studies, thin foils were prepared by mechanical grinding and jet polished using a Struers Tenupol 5 jet polisher. A solution of 10% Nitric acid in methanol was used at -40 °C. TEM and corresponding selected area electron diffraction pattern (SAED) analyses were performed with a Philips CM200 microscope operated at 200 kV. The EDS spectra were obtained by EDAX detector connected to the column. Precipitate diameter and particle size distribution (PSD) were determined by image analysis of the TEM micrographs. Precipitates (a minimum of 100 measurements per sample) were manually traced and the dimensions were determined using ImageJ software. The diameter of an area-equivalent circle was reported as precipitate size.

8.4 Experimental results and discussion

8.4.1 As-cast microstructure

Representative as-cast microstructures of the alloys with Mn content in the range of 0.0-1.0% are shown in Figs. 8.4a-d. The secondary dendrite arm spacing (SDAS) for each of the different alloys was measured to be 30 ± 5 μm showing no relation with the Mn content. Table 3 shows the different phases formed in this alloy system. The α-Al(Fe,Mo)Si phase is the only Mo-containing intermetallic that forms in the Al-7Si-0.5Cu-0.3Mg-0.1Fe-0.3Mo alloy during solidification and appears as blocky-shape bright-white intermetallics under SEM in the backscattered mode (Fig. 8.4a). EDS analysis shows that in the presence of Mn (Fig. 8.4b-c), Fe seems to substitute for Mn up to ~50% in the α-Al(Fe,Mo)Si phase. The amount of the α-Al(Fe,Mn,Mo)Si phase increases with increasing Mn (going from Fig. 8.4b to 8.4d).

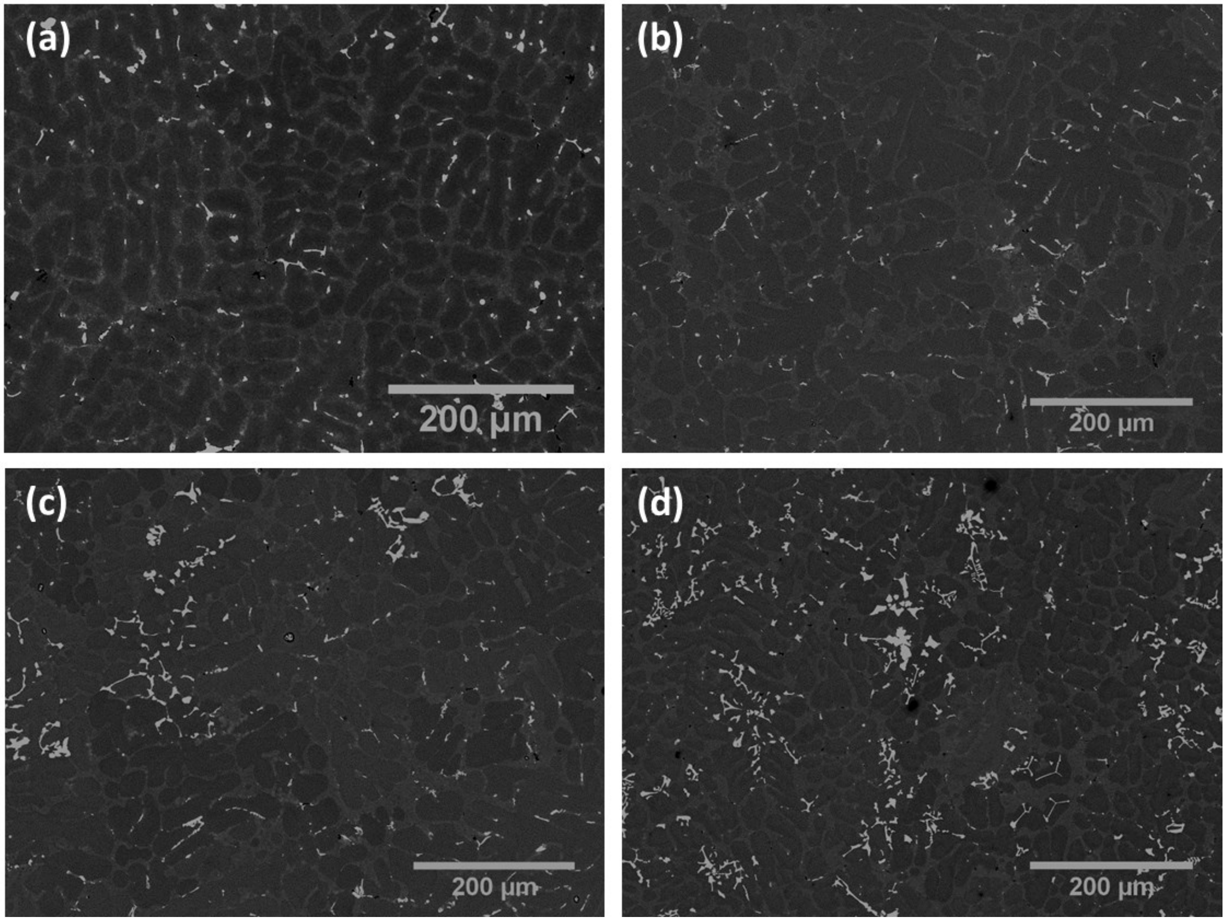

Fig. 8.4 BSE-SEM micrographs showing the as-cast microstructure of the (a) Al-7Si-0.5Cu-0.3Mg-0.1Fe-0.3Mo, (b) Al-7Si-0.5Cu-0.3Mg-0.1Fe-0.3Mo-0.15Mn, (c) Al-7Si-0.5Cu-0.3Mg-0.1Fe-0.3Mo-0.5Mn and (d) Al-7Si-0.5Cu-0.3Mg-0.1Fe-0.3Mo-1.0Mn alloys.

Two alloys, Al-7Si-0.5Cu-0.3Mg-0.1Fe-0.3Mo (containing Mo, with solid-liquid partition coefficient, $k_0 = C_S/C_L > 1$) and Al-7Si-0.5Cu-0.3Mg-0.1Fe-0.3Mo-0.15Mn (containing Mo and Mn with $k_0 = C_S/C_L < 1$) were selected to study the differences in solute segregation. In the MG3R3M alloy, during non-equilibrium solidification, the peritectic nature of the alloy system ($k_0 > 1$) leads to the Mo supersaturation of the dendrite cores. The first solid (α-Al) to form is rich in Mo and as solidification progresses the Mo concentration decreases gradually till the end of the solidification where Al dendrites impinge. In comparison, Mn in the MG3R3M15Mn alloy segregates towards the dendrite boundaries($k_0 < 1$). EDS elemental line scan was performed on the as-cast Al-7Si-0.5Cu-0.3Mg-0.1Fe-0.3Mo-0.15Mn (Fig. 8.5); it is seen the Mo atoms are mostly segregated into the Al dendrite core while the Mn atoms primarily partition into the interdendritic regions.

Table 8.3 Different phases formed in the alloys studied

Phase	Alloy	Composition (wt.%)						Crystal structure	Space group	Lattice parameters (A°)	Ref.
		Mo	Mn	Fe	Si	Mg	Cu				
α-Al(Fe,Mo)Si	MG3R3M	8.1		24.8	10.3		<1	BCC	Im3	$a = 12.54 \pm 3$	[3]
α-Al(Fe,Mn,Mo)Si	MG3R3MXMn	6.7	12.8	12.6	10		<1	BCC	Im3	$a = 12.56 \pm 4$	This work
θ-Al_2Cu	MG3R3M, MG3R3MXMn						53.2	Tetragonal	I4/mcm	$a = 6.07$, $c = 4.87$	[5]
Q-$Al_5Cu_2Mg_8Si_6$	MG3R3M, MG3R3MXMn				27	31.1	20.3	Hexagonal		$a = 10.32$, $c = 4.05$	[26]
π-$Al_8FeMg_3Si_6$	MG3R3M, MG3R3MXMn			10.9	32.9	14.1		Hexagonal	$P6\bar{2}m$	$a = 6.63$, $c = 7.94$	[27]

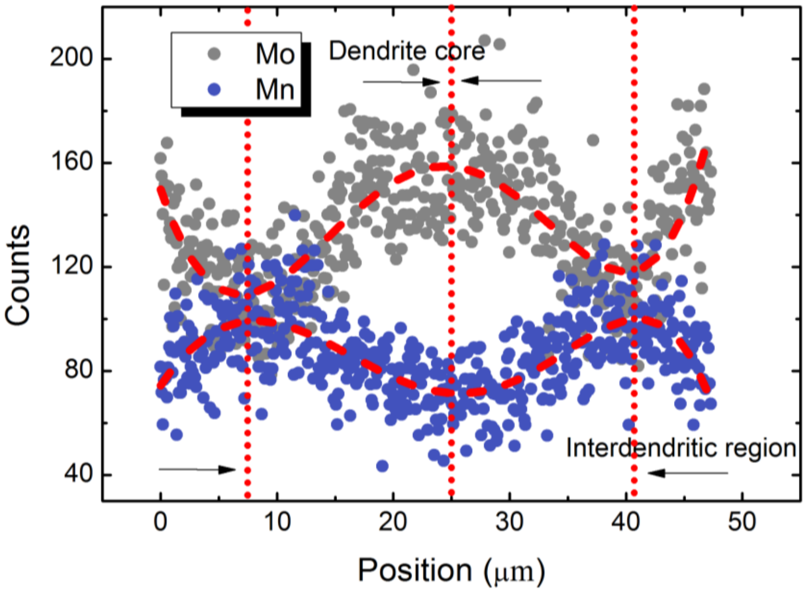

Fig.8.5 EDS elemental line scanning across a dendrite cell showing the concentration gradients of Mo and Mn (microsegregation) in the as-cast Al-7Si-0.5Cu-0.3Mg-0.1Fe-0.3Mo-1.5Mn alloy. It can be seen that Mo is segregated in the Al dendrite core while Mn is segregated in the interdendritic region.

8.4.2 Precipitation of dispersoids at 540 °C

After 10 hours of solution treatment at 540 °C, dispersoids appeared in the intradendritic regions of the alloys with 0.0, 0.15 and 0.5% Mn (Figs 8.6a-c). The morphology of the dispersoids is "rectangular/rhomboidal"; their particle size distribution (PSD) is bimodal (Fig. 8.6d).

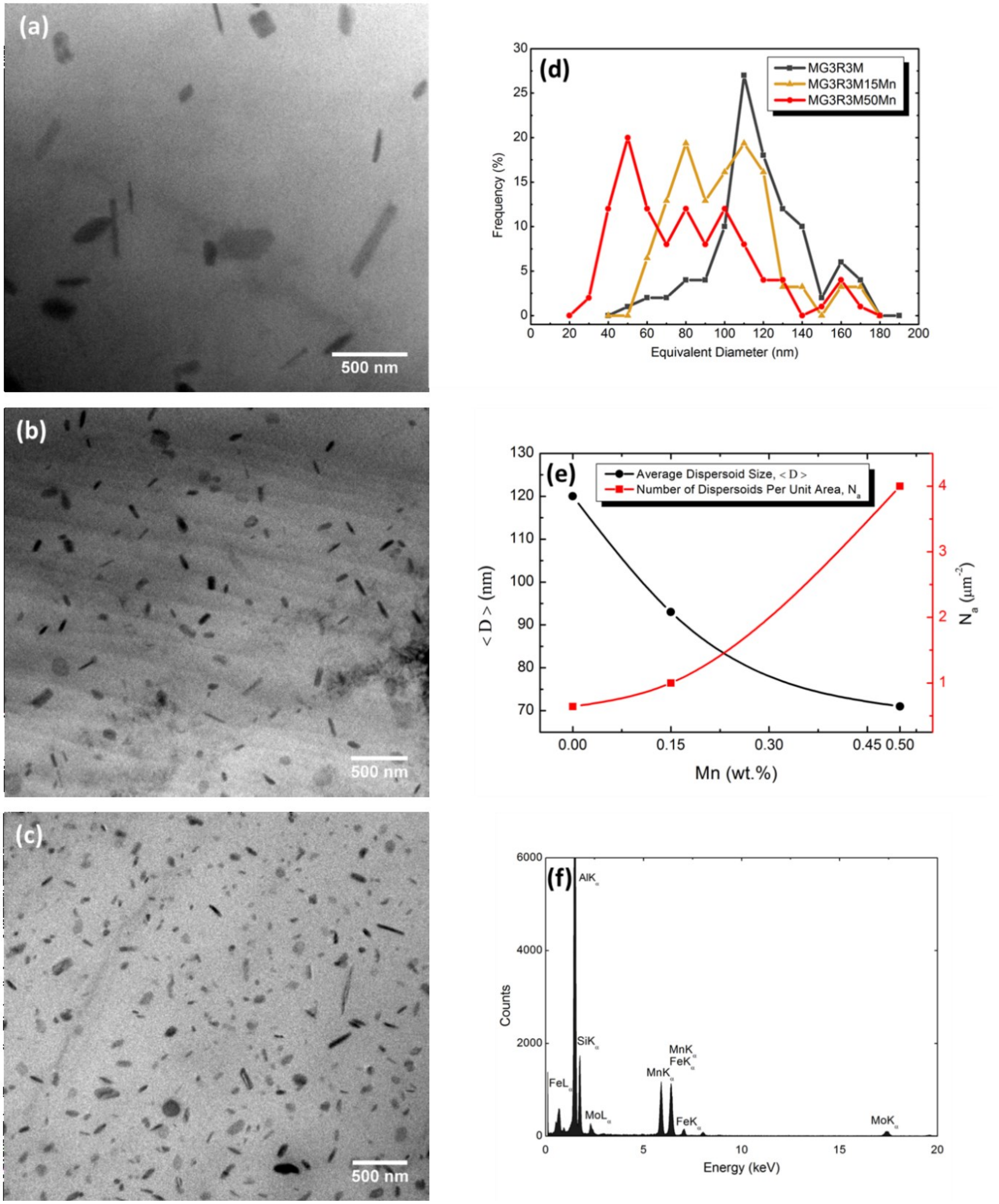

Fig. 8.6 BF-TEM micrographs showing dispersoids formed in (a) Al-7Si-0.5Cu-0.3Mg-0.1Fe-0.3Mo, (b) Al-7Si-0.5Cu-0.3Mg-0.1Fe-0.3Mo-15Mn and (c) Al-7Si-0.5Cu-0.3Mg-0.1Fe-0.3Mo-0.5Mn alloys at 540 °C after 600 minutes in intradendritic regions, along with (d) the particle size distribution of the dispersoids (histogram). (e) Average dispersoid size and the number of dispersoids per unit area (f) EDS spectrum of the dispersoids.

The number of dispersoids per unit area, N_a measured in the solution-treated alloys increases significantly (from ~ 0.6 to ~ 4 μm^{-2}) with increasing the Mn content (from 0.0 to 0.5%); while the average dispersoid size, < D > decreases from ~120 nm to ~70 nm (Fig. 8.6e), with increasing Mn and the PSD broadens. It has been reported that the dissolution of alloying elements with low diffusivity in the dispersoid phase can decrease the growth rate constant [18], which leads to a slower growth kinetics at the solution treatment temperature. This can explain the decreased size of the dispersoids as a result of Mn addition (diffusivity of Mn is 6.24×10^{-19} at 400 °C which is ~10 times lower than that of Fe, 5.41×10^{-18} at the same temperature [1]). The fact that PSD broadens with Mn suggests that the nucleation and growth of the dispersoids occurs concurrently at higher Mn contents because the Mn supersaturation of the Al matrix increases; by increasing the Mn content the amount of the Mn that remains in the Al matrix during solidification increases. The bimodal distribution of the dispersoids in the Al-7Si-0.5Cu-0.3Mg-0.1Fe-0.3Mo alloy shows that concurrent coarsening and dissolution of the dispersoids seem to occur during high temperature heat treatment; the rate is accelerated likely because of the rapid pipe-diffusion of solutes between the dispersoids located on the dislocations.

TEM-EDS analysis shows that the stoichiometric formula of α-Al(Fe,Mo,Mn)Si phase (intermetallic and dispersoids) in all the Mn-containing alloys studied is $Al_{22}(Fe_{1-3}Mn_{4-6}Mo)Si_4$; the Fe atoms seem to be substituted by Mn up to 50% (Fig. 8.6f). Fig. 8.7a shows the SEM-EDS line scanning across the intermetallic particle found in the interdendritic regions of the as-cast Al-7Si-0.5Cu-0.3Mg-0.1Fe-0.3Mo-0.15Mn alloy in which the Mo, Mn and Si concentrations are similar to the dispersoid seen in the same alloy after 20 hours of solution treatment (Fig. 8.7b).

TEM analysis was performed (samples were prepared by PPIPS) to further reveal the difference in dispersoid formation and distribution in the presence of Mn. Fig. 8.8a shows a DFZ in the Al-7Si-0.5Cu-0.3Mg-0.1Fe-0.3Mo alloy after 600 min of solution treatment at 540 °C. The last Al solid formed during the peritectic solidification of the alloy has negligible amounts of Mo solute atoms, below the amount required for the precipitation of the dispersoids, which leads to the formation of dispersoid-free zones after high temperature solution treatment. Assuming a SDAS of 30 μm, the area fraction of the DFZ is estimated to be ~10%. On the other hand, the presence of a dispersoid-free zone is not observed in the Al-7Si-0.5Cu-0.3Mg-0.1Fe-0.3Mo-0.15Mn alloy; considerable amounts of dispersoids are found in the interdendritic regions after solution treatment (Fig. 8.8b). As discussed above (Fig. 8.5), the Mn supersaturation was interdendritic in the Al-7Si-0.5Cu-0.3Mg-0.1Fe-0.3Mo-0.15Mn while the Mo segregation was intradendritic giving an opposing solute partitioning pattern (Fig. 8.5). This pattern leads to a more uniform distribution of the dispersoids after solution heat treatment which would minimize DFZs.

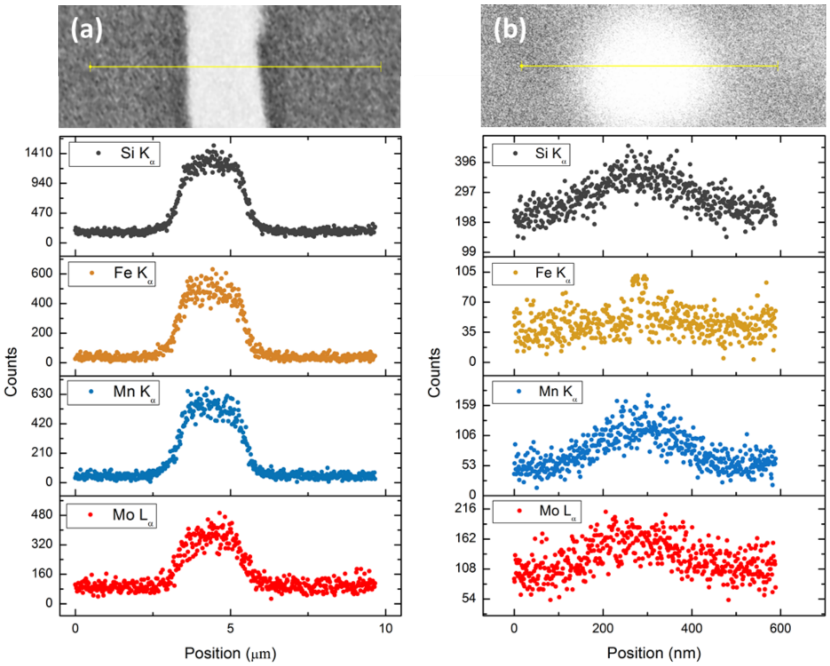

Fig. 8.7 SEM-EDS elemental line scanning across (a) a bulky intermetallic particle formed during solidification and (b) a dispersoid of about 250 nm formed in the Al-7Si-0.5Cu-0.3Mg-0.1Fe-0.3Mo-0.15Mn alloy after 1200 min of solution treatment.

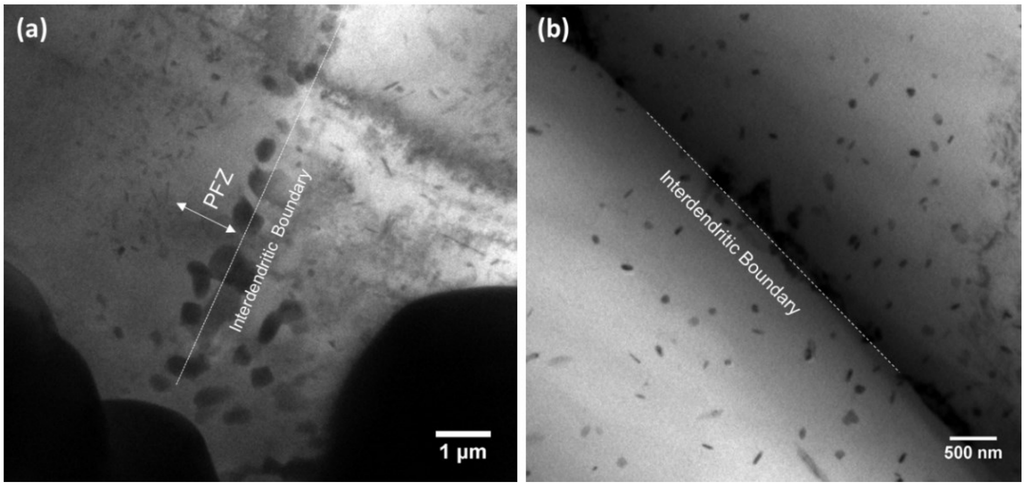

Fig. 8.8 Dispersoid distribution after 600 min of solution treatment at 540 °C in the interdendritic regions of the alloys, showing (a) a DFZ in Al-7Si-0.5Cu-0.3Mg-0.1Fe-0.3Mo and (b) presences of the dispersoids in an interdendritic region of Al-7Si-0.5Cu-0.3Mg-0.1Fe-0.3Mo-0.15Mn.

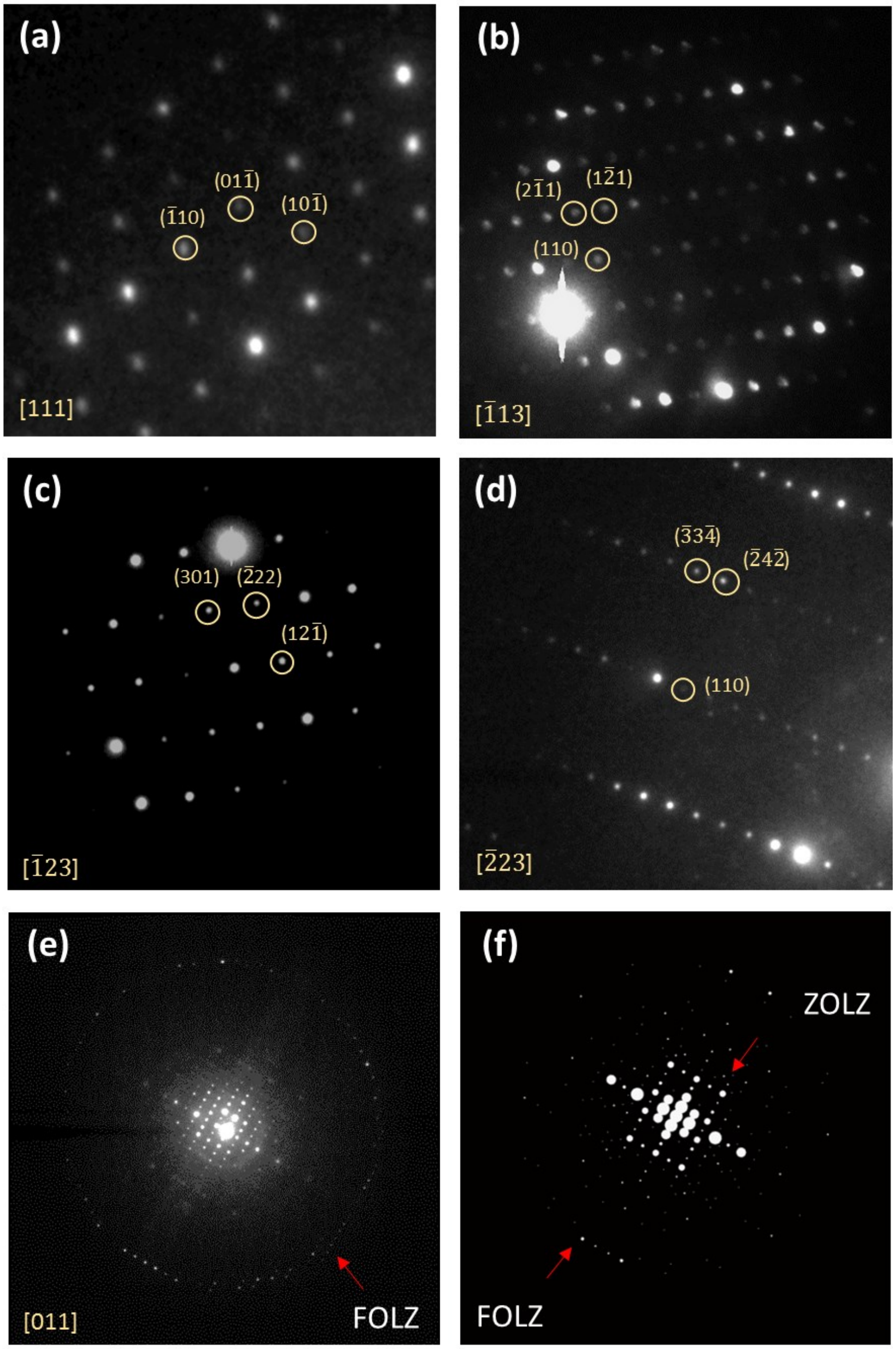

Fig. 8.9 Selected area electron diffraction patterns (SAEDs) recorded along the (a) [111], (b) $[\bar{1}13]$, (c) $[\bar{1}23]$, (d) $[\bar{2}23]$ and (e) [011] zone axes of an individual α-Al(Fe,Mn,Mo)Si dispersoid formed in the intradendritic regions of the Al-7Si-0.5Cu-0.3Mg-0.1Fe-0.3Mo-0.15Mn alloy during solution treatment at 540 ^{o}C. (f) Kinematically simulated [28] electron diffraction patterns of the α-phase along the [011] zone axis showing the FOLZ individual reflections surrounding the ZOLZ region. This pattern closely matches the experimental pattern in (e) confirming the BCC structure of the dispersoids.

8.4.3 The influence of Mn on the crystal structure of the precipitates

In our previous study [3] we demonstrated that the crystal structure of the dispersoids formed in the Al-7Si-0.5Cu-0.3Mg-0.1Fe-0.3Mo alloy was BBC (body centered cubic) with $a_0 = 12.54 \pm 0.03\ \mathring{A}$. To investigate the effect of Mn on the crystal structure of the dispersoids, SAED analysis was conducted. Figs. 8.9a-e show the SAED patterns recorded along the different zone axes of an individual dispersoid in the intradendritic regions of the solution-treated Al-7Si-0.5Cu-0.3Mg-0.1Fe-0.3Mo-0.15Mn alloy. Each pattern was indexed on the basis of a BCC lattice with reflections satisfying $h + k + l = 2n$. The lattice parameter was determined to be slightly larger: $a_0 = 12.56 \pm 0.04\ \mathring{A}$. From the symmetry elements observed in the diffraction patterns, the space group was deduced to be Im3. Although it has been reported that at high Mn:Fe ratios the α-phase transforms to a SC (simple cubic) structure (Pm3 space group) [10, 19], however, Mo has a stabilizing effect on the BCC structure; it can be clearly seen that the reflections for which $h + k + l \neq 2n$ are absent in all the SAED patterns of Fig. 8.9. To further investigate the stabilizing effect of Mo, the SAED patterns were kinematically simulated using a modified BCC structural model proposed by Cooper [20]. Some of the Fe atoms were substituted with the Mn and Mo atoms (to give the experimentally measured stoichiometry) and the experimentally determined lattice constant $\alpha_0 = 12.56\ A°$ was used. Fig. 8.9f shows the calculated SAED along the [011] zone axis, which closely matches the experimental SAED in Fig. 8.9e, confirming the BCC structure of the dispersoids. Because of the large lattice constant of the crystal, the first order Laue zone (FOLZ) ring can also be seen on both the experimental and simulated diffraction patterns. The FOLZ radius also matches the calculations and is compatible with the BCC structure.

8.4.4 Creep

Creep tests were conducted at 300 and 350 ºC to investigate the effect of 0.15% Mn addition (Al-7Si-0.5Cu-0.3Mg-0.1Fe-0.3Mo-0.15Mn alloy) on the creep resistance of the alloys studied. A solution treatment was performed (4 hours at 500 ºC followed by 1 hour at 540 ºC), which yields optimum dispersoid size and distribution for maximum creep resistance in the Al-7Si-0.5Cu-0.3Mg-0.1Fe-0.3Mo alloy [4]. Fig. 8.10 shows the plot of minimum creep rate, $\dot{\varepsilon}_m (= d\varepsilon/dt)_{min}$ versus the applied stress, σ, on a double-logarithmic scale for the Al-7Si-0.5Cu-0.3Mg-0.1Fe-0.3Mo and Al-7Si-0.5Cu-0.3Mg-0.1Fe-0.3Mo-0.15Mn alloys. The addition of a low amount of Mn (0.15%) significantly increases the creep resistance especially at 350 ºC.

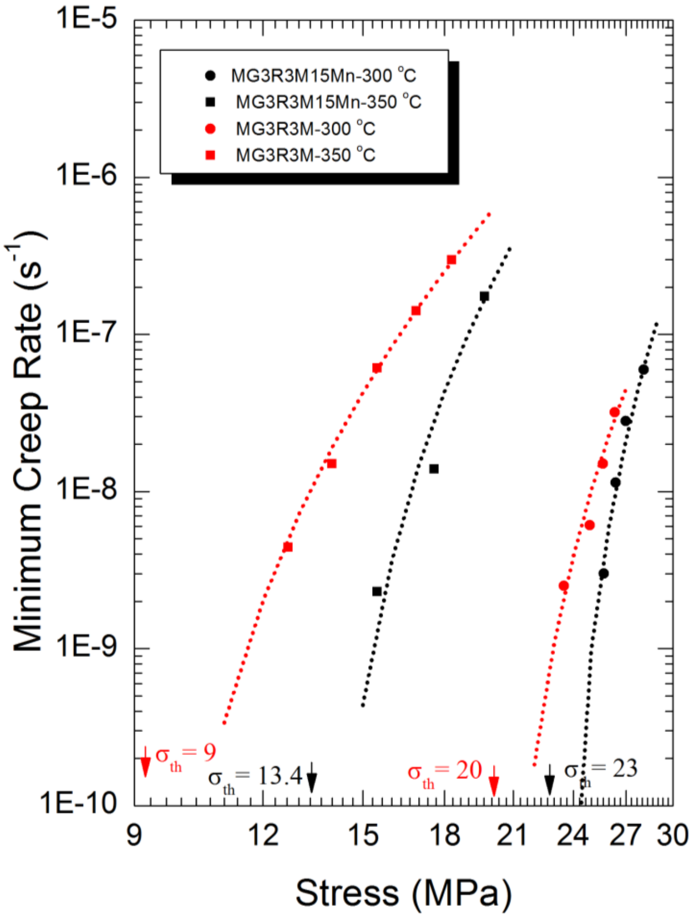

Fig. 8.10 Minimum creep rate vs. applied stress for the MG3R3M and MG3R3M15Mn alloys at 300-350 °C plotted on a double-logarithmic scale. Calculated threshold stresses are shown on the graph.

The apparent stress exponent, $n_a (= \partial \ln \dot{\varepsilon}_m / \partial \ln \sigma)$ is much higher than that for pure Al (4.4) [21] and varies with stress, which are indications of the dislocation creep in dispersion hardened alloys. As discussed in our previous study [4], a threshold stress approach can be used to rationalize the creep data. Introduction of the threshold stress, σ_{th}, below which dislocation creep is not significant, into the power-law equation and modulus corrections gives [22, 23]:

$$\dot{\varepsilon}_m = A' \left(\frac{\sigma - \sigma_{th}}{G}\right)^n \exp\left(-\frac{Q}{RT}\right) \tag{1}$$

where, Q is the activation energy, G is the shear modulus, n is stress exponent of the matrix, A' is a constant and RT has its usual meaning. The values for threshold stress were estimated using equation (1), plotting $\dot{\varepsilon}^{1/n}$ vs. σ and extrapolating the data to $\dot{\varepsilon} = 0$. The stress exponent, n = 4.4 for the dislocation creep of Al was applied, which yielded the best linear fit to the data points. It can be seen that 0.15% Mn addition increases the threshold stress by 3 and 4.4 MPa at 300 and 350 ºC, respectively (as indicated by arrows in Fig. 8.10). Because of the high apparent stress exponent, an increase of ~3 MPa in threshold stress translates into an order of magnitude decrease in minimum creep rate. This can be accounted for by the increased amount of the dispersoids following Mn addition. Furthermore, the absence of interdendritic DFZs (where dislocations can move freely at low stresses) in the Al-7Si-0.5Cu-0.3Mg-0.1Fe-0.3Mo-0.15Mn alloy increases effective dislocation pinning and decreases the creep deformation rate.

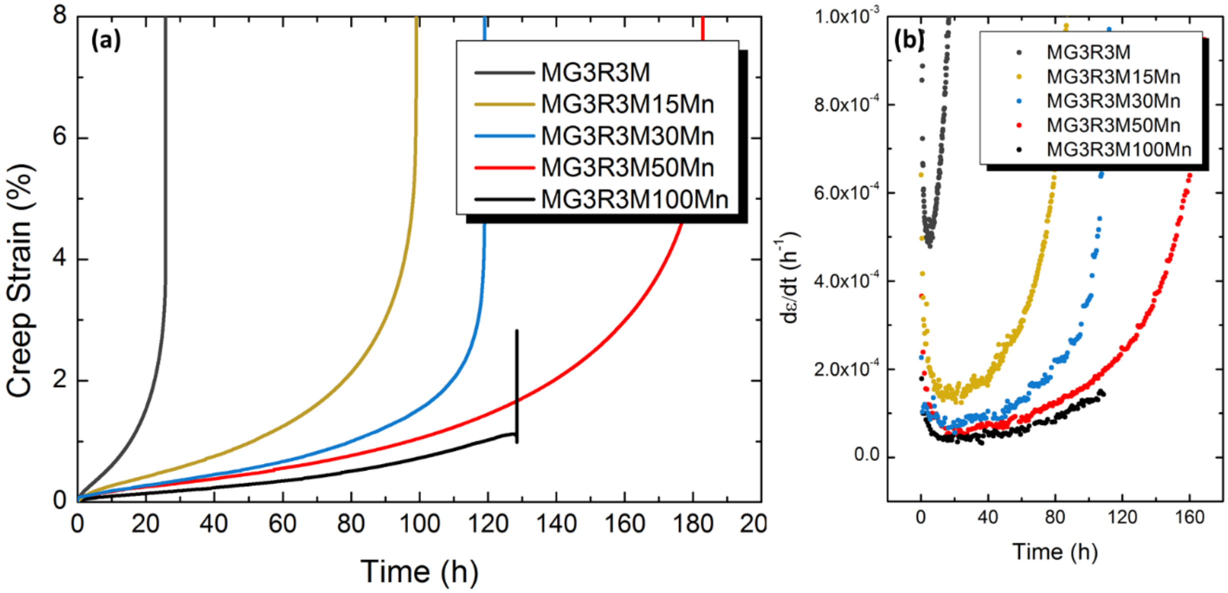

Fig. 8.11 (a) Tensile creep deformation vs. time for the alloys studied at 30 MPa and 300 ºC, (b) corresponding strain rate vs. time calculated from (a).

Fig. 8.11a shows the effect of Mn level on the creep deformation of the alloys studied. The minimum creep rate decreases with Mn (Fig. 8.11b), which is significant at low levels of Mn (0.15), however, it becomes less significant at higher Mn levels. By increasing the Mn content, the amount of the dispersoids increases, which lowers the dislocation processes during creep (increased threshold stress), and results in lower creep rate. At higher Mn content, the contribution of the dislocation creep to the total creep strain becomes less significant, thereby the reduction in minimum creep rate decreases with increasing the Mn content.

It can be seen that the creep time-to-fracture (Fig. 8.11a) increases from ~25 to ~180 hours as Mn increases from 0.0 to 0.5%, however, at 1% Mn, creep time-to-fracture dramatically decreases to 130 hours, which can be explained by the decreased ductility of the alloy at 1% Mn.

Microstructural investigations show the presence of a large amount of the interdendritic α-Al(Fe,Mo,Mn)Si intermetallics in the Al-7Si-0.5Cu-0.3Mg-0.1Fe-0.3Mo-1.0Mn alloy (Fig. 8.2d). Being more brittle than the Al matrix, these intermetallics at high volume fractions can deteriorate the ductility of the alloy; the dislocation pile-up at intermetallic/matrix interface can generate sufficiently high stresses that can cause fracture [24, 25].

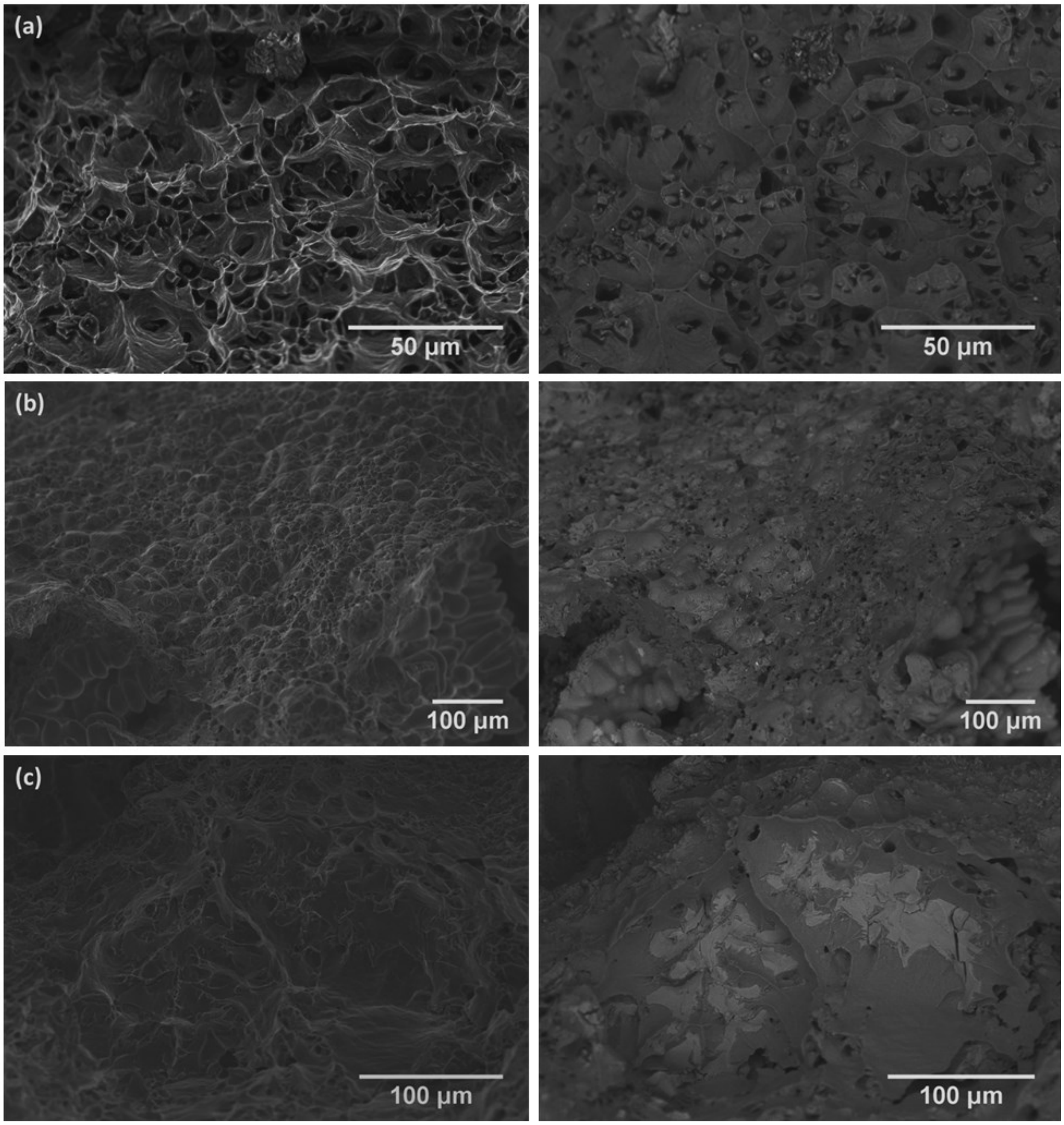

Fig. 8.12 SEM micrographs of the fracture surfaces (SE image on the left and BSE image on the right) after creep to fracture at 300 ºC 30 MPa, (a) Al-7Si-0.5Cu-0.3Mg-0.1Fe-0.3Mo, (b) Al-7Si-0.5Cu-0.3Mg-0.1Fe-0.3Mo-0.5Mn and (c) Al-7Si-0.5Cu-0.3Mg-0.1Fe-0.3Mo-0.5Mn at a higher magnification, the α-intermetallics on the BSE image of the fracture surface are visible.

8.4.5 The effect of Mn and DFZs on the creep fracture mechanism of the alloys

Fig. 8.12a shows the fracture surface of the Al-7Si-0.5Cu-0.3Mg-0.1Fe-0.3Mo alloy after creep to fracture at 300 ^{o}C, 30 MPa. Dimples, signature of ductile fracture and cavitation process, can be seen on the surface; Si particles are often observed at the bottom of the dimples. Our previous study [2] on the Al-7Si-0.5Cu-0.3Mg-0.1Fe-0.3Mo alloy showed that this alloy fractures in a ductile interdendritic mode at 300 ^{o}C, 30 MPa, and the creep fracture process occurs in three distinct stages: i) void nucleation and growth, ii) flow localization between primary larger pores and accelerated void growth and iii) void coalescence along the flow localization path. It was seen that the dispersoids in this alloy play an important role in hindering dislocation processes in the intradendritic regions and postponing void formation in interdendritic regions, which results in an increased creep time-to-facture at 300 ^{o}C, 30 MPa. However, the presence of dispersoids in this alloy has negligible influence on the creep strain-to-fracture and center-to-center dimple spacing (a measure of the microcavity density). It is inferred that the total strain-to-fracture is controlled mostly by stages ii and iii; these processes, controlled by dislocation creep, occur locally in the intradendritic regions (DFZs are softer than the dendrite interiors), which are not affected by the dispersoids. In contrast, it was seen that the creep strain-to-fracture (Fig. 8.13) increases from 3.8 to 7.7 with increasing the Mn from 0.0 to 0.5%. A dramatic decrease is seen at 1% Mn, which is due to the increased amount of the intermetallics that embrittles the alloy; thermodynamic calculations (Fig. 8.3c) show that the presence of Mn in excess of 0.5% cannot increase the amount of the dispersoids and appears in interdendritic intermetallics formed during solidification. Mn addition eliminates the DFZs and thereby strengthens the interdendritic regions with the dispersoids; it lowers the local dislocation creep rate, which impedes easy void growth (stage ii) and coalescence (stage iii), and allows the material to creep further before fracture, increasing the strain-to-fracture.

SEM analysis of the fracture surfaces showed that Mn addition changes the creep fracture mode at 300 ^{o}C, 30 MPa. Figs. 8.12b-c show that the Al-7Si-0.5Cu-0.3Mg-0.1Fe-0.3Mo-0.5Mn alloy, contrary to the Al-7Si-0.5Cu-0.3Mg-0.1Fe-0.3Mo alloy, fractures in a brittle interdendritic manner; the crack path along the secondary dendrite arms can be seen on the surface as well as the α-Al(Fe,Mo,Mn)Si intermetallics (Fig. 8.12c); no dimples are present on the surface. A combination of two factors appears to drive the transition from ductile interdendritic to brittle interdendritic creep fracture mode in these alloys: i) increased amount of the interdendritic intermetallics, which embrittles the interdendritic regions and ii) elimination of the DFZs, which prevents the easy growth and coalescence of the voids formed during the creep process.

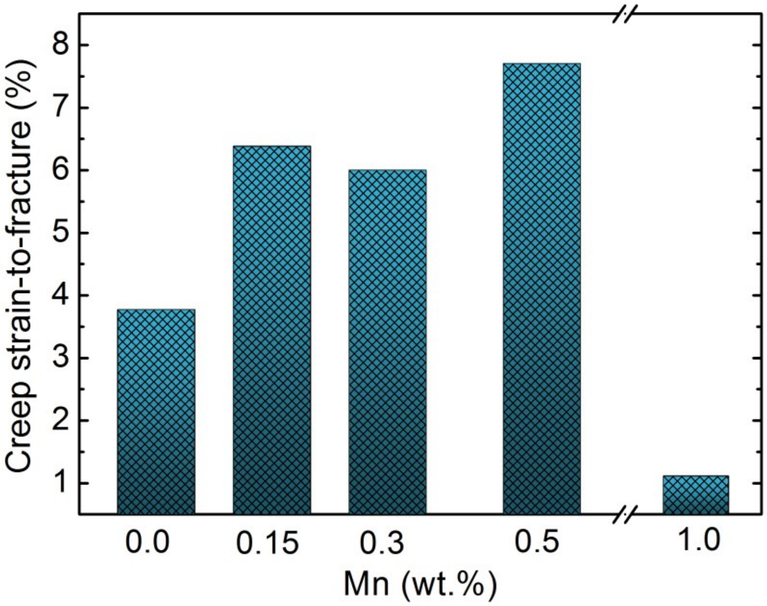

Fig. 8.13 Total creep deformation after failure as a function of Mn content.

8.5 Conclusions

The effect of combined additions of Mo and Mn on the precipitation and creep properties of the Al-7Si-0.5Cu-0.3Mg alloys has been investigated. The following conclusions can be drawn:

1. Mo forms a substantial amount of the α-Al(Fe,Mo)Si dispersoids in the intradendritic regions of the Al matrix. The number of the dispersoids per unit area increases with Mn addition, while the average dispersoid size decreases.
2. Mn addition (in combination with Mo) leads to a uniform distribution of dispersoids and elimination of the DFZ, which is attributed to the opposite partitioning of the Mo and Mn solute atoms during solidification.
3. TEM-EDS analysis revealed that Mn substitutes Fe atoms within the structure of the the α-Al(Fe,Mo)Si dispersoid phase. The dispersoids in each of the Mn-containing alloys studied have the approximate stoichiometric formula of $Al_{22}(Fe_{1-3}Mn_{4-6}Mo)Si_4$. SAED analysis shows that the crystal structure of the dispersoids does not change with the dissolution of Mn, however the lattice constant slightly increases.

4. Thermodynamic calculations show that Mn addition up to 0.5% can increase the amount of dispersoids. However, Mn exceeding 0.5% only increases the amount of the interdendritic intermetallics. Calculations are in good agreement with the SEM/TEM microstructural observations.
5. 0.15% Mn increases the threshold stress 3 and 4.4 MPa at 300 and 350 °C, respectively, leading to a significant enhancement in creep resistance, which is attributed to the increased amount of the dispersoids.
6. Minimum creep rate decreases with Mn content at 300 °C, 30 MPa. Creep time-to-fracture also increases from ~25 to ~180 hours as Mn increases from 0.0 to 0.5%. However, further addition of Mn decreases the creep time-to-fracture due to the formation of a large amount of interdendritic intermetallics.
7. Creep strain-to-fracture increases with Mn addition up to 0.5%, which is attributed to the elimination of DFZs.
8. SEM analysis of the fracture surfaces shows that Mn addition changes the creep fracture mode at 300 °C, 30 MPa, from ductile interdendritic to brittle interdendritic.

On the basis of these results, the authors suggest that the trace addition of Mo can be used to modify the common Mn-containing Al alloys (e.g. 3000 series), which contain α dispersoids. Mo is expected to increase the coarsening resistance of these dispersoids and increase their coherency strengthening effect and possibly lead to a higher strength at elevated temperature.

8.6 Acknowledgment

This work was supported by the NSERC (Natural Sciences and Engineering Research Council) of Canada Strategic Project grant with Rio Tinto Alcan (RTA) as well as a team grant from FQRNT (Fonds Québécois de la Recherche sur la Nature et les Technologies) and FQRNT Network REGAL Grant. The authors thank Pierre Vermette (McGill University) and Martin Bouchard (Université du Québec à Chicoutimi) for their assistance in experimental work. Amir Rezaei Farkoosh would like to gratefully acknowledge the financial support of McGill University through MEDA (McGill Engineering Doctoral Award) program and research support provided through the NSERC/RTA Industrial Research Chair in Metallurgy of Aluminum Transformation

at University of Québec at Chicoutimi. Thanks also to Dr. Xue-Dong Liu of McGill FEMR (Facility for Electron Microscopy Research) for fruitful discussions.

8.7 References

[1] K.E. Knipling, D.C. Dunand, D.N. Seidman, Criteria for developing castable, creep-resistant aluminum-based alloys-A review, Zeitschrift fur Metallkunde, 97 (2006) 246.

[2] A.R. Farkoosh, X.-G. Chen, M. Pekguleryuz, Dispersoid Strengthening of a High Temperature Al-Si-Cu-Mg Alloy via Mo Addition, submitted to Materials Science and Engineering: A, (2014).

[3] A.R. Farkoosh, X.-G. Chen, M. Pekguleryuz, Precipitation of coherent α-Al(Fe,Mo)Si dispersoids in an Al-Si-Cu-Mg cast alloy via Mo addition, submitted to journal of alloys and compounds, (2014).

[4] A.R. Farkoosh, X.-G. Chen, M. Pekguleryuz, Al-Si-Cu-Mg-Mo Alloy Strengthened by Thermally Stable Coherent Dispersoids: Creep Resistance and Mechanisms at 300-350 oC, submitted to Materials Science and Engineering: A, (2014).

[5] L.F. Mondolfo, Aluminum alloys : structure and properties, Butterworths, London; Boston, 1976.

[6] V. Raghavan, Al-Mo-Si (Aluminum-Molybdenum-Silicon), Journal of Phase Equilibria and Diffusion, 33 (2012) 329-333.

[7] V. Raghavan, Al-Fe-Mo (Aluminum-Iron-Molybdenum), Journal of Phase Equilibria and Diffusion, 32 (2011) 457-459.

[8] H. Okamoto, Al-Mo (Aluminum-Molybdenum), Journal of Phase Equilibria and Diffusion, 31 (2010) 492-493.

[9] N.A. Belov, D.G. Eskin, A.A. Aksenov, Multicomponent phase diagrams: applications for commercial aluminum alloys, Elsevier Science, 2005.

[10] P. Donnadieu, G. Lapasset, T.H. Sanders, Manganese-induced ordering in the α-(Al-Mn-Fe-Si) approximant phase, Philos. Mag. Lett., 70 (1994) 319-326.

[11] Y.J. Li, L. Arnberg, Quantitative study on the precipitation behavior of dispersoids in DC-cast AA3003 alloy during heating and homogenization, Acta Mater., 51 (2003) 3415-3428.

[12] H.Y. Kim, S.W. Han, H.M. Lee, The influence of Mn and Cr on the tensile properties of A356–0.20Fe alloy, Mater. Lett., 60 (2006) 1880-1883.

[13] Y.J. Li, A.M.F. Muggerud, A. Olsen, T. Furu, Precipitation of partially coherent α-Al(Mn,Fe)Si dispersoids and their strengthening effect in AA 3003 alloy, Acta Mater., 60 (2012) 1004-1014.

[14] Q. Du, W.J. Poole, M.A. Wells, N.C. Parson, Microstructure evolution during homogenization of Al–Mn–Fe–Si alloys: Modeling and experimental results, Acta Mater., 61 (2013) 4961-4973.

[15] A.M.F. Muggerud, Y. Li, R. Holmestad, Composition and orientation relationships of constituent particles in 3xxx aluminum alloys, Philosophical Magazine, 94 (2013) 556-568.

[16] A.M.F. Muggerud, E.A. Mørtsell, Y. Li, R. Holmestad, Dispersoid strengthening in AA3xxx alloys with varying Mn and Si content during annealing at low temperatures, Mater. Sci. Eng., A, 567 (2013) 21-28.

[17] R.E. Reed-Hill, R. Abbaschian, Physical metallurgy principles, (1973).

[18] C.J. Kuehmann, P.W. Voorhees, Ostwald ripening in ternary alloys, Metall. Mater. Trans. A, 27 (1996) 937-943.

[19] L. Lodgaard, N. Ryum, Precipitation of dispersoids containing Mn and/or Cr in Al–Mg–Si alloys, Mater. Sci. Eng., A, 283 (2000) 144-152.

[20] M. Cooper, The crystal structure of the ternary alloy [alpha](AlFeSi), Acta Crystallographica, 23 (1967) 1106-1107.

[21] H.J.A.M.F. Frost, Deformation-mechanism maps : the plasticity and creep of metals and ceramics, Pergamon Press, Oxford [Oxfordshire]; New York, 1982.

[22] H. Watanabe, H. Tsutsui, T. Mukai, M. Kohzu, S. Tanabe, K. Higashi, Deformation mechanism in a coarse-grained Mg–Al–Zn alloy at elevated temperatures, Int. J. Plast., 17 (2001) 387-397.

[23] J. Čadek, H. Oikawa, V. Šustek, Threshold creep behaviour of discontinuous aluminium and aluminium alloy matrix composites: An overview, Mater. Sci. Eng., A, 190 (1995) 9-23.

[24] A.R. Farkoosh, M. Pekguleryuz, The effects of manganese on the T-phase and creep resistance in Al–Si–Cu–Mg–Ni alloys, Mater. Sci. Eng., A, 582 (2013) 248-256.

[25] D. Hull, D.J. Bacon, Introduction to dislocations, Butterworth-Heinemann, 2011.

[26] D.J. Chakrabarti, D.E. Laughlin, Phase relations and precipitation in Al–Mg–Si alloys with Cu additions, Prog. Mater Sci., 49 (2004) 389-410.

[27] P.C.L.D. Villars, Pearson's handbook of crystallographic data for intermetallic phases, ASM International, Materials Park, OH, 1991.

[28] J.M. Zuo, J.C. Mabon, Web-Based Electron Microscopy Application Software: Web-EMAPS, Microsc. Microanal., 10 (2004) 1000-1001.

CHAPTER 9

ENHANCED MECHANICAL PROPERTIES OF AN AL-SI-CU-MG ALLOY AT 300 ^{O}C: EFFECTS OF MG AND THE Q-PRECIPITATE PHASE

This chapter presents a complementary approach towards enhancing the mechanical properties of the Al-7Si-0.5Cu-0.3Mg (MG3R) alloy at 300 °C via increasing the volume fraction of the age-hardening precipitates to promote Orowan strengthening. Increased Mg levels were investigated for their potential to enhance the precipitation response of the alloys. It is found that while there is an optimum Mg level for obtaining maximum elevated temperature strength of the base alloy, the effect is not as significant as Mo additions to form nanoscale coherent and stable dispersoids. However, The Mg level in the Mo and Mn containing alloys can also be optimized in view of the findings presented in this chapter. This chapter has been submitted for peer-review: *A.R. Farkoosh, M. Pekguleryuz, Enhanced mechanical properties of an Al-Si-Cu-Mg alloy at 300 °C: Effects of Mg and the Q-precipitate phase, Mater. Sci. Eng., A, 621 (2015) 277-286.*

ABSTRACT

Strategies to improve the strength of Al-Si alloys at elevated temperatures can follow two routes: 1) improving the age-hardening behavior and/or 2) producing effective dispersoid strengthening. In this study, the influence of Mg (in the range of 0.3-0.7 wt.%) on the precipitation characteristics and mechanical properties of the Al-7Si-0.5Cu-(Mg) alloy was investigated. Thermodynamic calculations via the CALPHAD method showed that Q-$Al_5Mg_8Cu_2Si_6$ is the main thermodynamically stable precipitate at 300 °C. The calculations were validated by transmission electron microscopy and differential scanning calorimetry analyses. Cooling curve analysis showed that Mg increases the freezing range under non-equilibrium conditions by ~ 4 °C per 1wt.% Mg. Increasing the Mg level to ~ 0.5 wt.% which is the maximum solid solubility increased the amount of the Q-$Al_5Mg_8Cu_2Si_6$ precipitates and significantly improved the tensile strength and creep resistance at the expense of some ductility. Further addition of Mg remained within the microstructure in the form of the large π-$Al_8FeMg_3Si_6$ and β-Mg_2Si intermetallics after solution treatment. Cracking of the brittle π-$Al_8FeMg_3Si_6$ intermetallics during deformation was accounted for the decreased ductility of the alloys at high Mg levels.

Keywords: Al-Si; Age hardening; Creep; Mg addition; Mechanical properties

9.1 Introduction

Diesel engine operation exposes the engine block material within the inter-valve regions to cyclic loading during engine heat-up and cool-down. Metal expansion in the inter-valve regions is prevented during engine heat-up placing the metal under compressive creep loading at 300 °C. During engine cool-down the metal in turn is prevented from contracting placing it under tensile loading in the temperature range of 150-300 °C [1]. This cycle eventually results in thermal fatigue and crack initiation. Designing an alloy with an optimum combination of properties is challenging for the alloy developer. There is no single property or parameter that can evaluate the thermal fatigue resistance of an alloy. It seems that the jury is still out on whether thermal fatigue prevention requires high ductility or high tensile strength [1]. From a crack initiation and propagation perspective, the present authors consider ductility to be of prime importance. However, in both cases creep resistance is also required. It has been suggested that the thermal fatigue resistance of an alloy under cyclic loading conditions resulting from thermal cycling between a maximum and a minimum temperature (300 °C to room temperature in the case of the Diesel engine) can be assessed by mechanical fatigue strength at the mid-cycle temperature (150 °C in the case of the diesel engine alloy) [2].

Recent research on the development of elevated temperature aluminum alloys for use above 250 °C in Diesel engines has focused on optimizing Al-Si alloys containing Mg and/or Cu [1, 3-5]. Of these age-hardening alloys, A356 (Al-7Si-0.3Mg) has higher ductility, and A319 (Al-7Si-4Cu) has higher tensile strength but low ductility and fracture toughness. Albeit these alloys are prone to coarsening and loss of strength above 250 °C. Feikus [6, 7] has shown that Cu addition up to 0.5 wt.% to A356 improves strength at 150-250 °C without loss of ductility and enhances creep time-to-fracture from 22 to 214 h at 200 °C and 120 MPa. Cu produces Q-$Al_5Mg_8Cu_2Si_6$ and θ-Al_2Cu precipitates and the precipitation sequence of the A356 alloy during ageing changes from [8, 9]:

$$Al_{SS} \rightarrow GP \rightarrow \beta'' \rightarrow \beta' \rightarrow \beta\text{–}Mg_2Si \rightarrow Si \qquad (1)$$

to [10]:

$$Al_{SS} \rightarrow GP\ zones \rightarrow \theta' + Q' \rightarrow \theta + Q. \qquad (2)$$

A recent approach for increasing the elevated temperature performance of the Al-Si based alloys involves increasing Cu content above 0.5 wt.% to enhance the θ-Al_2Cu precipitation, however, increased Cu leads to significant loss of ductility, hot-tear susceptibility [7] and increased porosity [11].

Another strategy to further develop these alloys for use at 300 °C is to introduce thermally stable dispersoids by adding transition metals of low diffusivity and limited solid solubility [12]. The present authors have previously reported on the Mo- and Mn-alloyed Al-Si-Cu-Mg alloys [13]. In our previous study [3], we have shown that in the A356 + 0.5Cu alloy, the θ precipitates are unstable at 300 °C. Therefore, Q-$Al_5Mg_8Cu_2Si_6$ remains as the only strengthening precipitate at this temperature, and because of its rapid coarsening kinetics and low amount, Orowan strengthening is insignificant for the applications that require high creep resistance and strength at this temperature.

In this study, a new approach that is aimed at increasing the amount of the Q-$Al_5Mg_8Cu_2Si_6$ precipitates at 300 °C is upheld. To this end, thermodynamic calculations were carried out along with experimental investigations to study the effect of Mg content on enhancing the precipitation of the Q-$Al_5Mg_8Cu_2Si_6$ phase at 300 °C and its effect on strength and creep resistance. The effect of Mg on the room temperature properties of the Al-Si-Cu-Mg alloys is well documented [10, 14-19], however, the elevated temperature properties of these alloys specially in the critical temperature range of 250-300 °C is very limited and the strengthening mechanisms are not well understood.

9.2 Experimental procedures

Alloys were prepared in a high frequency NORAX Canada induction furnace using commercial grade A356 alloy supplied by Rio Tinto Alcan Inc., Al-33 wt.% Cu master alloy and 99.98 wt.% pure Mg. All alloys were modified with 150 ppm Sr using an Al-10 wt.% Sr master alloy. All master alloys were supplied by KB Alloys Inc.. Melt was degassed with high purity argon gas at 730 °C before casting. Cylindrical bars of 30 mm diameter were cast in a pre-heated (400 °C) permanent mold at 730 °C. The chemical composition of the alloys determined by inductively coupled plasma (ICP) technique are presented in Table 1; alloys are designated as MG3R, MG5R and MG7R according to their Mg content. All compositions are given in wt.% hereafter, unless otherwise specified. Cooling curve analysis (CCA) was conducted in sand molds. K-Type (Chromel-alumel) thermocouples positioned at the bottom of the molds and a data acquisition system (Squirrel Data Logger Grant2020) were used to log the temperature variations of the melt (~200 g) at a data acquisition rate of 10 Hz. The thermal arrests associated with the phase transformations were obtained from the first derivative of the temperature with respect to time ($\partial T/\partial t$). A cooling rate of ~ 6 $^{o}C.s^{-1}$ was observed just prior to solidification.

Table 9.1 Chemical compositions of the alloys

Alloy	Chemical composition (wt.%)							
	Si	Mg	Cu	Fe	Ti	Mn	Sr	Al
MG3R	6.49	0.31	0.53	0.11	0.10	<0.01	0.014	Bal.
MG5R	6.59	0.49	0.54	0.12	0.09	<0.01	0.017	Bal.
MG7R	6.65	0.66	0.56	0.13	0.09	<0.01	0.019	Bal.

Creep and tensile tests were carried out on the over-aged (T7) alloys. The specimens with cylindrical gauge length and diameter of 50 and 12.7 mm were machined from the castings according to ASTM E8 standard and were given a two-step solution treatment (4 hours at 500 ^{o}C followed by 10 hours at 530 ^{o}C) in an electrically heated air-circulating chamber furnace, to avoid probable incipient melting; they were then water-quenched to room temperature and aged at 200 ^{o}C for 5 hours (T7). Tensile testing was carried out at room temperature (RT) and 300 ^{o}C at a nominal deformation rate of 0.01 s^{-1}. The 0.2% proof stress (YS), ultimate tensile strength (UTS) and elongation to fracture are reported. Fracture surfaces were inspected with a stereo microscope to ensure that surfaces are free from inclusions. Tensile creep testing was conducted at 300 ^{o}C under step loadings; at each step, after the establishment of the steady-state deformation the load was increased. Maximum five data points were obtained from each specimen and the total strain was less than 2%. Gauge length displacement was measured with two high precision extensometers with a resolution of 5 μm. Temperature was monitored with a thermocouple with an error of ± 0.1 ^{o}C attached to the specimen. All elevated temperature tests were conducted in air after 100 hours of soaking at 300 ^{o}C.

Microstructural characterization was performed on the as-cast and heat-treated alloys. Specimens were cut using a low speed diamond saw and ground with a series of SiC papers. Specimens were then polished on porous neoprene polishing cloth with Al_2O_3 solution. Final polishing was performed with a Buehler vibratory polisher using colloidal silica solution. A Hitachi S-4700 field emission gun scanning electron microscope (FEG-SEM) equipped with an Oxford INCA energy dispersive spectroscopy (EDS) detector was used at 15 kV with a beam current of 10 μA to study the microstructures and the fracture surfaces. For transmission electron microscope (TEM) analysis, thin foils of the aged samples were prepared by mechanical grinding and electropolished with a Struers Tenupol 3 jet polisher to electron transparency using a solution of 10% nitric acid in methanol at -40 ^{o}C. TEM analysis was performed utilizing a Philips CM200 microscope operating at 200 kV. For EDS spectra acquisition an EDAX detector connected to the column was used. High-resolution TEM (HRTEM) and high-angle annular dark field (HAADF) imaging was performed on a field emission scanning transmission electron microscope, FEI TecnaiG2 F20, operating at 200 kV. To enhance the image contrast, Fourier mask filtering was performed using DigitalMicrograph^{TM} software. Thermodynamic calculations are carried out via ThermoCalc software using the TTAL7 database [20].

9.3 Results and discussion

9.3.1 Al-Si-Cu-Mg-Fe phase equilibria

Solidification path

The calculated isopleth of the Al-Si-Cu-Mg-Fe system at 7% Si, 0.5% Cu, 0.1% Fe is given in Fig. 9.1. The dashed lines represent the alloys investigated in this study. It can be seen that the first phase to form is α-Al followed by the Al-Si eutectic. With decreasing temperature, the remaining liquid forms the β-Al_5FeSi phase through a ternary eutectic reaction (L → Al + Si + β). When Mg > 0.47% (MG5R and MG7R), a peritectic reaction transforms the β-Al_5FeSi phase into the quaternary π-$Al_8Mg_3FeSi_6$ phase (L + β → Al + Si + π). At Mg above 0.6% (MG7R), the β-Al_5FeSi phase is completely replaced by the π-$Al_8Mg_3FeSi_6$ phase, which consumes all the Fe content of the alloy, and the excess Mg appears in the form of the β-Mg_2Si phase. At lower temperatures, the π-$Al_8Mg_3FeSi_6$ phase is not stable and transforms into the β-Al_5FeSi phase through a peritectoid reaction (Al + π → β-Al_5FeSi + Q or β-Al_5FeSi + Q + M).

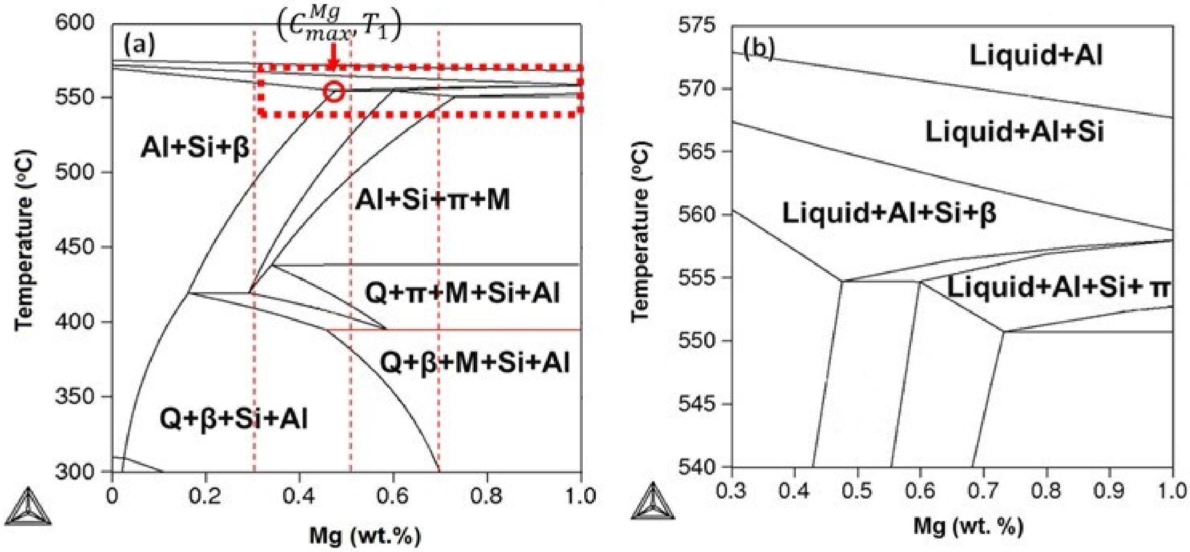

Fig. 9.1 (a) Calculated isopleth at 7% Si, 0.5% Cu, 0.1% Fe and (b) enlargement of the boxed area in (a); θ-Al_2Cu, Q-$Al_5Cu_2Mg_8Si_6$, β-Al_5FeSi, π-$Al_8Mg_3FeSi_6$, M-Mg_2Si.

Ageing simulation

The age-hardening process involves the dissolution of the Mg- and Cu-containing precipitates present in the as-solidified microstructure, and re-forming these precipitates at lower temperatures.

The complete dissolution of these phases depends on the maximum solid solubility of Mg (C_{max}^{Mg}) and Cu (C_{max}^{Cu}) in the Al matrix at the solution treatment temperature. The calculated maximum solid solubility values of these elements in the Al-7Si-0.1Fe system are given in Tables 2 and 3. It can be seen that Cu has negligible influence on C_{max}^{Mg}, however, C_{max}^{Cu} decreased significantly with increasing Mg. Calculations show that for the alloys studied (with 0.5% Cu), $C_{max}^{Mg} =$ 0.47% at 554 °C (Table 2); the excess Mg appears in the form of the π-$Al_8Mg_3FeSi_6$ and β-Mg_2Si phases (Fig. 9.1). At 300 °C (service temperature), the solid solubility decreases to $C_{300\,^oC}^{Mg} = 0.02\%$, and Mg below 0.7% (for all the alloys studied) forms the Q-$Al_5Cu_2Mg_8Si_6$ phase.

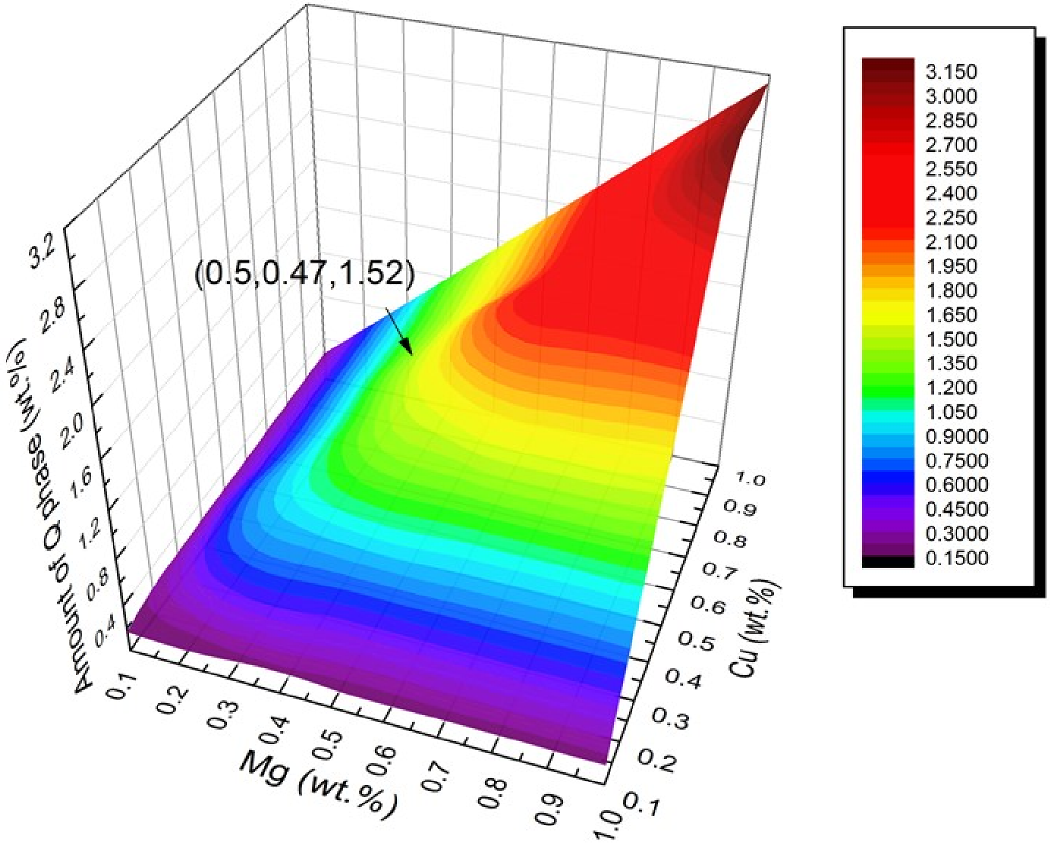

Fig. 9.2 The amount of the Q-$Al_5Cu_2Mg_8Si_6$ phase at 300 °C as a function of Cu and Mg.

Fig. 9.2 shows the calculated equilibrium amount of the Q-$Al_5Cu_2Mg_8Si_6$ phase at 300 °C as a function of Cu and Mg concentrations. At Cu = 0.5% and Mg = 0.3% (MG3R) the amount of the Q-$Al_5Cu_2Mg_8Si_6$ phase is 0.92%, which increases to 1.52% by increasing the Mg level to $C_{max}^{Mg} =$ 0.47%. Given that C_{max}^{Cu} (Table 3) is much higher than the Cu content of the alloys (0.5%), it can be concluded that, in this alloy system, the maximum amount of the Q-$Al_5Cu_2Mg_8Si_6$ phase that can be re-precipitated after solution treatment and ageing process is 1.52% at 0.47% Mg. It is worth mentioning that at 0.47% Mg (C_{max}^{Mg}), Cu above 0.5% has no significant effect on the amount of the Q-$Al_5Cu_2Mg_8Si_6$ phase (see Fig. 9.2).

Table 9.2 The effect of Cu content on the maximum solid solubility of Mg in the Al-7Si-0.1Fe system

Cu (wt.%)	T_1 (°C)	C_{max}^{Mg} (wt.%)	$C_{300\ ^oC}^{Mg}$ (wt.%)
0.1	560	0.484	0.034
0.3	557	0.478	0.023
0.5	554	0.474	0.023
0.75	552	0.470	0.022
1.0	548	0.463	0.021

Table 9.3 The effect of Mg content on the maximum solid solubility of Cu in the Al-7Si-0.1Fe system

Mg (wt.%)	T_1 (°C)	C_{max}^{Cu} (wt.%)	$C_{300\ ^oC}^{Cu}$ (wt.%)
0.1	521	4.480	0.066
0.3	513	4.360	0.066
0.5	517	3.540	0.065
0.75	537	1.560	0.065
1	537	1.550	0.065

9.3.2 Thermal analysis and thermodynamic calculations

Fig. 9.3 presents two thermal arrests detected during the solidification of the alloys studied: the first thermal arrest corresponds to the formation of the α-Al dendrites and the second one to the Al–Si eutectic reaction. The most evident influence of Mg is seen on the Al-Si eutectic temperature. The eutectic reaction temperature decreases with Mg at a slightly higher rate than liquidus, leading to a slightly wider pre-eutectic freezing range for the alloys with higher Mg content (freezing range increases at ~ 4 °C per 1% Mg). These temperatures are compared with the calculated equilibrium temperatures in Table 4. As expected, because of the non-equilibrium solidification, thermal arrests obtained from CCA are lower, and the freezing ranges are wider than the calculated ones. Calculations show that in the range of 0.0-1.0% Mg, the liquidus and the Al-Si eutectic temperature decrease almost linearly with Mg at ~ 3.5 and ~ 7 °C per 1% Mg, respectively (Fig. 9.1b), leading to an ~ 4 °C increase in the freezing range per 1% Mg.

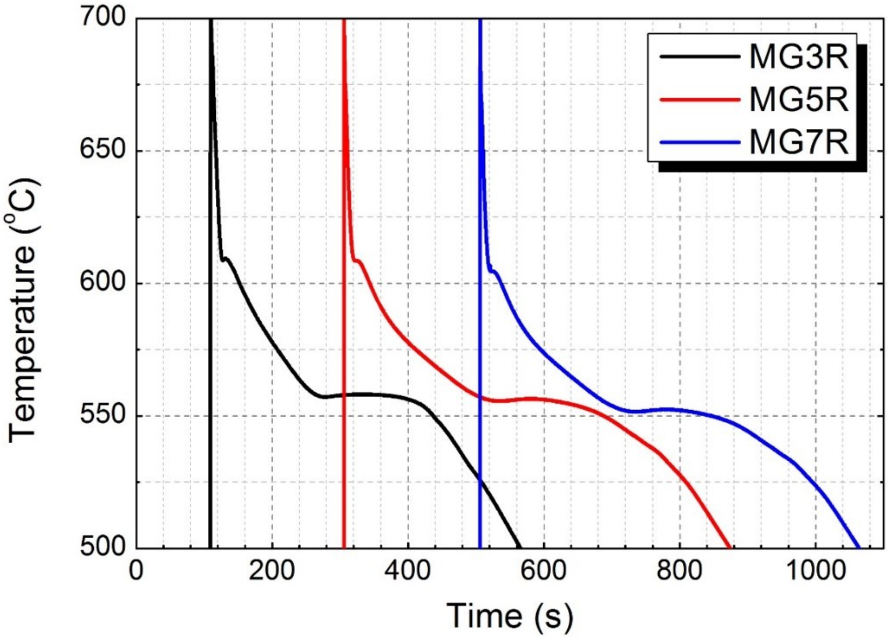

Fig. 9.3 Cooling curves of the alloys studied (with 0.3-0.7% Mg).

Table 9.4 Phase transformation temperatures obtained from CCA and equilibrium calculations

Alloy	**Liquidus (°C)**		**Eutectic reaction (°C)**		**Pre-eutectic freezing range (°C)**	
	CCA	Equilibrium	CCA	Equilibrium	CCA	Equilibrium
MG3R	608.5	613.5	557.0	572.2	51.5	41.3
MG5R	607.5	611.8	555.5	569.9	52.0	41.9
MG7R	604.5	611.7	551.5	568.7	53.0	42.9

9.3.3 Alloy microstructures and phase selection

As-cast microstructures

Fig. 9.4 represents the as-cast microstructure of the alloys with varying Mg content. The microstructures consist of primary aluminum (α-Al) dendrites surrounded by the eutectic Si and different intermetallic phases depending on the Mg content (Table 9.5). The secondary dendrite arm spacing (SDRS) was 30 ± 2 μm at all the Mg levels. Fig. 9.3a shows the interdendritic intermetallics in the MG3R alloy with 0.3% Mg. The phases were identified via EDS, WDS and XRD in combination with the known morphologies, details of which have been explained elsewhere [3]. The blocky bright white particles (with the highest effective atomic number, Z_{eff})

and the gray intermetallics with Chinese script morphology, in the backscattered imaging mode of SEM, are identified as the θ-Al_2Cu and quaternary Q-$Al_5Cu_2Mg_8Si_6$ phases, respectively. Fe combined with Mg and Si forms the π-$Al_8Mg_3FeSi_6$ phase, which appears as dark gray intermetallics. β-Al_5FeSi is the other Fe-containing phase that appears as plate-like intermetallics within the microstructure. At higher Mg levels, the MG5R and MG7R alloys (Figs. 9.3b and 9.3c), the amounts of the Q-$Al_5Cu_2Mg_8Si_6$ and π-$Al_8Mg_3FeSi_6$ phases increase, and the excess Mg appears as the dark black β-Mg_2Si phase with Chinese script morphology, the amount of which increases with increasing the Mg content. It is worth mentioning that no β-Al_5FeSi phase was observed within the microstructure of the MG5R and MG7R alloys, which can be attributed to the consumption of Fe in the formation of the π-$Al_8Mg_3FeSi_6$ phase. A high amount of the retained Fe-containing intermetallics after solution treatment is not desirable as it may lead to a lower ductility.

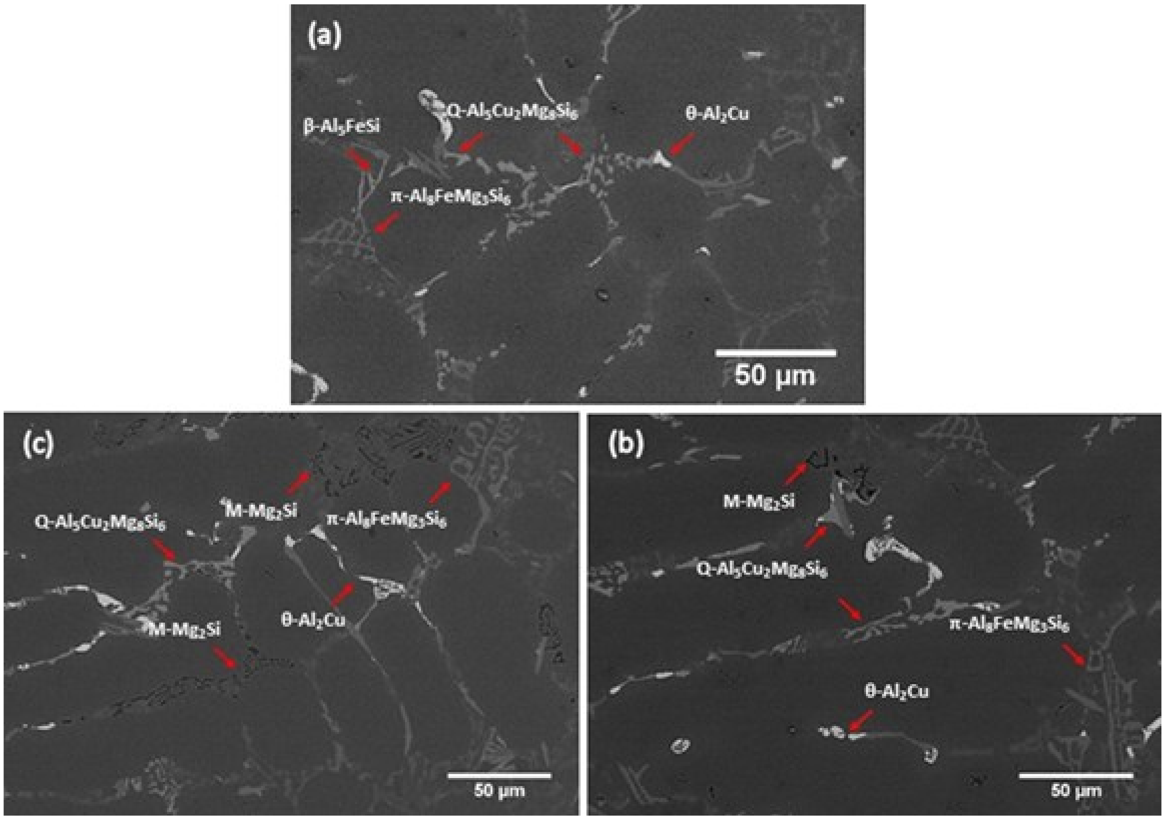

Fig. 9.4 SEM micrographs showing the as-cast microstructures of the (a) MG3R, (b) MG5R and (c) MG7R alloys.

Table 9.5 Intermetallic compounds observed in the as-cast and heat-treated conditions

Alloy	**Conditions**			
	As-cast	**As-quenched**	**200 °C**	**300 °C**
MG3R	θ-Al_2Cu, Q-$Al_5Cu_2Mg_8Si_6$, β-Al_5FeSi, π-$Al_8Mg_3FeSi_6$	β-Al_5FeSi	θ-Al_2Cu, Q-$Al_5Cu_2Mg_8Si_6$, β-Al_5FeSi	Q-$Al_5Cu_2Mg_8Si_6$, β-Al_5FeSi,
MG5R	θ-Al_2Cu, Q-$Al_5Cu_2Mg_8Si_6$, β -Mg_2Si	β-Al_5FeSi, π-$Al_8Mg_3FeSi_6$	θ-Al_2Cu*, Q-$Al_5Cu_2Mg_8Si_6$, β-Al_5FeSi, π-$Al_8Mg_3FeSi_6$	Q-$Al_5Cu_2Mg_8Si_6$, β-Al_5FeSi, π-$Al_8Mg_3FeSi_6$
MG7R	θ-Al_2Cu, Q-$Al_5Cu_2Mg_8Si_6$, β -Mg_2Si	π-$Al_8Mg_3FeSi_6$, β-Mg_2Si	θ-Al_2Cu*, Q-$Al_5Cu_2Mg_8Si_6$, π-$Al_8Mg_3FeSi_6$, β-Mg_2Si	Q-$Al_5Cu_2Mg_8Si_6$, π-$Al_8Mg_3FeSi_6$, β-Mg_2Si

* Low amount

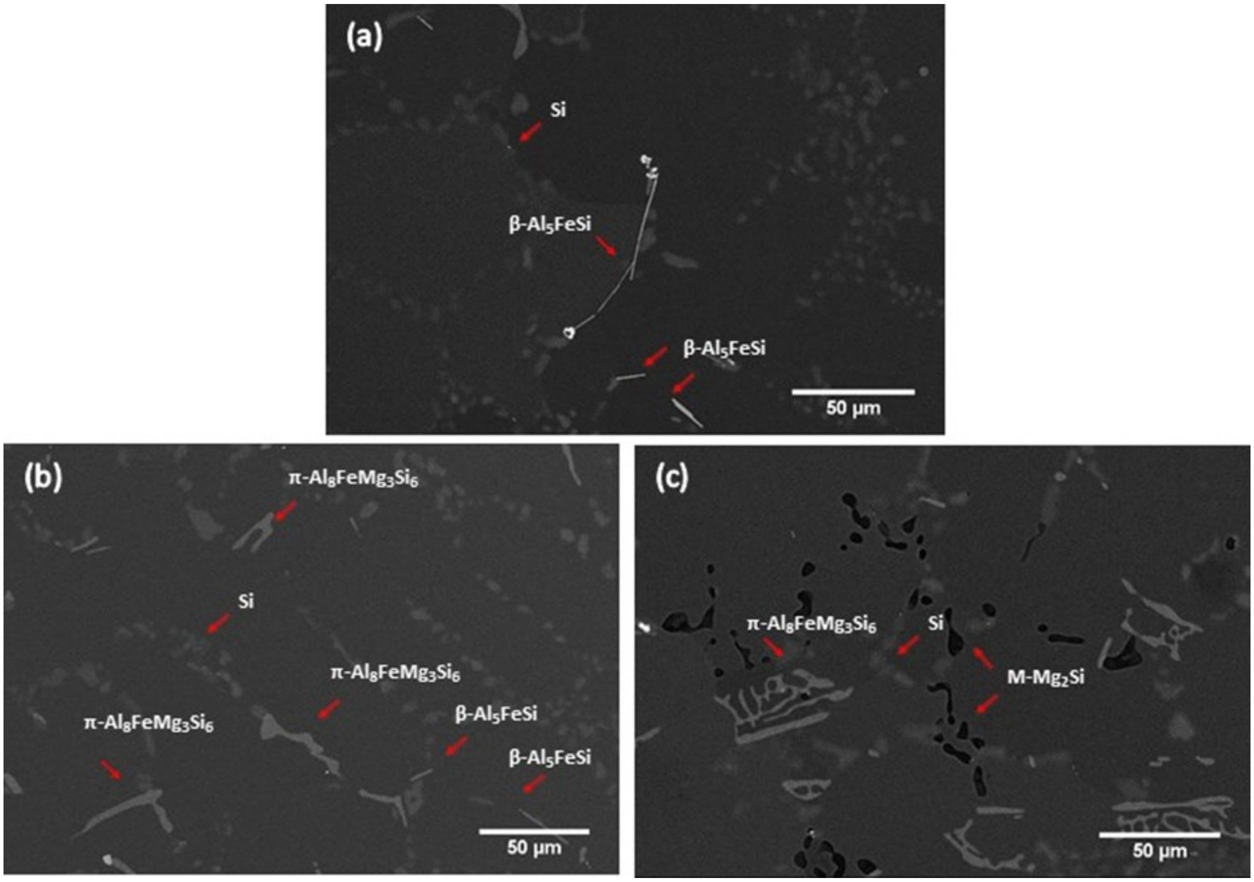

Fig. 9.5 SEM micrographs showing the microstructures of the (a) MG3R, (b) MG5R and (c) MG7R alloys after solution treatment (4 h at 500 °C and 10 h at 540 °C).

Heat-treated microstructures and differential scanning calorimetry (DSC)

Microstrucutres of the alloys after solution treatment (4 h at 500 °C and 10 h at 530 °C) are shown in Fig. 9.5. In the case of the MG3R alloy (Fig. 9.5a), the Q-$Al_5Cu_2Mg_8Si_6$, θ-Al_2Cu and π-$Al_8Mg_3FeSi_6$ phases are dissolved and only the β-Al_5FeSi phase is visible within the microstructure. Calculations revealed that this phase is thermodynamically stable at temperatures close to solidus (Fig. 9.1). The eutectic Si particles are spheroidized. The microstructure of the MG5R alloy (Fig. 9.5b) after solution treatment consists of the π-$Al_8Mg_3FeSi_6$ and β-Al_5FeSi phases. During solution treatment the Q-$Al_5Cu_2Mg_8Si_6$, θ-Al_2Cu and β-Mg_2Si phases are dissolved. Some of the π-$Al_8Mg_3FeSi_6$ phase transforms into the β-Al_5FeSi phase and some remains within the microstructure in decreased amounts. In the case of the MG7R alloy (Fig. 9.5c), only the β-Mg_2Si and π-$Al_8Mg_3FeSi_6$ phases are present in reduced amounts. It is noteworthy that the morphology of the β-Mg_2Si phase changes from Chinese script in the as-cast structure to fragmented smaller quasi-spherical particles in the solution-treated microstructure.

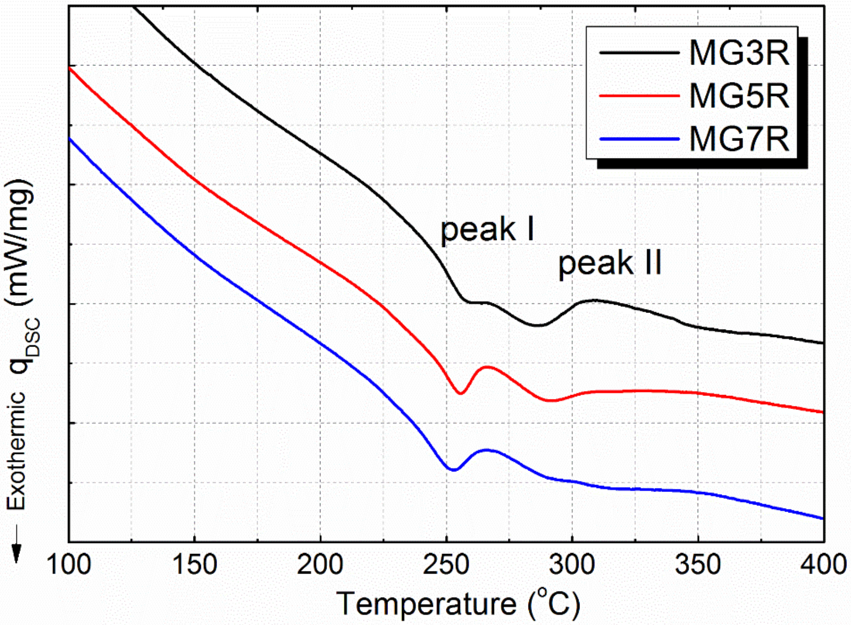

Fig. 9.6 DSC curves obtained at 10 °C.min^{-1} for the alloys with 0.3-0.7% Mg.

DSC analysis (Fig. 9.6) was conducted to determine the phase transformations during heating of the solution-treated alloys at 10 °C.min^{-1}. The first (I) and second (II) exothermic peaks of the curves are associated with the formation of the Q-$Al_5Cu_2Mg_8Si_6$ and θ-Al_2Cu precipitates (continuous transition from precursors to the equilibrium), respectively [21]. The area under each peak represents the amount of the precipitates formed during heating [22]. It can be seen that by increasing the Mg level from 0.3 to 0.5, the amount of the Q-$Al_5Cu_2Mg_8Si_6$ phase (peak I) increased (peak area increased from 75 to 425 mW^oCg^{-1}) and the θ-Al_2Cu phase (peak II) diminished. The MG5R and MG7R (peak I area for MG7R is 413 mW^oCg^{-1}) form almost the same amount of the Q-$Al_5Cu_2Mg_8Si_6$ phase during heating, which confirms the predictions made via the thermodynamic calculations; the maximum solid solubility of Mg in the Al matrix was shown to be $C_{max}^{Mg} = 0.47\%$ (Table 2). The calculated isopleth of Fig. 9.1 shows that, at high temperatures, Mg exceeding 0.47% will remain within the microstructure in the form of the π-$Al_8Mg_3FeSi_6$ and β-Mg_2Si phases. Therefore, both the MG5R and MG7R alloys will have 0.47% Mg and 0.5% Cu in solid solution.

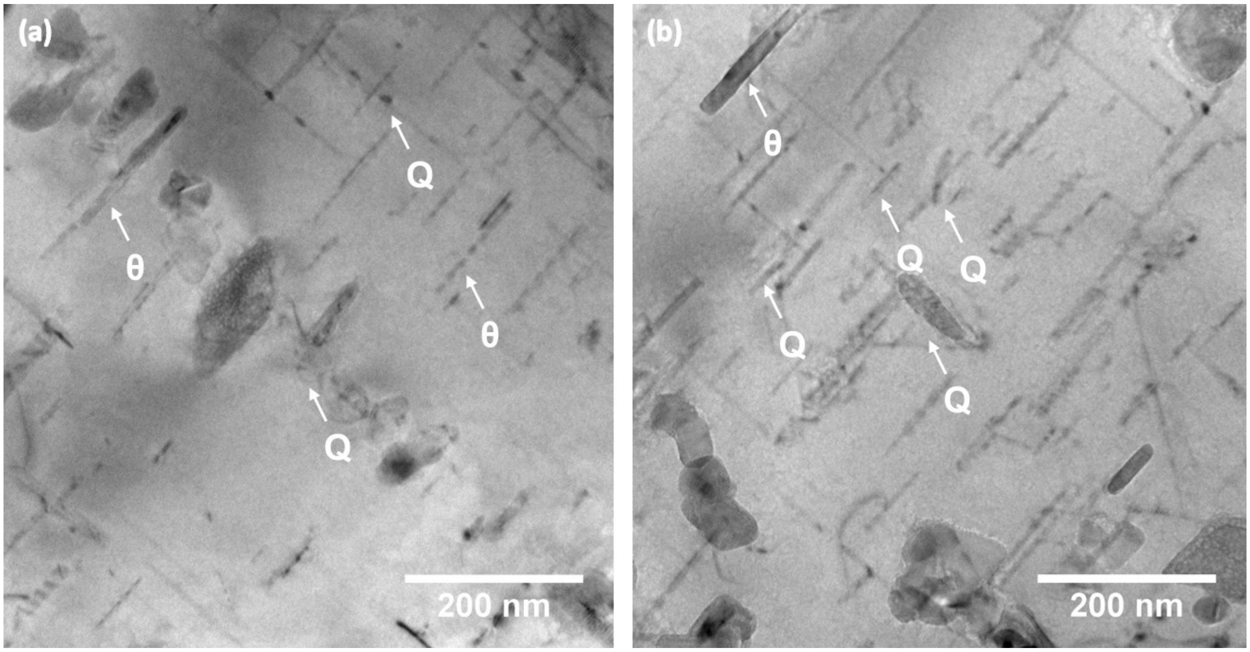

Fig. 9.7 Bright field-TEM microstructure of the (a) MG3R and (b) MG5R alloy after 450 hours of ageing at 200 °C, higher amount of the age-hardening precipitates can be seen in the MG5R alloy.

Overaged microstructures at 200 and 300 °C and the Q precipitates at 300 °C

Fig. 9.7 shows the TEM microstructures of the MG3R and MG5R alloys after solution treatment and 450 hours of ageing at 200 °C, with the equilibrium θ and Q precipitates (identified by the TEM-EDS analysis) marked with arrows; as seen the MG5R alloy has a higher amount of the ageing precipitates. TEM investigation of the alloys after T7 heat treatment and soaking at 300 °C for 100 hours (Fig. 9.8) shows that the rod shaped Q precipitates are the only age-hardening precipitate that remain within the microstructure, albeit coarsened; no θ precipitates are seen at this temperature. The MG5R alloy has again a higher amount of Q, which can promote the Orowan strengthening of the matrix at 300 ºC and make this alloy a better candidate for high temperature applications. The Q precipitates in this alloy are elongated rather than dispersed.

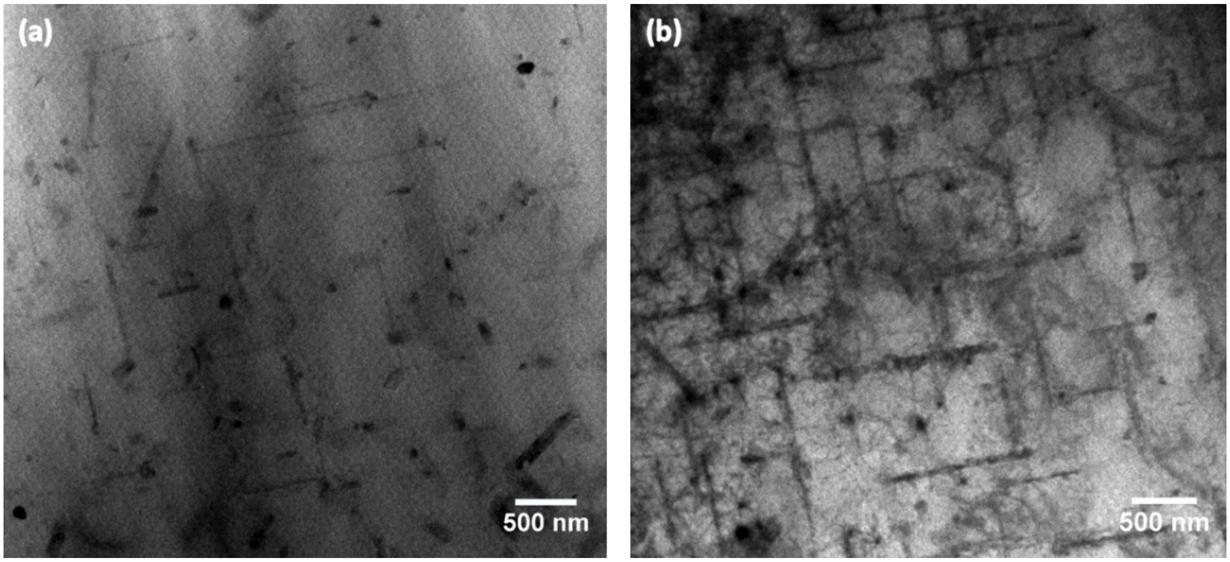

Fig. 9.8 Bright field-TEM microstructure of the (a) MG3R and (b) MG5R alloy after T7 heat treatment and 100 hours of soaking at 300 ºC, showing the Q precipitates, higher amount of the Q precipitates can be seen in the MG5R alloy.

Fig. 9.9a shows a HRTEM image of a rod-shaped Q precipitate in the MG5R alloy along the $[2\bar{4}1]$ zone axis. The enlarged FFT filtered image is shown in Fig. 9.9b. The measured lattice fringe spacing matches the inter-planar spacing of the $(21\bar{3}1)$ planes of the equilibrium Q phase (with HCP crystal structure, $a = 10.35\text{–}\,10.40\ A^o$ and $c = 4.02\text{–}\,4.05\ A^o$ [23]). The composition of the Q precipitates after 100 hours of soaking at 300 ºC was determined with EDS analysis. The Mg:Si and Mg:Cu ratios were 0.9 ± 0.3 and 4.1 ± 0.6, respectively, which are close to the values that Wolverton et al. [24] obtained (Mg:Si = 1.28 and Mg:Cu = 4.5) for the most stable type of the Q phase by first-principle calculations. It is worth noting that the Cu content of these quaternary precipitates at 300 ºC was slightly (~ 10%) lower than that at 200 ºC, which is in accord with the recent findings of Biswas et al. [23]. Their atom probe tomography (APT) analysis has shown that upon ageing at 165 ºC, the Q precipitates in a W319 (Al-7.4Si-3.5Cu-0.35Mg) alloy first appear within the microstructure as the Cu-rich precipitates (Mg:Cu = 0.66) and at 260 ºC, transform to the equilibrium Q precipitates, which have lower Cu concentration (Mg:Cu = 4.1). Different factors govern the precipitation sequence, most of which are related to the hetrophase interface energy (both structural and chemical) [25, 26]. Precipitation of the Cu-rich phase despite its thermodynamical instability can be attributed to the lower misfit strains at the precipitate/matrix interface, which lowers the height of energy barrier for nucleation [27, 28].

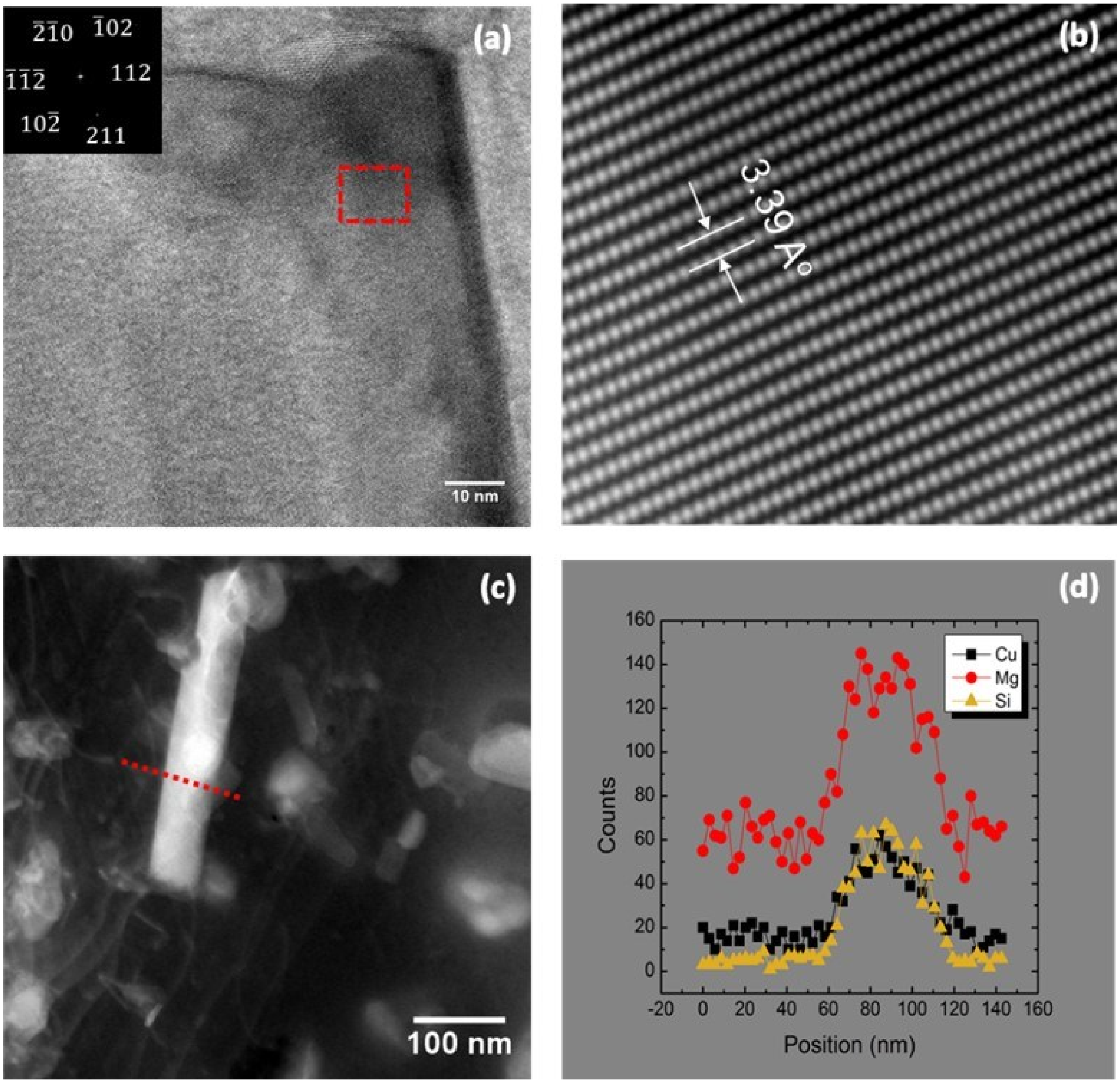

Fig. 9.9 (a) HRTEM image of a Q precipitate in the MG5R alloy after T7 heat treatment and 100 hours of soaking at 300 ºC along $[2\bar{4}1]$ with the corresponding FFT, (b) FFT filtered image of the boxed area in (a), (c) STEM–HAADF image of a Q precipitate and (d) the accompanying high resolution EDS line scan.

Cu segregation at the Q´-precipitate/matrix heterophase interface is reported by Matsuda et al. [29] in a low Si Al alloy, which can potentially lead to the coarsening resistance of these precipitates. Cu segregation may occur to help accommodate the large misfit strains (~ 11%) [29] that exist between the Q phase and the Al lattice or the shear component of the transformation strains at early stages of precipitations [30]. However, such segregation was not observed for the Q precipitate studied after 100 hours of soaking at 300 ºC. The STEM–HAADF micrograph of Fig. 9.9c shows a uniform concentration of the constituent atoms; Cu because of its higher atomic number if segregated to the interface should lead to a brighter interface in the STEM–HAADF micrograph. The EDS line scan across the precipitate (Fig. 9.9d) confirms the observations. No analysis of the interface was done at the early stages of precipitation, however, in a similar alloy with higher Cu content (W319), APT analysis by Biswas et al. [23] also showed no evidence of solute segregation at the Q-precipitate/matrix interface even at the early stages of precipitations.

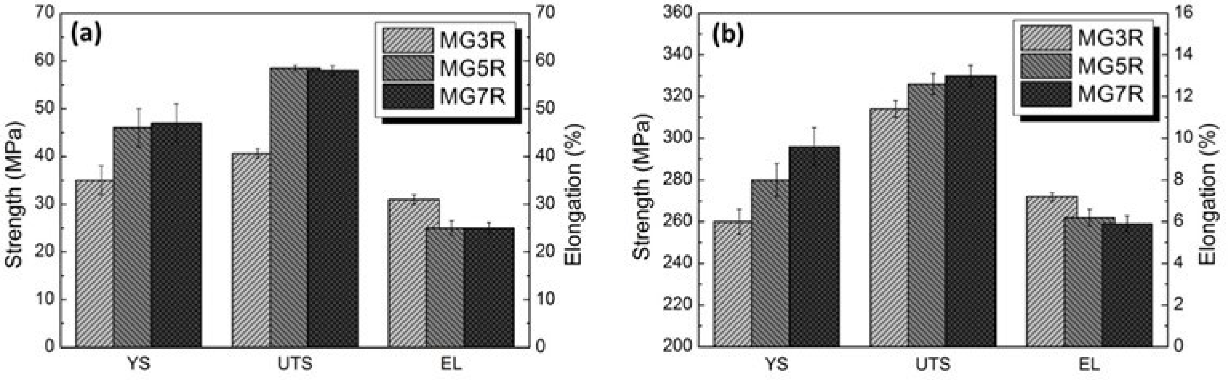

Fig. 9.10 Tensile properties of the alloys at (a) 300 ºC and (b) room temperature.

9.3. 5 Tensile properties

Fig. 9.10a shows the effect of Mg content on the tensile properties of the alloys studied at 300 ºC. The 0.2% proof stress (YS) and ultimate tensile strength (UTS) of the MG3R alloy at 300 ºC are 35 ± 3 and 40 ± 2 MPa, respectively, which increase to 46 ± 4 and 59 ± 1 MPa when the Mg level increases to 0.5% (MG5R). However, the elongation drops from 32 to 25%. Further increase of Mg level (MG7R) has no major influence on the tensile properties. At room temperature (Fig. 9.10b), YS and UTS increase progressively with Mg, while a slight decrease in elongation was observed as a result of the increased Mg content.

The fracture surfaces of the alloys after static tensile testing at room temperature (Fig. 9.11) exhibit, in general, mixed cellular mode of fracture (having both brittle and ductile fracture features). This mode of fracture is common in Al-Si alloys [31]. The tear ridges of the ductile Al matrix formed around the cracked round Si particles are seen in the MG3R alloy (Fig. 9.11a). In addition to the Si particles, the cracked π intermetallics are seen on the fracture surface of the MG5R (Fig. 9.11b) and MG7R (Fig. 9.11c) alloys; the cleavage facets of the cracked π intermetallics are visible inside the cells of the deformed Al matrix. The π intermetallics have embrittling effect on the alloy, however, no decohesion was observed at the matrix/π interface. Strong bonding between the intermetallic and the matrix is essential for high ductility. The authors have previously seen [4] that the Al_9FeNi intermetallics in the Ni-containing Al-Si alloys crack and detach from the matrix, resulting in poor ductility.

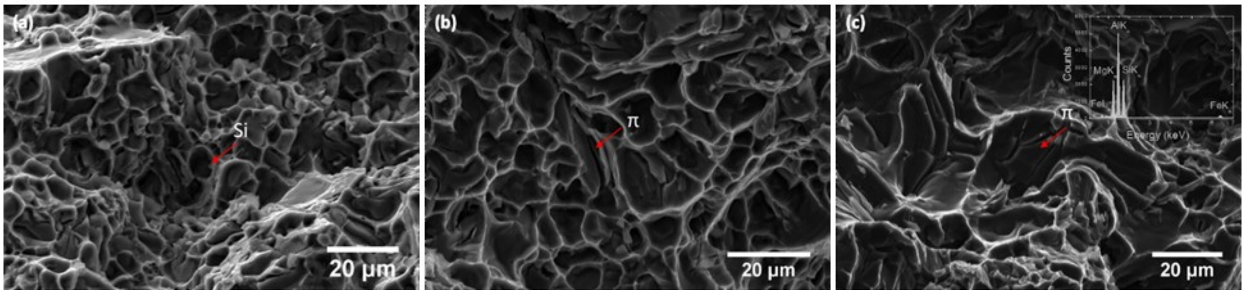

Fig. 9.11 Fracture surface of the (a) MG3R, (b) MG5R and (c) MG7R alloy, fracture after static tensile test at room temperature showing mixed cellular-mode of fracture.

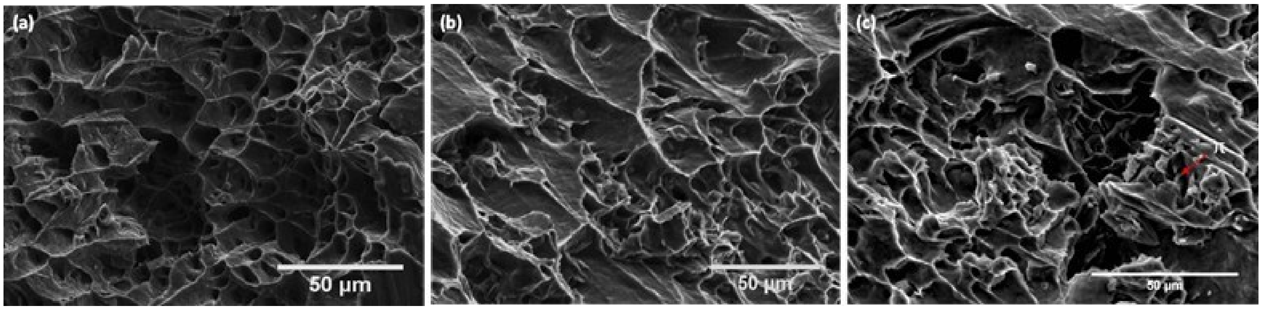

Fig. 9.12 Fracture surface of the (a) MG3R, (b) MG5R and (c) MG7R alloy, fracture after static tensile test at 300 °C, showing the dimpled fracture surface.

At 300 °C (Figs. 9.12a-c), all the alloys studied exhibit a ductile fracture mode with characteristics shear dimples [31]. At higher Mg contents, the remnants of the cracked π intermetallics are occasionally seen on the fracture surface of the alloys. Microstructural observations of the solution-treated alloys revealed the presence of the large π intermetallics in the interdendritic regions of the alloys (Fig. 9.5). These intermetallics remain within the structures of the MG5R and MG7R alloys even after 100 hours of soaking despite their thermodynamic instability at 300 °C (Fig. 9.1), which can be attributed to the slow kinetics of the phase transformation at this temperature. The decreased ductility of the MG5R and MG7R alloys can be related to their presence. Caceres et al. [16], by comparing the tensile properties of the A356 (0.4% Mg) and A357 (0.7% Mg) alloys, have shown that the lower ductility of the A357 is due to the formation of the large π intermetallics. Wang et al. [32] also have shown that in a Sr-modified A357 alloy, the majority of the damage during tensile testing is caused by the cracking of the large π intermetallics. The π phase has a hexagonal lattice ($a = 6.63\,A^o, c = 7.94\,A^o$, with 18 atoms in the unit cell) and space group of P$\bar{6}$2m [33]. Its relatively low density (2.82 g/cm^3, compared to ~ 3.6 g/cm^3 for the β-Al_5FeSi and α-AlFeSi phases) along with its low Fe concentration (~ 12%, compared to 25-30% for β-Al_5FeSi [33]) leads to the formation of this phase in high volume fractions, which increase dramatically with Mg level. At low volume fractions, because of its compact morphology and lower hardness (5.86 and 3.76 GPa at room temperature and 300 ºC, respectively, compared to 11.47 and 7.85 GPa for β-Al_5FeSi [34]), this phase is less detrimental than the β-Al_5FeSi platelets. However, at high volume fractions (with increased Mg level), its detrimental effect on ductility becomes significant as seen in the MG5R and M7R alloys.

9.3.6 Creep resistance at 300 ºC

Fig. 9.13 shows the minimum creep rate, $\dot{\varepsilon}_m (= d\varepsilon/dt)_{min}$ at 300 ºC as a function of the applied stress, σ for the MG3R, MG5R and MG7R alloys. The apparent stress exponents, $n_a (= \partial \ln \dot{\varepsilon}_m / \partial \ln \sigma)$ are in the range of 7-10; this high and varying stress exponent is typical of dispersion-hardened alloys when dislocation processes are rate-controlling creep mechanism [35, 36]. For the dispersion-hardened alloys, a threshold stress approach is usually used to rationalize the creep data. Introduction of the threshold stress, σ_{th}, below which dislocation creep is not significant, into the power-law equation gives [37, 38]:

$$\dot{\varepsilon}_m = A' \left(\frac{\sigma - \sigma_{th}}{G}\right)^n \exp\left(-\frac{Q}{RT}\right). \tag{3}$$

Here, A' is a constant, Q is the activation energy which is usually close to the activation energy for self-diffusion, G is the shear modulus, n is stress exponent of the matrix, and RT has its usual meaning. The threshold stress values are estimated using equation (3) and plotting $\dot{\varepsilon}^{1/n}$ vs. σ and extrapolating the data to $\dot{\varepsilon} = 0$. The stress exponent, n is assumed to be equal to that of the matrix (n = 4.4) [39], which gives the best linear fit to the data points. The estimated values for the threshold stress are given in Fig. 9.13. It can be seen that increasing the Mg level from 0.3 (MG3R) to 0.5 (MG5R) leads to a significant decrease in the minimum creep rate and the threshold stress increases by ~ 35%. Further Mg addition (MG7R) has negligible influence on the creep resistance.

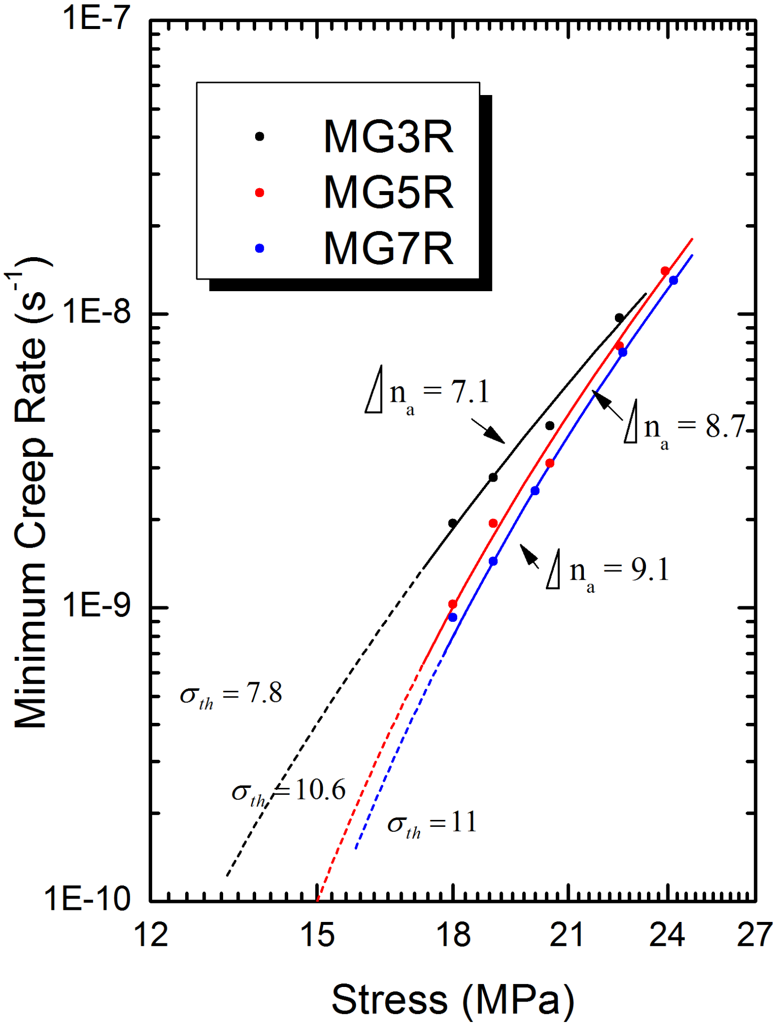

Fig. 9.13 Plot of minimum creep rate versus applied stress at 300 °C.

The effect of Mg on the strength at 300 °C can be explained by considering the strengthening mechanism in the alloys. The microstructures of the alloys studied consist of the α-Al dendrites containing intradendritic Q precipitates and interdendritic Si particles and intermetallics. The Q precipitates are coarse (Fig. 9.8) and are known to be non-coherent (non-shearable). Therefore, Orowan bowing between the Q precipitates is the likely deformation mechanism at this temperature. TEM observations (Fig. 9.8b) showed that as the amount of the Q precipitates increases (MG5R and MG7R alloys), they become more elongated (aspect ratio increases). This decreases the effective inter-particle spacing, distance between pinning points over which dislocations bow out, and leads to a greater Orowan strengthening. The effect of precipitate aspect ratio on the strength of the Al alloys has been studied by Bahrami et al. [40] where increasing the aspect ratio of the elongated Q and β ageing precipitates in an AA6061 alloy resulted in higher strength.

However, creep mechanisms such as dislocation climb would not be significantly affected by a simple increase in the precipitate amount. It has been observed in cast alloys that the creep resistance can be severely influenced by the presence of an interdendritic region with coarse and brittle phases [4, 41]. These phases can accumulate dislocations, causing void formation and cracking within the intermetallics and lead to early failure. The increase in the amount of Q phase may also have a delaying effect on the interdendritic failure by slowing down slip in the intragranular region. Thermodynamic calculations showed that the amount of the Q precipitates increases from 0.92% in the MG5R alloy to 1.52% in the MG5R and MG7R alloy.

Table 9.6 Mechanical properties of the MG5R and dispersion strengthened MG3R alloys at 300 ºC

Alloy	Tensile			Creep	
	$YS\ (MPa)$	$UTS\ (MPa)$	$El\ (\%)$	$\sigma_{th}\ (MPa)$	n_a
MG5R	46	58.5	25	10.6	~ 9
MG3R + 0.3Mo	45	55	51.7	20	~ 22

Table 6 compares the mechanical properties of the MG3R alloy strengthened by Mo-containing dispersoids [13] and MG5R with a higher amount of the Q precipitates. Both alloys show almost the same YS and UTS, however, the elongation of the Mo-containing alloy is ~ 100% higher than the MG5R alloy. Lower ductility of the MG5R alloy is due to the presence of the π intermetallics within the microstructure after solution treatment. The Mo-containing alloy also exhibits higher creep resistance; Mo forms thermally stable coherent dispersoids within the Al matrix which results in an effective dislocation pinning during creep deformation. From an alloy design perspective, the MG5R alloy may be used if strength is of prime concern. For applications where thermal fatigue is a concern (such as the Diesel engine) both strength and ductility are required. Further development could involve MG5R as a base alloy with additions such as Mo to increase ductility by eliminating the π phase and to improve creep resistance by forming thermally stable coherent dispersoids.

9.4 Conclusions

The effect of Mg on phase formation of the Al-7Si-0.5Cu-(0.3-0.7Mg) alloys was investigated via thermodynamic calculations, microstructural characterizations, DSC and CCA. The tensile strength (room temperature and 300 °C) and creep resistance were explained in terms of the constituent phases. The following conclusions can be drawn:

1. Calculations show that in this alloy system the maximum solid solubility of Mg in the Al matrix is 0.47% at 554 °C. Mg above this was seen to remain within the microstructure in the form of the π-$Al_8Mg_3FeSi_6$ and β-Mg_2Si intermetallics after solution treatment.
2. Thermodynamic calculations show that the Q-$Al_5Cu_2Mg_8Si_6$ phase is the only age-hardening phase stable at 300 °C, the amount of which increases from 0.9 to 1.5 % by increasing the Mg content from 0.3 to 0.5%. Results were confirmed by the DSC analysis and TEM observations.
3. The YS and UTS at 300 °C showed ~ 30% and ~ 50% increase, respectively when the Mg level increased from 0.3% to 0.5%. The elongation was decreased by ~ 20%. A significant improvement in creep resistance was also observed at high Mg levels.
4. The increase in strength with Mg is attributed to the higher amounts of the Q precipitate and the promotion of Orowan strengthening.
5. The lower ductility of the alloys with increased Mg content is attributed to the presence of the brittle π-$Al_8Mg_3FeSi_6$ intermetallics which undergo cracking during deformation. It is important to eliminate or modify this phase for the development of an effective elevated temperature Al alloy.

9.7 Acknowledgments

This work was supported by the NSERC (Natural Sciences and Engineering Research Council of Canada) Strategic project grant with Rio Tinto Alcan (RTA). Amir Rezaei Farkoosh would like to gratefully acknowledge the financial support of McGill University through MEDA (McGill Engineering Doctoral Award) program. A part of the research presented in this paper was financed by the Fonds de recherche du Québec - Nature et technologies by the intermediary of the Aluminium Research Centre – REGAL. Special thanks to Mousa Javidani for fruitful discussions.

9.6 References

[1] M. Garat, G. Laslaz, Improved Aluminum Alloys for Common Rail Diesel Cylinder Heads, in: AFS, IL, USA, 2007, pp. 1-8.

[2] G.E. Dieter, Mechanical metallurgy, McGraw-Hill, New York, 1986.

[3] A.R. Farkoosh, M. Javidani, M. Hoseini, D. Larouche, M. Pekguleryuz, Phase formation in as-solidified and heat-treated Al–Si–Cu–Mg–Ni alloys: Thermodynamic assessment and experimental investigation for alloy design, J. Alloys Compd., 551 (2013) 596-606.

[4] A.R. Farkoosh, M. Pekguleryuz, The effects of manganese on the T-phase and creep resistance in Al–Si–Cu–Mg–Ni alloys, Mater. Sci. Eng., A, 582 (2013) 248-256.

[5] A. R. Farkoosh , X. G. Chen , M. Pekguleryuz, The Effects of Mg, Mo and Cr on the Microstructure and Elevated Temperature Mechanical Properties of an Al-Si-Cu-Mg Alloy, Mater. Sci. Technol., (2013) 1220-1227.

[6] L. Heusler, F.J. Feikus, M.O. Otte, Alloy and Casting Process Optimization for Engine Block Application, in: AFS Trans, 2001, pp. 215-223.

[7] F.J. Feikus, Optimisation of AlSi Cast-Alloys for Cylinder Head Applications, in: AFS, Georgia, USA, 1998, pp. 1-21.

[8] M. Murayama, K. Hono, Pre-precipitate clusters and precipitation processes in Al–Mg–Si alloys, Acta Mater., 47 (1999) 1537-1548.

[9] G. Sha, H. Möller, W.E. Stumpf, J.H. Xia, G. Govender, S.P. Ringer, Solute nanostructures and their strengthening effects in Al–7Si–0.6Mg alloy F357, Acta Mater., 60 (2012) 692-701.

[10] J.Y. Hwang, R. Banerjee, H.W. Doty, M.J. Kaufman, The effect of Mg on the structure and properties of Type 319 aluminum casting alloys, Acta Mater., 57 (2009) 1308-1317.

[11] C.H. Cáceres, M.B. Djurdjevic, T.J. Stockwell, J.H. Sokolowski, The effect of Cu content on the level of microporosity in Al-Si-Cu-Mg casting alloys, Scripta Mater., 40 (1999) 631-637.

[12] K.E. Knipling, D.C. Dunand, D.N. Seidman, Criteria for developing castable, creep-resistant aluminum-based alloys-A review, Zeitschrift fur Metallkunde, 97 (2006) 246.

[13] A.R. Farkoosh, X.-G. Chen, M. Pekguleryuz, Dispersoid Strengthening of a High Temperature Al-Si-Cu-Mg Alloy via Mo Addition, submitted to Materials Science and Engineering: A, (2014).

[14] Q.G. Wang, C.J. Davidson, Solidification and precipitation behaviour of Al-Si-Mg casting alloys, J Mater. Sci, 36 (2001) 739-750.

[15] P. Ouellet, F.H. Samuel, Effect of Mg on the ageing behaviour of Al-Si-Cu 319 type aluminium casting alloys, J Mater. Sci, 34 (1999) 4671-4697.

[16] C. Caceres, C. Davidson, J. Griffiths, Q. Wang, The effect of Mg on the microstructure and mechanical behavior of Al-Si-Mg casting alloys, Metall. Mater. Trans. A, 30 (1999) 2611-2618.

[17] Q.G. Wang, C.H. Cáceres, The fracture mode in Al–Si–Mg casting alloys, Mater. Sci. Eng., A, 241 (1998) 72-82.

[18] Q.G. Wang, D. Apelian, D.A. Lados, Fatigue behavior of A356/357 aluminum cast alloys. Part II – Effect of microstructural constituents, Journal of Light Metals, 1 (2001) 85-97.

[19] S. Murali, K.S. Raman, K.S.S. Murthy, Effect of magnesium, iron (impurity) and solidification rates on the fracture toughness of Al-7Si-0.3Mg casting alloy, Mater. Sci. Eng., A, 151 (1992) 1-10.

[20] J.O. Andersson, T. Helander, L. Höglund, P. Shi, B. Sundman, Thermo-Calc & DICTRA, computational tools for materials science, Calphad, 26 (2002) 273-312.

[21] C.-T. Wu, S.-L. Lee, M.-H. Hsieh, J.-C. Lin, Effects of Mg Content on Microstructure and Mechanical Properties of Al-14.5Si-4.5Cu Alloy, Metall. Mater. Trans. A, 41 (2010) 751-757.

[22] G.H.W.F.H.J. Höhne, Differential scanning calorimetry : an introduction for practitioners, Springer, Berlin; New York, 2003.

[23] A. Biswas, D.J. Siegel, D.N. Seidman, Compositional evolution of Q-phase precipitates in an aluminum alloy, Acta Mater., 75 (2014) 322-336.

[24] C. Wolverton, Crystal structure and stability of complex precipitate phases in Al–Cu–Mg–(Si) and Al–Zn–Mg alloys, Acta Mater., 49 (2001) 3129-3142.

[25] D.A. Porter, K.E. Easterling, Phase Transformations in Metals and Alloys, (Revised Reprint), CRC press, 1992.

[26] A.P. Sutton, R.W. Balluffi, Interfaces in Crystalline Materials, OUP Oxford, 2006.

[27] V. Vaithyanathan, C. Wolverton, L.Q. Chen, Multiscale modeling of θ′ precipitation in Al–Cu binary alloys, Acta Mater., 52 (2004) 2973-2987.

[28] A. Biswas, D.J. Siegel, D.N. Seidman, Simultaneous segregation at coherent and semicoherent heterophase interfaces, Phys. Rev. Lett., 105 (2010) 076102.

[29] K. Matsuda, D. Teguri, Y. Uetani, T. Sato, S. Ikeno, Cu-segregation at the Q′/α-Al interface in Al–Mg–Si–Cu alloy, Scripta Mater., 47 (2002) 833-837.

[30] C.R. Hutchinson, X. Fan, S.J. Pennycook, G.J. Shiflet, On the origin of the high coarsening resistance of Ω plates in Al–Cu–Mg–Ag Alloys, Acta Mater., 49 (2001) 2827-2841.

[31] M. Warmuzek, Aluminum-silicon casting alloys: atlas of microfractographs, Asm Intl, 2004.

[32] Q. Wang, C. Caceres, J. Griffiths, Damage by eutectic particle cracking in aluminum casting alloys A356/357, Metall. Mater. Trans. A, 34 (2003) 2901-2912.

[33] L.F. Mondolfo, Aluminum alloys : structure and properties, Butterworths, London; Boston, 1976.

[34] V.S. Zolotorevskii, N.A. Belov, M. Glazoff, Casting aluminum alloys, in, Elsevier, Amsterdam; Boston; London, 2007.

[35] S. Spigarelli, E. Evangelista, S. Cucchieri, Analysis of the creep response of an Al–17Si–4Cu–0.55Mg alloy, Mater. Sci. Eng., A, 387–389 (2004) 702-705.

[36] E. Arzt, Creep of dispersion strengthened materials: a critical assessment, Res. Mechanica, 31 (1991) 399.

[37] R. Kaibyshev, F. Musin, E. Avtokratova, Y. Motohashi, Deformation behavior of a modified 5083 aluminum alloy, Mater. Sci. Eng., A, 392 (2005) 373-379.

[38] H. Watanabe, H. Tsutsui, T. Mukai, M. Kohzu, S. Tanabe, K. Higashi, Deformation mechanism in a coarse-grained Mg–Al–Zn alloy at elevated temperatures, Int. J. Plast., 17 (2001) 387-397.

[39] K.E. Knipling, D.C. Dunand, Creep resistance of cast and aged Al–0.1Zr and Al–0.1Zr–0.1Ti (at.%) alloys at 300–400 °C, Scripta Mater., 59 (2008) 387-390.

[40] A. Bahrami, A. Miroux, J. Sietsma, An Age-Hardening Model for Al-Mg-Si Alloys Considering Needle-Shaped Precipitates, Metall. Mater. Trans. A, 43 (2012) 4445-4453.

[41] M. Celikin, A.A. Kaya, M. Pekguleryuz, Effect of manganese on the creep behavior of magnesium and the role of α-Mn precipitation during creep, Mater. Sci. Eng., A, 534 (2012) 129-141.

CHAPTER 10

CONCLUSIONS AND SUGGESTIONS FOR FUTURE RESEARCH

11.1 Conclusions

The long-term goal of this doctoral work was to develop creep resistant Al-Si cast alloys for Diesel engine applications. To this end, new alloys with Ni, Mn and Mo additions to Al-Si-Mg-Cu based alloys were developed. The alloy development strategy was to create thermally stable dispersoids in order to enhance mechanical performance at elevated temperature. The following major conclusions are drawn from this research:

11.1.1 Al–Si–Cu–Mg–Ni alloys

Phase formation

1. The as-solidified microstructures of the Ni-containing alloys consisted of *T*-Al_9FeNi, γ-Al_7Cu_4Ni, δ-Al_3CuNi and ε-Al_3Ni intermetallic phases formed in the interdendritic regions of the Al-7Si-0.5Cu-0.35Mg alloys during solidification. Calculations revealed that the Ni:Cu and Ni:Fe ratios control precipitation in this alloy system. The pre-eutectic freezing range of the alloys increased with Ni content leading to higher amounts of porosity.

2. No Ni-containing dispersoid phases were observed; aged microstructures mainly consisted of the θ-Al_2Cu and Q-$Al_5Mg_8Cu_2Si_6$ age-hardening precipitates, coarse *T*-Al_9FeNi intermetallics, as well as the Si particles in the interdendritic regions. The γ-Al_7Cu_4Ni and δ-Al_3CuNi intermetallics decompose during solution treatment and do not re-form after ageing at 200 °C; at 300 °C, the δ-Al_3CuNi phase re-appears within the microstructure.

Creep resistance and the effect of Mn modification

3. Ni up to 0.6%, increased the yield strength of the overaged alloys at 300 °C, because of the presence of thermally stable Ni-containing intermetallics within the microstructure, however, the effect is negligible at low temperatures.

4. The δ-Al_3CuNi phase made a greater contribution to the strength of the overaged alloys as compared to the other Ni-bearing intermetallics. The maximum amount of this phase can be obtained at Ni:Cu ≈ 1.5.

5. The creep resistance decreased with Ni, due to the severe cracking of the brittle *T*-Al_9FeNi intermetallics in the early stages of creep deformation, which lead to the weakening of the interdendritic regions and a decrease in creep resistance. The decrease in the creep resistance was proportional to the amount of the *T*-Al_9FeNi intermetallics within the alloy microstructure.

6. The re-formation of the Ni- and Cu-containing phases during creep process at 300 °C, which decreased the Cu content of the matrix, was another factor that led to the accelerated creep deformation of the Ni-containing alloys.

7. Mn addition to the Ni-containing alloys mitigated the adverse effects of the *T*-Al_9FeNi intermetallics on creep resistance by modifying these intermetallics, preventing cracking during early stages of creep deformation.

11.1.2 Al–Si–Cu–Mg–Mo alloys

Dispersoid formation with Mo and the effect on creep

8. A low level (0.3%) addition of Mo leads to the formation of a substantial amount of nanoscale α-Al-(Fe,Mo)-Si dispersoids during solution treatment in the Al-7Si-0.5Cu-0.3Mg alloy. These dispersoids exhibit thermal stability; no coarsening is observed at 300 °C.

9. The presence of these thermally stable dispersoids results in significant improvements in the tensile and creep properties of the Mo-containing alloy at 300 °C compared to the base alloy. The YS, UTS and El of the Mo-containing alloy were increased by about 25, 15 and 35% respectively. As much as a 95% decrease in the minimum creep rate was observed at 30 MPa and the creep time-to-fracture increased by two orders of magnitude (from 50 min to 1500 min). Improvements in elongation were attributed to the elimination of the brittle β-Al_5FeSi intermetallics upon Mo addition.

10. Both the Mo-containing and base alloys fractured in a ductile manner after tensile creep testing at 300 °C and 30 MPa. Three distinct stages of fracture were identified as: i) void nucleation and growth, ii) flow localization between primary larger pores and accelerated void growth and iii) void coalescence along the flow localization path. Stage (i) was delayed in the Mo-containing alloy because of the reduced dislocation activity by dispersoids which resulted in the increased creep time-to-failure.

Precipitation and crystallography of the α-Al(Fe,Mo)Si dispersoids

11. Quantitative EDS analysis revealed that these dispersoids are quaternary with the approximate stoichiometric formula of $Al_{22}(Fe_{6-8}Mo)Si_4$. Their crystal structure was determined to be BCC with lattice parameter, $a_0 = 12.54 \pm 0.03\, \overset{\circ}{A}$ and space group Im3. Structural analysis revealed that the BCC dispersoids (icosahedral phase) are strongly correlated with the FCC Al matrix. The following orientation relationship was determined between the Al matrix and most of the dispersoids: $\langle 001\rangle_d // \langle 001\rangle_m$ and $\{350\}_d // \{002\}_m$.

12. The average equivalent diameter of the dispersoids increased with time during solution treatment at 540 °C. Fine dispersoids were seen to be coherent with the Al matrix with a high coherency strain at the dispersoid/matrix interface.

13. The superior strengthening efficiency of the dispersoids was related to their coherency with the matrix and their large amounts.

Creep resistance and mechanisms of the Al-Si-Cu-Mg-Mo alloy at 300-350 °C

14. A detailed creep investigation of the Mo-containing alloy revealed three distinct creep deformation regions: (i) diffusion creep, (ii) dislocation creep and (iii) Orowan bowing.

15. Dislocation creep region exhibited high activation energy values in the range of 445-568 kJ/mol. Threshold stress approach yielded activation energy values in the range of 145-185 kJ/mol, consistent with the dislocation climb controlled mechanism.

16. Decreasing the dispersoid size significantly increased the creep resistance and delayed the transition to region (iii) by promoting the Orowan strengthening.

11.1.3 The important role of Mn: the interaction between molybdenum and manganese and its influence on creep resistance at 300-350 ^{o}C

17. Mn addition up to 0.5% to the Mo-containing alloy increased the number of the dispersoids per unit area; the average dispersoid size decreased. Mn addition also eliminated the dispersoid-free zones (DFZ) and led to a uniform distribution of dispersoids. Mn at more than 0.5% increased the amount of the interdendritic intermetallics.

18. The crystal structure of the dispersoids did not alter with Mn addition, however, the lattice constant slightly increased.

19. The minimum creep rate, creep time-to-fracture and strain-to-fracture at 300 ^{o}C, 30 MPa increased significantly with increasing Mn up to 0.5 wt.%, which is attributed to the increased amount of the dispersoids and the elimination of DFZs.

20. Mn exceeding 0.5% decreased the creep time-to-fracture because of the formation of a large amount of interdendritic intermetallics.

21. The creep fracture mode at 300 ^{o}C, 30 MPa, changed from ductile interdendritic to brittle interdendritic.

11.1.4 The Effects of Mg and the Q-precipitate phase on mechanical properties at 300 ^{o}C

22. Mg up to 0.47 wt.% significantly increased the tensile strength and creep resistance at the expense of some ductility.

23. The Q-$Al_5Mg_8Cu_2Si_6$ phase was the main strengthening precipitate phase that is thermodynamically stable at 300 ^{o}C.

24. Mg, up to 0.47 wt.%, can completely dissolve in the matrix after solution treatment and contribute to the dispersion hardening (Orowan strengthening) of the alloys by increasing the amount of the Q-$Al_5Mg_8Cu_2Si_6$ precipitates.

25. The lower ductility of the alloys with high Mg content was related to the presence of the brittle π-$Al_8FeMg_3Si_6$ intermetallics within the heat-treated microstructure of these alloys.

11.2 General Conclusion

The most performant alloy developed and investigated in this doctoral study is the Al-Si-Cu-Mg-Mo-Mn alloy because of its fine and uniform distribution of thermally stable coherent dispersoids and improved creep resistance which make it a highly potential alloy for use in Diesel engines. Mo addition is very significant as it leads to the formation of thermally stable dispersoids which are further improved with Mn. Although, Mg was found to be important for increasing the strength of the base alloy, it may lead to lower ductility and have an adverse effect on crack initiation. Ni did not provide a good basis for mechanical performance because of the appearance of brittle phases in the microstructure. The table below gives a synopsis of the general conclusions for each of the alloys investigated in this dissertation.

Alloy	**Composition (wt.%)**	**Comments and comparison to the base alloy**
MG3RXN	Al7Si0.5Cu0.3Mg (0.1-1.0)Ni(0.0-1.0)Mn	These alloys showed higher strength at 300 °C, but lower creep resistance, can be used if strength is of prime concern
MG3R3M	Al7Si0.5Cu0.3Mg 0.3Mo	Shows a good combination of elevated temperature strength, creep and ductility
MG3R3MXMn	Al7Si0.5Cu0.3Mg 0.3Mo(0.0-1.0)Mn	The most performant alloy developed, creep resistance is higher than the MG3R3M alloy
MG3-7R	Al7Si0.5Cu(0.3-0.7)Mg	The alloys with higher Mg levels showed higher strength and creep resistance at elevated temperatures, further modification for improved ductility is required

11.2 Suggestions for future research

Excellent progress has been made in this doctoral study towards the development of an aluminum alloy for use in Diesel engine applications. The future work in this study are both scientific, developmental and commercial.

11.2.1 Scientific research

1. A study on the coarsening kinetics of dispersoids at solution treatment temperatures, coarsening mechanism should be understood by determination of the activation energies.
2. The effect of Mn on the orientation relationship and coherency of the Mo-containing dispersoids with the Al matrix should be investigated.
3. Molecular Dynamic (MD) or Phase Field Crystal (PFC) simulation of the interaction of dislocations and slow-diffusing alloying elements during creep deformation.
4. Atom Probe Tomography (APT) analysis of dislocations in the alloys developed to investigate the core structure of the dislocations.

11.2.2 Alloy development studies

1. Fatigue and thermal fatigue study on the alloys developed with Mo and Mn additions.
2. The effect of increased Mg content on the mechanical properties of the Mo-containing alloys. Optimum amount of Mo addition should be determined with respect to Mn addition. Studying the effect of other alloying elements in combination with Mo and Mn.
3. A study of the effect of cooling rate on the dispersoid formation.
4. It is of interest to see the behaviour of the alloys developed in large scale castings with inhomogeneous cooling rates.

12.2.3 Commercial development

Alloys developed at an R&D level need to be evaluated, optimized and validated at the industrial level before they can be adopted for commercial use. These are best addressed through industrial partnerships. A McGill report of invention (ROI) has been prepared for the most potential alloy (with Mo and Mn additions) and a patent application is envisaged. Along these lines, potential industrial partnerships should be realized especially with European OEMs or engine suppliers. Among the potential OEMs, BMW and Renault can be cited. BMW is an ideal partner because they have tendency to heavily invest in engine development. Renault is suggested because of their previous recent involvement in aluminum Diesel engine development with Rio Tinto Alcan.

CHAPTER 11

CONTRIBUTIONS TO ORIGINAL KNOWLEDGE

In this doctoral work, through studying the behaviour of three slow diffusing alloying elements, Ni, Mn and Mo, in Al and systematic combination of these elements, highly creep resistant Al-Si cast alloys have been developed.

11.1 Nickel in Al-Si alloy systems

1. The behaviour of Ni at low levels in Al-Si cast alloys has been studied. For the first time, multicomponent Al–Si–Cu–Mg–Ni–Fe phase diagrams in the range of engine alloys and Ni below 1% have been calculated and validated by experimental analysis. Non-equilibrium microstructures developed during solidification have also been studied through Scheil calculations and experimental investigations.

2. The effect of different Ni-containing intermetallics of the Al–Si–Cu–Mg–Ni–Fe system on strengthening mechanisms has been identified. The role of the brittle Ni-containing interdendritic intermetallics (*T*-Al_9FeNi) in deteriorating the creep resistance was

investigated and related to the early cracking of these intermetallics as a result of dislocation pile-up at the intermetallic/matrix interface. This finding is important to the general understanding of the creep mechanism in alloys containing brittle phases.

3. It was shown that contrary to general expectations, Ni-containing Al-Si-Cu-Mg alloys do not provide an appropriate base for development of creep-resistant elevated temperature cast alloys. However, it was discovered that Mn at trace level can modify the *T*-Al_9FeNi and prevent early cracking of the intermetallics during creep deformation. This opens a new research field in investigating the effects of trace additions to Al alloys to develop performant high temperature alloys.

12.2 Molybdenum in Al-Si alloy systems

1. For the first time, the behaviour of Mo as an alloying addition in conventionally cast Al alloys has been studied. It was shown that Mo addition at low levels can form a large amount of thermally stable dispersoid phase in the Al matrix.

2. The crystal structure and orientation relationship of the novel Mo-containing dispersoids with the Al matrix have been determined through experimental TEM and HRETM analysis along with SAED pattern and HRTEM image simulations.

3. A structural correlation between the crystals of the dispersoids (BCC, complex Icosahedral phase) and Al (FCC) has been found and explained in terms of the similarity between Mackay icosahedron and cuboctahedral shells of Al atoms.

4. The interfacial structure of the Mo-containing dispersoids with the Al matrix has been studied with experimental HRTEM and interface simulations. The possibility of having coherent Mo-containing dispersoids in the Al matrix with high misfit strains was explained.

5. The formation of the dispersoids in large amounts and their coherency with the Al matrix was related to the structural correlation between the dispersoids and Al.

6. The underlying creep deformation mechanisms and micro-mechanisms in the Al-7Si-0.5Cu-0.3Mg-0.3Mo alloy, possessing fine Mo-containing dispersoids were identified in

different stress and temperature ranges by determining the activation energies and stress exponents, applying threshold stress approach and in-depth TEM investigations. The role of the dispersoids in creep deformation processes was explained.

7. A new method for determining the apparent activation energies has been implemented, which yields a temperature and stress dependent apparent activation energy for creep of dispersion hardened alloys.
8. A direct method of estimating activation energies for creep of dispersion strengthened alloys has been proposed based on discrete creep micro-mechanisms.
9. Creep fracture mechanisms of the alloys at 300 °C were identified by interrupted creep tests and SEM analysis; the role of dispersoids in this regard was explained.

11.3 Molybdenum and Manganese interaction in Al-Si alloy systems

1. The present work is the first to study the combined addition of Mo and Mn in Al-Si alloys. On the basis of this study, a new multicomponent alloy system, Al-Si-Mo-Mn has been proposed which provides a basis for development of highly creep resistant cast alloy.
2. It was shown that Mn incorporates into the crystal structure of the Mo-containing dispersoids which leads to a significant increase in the amount of dispersoids within the Al matrix and consequently superior creep resistance. Mn also increased the homogeneity of the dispersoid distribution within the Al matrix.
3. The precipitation and distribution of the new Mo- and Mn-containing dispersoids has been studied. Their crystal structure has been determined by TEM analysis.
4. Creep fracture mechanisms of the alloys at 300 °C were identified. It was shown that strengthening the interdendritic regions of Al-Si cast alloys by dispersoid phase may change the fracture behaviour of the alloys; the role of dispersoids in this regard was explained.
5. The fundamental concept developed as a result of this study is that a specific combination of solutes with opposite partitioning coefficients can be applied to generate a uniform

distribution of dispersoids in cast alloys and prevent the formation of dispersoid-free zones (DFZ) near the dendrite and grain boundaries. The uniform dispersoid distribution and the elimination of the DFZ can greatly improve creep resistance. This finding is a major contribution to future alloy development activities in creep resistant alloys.

11.4 Magnesium in Al-Si-Cu-Mg system

1. Thermodynamic calculations and TEM investigations revealed that the Q-$Al_5Mg_8Cu_2Si_6$ phase is the only age-hardening precipitate in this alloy system that is thermodynamically stable at 300 °C.

2. The maximum solid solubility of Cu and Mg in this alloy system was calculated.

3. On the basis of these findings, it was proposed and proved that increasing the volume fraction of the Q-$Al_5Mg_8Cu_2Si_6$ precipitates is possible by increasing the Mg content of the alloys.

4. The strengthening effect of the age-hardening precipitates at temperatures well above the ageing temperature has been investigated.

11.5 Insight into alloy design principles for creep resistance in Al-Si cast alloys

The following key design principles and considerations were developed during the course of this study, which provides a basis for development of a new class of creep resistant Al cast alloys:

1. Interdendritic intermetallics may impart strength and provide grain boundary strengthening, however, their ductility is crucial to avoid early cracking during creep as a result of dislocation pile-up at the intermetallic/precipitate interface.

2. Alloying additions that form intermetallic phases with the constituent elements of the age-hardening precipitates must be avoided as they may lead to lower strength and creep resistance over time by depletion of age-hardening precipitates of the matrix.

3. Slow-diffusing alloying elements should have some solubility in liquid and solid Al to form a supersaturated solid solution during solidification. Such additions can form a large amount of

thermally stable dispersoid within the Al matrix. Highly desirable precipitates are those with high coherency strain.

4. It is possible to increase the volume fraction of the dispersoid phase in the Al matrix by further alloying with elements of specific properties. The choice of additional alloying element depends on the nature of the dispersoids: it must be (i) able to incorporate into the structure of the dispersoids or from similar dispersoids, (ii) slow-diffuser in Al and (iii) soluble in solid Al.

5. A uniform distribution of dispersoids can be obtained through combined addition of dispersoid formers with opposite partitioning behaviours (eutectic and peritectic).

6. On the basis of the results of this study, it is suggested that the trace addition of Mo can be used to modify the common Mn-containing Al alloys for improved dispersoid properties.

APPENDIX A

The thermal stability of the Mo-containing dispersoids

The coarsening rate constant, K, at 300 °C of the common thermally stable precipitates formed in Al alloys are estimated using $K \propto \frac{\gamma D C_m}{RT}$ [1] and given in Table 1. The interfacial free energy, γ is assumed to be constant (500 mJm^{-2}) for all the precipitates. The solubility limit of the rate-controlling solute atoms, C_m are calculated using FactSage. Calculations show that the coarsening rate constant for Mo–containing dispersoids is orders of magnitude less than the common thermally stable precipitates in Al alloys. This suggests that these dispersoids are highly stable at the service temperature of Diesel engines.

Table 1 Coarsening rate constants at 300 °C for common thermally stable precipitates in Al alloys along with the diffusivity of the rate-controlling constituent solutes [2-5]

Solute	Precipitate	D_o (m^{2}s^{-1})	Q (kJ mol^{-1})	D at 300°C (m^{2}s^{-1})	C_m at 300°C (wt.%)	K at 300°C (mol s^{-1})
Al	FCC	1.4×10^{-5}	143	1.3×10^{-18}	*NA*	*NA*
Sc	Al_3Sc	5.3×10^{-4}	173	9.0×10^{-20}	2.7×10^{-3}	$\sim 10^{-26}$
Zr	Al_3Zr	7.3×10^{-2}	242	6.3×10^{-24}	3.1×10^{-3}	$\sim 10^{-30}$
Mo	Al-(Fe,Mo)-Si	1.4×10^{-3}	250	2.3×10^{-26}	1.8×10^{-3}	$\sim 10^{-33}$
Mn	Al-(Fe,Mn)-Si	8.7×10^{-3}	208	9.5×10^{-22}	1.9×10^{-2}	$\sim 10^{-27}$
Cu	Al_2Cu	6.5×10^{-5}	136	2.6×10^{-17}	4.8×10^{-1}	$\sim 10^{-22}$

References

[1] H. Calderon, P. Voorhees, J. Murray, G. Kostorz, Ostwald ripening in concentrated alloys, Acta Metall. Mater., 42 (1994) 991-1000.

[2] K.E. Knipling, D.C. Dunand, D.N. Seidman, Criteria for developing castable, creep-resistant aluminum-based alloys-A review, Zeitschrift fur Metallkunde, 97 (2006) 246.

[3] N. van Chi, D. Bergner, Diffusion of Mo and W in Al, in: F.J. Kedves, D.L. Beke (Eds.) DIMETA-82: Diffusion in Metals and Alloys, Trans Tech Publications, Switzerland, 1983, pp. 334-337.

[4] Y. Du, Y.A. Chang, B. Huang, W. Gong, Z. Jin, H. Xu, Z. Yuan, Y. Liu, Y. He, F.Y. Xie, Diffusion coefficients of some solutes in fcc and liquid Al: critical evaluation and correlation, Mater. Sci. Eng., A, 363 (2003) 140-151.

[5] D.A. Porter, K.E. Easterling, Phase transformations in metals and alloys, Chapman & Hall, London; New York, 1992.